ION PERMEATION AND

CALCIUM-DEPENDENT REGULATION

OF THE BESTROPHIN CHANNEL

by

George Vaisey

A Dissertation

Presented to the Faculty of the Louis V. Gerstner, Jr.

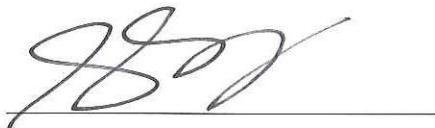Graduate School of Biomedical Sciences,

Memorial Sloan Kettering Cancer Center

In Partial Fulfillment of the Requirements for the Degree of

Doctor of Philosophy

New York, NY

September, 2018

_____   October 12, 2018
Stephen B. Long, PhD   Date
Dissertaion Mentor

DEDICATION

In memory of my great uncle, Harry Persaud, whose lively and curious imagination could swell a room and who would've been sincerely thrilled to read this work.

ABSTRACT

Bestrophins (BEST) are a family of Ca^{2+}-activated Cl^- channels, consisting of four paralogs in humans, BEST1-4, with broad tissue distribution and proposed biological roles in a range of sensory transduction processes. BEST1, the most characterized of the four, is expressed in the retinal pigment epithelium, and mutations in human BEST1 are associated with retinal degenerative diseases. Electrical recordings of bestrophins by whole-cell patch clamp studies have elucidated key biophysical properties of these channels. Bestrophins are selective for monovalent anions (of which Cl^- is the most abundant biologically) and obey a lyotropic permeability sequence such that $SCN^- > I^- > Cl^- > Br^-$. Bestrophins require Ca^{2+} for activation and also appear to be regulated by phosphorylation and changes in cell volume.

Because bestrophins are unrelated to any other family of ion channels, what endows them with their characteristic properties and the mechanisms of their function, at the molecular level, remain unclear. A major breakthrough came in 2014 when our lab determined the first high-resolution structure of a eukaryotic bestrophin, chicken BEST1, using x-ray crystallography. The crystal structure revealed the pentameric architecture of bestrophins and distinguishing features, including notable constrictions within the ion pore as well as a Ca^{2+}-binding site. Still, how these featues determine the behaviors of BEST1 and how the channel opens and closes, was unknown.

Here, using the crystal structure as a starting point and framework, I employ a combination of electrophysiology, biochemical approaches and structural methods to interrogate ion permeation and Ca^{2+}-dependent regulation of BEST1. From electrophysiological recordings of purified wild type and mutant BEST1 channels I

identify regions important for ion selectivity and Ca^{2+} activation. A "neck" region, consisting of three highly conserved hydrophobic amino acids, acts as the activation gate, responding to Ca^{2+}-binding at a cytosolic "clasp". A constriction at the cytosolic side of the channel, the "aperture", acts as a size-selective filter, endowing the channel with its characteristic lyotropic permeability sequence.

Electrical recordings of purified BEST1 enabled me to investigate a current "rundown" phenomenon, whereby currents recorded by whole cell patch clamp were shown to decrease over time. I find that current rundown is an inherent property of BEST1, now characterized as inactivation. Inactivation depends on the cytosolic concentration of Ca^{2+}, with higher concentrations stimulating inactivation and is governed by an allosteric mechanism of a C-terminal inactivation peptide binding to a receptor site on the channel.

Using a non-inactivating mutant of BEST1 I am able to obtain both the Ca^{2+}-bound closed and Ca^{2+}-bound open channel states, revealing for the first time the conformational changes that drive channel opening. Repositioning of tethered pore-lining helices dramatically widen the pore at the neck to generate an open conformation, consistent with electrophysiological studies identifying this region as the channel activation gate.

Preliminary studies demonstrate that BEST1 is inhibited by increases in the cytosolic concentration of Cl^-, which may be a mechanism by which this channel is regulated by cell volume.

The work presented here enables a detailed description of BEST1 channel gating and function at the molecular level. Our improved understanding lays the groundwork for

interrogation of additional bestrophin channel properties, such as cell volume-dependent

regulation, and provides a lens through which to understand molecular differences

between bestrophin paralogs, which appear to have distinct physiological roles.

ACKNOWLEDGEMENTS

First and foremost I would like to thank my mentor, Dr. Stephen Long. The work of Steve's lab stood out to me during my final year as an undergraduate in the UK and I am so thrilled to have made a contribution to its legacy. It has been a special experience to witness first-hand how Steve thinks and writes about science. I am leaving this lab a better scientist than I could've hoped for and for that I am forever grateful.

I would also like to thank the lab as a whole – members past and present. The nightmarish stories about competition and animosity that can be prevalent in successful labs have never been true here. From the beginning to the end of my time in this lab everyone has been supportive, encouraging and a delight to work with. In particular I would like to thank Dr. Melinda Diver for being a source of inspiration - I was in awe of the stamina and tenacity she displayed working through a very challenging project. I would also like to thank Dr Alexandria Miller for being a superb colleague to team up with on some of the work discussed here.

I have been very fortunate to have a wonderful thesis advisory committee: Dr. Christopher Lima, Dr. Scott Keeney and Dr. David Gadsby. Having a team of people who are able to help me think about my work in different and smarter ways has been a great boon to my progress. I would like to thank David for supplying me with tea, beer and very astute advice about my future in science.

My trajectory in life would not be what it is if not for three teachers at secondary school who took an interest in my development: Siobhan Lancaster, John Lee and Monica Islam. They introduced me to my favorite writers: Austen, Donne and Auden (and how to read them properly) and to imagine a future for myself that I may not otherwise have imagined.

I am indebted to the Department of Biochemistry at the University of Oxford, where I received the best possible kind of education. The notion that before deciding what you want to do you should know as much as possible (genetics, structural biology, developmental biology etc), though making this degree likely one of the hardest things I will ever have done, has and will continue to serve me well. Particularly I would like to

TABLE OF CONTENTS

LIST OF TABLES

LIST OF FIGURES

LIST OF ABBREVIATIONS

ACMA   9-amino-6-chloro-2-methoxyacridine

AEBSF   4-2(2-aminoethyl)benzenesulfonyl fluoride hydrochloride

ARB   Autsomal recessive bestrinopathy

BAPTA   1,2-bis(o-aminophenoxy)ethane-N,N,N',N'-tetraacetic acid

BEST   Bestrophin

BVMD   Best vitelliform macular dystrophy

CCCP   Carbonyl cyanide m-chlorophenyl hydrazone

DDM n-Dodecyl β-D-maltoside

DIDS   4,4'-Diisothiocyanatostilbene-2,2'-disulfonic acid disodium salt

DMSO   Dimethyl sulfoxide

DTT   Dithiothreitol

ECL   Enhanced chemiluminescence

EGTA   Ethylene glycol-bis(2-aminoethylether)-N,N,N',N'-tetraacetic acid

EM   Electron microscopy

EOG   Electrooculogram

Fab   Fragment, antigen binding region of an antibody

FSC   Fourier shell correlation

HEK   Human embryonic kidney

HRP   Horseradish peroxidase

I-V   Current-voltage

iPSC   Induced pluripotent stem cell

mAb   Monoclonal antibody

MTS   Methanethiosulfonate

NPPB   5-Nitro-2-(3-phenylpropylamino)benzoic acid

PCR   Polymerase chain reaction

PDB   Protein data bank

PEG   Poly(ethylene glycol)

PKC   Protein kinase C

PMA   Phorbol 12-myristate 13-acetate

POPE   1-palmitoyl-2-oleyoyl-sn-glycero-3-phosphoethanolamine

POPG   1-palmitoyl-2-oleoyl-sn-glycero-3-phospho-(1'-rac-glycerol)

POS   Photoreceptor outersegment

PP2A   Protein phosphatase 2A

PVDF   Polyvinylidene difluoride

RMSD   Root-mean-square deviation

RPE   Retinal pigment epithelium

SCN   Thiocyanate

SDS-PAGE   Sodium dodecyl sulfate polyacrylamide gel electrophoresis

SEC   Size exclusion chromatography

CHAPTER 1

1.   INTRODUCTION

1.1 Discovery of bestrophin

Best vitelliform macular dystrophy (BVMD) is a dominantly inherited, juvenile-onset form of macular degeneration, named after the German ophthalmologist Friedrich Best, who first described a family with a history of early-onset macular degeneration in 1905 (Best, 1905). Studies in the 1970s that analyzed the inheritance pattern of BVMD in a large Swedish family began the identification of the gene responsible for this disease (Nordström and Barkman, 1977). Linkage analysis determined the locus of BVMD to be a pericentric region on chromosome 11, at 11q13 (Forsman et al., 1992; Stone et al., 1992). After further refinement of the BVMD locus (Cooper et al., 1997; Stöhr et al., 1998; Weber et al., 1994), the gene was cloned by recombination breakpoint analysis by two groups in 1998 (Marquardt et al., 1998; Petrukhin et al., 1998).

The gene was initially called VMD2 (for vitelliform macular dystrophy type 2) and mammalian homologs that were subsequently discovered were called VMD2L1 (VMD2-like protein 1), VMD2L2, and VMD2L3 (Krämer et al., 2004; Marquardt et al., 1998; Stöhr et al., 2002). Other groups referred to mammalian bestrophins as BEST-1, -2, -3, and -4 (Sun et al., 2002; Tsunenari et al., 2003) and this nomenclature has been recommended by the HUGO and Mouse Genome Database nomenclature committees (Hartzell et al., 2008). I will refer to bestrophins using the BEST nomenclature in this work.

1.2 Paralogs and phylogenetic relationships

Bestrophins are an ancient family of proteins exhibiting a remarkable degree of evolutionary conservation. They have been identified throughout life, in organisms ranging in complexity from bacteria (Hagen et al., 2009; Yang et al., 2014) to flatworms (Cross et al., 2015; Lapan and Reddien, 2012) and mammals (Bakall et al., 2003; Marmorstein et al., 2000). There is a complex array of gene orthologs and paralogs within the phylogenetic tree (Hartzell et al., 2008). The human genome contains four bestrophin paralogs (Stöhr et al., 2002; Tsunenari et al., 2003) and all other mammals have three or four bestrophin paralogs. Mice have three bestrophin paralogs and one pseudogene (Krämer et al., 2004) whilst insects, such as the fruit fly *Drosophila*, also have four paralogs (Hartzell et al., 2008; Petrukhin et al., 1998). Interestingly, the nematode worm, *Caenorhabditis elegans*, has 25 bestrophin paralogs (Hartzell et al., 2008) although the evolutionary reason for this remains unclear. The first 350 amino acids show the most conservation between bestrophin paralogs and orthologs (Hartzell et al., 2008).

1.3 Bestrophins are calcium-activated chloride channels

Initial evidence that bestrophins are Cl^- channels came from experiments expressing bestrophins from human (hBEST1 and hBEST2), as well as *C. elegans* (ceBEST1) and *Drosophila melanogaster* (dmBEST1), in HEK cells and observing induced Cl^- currents (Sun et al., 2002) (Fig.1.1). These experiments also indicated for the first time that bestrophin channels are activated by intracellular Ca^{2+}. Fig.1.1 A-D compares currents from untransfected HEK cells with those transfected with BEST1. Clearly, transfection with hBEST1 induces large Cl^- currents, but only when intracellular Ca^{2+} is present. At
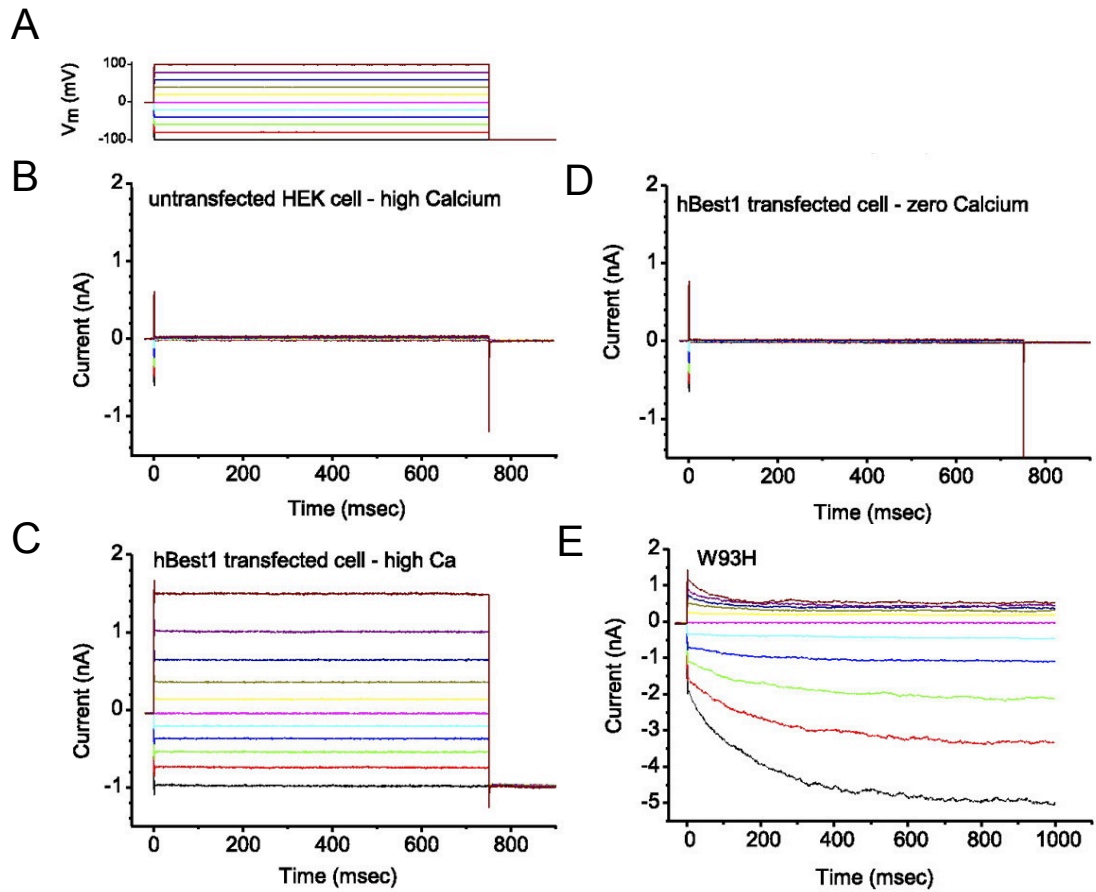
Figure 1.1 Bestrophin Cl⁻ currents recorded by whole cell voltage clamp of HEK cells, adapted from (Hartzell et al., 2008). (A) Voltage protocol used for traces shown in *B-E.* (B) non-transfected HEK cell recorded with high intracellular Ca^{2+}. (C) HEK cell transfected with wild-type hBEST1 and recorded with high intracellular Ca^{2+}. (D) HEK cell transfected with wild-type hBEST1 and recorded with nominally zero intracellular Ca^{2+}. (E) HEK cell transfected with mBEST2 W93H mutation and recorded with high intracellular Ca^{2+}.

nominally zero free Ca^{2+}, using the chelator EGTA, the currents are essentially abolished.

The currents of hBEST1 show slight outward rectification (Hartzell et al., 2008; Sun et al., 2002) (Fig.1.1). Interestingly, other bestrophins show very significant rectification properties: ceBEST1 is strongly inward rectifying whilst dmBEST1 is strongly outward rectifying (Sun et al., 2002). This is good evidence that bestrophins actually form the ion pore responsible for the observed Cl^- conductance when HEK cells are transfected with these genes. If bestrophins were simply Cl^- channel regulators it would be harder to rationalize these differences in current rectification properties.

Additional evidence that bestrophins are Cl^- channels comes from mutagenesis studies of these proteins (Qu and Hartzell, 2004; Qu et al., 2006a; 2004; 2003; Tsunenari et al., 2003) . In figure 1.1, for example, currents are shown for HEK cells transfected with the mBEST2 mutant, W93H. Unlike wild-type currents of mBEST2, which display a nearly linear current-voltage (*I-V*) curve and no significant time-dependence for activation (Qu et al., 2004), similarly to hBEST1, the W93H channel activates slowly upon hyperpolarization and is a strong inward rectifier (Fig.1.1 E). Other current properties demonstrably altered by mutagenesis of bestrophins include relative ion permeabilities and inhibition by channel blockers (Qu and Hartzell, 2004; Tsunenari et al., 2003). As is common for Ca^{2+}-activated chloride channels (CaCCs) (Hartzell et al., 2005a), bestrophins display a lyotropic permeability sequence among anions, where larger anions are more permeant, such that $SCN^- > NO_3^- > I^- > Br^- > Cl^- > F^-$. SCN^- is ~ 8 times more permeant than Cl^- for mBEST2, whose anionic selectivity has been most extensively characterized (Qu and Hartzell, 2004; Qu et al., 2004). Mutation of S79 to cysteine reduced this relative permeability to ~4 and also abolished the SCN-dependent

block observed for wild-type mBEST2 currents (Qu et al., 2004). These observations further support that bestrophins encode Cl^- channels.

Multiple bestrophin channels have been shown to require Ca^{2+} for activation. Initial studies characterizing Cl^- currents induced by hBEST1 expression in HEK cells demonstrated the Ca^{2+}-dependence of these currents using a photolyzable caged-Ca^{2+} compound, Ca^{2+}-NP-EGTA (Ellis-Davies and Kaplan, 1994; Sun et al., 2002). In these experiments, HEK cells were loaded with Ca^{2+}-NPEGTA, from a whole-cell pipette, and flashes of light were used to cause the photolytic release of Ca^{2+}. Such flashes caused ~ 5-fold increases in currents and this effect could be prevented if the cells were preloaded with the Ca^{2+}-chelator BAPTA, confirming the effect of increases in free Ca^{2+} on hBEST1 currents (Sun et al., 2002). Recordings of mBEST2 transfected in HEK cells looked at the Ca^{2+}-dependence of bestrophin currents in a concentration-dependent manner and gave an apparent K_d for activation by Ca^{2+} of ~ 200 nM (Qu et al., 2004). When two bestrophins were cloned from *Xenopus* oocytes, measurements of Cl^- currents induced after transfecting these genes in HEK cells resulted in an almost identical apparent K_d for Ca^{2+}-dependent activation (Qu et al., 2003). Interestingly, if these Ca^{2+} sensitivities measured for heterologously expressed channels are the same for native bestrophin, this channel would be expected to at least be partially Ca^{2+}-bound at all times, since the basal free cytosolic Ca^{2+} is typically around 100 nM.

 Whilst these experiments clearly demonstrated the Ca^{2+}-dependent activation of bestrophins, the mechanism of regulation by Ca^{2+} remained unknown: does Ca^{2+} directly bind and activate bestrophin, or does it work indirectly via a Ca^{2+}- binding protein like calmodulin? The recordings of bestrophins in excised, inside-out membrane patches helps address this question because here channels can be studied in the absence of

additional cellular factors other than the contents of the bath solution (facing the

cytoplasmic side of the channel). Measurements of hBEST4 in this way yielded currents

that were activated in a dose-dependent manner, with an apparent K_d of 230 nM

(Tsunenari et al., 2006), indicating that bestrophins are likely directly activated by Ca^{2+}.

This was more recently confirmed by measurements of purified, reconstituted chicken

BEST1 (cBEST1) in liposomes and assessment by a fluorescence-based flux assay,

which demonstrate that activity of the isolated protein is clearly Ca^{2+}-dependent (Kane

Dickson et al., 2014).

1.4 Tissue distribution and proposed biological roles

Assessment of the expression profiles and tissue distributions of bestrophins is a

continued effort. Most of the available data currently comes from reverse transcriptase

(RT) PCR and northern analysis used to quantify mRNA levels, with limited information

about protein levels. Each of these methods suffers from serious limitations, with

northern analysis having relatively low sensitivity and RT-PCR sometimes leading to

amplification of an RNA pool only expressed in a small subset of cells (Hartzell et al.,

2008). A more thorough quantification of bestrophin protein levels in tissues is needed,

but this has been precluded by a limited availability of good antibodies. Below I discuss

our current knowledge of the four human bestrophin paralogs.

1.4.1   BEST1

 Initial northern analysis and RT-PCR data suggested that expression of hBEST1 is

highly restricted to the retinal pigment epithelium (RPE) (Petrukhin et al., 1998),

consistent with mutations in this gene causing retinal disease. Retinopathies associated

with hBEST1 and the channel's proposed roles in the RPE are discussed in more detail

in sections 1.5 and 1.6. Other experiments, counting expressed sequence tags (ESTs)

of cDNA, suggested a broader tissue distribution of hBEST1, including cerebellum, melanocytes and the colon (Marquardt et al., 1998). The first analysis of hBEST1 protein levels, using novel monoclonal and polyclonal anitbodies, reported that the protein was uniquely expressed in RPE (Marmorstein et al., 2000). Consistently, a systematic examination of BEST1 expression in multiple organs from pigs did not identify any BEST1 outside of the eye (Marmorstein et al., 2009; Stanton et al., 2006). A more recent study, using antibodies targeted to the C-terminus of different bestrophins, showed for the first time that whilst BEST1 protein is highly expressed in the human RPE, mouse BEST1 is not and is instead primarily expressed in the testes (Milenkovic et al., 2015). This was an important finding, as the observation that mBEST1 knockout mice had no ocular pathology and normal currents in the RPE (Marmorstein et al., 2006) cast a shadow over the field and stifled support for the idea that BEST1 was responsible for the Ca^{2+}-activated Cl^- current in these cells. Instead, mice with mBEST1 knocked out exhibit severely compromised fertility, which is likely due to the impaired motility of spermatocytes from these knockout animals (Milenkovic et al., 2015).

1.4.2. BEST2

BEST2 appears to have a limited distribution that is similar in human and mouse (Hartzell et al., 2008). Replacement of the first few exons of mBEST2 with the reporter LacZ and subsequent X-gal staining, followed by immunohistochemistry, showed mBEST2 expression primarily in the colon and the ciliary epithelium of the eye (Bakall et al., 2008). BEST2 knockout mice exhibited a significantly reduced intraocular pressure (Bakall et al., 2008; Zhang et al., 2009), consistent with its expression in the eye. In the goblet cells of the colon, BEST2 has been shown to mediate bicarbonate transport (Yu et al., 2010), which is thought to be important for hydration and pH homeostasis of the colonic lumen. Interestingly, currents of hBEST2 recorded in HEK cells are more

permeant and conductive to HCO_3^- relative to Cl^-, compared to hBEST1 (Qu and

Hartzell, 2008). Further, studies on mBEST2 knockout mice indicate that BEST2 also

mediates bicarbonate transport in sweat glands and mice lacking BEST2 suffer from a

complete inability to sweat (Cui et al., 2012).

1.4.3 BEST3

BEST3 appears to have a very broad tissue distribution, however this is based primarily

on experiments assessing RNA levels, with little work being done to characterize protein

expression (Hartzell et al., 2008). Evidence is accumulating that BEST3 plays a

protective role under cellular stress conditions. For example, BEST3 expression is

upregulated under ER stress condtions induced in cultured rat kidney cells (Lee et al.,

2012). Additionally, BEST3 is reported to be expressed in human endothelial cells,

where it appears to suppress TNF-α induced inflammation (Song et al., 2014).

1.4.4 BEST4

Much less is known about BEST4. Currently, the only data assessing BEST4 protein

level indicates that the channel is expressed in the absorptive cells of the intestinal

epithelia, where it might be important for regulating the absorption and secretion of

HCO_3^- and Cl^- (Ito et al., 2013).

1.5 BEST1 and retinopathies

Over 200 mutations in the BEST1 gene are reported to cause some kind of retinal

degeneration disorder. There are at least five clinically distinct forms of retinal

degeneration associated with BEST1 gene mutations, that collectively are referred to as

"bestrinopathies" (Johnson et al., 2017). These consist of BVMD, (Marquardt et al.,

1998; Petrukhin et al., 1998), adult-onset vitelliform macular dystrophy (AVMD)

(Allikmets et al., 1999; Krämer et al., 2000), autosomal recessive bestrinopathy (ARB)

(Burgess et al., 2008; Johnson et al., 2015), autosomal dominant

vitreoretinochoroidopathy (ADVIRC) (Yardley et al., 2004) and retinitis pigmentosa (RP)

(Davidson et al., 2009). More detail on each of these bestrinopathies is given below.

1.5.1 Best vitelliform macular dystrophy

BVMD is the classically described, autosomal-dominant, progressive, juvenile-onset

macular degeneration disorder that is the most common among the bestrinopathies

(Hartzell et al., 2008). BVMD is associated with large deposits of a yellow pigmented

material centered in the macula, that initially resembles an egg yolk ("vitelliform")

(Fig.1.2) (Mohler and Fine, 1981; Pianta et al., 2003; Yannuzi, 1987). This lesion is

autofluorescent and at least a portion of this fluorescence is likely due to the

accumulation of lipofuscin in the RPE (Bakall et al., 2007; Weingeist et al., 1982).

Lipofuscin is a yellow pigment that typically builds up with age in the lyososomal

compartment of RPE cells (Sparrow and Boulton, 2005). The major fluorescent

component of lipofuscin is *N*-retinylidene-*N*-retinylethanolamine (A2E), which is thought

to disrupt membrane integrity by a detergent-like effect (Eldred and Lasky, 1993; Hartzell

et al., 2008). After initial forming of the macula lesion, it can layer down due to partial

resorption of fluid (Marmorstein et al., 2009). Over time, the vitelliform lesion can

scramble, leading to significant worsening of vision (Johnson et al., 2017).

Like other autosomal dominant diseases, there is significant variability in expression and

and the age of onset of BVMD (Boon et al., 2009; Marmorstein et al., 2009). Because of

this, prevalence studies are only approximations. Further, the clinical presentation of

BVMD is not predictable, since roughly 7-9% of patients with disease-causing mutations

in BEST1 have normal vision. Nevertheless, almost all individuals with BEST1 mutations

A   B

Figure 1.2. Clinical presentation of Best vitelliform macular dystrophy, adapted from (Johnson et al., 2017).(A) A classic vitelliform lesion found in the right eye of an 80 year old female patient with BVMD. (B) Short wavelength fundus autofluorescence shows hyperfluorescence of the vitelliform lesion.

have abnormal electro-oculograms (EOGs) (Boon et al., 2009; Cross and Bard, 1984; Deutman, 1969; Marmorstein et al., 2009). The EOG is an indirect measure of the transepithelial potential across the RPE (Ardenn, 1962; Arden et al., 1962). There is a voltage difference across the RPE of ~ 6mV, with the apical side positive relative to the basolateral side, due to the polarized distribution of channels and transporters on these sides of the cells (Gallemore et al., 1997; Hartzell et al., 2008). During light adaptaion, this voltage difference increases to ~ 12mV, which is due to an increased basolateral Cl^{-} conductance, hypothesized to be BEST1 channels opening (Hartzell et al., 2005b; Sun et al., 2002). The EOG involves placing electrodes on either side of the eye and instructing the patient to look alternately left and right. The voltage recorded is different because of the orientation of the dipole due to the RPE transepithelial potential. The voltage increases during light adaptation, as explained, and the maximum voltage recorded is termed the light peak. The ratio of the voltage recorded in the dark to the light peak is called the Arden ratio (Arden et al., 1962), typically values are 2.0 or greater, but fall below 1.5 in patients with Best disease (Johnson et al., 2017).

The dominance inheritance pattern of BVMD is still not fully understood, but might be due to a variety of mechanisms, depending on the nature of the mutation. In some cases, haploinsufficiency, whereby reduced levels of functional protein caused by a nonfunctional gene product from one allele, may be the underlying mechanism (Yu et al., 2006). Another possibility, supported by multiple studies (Marchant et al., 2006; Sun et al., 2002; Yu et al., 2007), is that mutations are dominant negative because of inhibition of the oligomeric channel composed of wild-type and mutant subunits. Other studies suggest that the dominant inheritance is because of gain of function mutants in bestrophin (Marmorstein et al., 2006). More work is needed to thoroughly assess the effects of BEST1 mutations on channel behavior and how this determines RPE function.

Recent studies using induced pluripotent stem cell (iPSC) derived RPE cells taken from patients with Best's disease show great promise (Li et al., 2017; Marmorstein et al., 2018; Milenkovic et al., 2015).

1.5.2 Adult-onset vitelliform macular dystrophy

AVMD refers to a heterogeneous group of diseases with variable histopathological and clinical features (Hartzell et al., 2008). AVMD patients have mutations in both BEST1 and PRPH2, which encodes a protein called peripherin 2, thought to be important for the structural stability of light-sensing pigments (Allikmets et al., 1999; Boon et al., 2009; Krämer et al., 2000; Lotery et al., 2000; Seddon et al., 2001; Zhuk and Edwards, 2006). Typically, the vitelliform lesions observed in AVMD are smaller than BVMD, and this is associated with a milder degree of vision loss (Johnson et al., 2017). However, it has been proposed that patients diagnosed with AVMD due to mutations in BEST1 should be reclassified as BVMD patients (Hartzell et al., 2008; Johnson et al., 2017)

1.5.3 Autosomal recessive bestrinopathy

First recognized in 2008, parents of the ARB patient did not have any abnormal fundus findings or EOG results, consistent with the pattern of inheritance for this disease not being autosomal dominant (Burgess et al., 2008). Patients with ARB display small vitelliform lesions and yellow, subretinal deposits as well as a decreased Arden ratio as assessed by the EOG (Boon et al., 2009; Johnson et al., 2015; Marmorstein et al., 2009). ARB was initially hypothesized to represent the human "null" phenotype, due to several patients identified with a truncation mutation at BEST1^{R200X}, which was associated with a loss of Cl$^-$ channel activity (Burgess et al., 2008). This is disfavored by a more recent study identifying an ARB patient with a mutation that causes truncation at residue 366 of BEST1, since this channel was shown to be functional in HEK cells

(Johnson et al., 2015). Instead, this hinted that loss of the C-terminal region of BEST1, and subsequently the regulatory mechanisms it encodes (discussed further in later sections), could be pathological.

1.5.4. Autosomal dominant vitreoretinochoroidopathy

First described in 1982 (Kaufman et al., 1982), ADVIRC appears differently to other disorders discussed. The retinal dystrophy includes peripheral hyperpigmentation as well as macular edema. Three hBEST1 mutations have been predominantly associated with ADVIRC: V86M, Y236C and V239M (Yardley et al., 2004). The effects of these mutations *in vivo* is unclear, but one study has shown that they cause exon skipping of a reporter construct *in vitro* (Yardley et al., 2004).

1.5.5. Retinitis pigmentosa

RP is a peripheral retinal disease first described in 2009 (Davidson et al., 2009). Here, four previously unreported missense mutations were identified: L140V, I205T, D228N and Y227C. Experiments in HEK cells showed that L140V and I205T caused significantly impaired Cl⁻ channel activity, but only L140V and D228N caused protein mislocalization in polarized epithelial cells (Davidson et al., 2009). Symptoms of patients with RP include yellow deposits, macular edema and pigment changes in the peripheral regions of the retina.

1.6 Regulatory mechanisms of BEST1

In addition to requiring Ca^{2+} for activation, it has been shown that higher concentrations of Ca^{2+} inhibit ionic currents of hBEST1. Phosphorylation of the channel and changes to cell volume have also been proposed as regulatory mechanisms of BEST1. Evidence for these additional regulatory mechanisms is described below.

1.6.1   Current rundown of hBEST1: regulation by Ca^{2+} and phosphorylation

Initial recordings of hBEST3 and mBEST3 in HEK cells gave very small currents. It was

shown that truncations within the conserved region of the C-terminal portion of the

channel (to residue 353) activated currents dramatically (Qu et al., 2006b). Subsequent

mutagenesis identified what was termed an "autoinhibitory domain" within this region,

consisting of amino acids $_{356}$IPSFLGS$_{362}$ (Qu et al., 2006b). This sequence is almost

perfectly conserved across bestrophin homologs and paralogs and was shown to be

inhibitory to BEST1 and BEST2 currents also (Qu et al., 2007; Xiao et al., 2008).

More extensive recordings of hBEST1 in HEK cells over time showed a time-dependent

current rundown (Xiao et al., 2008). The rate and extent of current rundown was greater

at higher concentrations of Ca^{2+}, showing for the first time that Ca^{2+}, as well as being

required for activation of BEST1, had an inhibitory effect at higher concentrations. It was

shown that activation of PKC in HEK cells, using the activator phorbol 12-myristate 13-

acetate (PMA), slowed current rundown (Xiao et al., 2009) , suggesting that

phosphorylation of BEST1 might attenuate this behavior. Within the autoinhibitory

sequence a PKC phosphorylation site was identified at residue S358, and mutation of

this residue to glutamate, to approximate the phosphorylated state, prevented current

rundown altogether (Xiao et al., 2009). Dephosphorylation of hBEST1 appeared to be

mediated by protein phosphatase 2A (PP2A) as addition of PP2A inhibitors to cells, such

as okadaic acid, significantly slowed current rundown of the WT channel. This is

consistent with an earlier observation that hBEST1 coimmunoprecipitates with PP2A in

RPE cells (Marmorstein et al., 2002).

1.6.2 Volume regulation of BEST1

When cells are placed in a hypotonic solution they swell as water flows down its osmotic potential gradient, into the cell. As the cells expand, volume-regulated ion channels are activated, enabling the efflux of ions which shifts the osmotic balance across the cell membrane, causing the outward flow of water and consequently cell volume decrease (Hoffmann and Ussing, 1992; Lang et al., 1998). Cl$^-$ currents of hBEST1 or mBEST2 in HEK cells were shown to be inhibited when cells were placed in hyperosmotic solutions: conditions that promote cell shrinkage (Fischmeister and Hartzell, 2005). Currents of native dBEST1 in *Drosophila* S2 cells also appeared sensitive to osmolarity changes, and RNAi-mediated knockdown of dBEST1 abolished this volume-regulated current (Chien and Hartzell, 2007). More recently, recordings of Cl$^-$ currents in iPSC-derived RPE cells were shown to be volume-activated (Milenkovic et al., 2015). Further, when such cells were derived from patients harboring disease-causing mutations in BEST1, this volume-activated current was severely diminished (Milenkovic et al., 2015).

Presently, it remains unclear how BEST1 is volume-regulated. The best evidence for a possible mechanism thus far comes from studies of hBEST1 in HEK cells, and is linked to phosphorylation-dependent regulation of the channel, described in section 1.6. Promotion of hBEST1 phosphorylation, by the addition of PKC activators or PP2A inhibitors, reduces inhibition caused by hypertonic solution placement of HEK cells (Xiao et al., 2009). Mutation of S358 to glutamate, to approximate a permanently phosphorylated hBEST1, abolished hypertonic solution-dependent current inhibition. Ceramide, an activator of PP2A, appears to be the signal that relays cell shrinkage (hypertonic solution exchange) to the phosphorylation state of the channel as addition of ceramide inhibits the observed currents in a similar manner. Further, inhibition of sphingomyelinase, which is proposed to stimulate release of ceramide during cell

shrinkage (Kolesnick and Krönke, 1998; Ruvolo, 2001), blocks the effects of hypertonic stress. More detail on possible mechanisms of volume-dependent regulation of BEST1 is given in chapter 4.

1.7 BEST1 in the retinal pigment epithelium

As discussed in section 1.4.1, hBEST1 expression appears primarily restricted to the RPE. More specifically, immunohistochemical staining of porcine and macaque eyes showed that BEST1 is localized to the basolateral plasma membrane, which was supported by confocal microscopy (Marmorstein et al., 2000). Subsequent studies have confirmed the basolateral plasma membrane localization of BEST1 using several different native models, including fetal human RPE cells (Marmorstein et al., 2015), iPSC-derived RPE cells (Johnson et al., 2015; Milenkovic et al., 2015), rhesus monkeys (Gouras et al., 2009) and humans (Dalvin et al., 2015).

Whilst multiple studies have demonstrated the importance of BEST1 in contributing to anion currents of the RPE (Li et al., 2017; Marmorstein et al., 2015; Milenkovic et al., 2015), its role in the RPE remains unclear. One speculative hypothesis links volume-dependent activation of BEST1 to phagocytosis of the RPE, as illustrated in figure 1.3. In the light, as POS are shed, large amounts of osmolytes such as taurine are released (Salceda et al., 1977; Schmidt, 1978). These osmolytes will be taken up by the RPE cells, for example by the Na^{2+}-dependent taurine cotransporter identified in the apical membrane (Kundaiker et al., 1996), which will subsequently be followed by water influx, leading to RPE cell swelling. Cell swelling would activate hBEST1, not only through volume-dependent activation, but also due to an increase in intracellular Ca^{2+} (McCarty and O'Neil, 1992). Cl^- efflux would in turn lead to cell shrinkage, and it has been proposed that the mechanical forces involved in dynamic cell volume changes might be

important for phagocytosis (Hartzell et al., 2008; Xiao et al., 2010). Cell shrinkage would also lead to inhibition of BEST1, for example through the release of ceramide, as discussed in section 1.7. Whilst more work is needed to properly interrogate the role of BEST1 in RPE phagocytosis, it was recently shown that iPSC-derived RPE cells taken from patients with disease-causing mutations in BEST1 were significantly impaired in their ability to phagocytose fluorescently-labeled outer segment proteins, compared to their wild-type counterparts (Marmorstein et al., 2018).

1.8 A high resolution structure of chicken BEST1

In 2014, the first high resolution structure of a eukaryotic BEST1 protein was determined by X-ray crystallography (Kane Dickson et al., 2014). Chicken BEST1 (cBEST1) was chosen on the basis of exhibiting good biochemical stability and a construct containing amino acids 1-405, which shares 74% sequence identity with human BEST1 (Fig.1.4), was used for crystallization. The function of this construct was tested in liposomes using a fluorescence-based flux assay. cBEST1 in liposomes demonstrated Ca^{2+}-activated Cl^- flux, as well as an apparent lyotropic sequence of permeability of $NO_3^- > Cl^- > Br^-$, as indicated by relative flux rates. To obtain well-diffracting crystals, the protein was crystallized in complex with a Fab monoclonal antibody fragment (discussed further in chapter 3) that binds in a 1:1 stoichiometry to the cytosolic region of cBEST1.

The structure revealed BEST1 to be a pentamer, with five subunits arranged symmetrically around a central ion pore (Fig. 1.5). Overall the channel appears as a
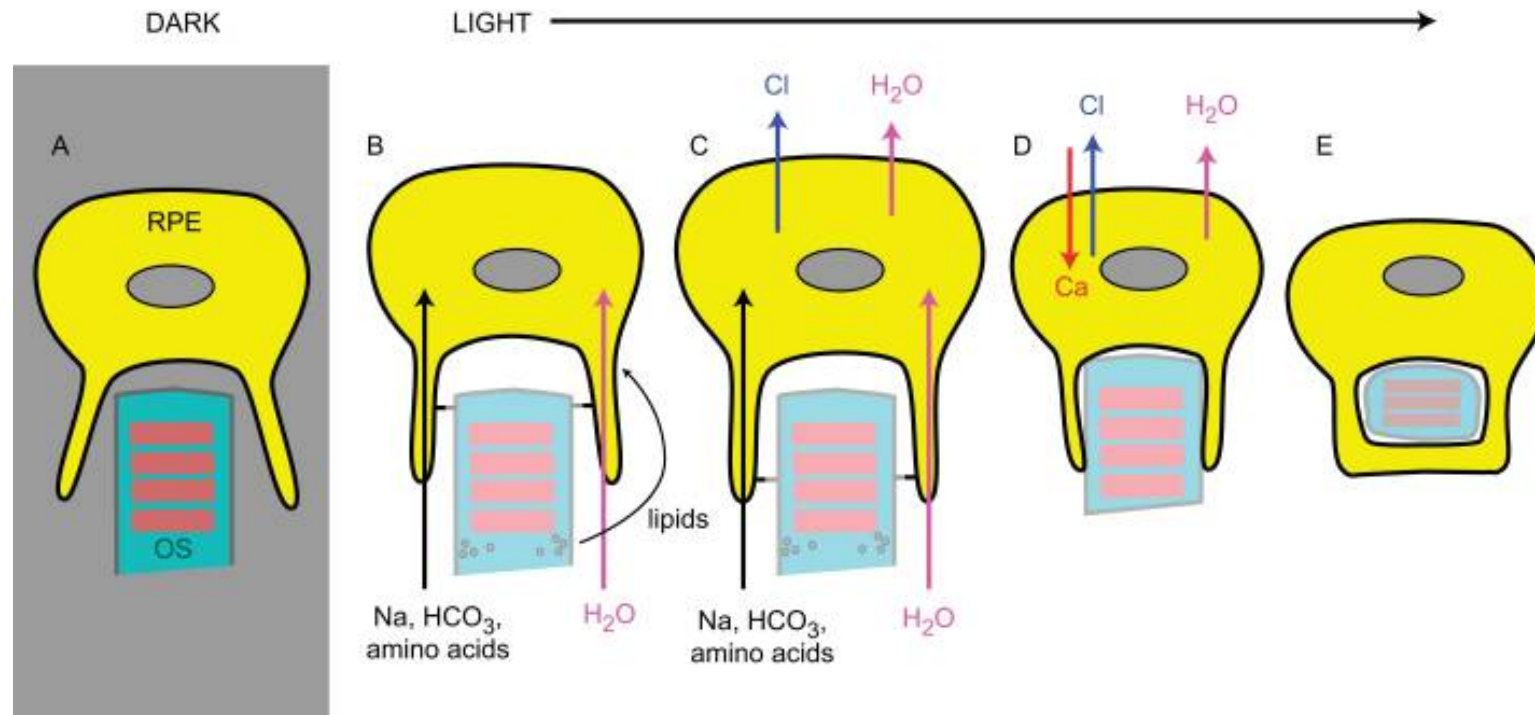
Figure 1.3 Model of hBEST1 as a volume regulated Cl⁻ channel in regulation of phagocytosis of photoreceptor outer segments (POS). Adapted from (Xiao et al., 2010). (A) In the dark, RPE and photoreceptors are not closely attached. (B) In the light, a large amount of osmolytes such as glutamate, aspartate and glycine are leaked from POS, accumulate in the extracellular space and are subsequently transported into RPE. Water is passively absorbed into RPE. (C) RPE cells swell as water enters, which in turn activates hBEST1. (D) Opening of hBEST1 channels causes Cl⁻ efflux, which shifts the osmotic balance, in turn causing water efflux and subsequent cell shrinkage. (E) POS are phagocytosed into RPE.
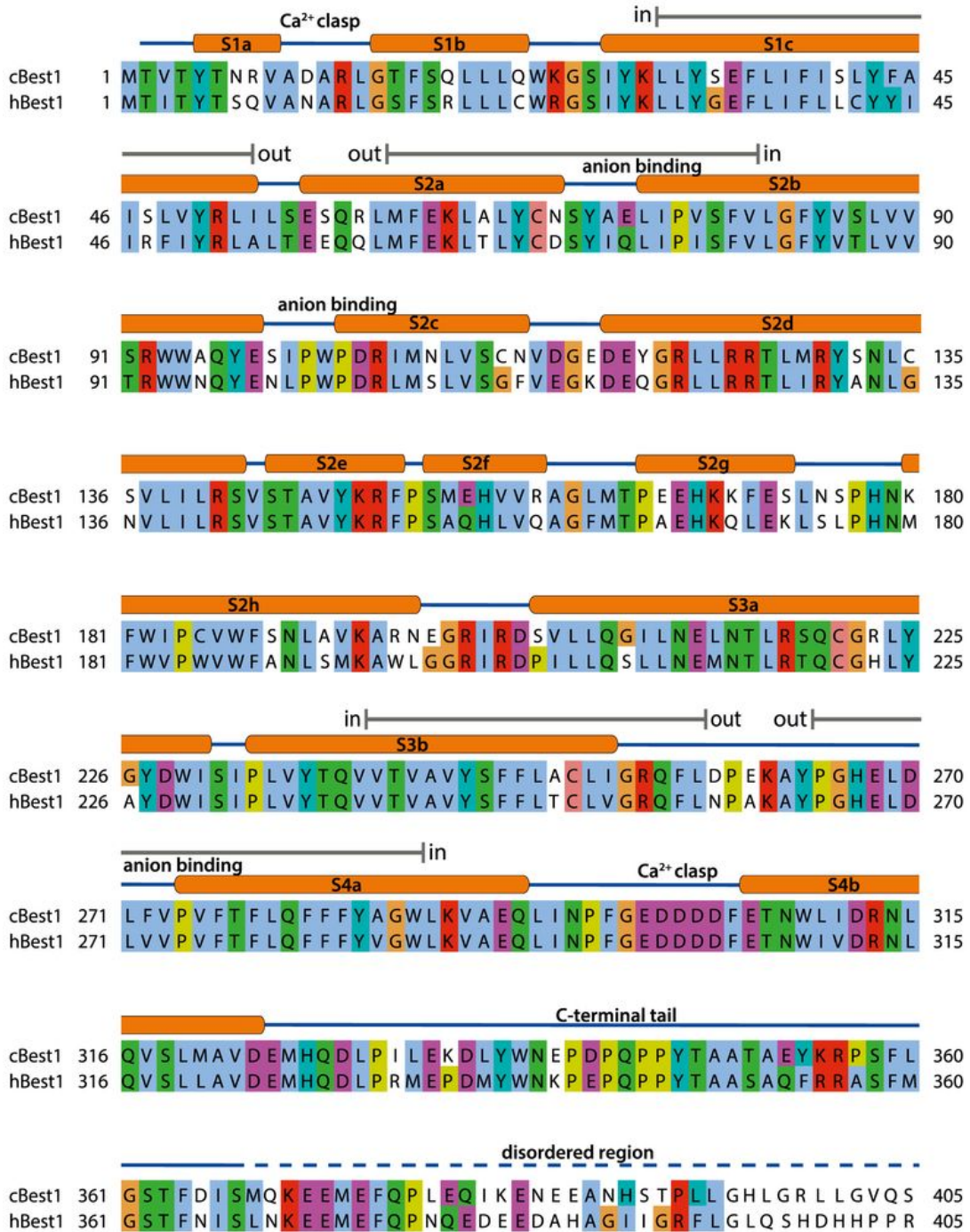
Figure 1.4. Sequence alignment and secondary structure of BEST1. Adapted from (Kane Dickson et al., 2014). Amino acid sequence of the crystallized chicken BEST1 and human BEST1 are aligned and colored according to ClustalW convention. The secondary structure is illustrated with cylinders representing α-helices, solid lines representing structured loop regions, and dashed lines representing disordered regions.
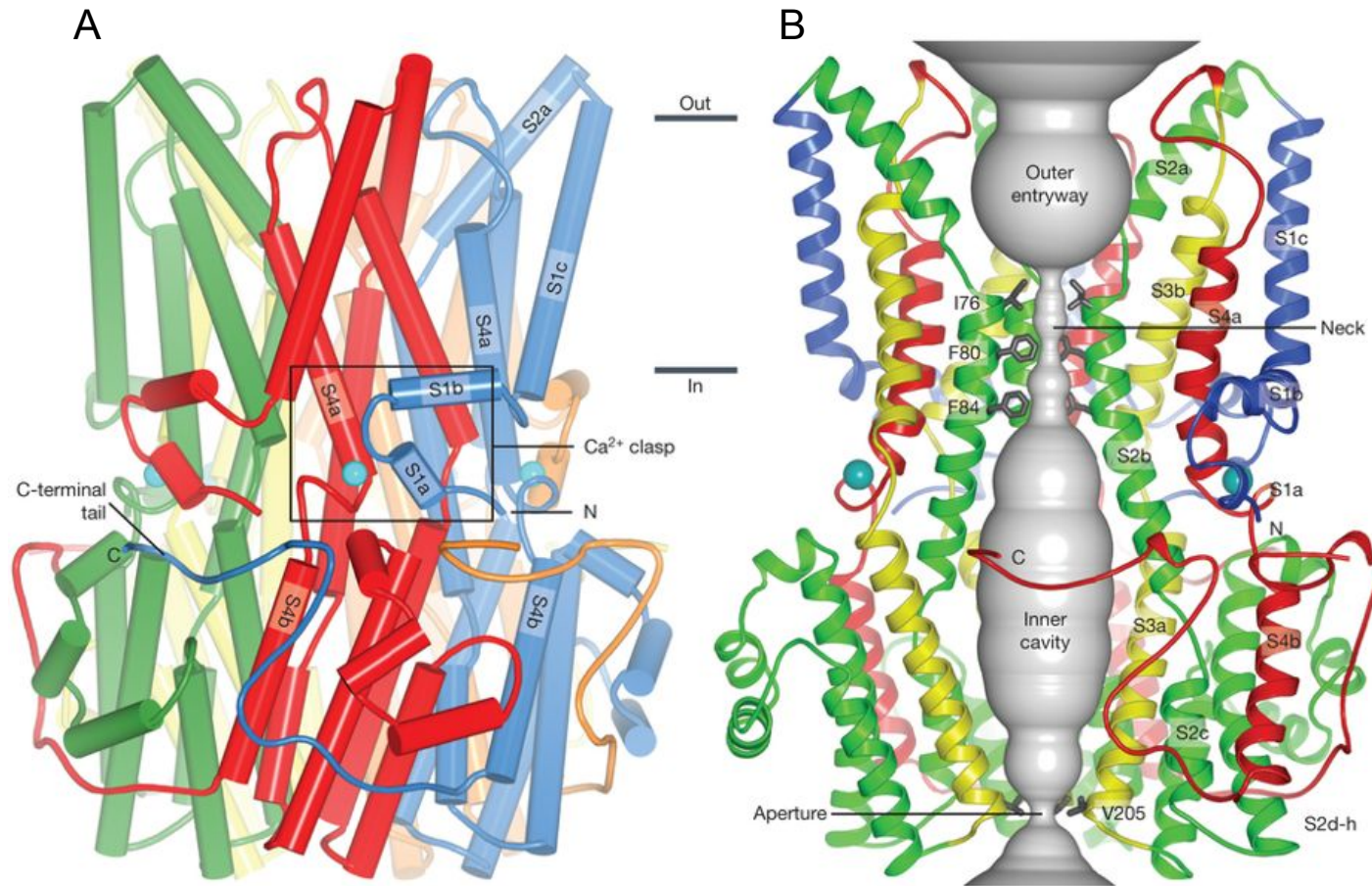
Figure 1.5 Architecture and ion pore of cBEST1. Adapted from (Kane Dickson et al., 2014). (A) Overall structure of cBEST1. The perspective is from within the membrane, with subunits colored individually, α-helices depicted as cylinders, and approximate boundaries of the membrane indicated. The boxed region highlights a Ca^{2+} clasp with bound Ca^{2+} (teal sphere). (B) Ion pore. Within a ribbon representation of three subunits of BEST1 (two in the foreground are removed) is a representation (grey color) of the minimal radial distance from the center of the pore to the nearest van der Waals protein contact. Secondary structural elements are colored according to their four segments (S1, blue; S2, green; S3, yellow; S4 and C-terminal tail, red).

barrel with a transmembrane region that is predominantly buried in what would be the plasma membrane, and a larger cytosolic region that protrudes ~ 55 Å into the cytosol. The secondary structure of cBEST1 can be divided into four segments (S1-S4) and each of these contributes to the intracellular region, which appears integral to the channel as a whole rather than a separate domain. More detail on particular structural features of the channel, and the questions they raise about BEST1's function, is given below.

1.8.1   The ion pore

The ion pore is a continuous, ~95 Å long pathway between the extracellular and intracellular sides of BEST1. It is lined by portions of the S2, S3 and S4 segments of the channel. Looking at figure 1.5 B we can see that the pore, starting from the extracellular side of the channel, begins as a large outer entryway which first narrows at a region called the "neck". The neck consists of three highly conserved hydrophobic amino acids: I76, F80 and F84 within the S2 helix. This part of the channel was first suggested to form the pore from experiments assessing accessibility of extracellulary applied MTSET$^+$ to cysteine-substituted mutants made between amino acids 69-99 of hBEST1 (Tsunenari et al., 2003). This was supported by recordings of mBEST2 (Qu and Hartzell, 2004; Qu et al., 2004). Cysteine mutations made to amino acids from position 69 to 105 altered relative conductance and permeability values of SCN$^-$ relative to Cl$^-$. None of the changes were dramatic, suggesting that determinants of ion selectivity within the BEST1 pore may be less "specialized" and instead distributed more broadly throughout the channel. Still, the extended, bottleneck-like arrangement of the neck residues is reminiscent of the classical selectivity filter of potassium channels (Doyle, 1998) which, together with the high conservation of these amino acids, begs the question: is the neck important for ion selectivity and permeation? F80L has been identified as a disease

mutation that impairs Cl⁻ channel function (Chien and Hartzell, 2008; Milenkovic et al., 2011), supporting the notion that this region is important for BEST1 activity.

Below the neck, the S2b helices bend slightly and the pore opens into a larger "inner cavity" that includes the majority of the channel's cytosolic region before constricting again at the "aperture" (Fig.1.5 B). In cBEST1 the aperture is formed by valine 205. The identity of this residue is variable between bestrophin homologs and paralogs, but its importance is underscored by the finding that mutation of the equivalent residue in hBEST1, I205, to threonine, is disease-causing and currents of this mutant in HEK cells were significantly impaired compared to wild type (Davidson et al., 2009). In the structure of cBEST1, both the neck and the aperture are narrow enough that a permeating Cl⁻ ion would need to be dehydrated to pass through them. Thus each of these regions could contribute to ion selectivity of the channel, particularly the lyotropic permeability sequence characteristic of BEST1, which is thought to arise from ion dehydration such that larger ions (eg. SCN^-, I^-, NO_3^-) are more permeable because their energy cost of dehydration is smaller (Hartzell et al., 2005a; Qu and Hartzell, 2000). The neck and aperture could conceivably act as channel gates too, whereby narrowing and widening of either or both of these regions could dictate the flow of ions through the BEST1 pore. Mutagenesis of these regions and assessment of the properties of ion selectivity and Ca^{2+}-dependent activation is presented in chapter 2.

1.8.2   The Ca^{2+} clasp

The Ca^{2+} clasp is so named because these five symmetrical Ca^{2+} binding sites resemble a belt around the midsection of the channel (Fig.1.5 A). The clasp consists of an acidic cluster between S4a and S4b (E300, D301, D302, D303 and D304) from one sunbunit and the S1b helix-turn-helix of an adjacent subunit (Fig.1.6). Electron density was

observed within this binding site and is consistent with being a Ca^{2+} based on the coordination observed in the structure as well as a corresponding peak appearing in an anomalous electron density map (Fig.1.6 A). The Ca^{2+} is coordinated in a pentagonal bipyramidal geometry, with bidentate coordination by the side chain of D304 as well as with the carbonyl oxygen atoms of A101 and Q293 and an ordered water molecule aligning along the vertices of a planar pentagon and the side chain of D301 and the backbone carbonyl of N296 taking axial positions (Fig.1.6 B).

D301 and D304 form part of a conserved acidic cluster thought to be important for bestrophin channel function (Hartzell et al., 2008) but were not previously hypothesized to form the Ca^{2+} binding site of BEST1. Recordings of hBEST1 channels in HEK cells with mutations made to this acidic cluster identified D312 as a putative Ca^{2+}-binding residue because its mutation to glycine reduced the $K_{1/2}$ for Ca^{2+} by ~ 20-fold (Xiao et al., 2008). Still, in this study mutation of D301 or D304 produced nonfunctional channels, consistent with these forming the Ca^{2+}-binding site, mutation of which would render the channels unable to bind Ca^{2+} thus unable to open. The strong electron density, together with the structural observation that the absence of Ca^{2+} at the clasp could cause significant conformational changes, suggests that this is likely the Ca^{2+} sensor of the channel that dictates channel opening, but more work is needed to prove this.

1.8.3 Anion binding sites

In the initial X-ray structure of cBEST1, electron densities consistent with bound Cl^- ions were observed at several sites (Kane Dickson et al., 2014). To unambiguously assign these halide-ion binding sites, crystals were grown in Br^-, and anomalous X-ray
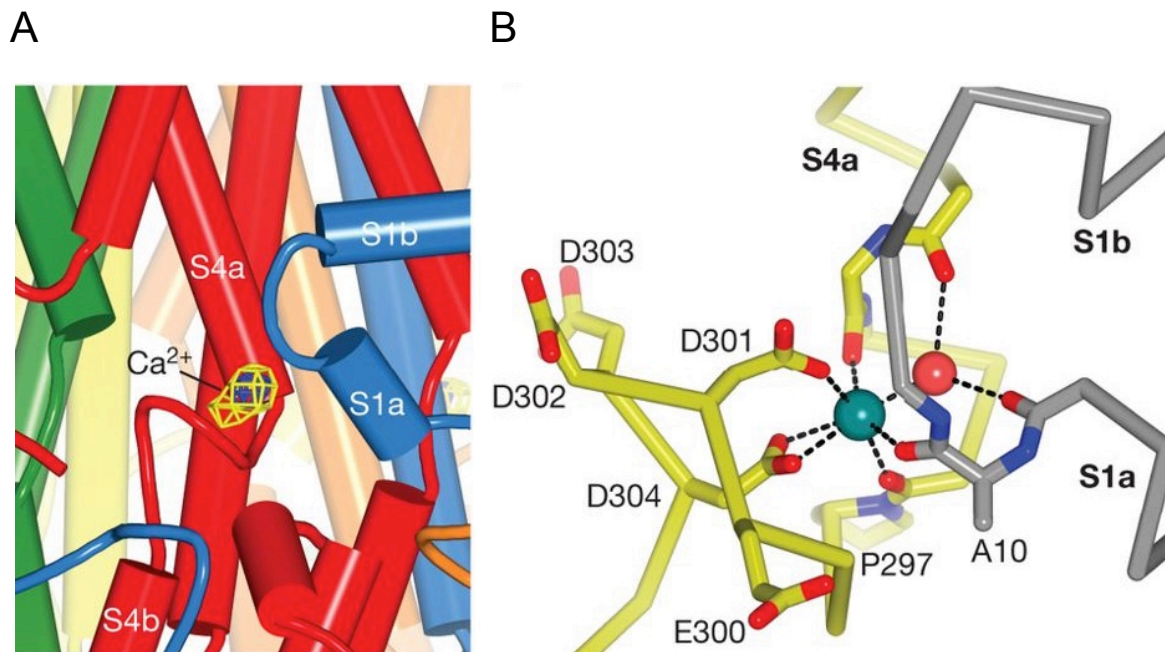
Figure 1.6. The Ca^{2+} clasp. Adapted from (Kane Dickson et al., 2014). (A) View of a Ca^{2+} clasp, showing electron density for Ca^{2+}: $F_O - F_C$ density (blue mesh; simulated annealing omit, 40-2.85 Å, 8σ contour) and anomalous difference density (yellow mesh, 40-4.0 Å, 3σ contour). (B) Coordination in the Ca^{2+} clasp. The acidic cluster and the backbone carbonyls that coordinate (dotted lines) the Ca^{2+} (teal sphere) are depicted as sticks on a Cα representation. Dotted lines also indicate hydrogen bonds between the water molecule (red sphere) and the protein (backbone carbonyls of Val 9 and Glu 292). Carbon atoms of one subunit are grey and those from another are yellow.

scattering used. Anomalous difference electron density maps indicated the presence of Br$^-$ at three locations within the pore, assigned sites 1-3 (Fig.1.7). Sites 1 and 2 are located within the outer entryway and site 3 is found within the inner entryway – all sites are accessible to the aqueous environment. In each of the sites, the halide ion appears adjacent to the N-terminal end of an α-helix where it would be stabilized by the positive electrostatic potential of the helical peptide dipole (Fig. 1.7 B).

The role of these anion-binding sites is unclear but one hypothesis is that they could serve to increase the local concentration of anions, which may contribute to anion selectivity. A similar mechanism was proposed for the anion-selective Cys-loop receptor (Hibbs and Gouaux, 2011). It is important to note that unlike K$^+$ channels, which can select for K$^+$ over Na$^+$ by a factor > 100-fold (Doyle, 1998; Hille, 2001), bestrophins, like most Cl$^-$ channels, only select ~10-50-fold for Cl$^-$ over Na$^+$ (Hille, 2001; Hartzell et al., 2005a; Qu and Hartzell, 2000; Yang et al., 2014). Thus, the canonical model of a specialized selectivity filter, most well described for the K$^+$ channel (Doyle, 1998; Hille, 2001), may not be relevant for bestrophin. Instead, overall anion selectivity may be achieved by a more distributed mechanism, such as the presence of anion-binding sites that increase the local concentration of Cl$^-$ relative to cations in bulk solvent. Because N-terminal helix dipole interactions rather than amino acid side chains primarily form the anion binding sites, it would be challenging to eliminate them by point mutagenesis. Still, structurally guided mutagenesis to introduce negatively charged amino acids proximal to the binding sites could be one means of disrupting these interactions and assessing potential changes to ion selectivity.
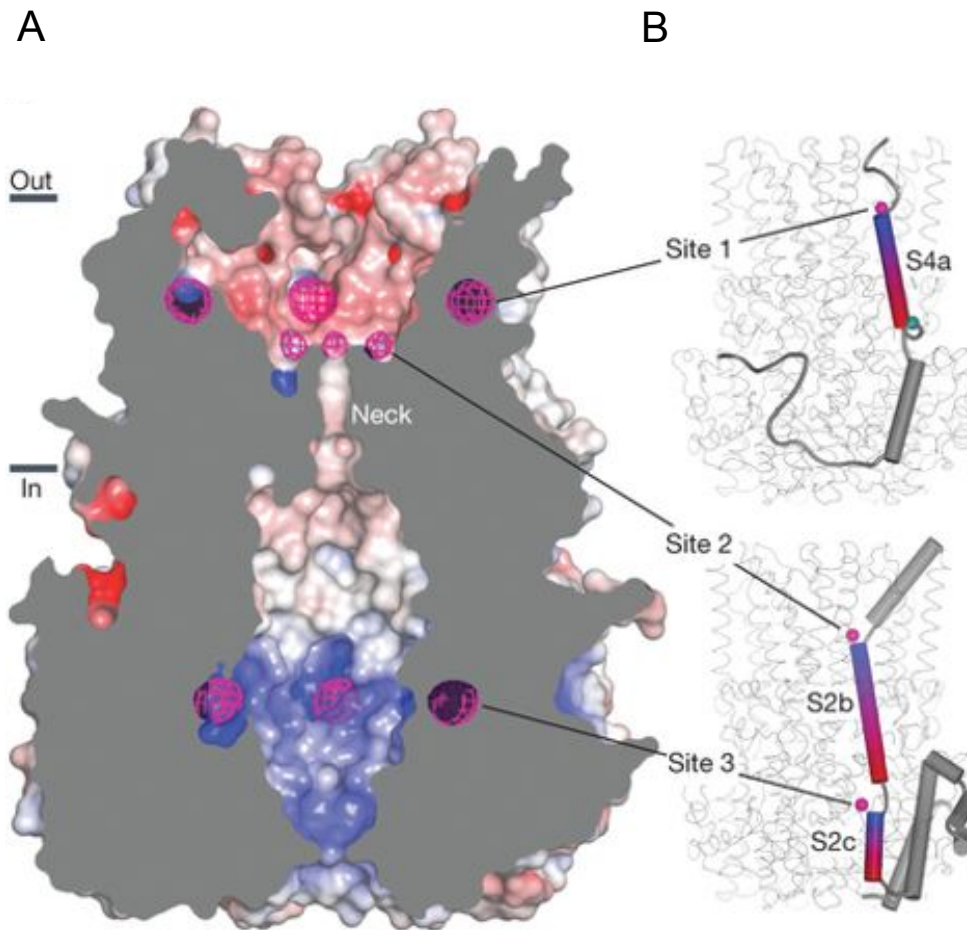
Figure 1.7 Anion binding sites. Adapted from (Kane Dickson et al., 2014). (A) Cut-away view of BEST1, revealing the surface of the pore (colored by electrostatic potential; red, -10 kT e^{-1}; white, neutral; blue, + 10 kTe^{-1}) and anomalous difference electron density for Br$^-$ ions (magenta mesh 45-5 Å, non-crystallographic symmetry averaged, 8σ contour). (B) Anion binding sites (magenta spheres) at the N-terminal ends of α-helices. Representations of the S4 and S2 segments of one subunit (upper and lower panels, respectively) are shown in the context of the entire channel. α-Helices (cylinders) interacting with Cl$^-$/Br$^-$ are colored blue-to-red from their N- to their C-terminal ends. A teal sphere (upper panel) denotes Ca^2.

1.8.4 The C-terminal tail

Following the S4b helix, amino acids 326-367 adopt an elongated conformation, called the "C-terminal tail", which wraps around the cytosolic regions of two adjacent subunits (Fig.1.5 and Fig.1.8). Amino acids 367-405 do not appear in the electron density, presumably because they are disordered. The C-terminal tail contains the autoinhibitory sequence discussed in section 1.6, including the PKC target site, S358. Electron density for the C-terminal tail is shown in figure 1.8 and is consistent with S358 being unphosphorylated in this structure. This was further supported by mass spectrometry data of purified cBEST1 (Kane Dickson et al., 2014). The unphosphorylated state of S358 may indicate that the channel is in an inactivated conformation. Additional experiments are needed to assess how the C-terminal tail modulates BEST1 activity and what conformation the X-ray structure represents.

1.8.5 Structure of a prokaryotic homolog of bestrophin

In 2014, a structure of a bacterial homolog of bestrophin from *Klebsiella pneumoniae* (KpBEST) was also published (Fig. 1.9) (Yang et al., 2014). This channel is neither Ca^{2+} activated, nor a Cl^- channel (it is almost equally permeable to Na^+ and K^+) and so functionally is very different to eukaryotic bestrophins. Nevertheless, as shown in figure 1.9, the overall architecture is very similar, despite KpBEST sharing only 18% sequence identity with cBEST1. KpBEST is a pentamer, with five subunits arranged symmetrically around a central pore. Within the ion pore, there are two major constrictions, like eukaryotic bestrophins, a neck and an aperture, suggesting conserved functional roles for these parts of the channel.
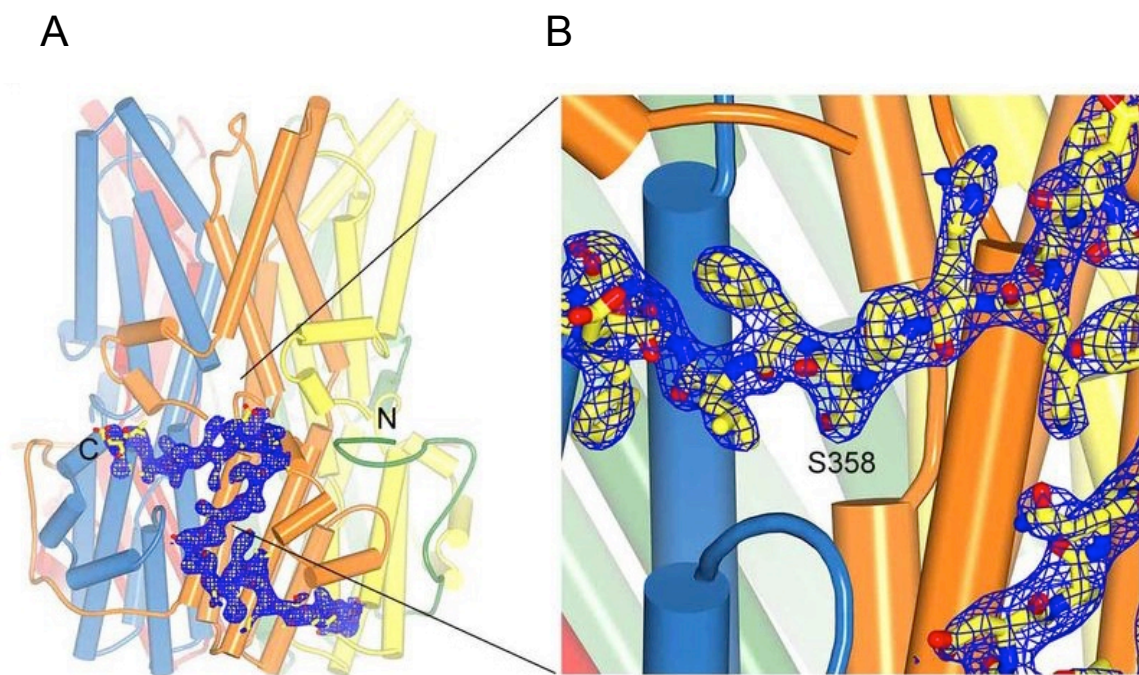
Figure 1.8 Electron density of the C-terminal tail. Adapted from (Kane Dickson et al., 2014) (A) $2F_o - F_c$ electron density (blue mesh, calculated from 40 to 2.85 Å, and contoured at 1.5σ) is shown for the C-terminal tail of the yellow colored subunit. (B) Expanded view highlighting the electron density near S358. Consistent with the electron density, mass spectrometry analysis of tryptic peptides of purified cBEST1 detected only peptides containing S358 that were not phosphorylated.
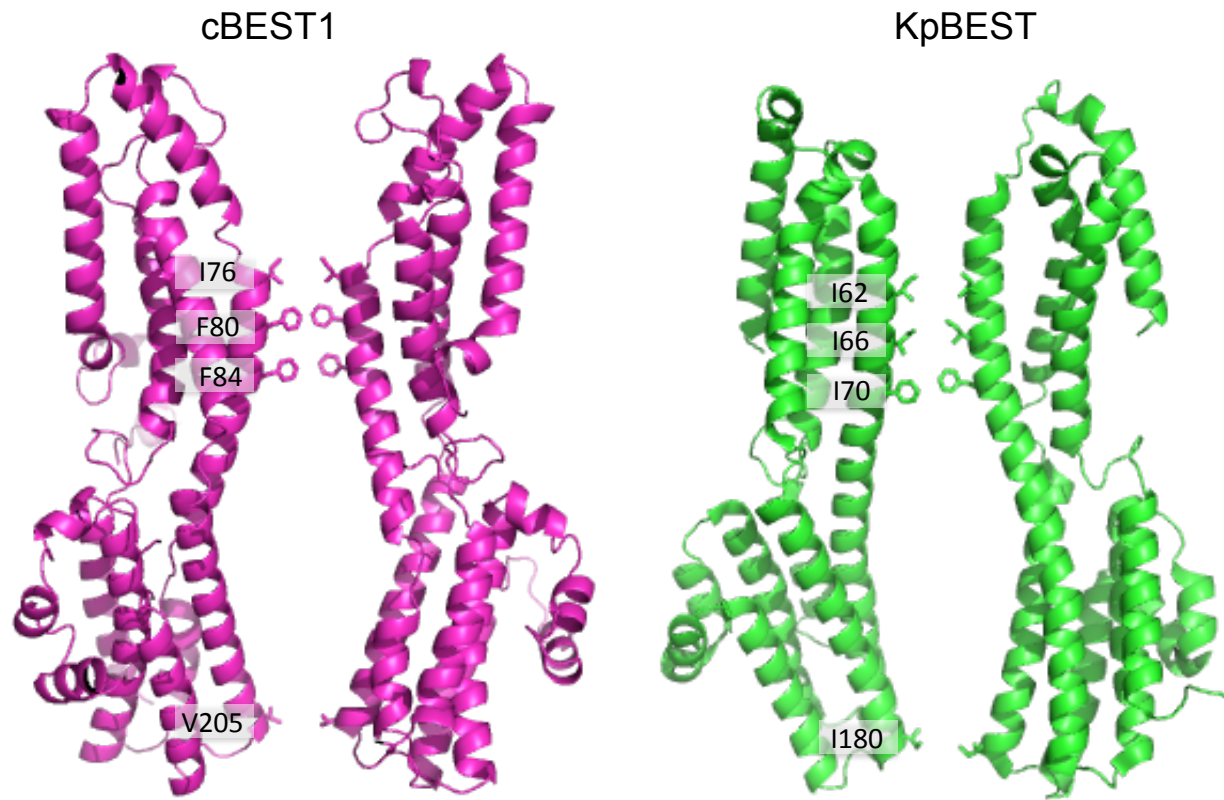
Figure 1.9 Comparison of cBEST1 and KpBEST structures. Two subunits are shown for cBEST1 (left) and KpBEST (right), with residues forming the neck and aperture highlighted in each.

Based on recordings of wild type and mutant KpBEST channels in bilayers, the authors concluded that the neck region was important for selectivity (Yang et al., 2014). Specifically, they suggested that the difference of the second neck amino acid (F80 in cBEST1 and hBEST1 and I66 in KpBEST) dictated anion vs cation selectivity of bestrophin channels. It's unclear how the difference between these two hydrophobic amino acids would dictate charge selectivity within the pore and unfortunately the data in the study is limited and qualitative, without a permeability ratio for Cl^- vs Na^+ or K^+ being reported. Further discussion about the differences between cBEST1 and KpBEST and possible determinants of bestrophin ion charge selectivity is given in section 2.5.

1.9 Aims of this thesis

BEST1 is an important channel in the function of the RPE, mutations of which are associated with a number of macular degenerative disorders. Over 200 mutations of human BEST1 have been identified but a detailed understanding of how most of these mutations are disease-causing is still lacking. Whole-cell recordings of bestrophins expressed in heterologous cell systems have elucidated some of the key biophysical properties of the channel, such as its lyotropic permeability sequence and Ca^{2+}-dependence. But which regions of the channel are responsible for these properties as well as fundamental mechanisms of function, such as how the channel opens and closes, remain unknown. The structure of chicken BEST1, which is unrelated to any other family of ion channels, provided hints but also raised many questions about how the channel functions. A more thorough understanding of how the structural features of BEST1 endow the channel with its characteristic properties, as well visualization of other possible conformations, would enable a better description of how this unusual family of channels works and why some mutations are disease-causing.

In my work I have taken a reductionist approach to studying BEST1. Using purified protein, I have studied the chicken BEST1 channel in bilayers, enabling me to probe its function in the absence of additional cellular factors. With the X-ray structure as a framework, I have designed mutants and used a combination of electrophysiological, biochemical and structural approaches to assess fundamental properties of the channel. Chapter 2 reports a series of functional and structural studies used to identify regions within the channel responsible for ion selectivity and Ca^{2+}-dependent activation. Chapter 3 describes an investigation of the mechanism of BEST1 Ca^{2+}-dependent inactivation. In chapter 4 I describe cryo-electron micrsocopy studies that reveal, for the first time, the open conformation of BEST and rationalize these findings in the context of my functional studies. Finally, in chapter 5 I report electrophysiological data that begins to address how BEST1 activity is modulated by intracellular $[Cl^-]$ and how the channel might be regulated by cell volum

CHAPTER 2

2. Distinct regions control ion selectivity and calcium-dependent activation in the bestrophin ion channel

2.1 Summary

To characterize the properties of Ca^{2+}-dependent activation and ion selectivity of BEST1, and the contributions of the two major constrictions within the channel pore, a combination of biochemical, electrophysiological and structural studies were used. To functionally probe BEST1 activity the first electrophysiological recordings of the purified channel in a reconstituted system were established, using the planar lipid bilayer technique. Mutagenesis of conserved hydrophobic amino acids that form the channel neck had no effect on ion selectivity, contrary to assumptions based on other ion channels. Instead, alanine substitutions within the neck, which widen it, cause the channel to be constitutively active, irrespective of Ca^{2+}. Further, whilst mutation of the Ca^{2+} clasp renders the channel inactive, in combination with the neck mutant activity is restored, confirming the clasp as the Ca^{2+} sensor and the neck as the Ca^{2+}-dependent gate of the channel. A high-resolution structure of the neck mutant, determined by X-ray crystallography, demonstrates that a widening of the channel pore at this region is sufficient for Ca^{2+}-independent activity. Mutation of the cytosolic aperture does not perturb the Ca^{2+} dependence of the channel or its preference for anions over cations, but its mutation dramatically alters relative permeabilities among anions. The data suggest that the aperture functions as a size-selective filter that permits the passage of small entities such as partially dehydrated ions while excluding larger molecules such as amino acids. Thus, unlike ion channels that have a single "selectivity filter", in bestrophin, distinct regions of the pore govern anion-vs.-cation selectivity and the

relative permeabilites among anions. The work presented in this chapter has been

published (Vaisey et al., 2016).

2.2 Background

Electrophysiological studies of bestrophin proteins expressed in cells have elucidated

ion selectivity and gating properties of the channels. The channels are activated by

intracellular Ca^{2+} (Qu et al., 2004; Tsunenari et al., 2003; 2006), selective for monovalent

anions, and exhibit a lyotropic sequence of relative anion permeabilites where SCN^- >

NO_3^- > I^- > Br^- > Cl^- (Hartzell et al., 2008; Qu et al., 2004). However, the mechanisms for

ion selectivity and Ca^{2+}-dependent gating, and the regions of the channel involved in

these processes, are not known. Making these matters more mysterious, a prokaryotic

protein, KpBEST, which shares 14% identity to human BEST1 and is not Ca^{2+} activated,

is cation selective despite a similar structural architecture to BEST1 (Kane Dickson et

al., 2014; Yang et al., 2014). Pharmacologically, BEST1 is inhibited by anion channel

blockers, including 4,4'-diisothiocyanatostilbene-2,2'-disulfonic acid disodium salt

hydrate (DIDS), tannic acid, and NPPB (Liu et al., 2014; Qu et al., 2004). The N-terminal

region (amino acids 1-390) is highly conserved in eukaryotic bestrophin channels and

has been shown to be sufficient for calcium-activated chloride channel (CaCC) activity in

whole-cell studies (Xiao et al., 2008). Previously, it was shown that purified chicken

BEST1 encompassing the N-terminal region (amino acids 1-405), reconstituted into

liposomes and assessed by a flux assay, exhibited activity consistent with a monovalent

anion channel activated directly by Ca^{2+} (Kane Dickson et al., 2014), but no purified

eukaryotic bestrophin channel has yet been studied by electrical recordings.

The X-ray structure of chicken BEST1, as described in chapter 1, was suggestive but three fundamental properties of the channel were unknown: where is the Ca^{2+} sensor? What portion of the pore acts as a gate to control the flow of Cl^- ions in a Ca^{2+}-dependent manner? Finally, what endows the channel with selectivity not only for anions over cations but also its lyotropic permeability sequence among permeant anions?

2.3 Materials and Methods

2.3.1 Cloning, Expression, and Purification of BEST1

A construct spanning amino acids 1-405 (unless stated) of chicken BEST1, cloned into pPICZ (invitrogen) and followed by an affinity tag (Glu-Gly-Glu-Glu-Phe) that is recognized by an anti-tubulin antibody ($YL^1/_2$) (Kilmartin et al., 1982) was used for transformation into *Pichia pastoris* by electroporation (BioRad Micropulser). Transformants were selected on YPDS plates (Invitrogen) containing 1000-2000µg/ml Zeocin (Invitrogen). Resistant colonies were grown in liquid culture using glycerol as a carbon source before induction with methanol. Pelleted cells were frozen in liquid nitrogen and stored at -80 °C. Lysis was carried out in a Retsch, Inc. Model MM301 mixer mill (3 x 3.0 minutes at 30 cps).

Lysed cells were resuspended (using ~ 10 ml of buffer for each gram of cells) in solubilisation buffer consisting of 50 mM Tris-HCl, pH 7.5, 75 mM NaCl, 75 mM KCl, 0.1 mg ml^{-1} DNase I (Sigma-Aldrich), a 1:600 dilution of Protease Inhibitor Cocktail Set III, EDTA-free (CalBiochem), and 0.5 mm 4-(2-aminoethyl) benzenesulphonyl fluoride hydrochloride (AEBSF, Gold Biotechnology). 0.14 g of *n*-dodecyl-β-D-maltopyranoside (DDM; Anatrace) was added per 1 g of cells. The pH was adjusted to pH 7.5 using 1 M NaOH and the sample was agitated for 45 min at room temperature. After extraction, the

sample was centrigued at 43,000g at 12 ^{o}C for 40 min and filtered using a 0.45 µM

polyethersulphone membrane. BEST1 protein was affinity purified using YL^{1}/$_{2}$ antibody

coupled to CNBr-activated sepharose beads according to the manufacturer's protocol

(GE Healthcare). For each 1g of cell lystate, 1.0-2.0 ml of resin was added and the

mixture was rotated at room temperature for 1 hour. The mixture was applied to a

column support and washed with ~5 column volumes of buffer containing 20 mM Tris-

HCl, pH7.5, 75 mM NaCl, 75 mM KCl and 3 mM DDM. Elution was carried out using 4

column volumes of elution buffer: 100 mM Tris-HCl, pH7.5, 75 mM NaCl, 75 mM KCl,

3mM DDM and 5mM Glu-Glu-Phe peptide (Sigma-Aldrich). The elution fraction was

concentrated to a volume of 0.5ml using a 100,000 Da concentrator (Amicon Ultra; EMD

Millipore) before further purification by size exclusion chromatography (SEC) (Superose

6 increase 10/300 GL; GE Healthcare).

2.3.2 Reconstitution into liposomes for planar lipid bilayer recordings

SEC-purified protein [in gel filtration buffer: 150 mM NaCl, 20 mM Tris-HCl, pH7.5, 3 mM

n-decyl-β-D-maltoside (Anatrace)] was reconstituted into liposomes. A 3:1 (wt/wt)

mixture of POPE (Avanti) and POPG (Avanti) lipids was prepared to 20 mg ml^{-1} in

reconstitution buffer (10 mM Hepes-NaOH, pH 7.6, 450 mM NaCl, 0.2 mM EGTA, 0.19

mM CaCl$_2$) and the lipids were solubilized by adding 8% (wt/vol) *n*-octyl-β-D-

maltopyranoside (Anatrace) and incubated with rotation for 30 min at room temperature.

Purified protein was mixed with an equal volume of the solubilized lipids to give a final

protein concentration of 0.2-1 mg ml^{-1} and a lipid concentration of 10 mg ml^{-1}. This

sample was dialyzed (8000 Da molecular mass cutoff) overnight at 4 ^{o}C against 2-4 L of

reconstitution buffer to remove detergent. Liposomes were then flash frozen in liquid

nitrogen and stored at -80 ^{o}C.

2.3.3 Electrophysiological Recordings

Frozen liposomes were thawed and sonicated for approximately 10 s using an Ultrasonic Cleaner (Laboratory Supplies Company). All data are from recordings made using components analogous to the Warner planar lipid bilayer workstation (Warner Instruments) (Lee et al., 2013; Miller, 2013). An illustration of the setup is depicted in figure 2.1. Briefly, two aqueous chambers (4 ml) were filled with bath solutions. The standard bath solutions consisted of the following: 30 mM KCl (*cis* side) or 10 mM KCl (*trans* side), 20 mM Hepes-NaOH, pH 7.6, 0.21 mM EGTA, and 0.19 mM CaCl$_2$ (free [Ca^{2+}], ~300 nM, as determined using Fura-2). Chlorided silver (Ag/AgCl) wires were used as electrodes, submerged in 3 M KCl, and connected to the bath solutions via agar–KCl salt bridges [2% (wt/vol) agar, 3 M KCl]. The bath solutions were separated by a polystyrene partition with a ~200-µm hole across which a bilayer was painted using POPE:POPG in *n*-decane [3:1 (wt/wt) ratio at 20 mg·ml^{-1}]. Liposomes containing BEST1 were added, 1 µL at a time, to the *cis* chamber above the partition to a preformed bilayer until currents were observed. Solutions were stirred using a stir plate (Warner Instruments) to aid vesicle fusion to the bilayer. For recordings using 30 or 90 mM KCl on the *trans* side, KCl was added to the *trans* side (from a 3.5 M KCl stock) as necessary after vesicle fusion. NaCl was substituted for KCl in the bath solutions for experiments using NaCl. Unless noted, all reagents were purchased from Sigma-Aldrich. All electrical recordings were taken at room temperature (22–24 °C).

For Ca^{2+} reactivation experiments, after recording currents from standard symmetric KCl (30/30 mM) bath solutions, 10 mM EGTA was added to the *cis* chamber to deactivate channels with their cytosolic side facing this direction. Using a perfusion system (Nanion Technologies), the *trans* chamber was then perfused with 20 ml (5 chamber volumes) of bath solutions containing EGTA-Ca buffers (mixtures of 1 mM EGTA and 1 mM EGTA-
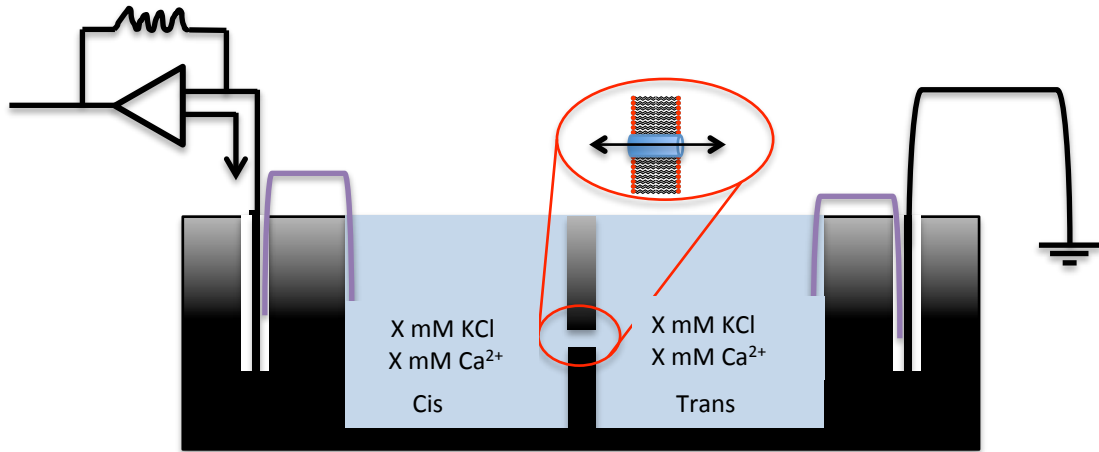
Figure 2.1. Planar lipid bilayer setup used for electrophysiological recordings of purified BEST1. See section 2.3.3 for detailed description of methods. Two chambers, filled with solutions of desired components (eg. KCl and Ca^{2+}) are connected to electrodes via salt bridges (purple). The voltage signal is applied on the *cis* side and the *trans* is held at virtual ground (0 V). The current signal is amplified using a voltage-current amplifier. A ~200 µm aperture separates the solutions and lipid solution is painted over this until a bilayer spontaneously forms. Vesicles containing purified BEST1 are applied to the *cis* side of the bilayer and increases in observed currents are used to detect channel fusion events.

Ca made according to ref (Bers et al., 1994)) to yield varying amounts of free $[Ca^{2+}]$ from ~0 to ~350 nM. Free $[Ca^{2+}]$ in these solutions was estimated using the maxchelator software (maxchelator.stanford.edu/webmaxc/webmaxcS.htm) and was verified using standard solutions (Invitrogen; pH adjusted to 7.6 with NaOH) and Fura-2 (Invitrogen) according to the manufacturer's instructions. For experiments comparing the Ca^{2+} dependency of $BEST1_{WT}$ and channel mutants, currents were recorded using standard symmetric (30/30 mM KCl) bath solutions before and after the addition of 10 mM EGTA (to both chambers, from a 0.5 M EGTA, pH 7.6, stock, followed by 4 min of stirring).

To assess permeabilities to anions other than Cl^-, currents were first recorded in asymmetric (10/30 mM) and symmetric (30/30 mM) KCl conditions. The bath solution in the *trans* chamber was then replaced by perfusion, as described above, with standard bath solutions in which KCl was replaced by various potassium salts (30 mM). For experiments with DIDS (Sigma-Aldrich), freshly made solutions of DIDS (up to 100 mM in DMSO, stored at −20 °C before the experiment, and kept in the dark) were added to both the *cis* and *trans* bath solutions (with mixing for 1 min) to yield the desired final concentrations. Control experiments showed that the amount of DMSO in the bath solutions (maximally 2% for the 1 mM DIDS concentration) did not noticeably alter currents.

Currents were recorded using the Clampex 10.4 program (Axon Instruments) with an Axopatch 200B amplifier (Axon Instruments) and were sampled at 200 μs and filtered at 1 kHz. Data were analyzed using Clampfit 10.4 (Axon Instruments), and graphical display and statistical assessment were carried out using GraphPad Prism 6.0 software. In all cases, currents from bilayers without channels are subtracted. Measurements were

corrected for any offset voltage (typically <1 mV) at the end of the experiments by

breaking the bilayer and using the Axopatch 200B pipette offset control. Error bars

represent the SEM of at least three separate experiments, each in a separate bilayer.

We define the side to which the vesicles are added as the *cis* side and the

opposite *trans* side as electrical ground, so that transmembrane voltage is reported

as V_{cis}–V_{trans}. It is important to note that ion channels are inserted in both orientations in

the bilayer.

2.3.4 Chloride flux assay

For assays in the presence of ~1 μM free Ca^{2+}, purified BEST1 was reconstituted into

liposomes using the reconstitution buffer: 100 mM Na_2SO_4, 10 mM Hepes-NaOH, pH7.0,

0.2 mM EGTA, and 0.19 mM $CaCl_2$. For flux assays that were used to monitor

Ca^{2+} activation, the reconstitution buffer was 100 mM Na_2SO_4, 10 mM Hepes-NaOH, pH

8.2, and 1 mM EGTA. Protein was mixed with solubilized lipids to give a final protein

concentration of 0.1 mg·ml^{-1} (0.01 mg·ml^{-1} was used for Fig.2.10 A) and a lipid

concentration of 10 mg·ml^{-1}. Empty vesicles were prepared in parallel in the same

manner in the absence of protein. The samples were dialyzed for 4–6 d in 2 L of

reconstitution buffer with daily buffer changes. Following dialysis, the liposomes were

sonicated for ~20 s in a water bath, divided into 50-μL aliquots, and flash frozen in liquid

nitrogen for storage at −80 °C. On the day of the experiment, liposomes were thawed,

incubated for ~1 h at room temperature, and then sonicated briefly (~10 s) before use.

Vesicles were diluted 100-fold into flux assay buffer, which contained 125 mM NaCl, and

Cl^- influx into the vesicles was detected from the fluorescence decrease of 9-amino-6-

chloro-2-methoxyacridine (ACMA), which is a pH-sensitive indicator, after initiation of the

assay by addition of the proton ionophore carbonyl cyanide *m*-chlorophenyl hydrazone

(CCCP)(Kane Dickson et al., 2014). For comparative analyses (e.g., data presented on

the same graph) BEST1$_{WT}$ and mutant proteins were purified and reconstituted into liposomes in parallel and the flux assays were performed on the same day.

2.3.5 Crystallization and structure determination of BEST1$_{TripleA}$

Crystals of BEST1$_{TripleA}$ were obtained using the methods described previously for BEST1$_{WT}$ (Kane Dickson et al., 2014). A complex between BEST1$_{TripleA}$ and a Fab monoclonal antibody fragment (designated 10-D10) was formed by mixing the two in a molar ratio of 1:1.2, concentrated (Vivaspin 15R; Sartorius; 10-kDa molecular weight cutoff), and purified using size exclusion chromatography (SEC) (Superdex-200; GE Healthcare). The SEC buffer contained 10 mM Tris, pH 7.5, 75 mM NaCl, 75 mM KCl, and 0.5 mM 2,2-bis(3′-cyclohexylbutyl) propane-1,3-bis-β-D-maltopyranoside (Anatrace). Crystals of the BEST1$_{TripleA}$–Fab complex were obtained by vapor diffusion at 20 °C [300 nL of protein plus 300 nL of well solution: 6% (wt/vol) PEG 4000, 50 mM sodium acetate, pH 4.0, and 20% (vol/vol) glycerol]. Although not explicitly added, Ca^{2+} is present at ~1 µM in the solutions, as determined using Fura-2 calcium indicator (Kane Dickson et al., 2014). Crystals were harvested after 5–10 d and flash-cooled in liquid nitrogen. Diffraction data were collected at 100 K and processed with HKL-3000 (Minor et al., 2006). Resolution limits were assessed using the CC$_{1/2}$ statistic (Karplus and Diederichs, 2012). Phases were determined using molecular replacement (BEST1$_{WT}$, PDB ID code 4RDQ, as a search model), and the atomic coordinates were improved by model building in Coot (Emsley et al., 2010) and refinement using CNS and Phenix (Adams et al., 2012; Brunger, 2007). Data collection and refinement statistics are shown in table 2.1. Molecular graphics figures were prepared using the programs PyMOL (www.pymol.org) and HOLE (Smart et al., 1996).

2.4 Results

2.4.1 Electrical recordings of BEST1 in bilayers

In order to make direct comparisons with the X-ray structure of chicken BEST1 (Kane Dickson et al., 2014), functional analyses using the same construct was performed. Electrical recordings, made using purified lipids and purified protein, allowed investigation of ion selectivity, Ca^{2+} dependence and pharmacological properties of the channel, and to compare these properties with those observed previously for mammalian bestrophins in cellular contexts. Following expression and purification (Fig.2.2), the protein was reconstituted into liposomes containing a 3:1 mixture of 1-palmitoyl-2-oleoyl-*sn*-glycero-3-phosphoethanolamine (POPE):1-palmitoyl-2-oleoyl-*sn*-glycero-3-phospho-(1'-rac-glycerol) (POPG) and applied to planar lipid bilayers of the same lipid composition for electrophysiological analysis following procedures established for other ion channels (Lee et al., 2013; Miller, 2013). Macroscopic currents recorded from bilayers containing BEST1 in the presence of ~300 nM free Ca^{2+} are shown in figure 2.3.

Selectivity for Cl^- over K^+ is evidenced by the "reversal potential", that is, the voltage needed to null the current when a transmembrane KCl gradient is present. When recorded using asymmetric conditions of 10 mM KCl on the "trans" side of the bilayer, which is held at ground, and 30 mM KCl on the "cis" side, the reversal potential is +25.1 ± 0.8 mV (*n* = 8). To determine the permeability ratio for Cl^- versus K^+, the Goldman-Hodgkin-Katz equation was used in the following form:

$$E_{REV} = \frac{RT}{zF} \mathrm{Ln} \left(\frac{P_K [K^+]_o + P_{Cl}[Cl]_i}{P_K [K^+]_i + P_{Cl}[Cl]_o} \right)$$

A
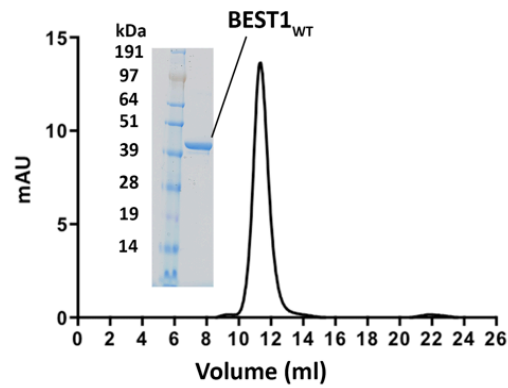
B
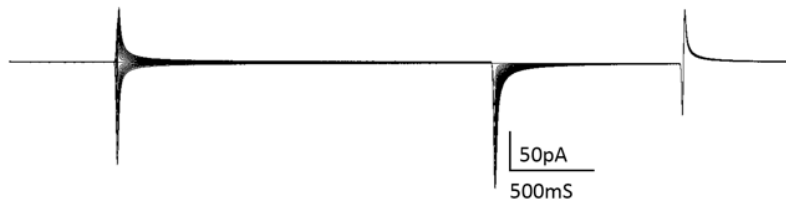
Figure 2.2. (A) Purified BEST1 protein. The elution profile from a size exclusion column (Superdex 200; GE healthcare; black UV trace) and SDS-PAGE analysis of the purified protein (*Inset;* molecular weight marker, *Left;* purified BEST1$_{WT}$, *Right*) are shown. All mutants studied in this chapter eluted as monodisperse peaks on a size exclusion column, equivalent to wild-type protein. (B) Currents observed for an "empty" lipid bilayer without channels using the following protocol: from a holding potential of 0 mV, the voltage was stepped to test values between -100 and +100 mV, in 10-mV increments, for 2 s. After a further 1-s step to -100 mV, the voltage was returned to 0 mV.

where E_{REV} is the measured reversal potential and all other terms have their usual meanings. This gives a permeability ratio of P_K/P_{Cl} = 0.05 ± 0.01 (Fig.2.3 A, D), consistent with Cl$^-$ selectivity of the channel. As has been observed for mammalian BEST1 from whole-cell measurements (Sun et al., 2002), the currents reach a steady-state level after relaxation of the transient capacitive current and do not exhibit noticeable voltage or time dependence on the timescale of the measurements (Fig. 2.3 A,B).

Chelation of Ca^{2+} using EGTA on both the *cis* and *trans* sides abolishes the currents (Fig.2.3 C, D), and the addition of EGTA to either side partially reduces the currents, consistent with Ca^{2+}-activated channels being inserted in the bilayer in both orientations (Fig.2.3 E). The subsequent addition of Ca^{2+}, introduced by exchanging bath solutions with varying free [Ca^{2+}], activates the currents in a dose-dependent manner, with an apparent $K_{1/2}$ for Ca^{2+} of 17 ± 3 nM (n = 3) (Fig. 2.4). This value is smaller than reported for mammalian bestrophin channels (~100 nM) (Hartzell et al., 2008; Qu et al., 2004; Tsunenari et al., 2006) and may be due to specifics of the chicken ortholog and/or differences between working with purified protein in the simplified planar lipid bilayer system vs. whole-cell studies (e.g., differences in membrane lipid composition).

Starting from symmetric 30 mM KCl on both sides and replacing KCl on the *trans* side with 30 mM Br$^-$, I$^-$, or SCN$^-$ shifts the reversal potential to increasingly negative values to reveal the hallmark lyotropic order of anion permeability for bestrophin channels : SCN$^-$ > I$^-$ > Br$^-$> Cl$^-$ (Fig. 2.5 A,B). The permeability ratios between monovalent anions was solved using a derivation of the Goldman-Hodgkin-Katz equation for biionic conditions of
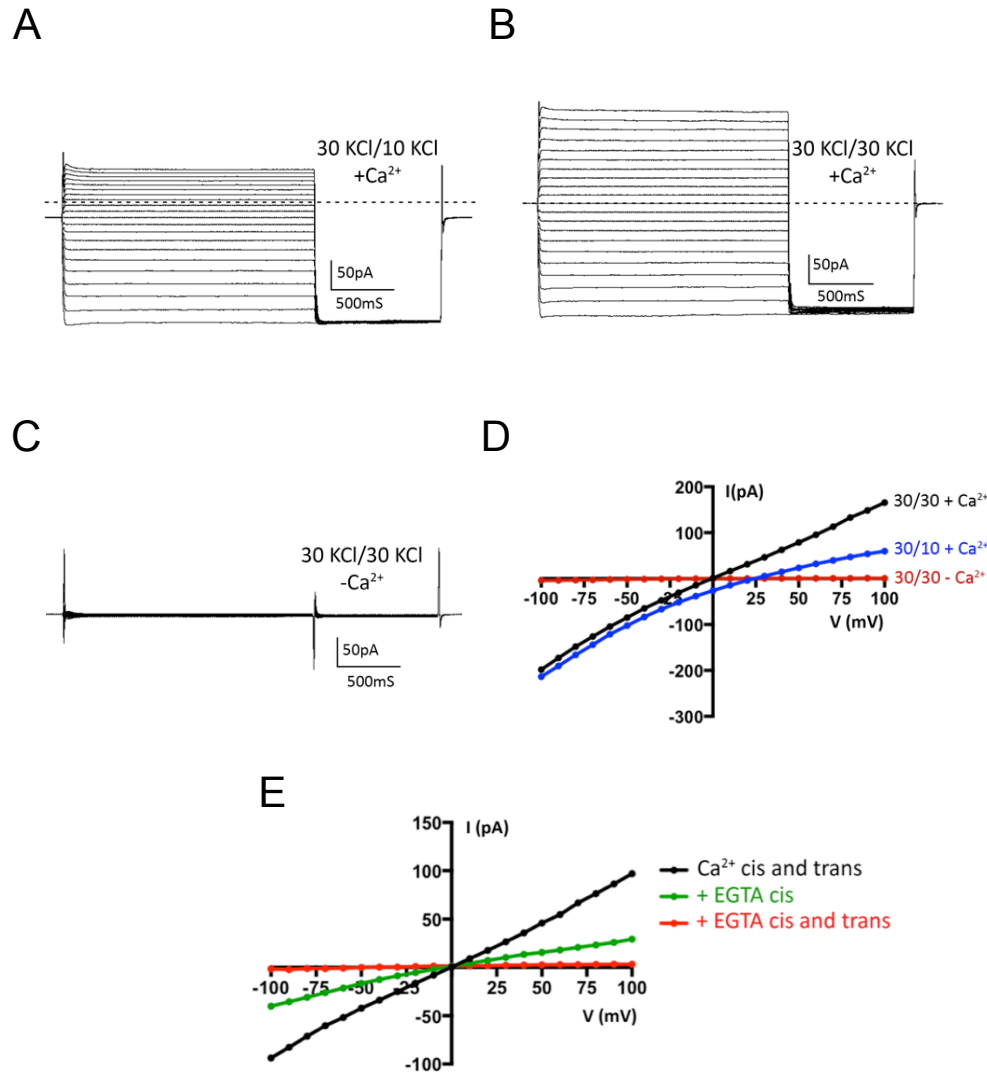
Figure 2.3. Electrical recordings of planar lipid bilayers containing purified chicken BEST1 protein. A-C are representative experiments using the same bilayer. The dashed lines represent the zero current level. (A) With ~300 nM Ca^{2+} on both sides of the membrane, currents were measured using asymmetric KCl (30 mM *cis* and 10 mM *trans*) using the same voltage pulse protocol described in figure 2.2. (B) Currents recorded using ~300 nM Ca^{2+} and symmetric 30 mM KCl. (C) Currents recorded after 10 mM EGTA had been added to each side. (D) Current-voltage (I-V) relationships of the data shown in A-C, which were obtained by plotting the test voltages vs. the average currents from 200-ms windows at the end of the 2-s pulses (connected filled circles). Annotations such as "30/10" indicate the concentrations of KCl, in millimolar, on the cis/trans sides. (E) BEST1 channels insert in both orientations in the bilayer. *I-V* relationships are shown for macroscopic currents recorded using the same pulse protocol as in Figure 2.1. The voltage is stepped to values between -100 and +100 mV under symmetrical conditions before (black; ~300 nM Ca^{2+}) and after addition of 10 mM EGTA to standard solutions on the *cis* (green) and then *trans* (red) sides. The stepwise reduction in currents observed by chelation of Ca^{2+} by EGTA on the *cis* and *trans* sides is indicative that channels are inserted in both orientations in the bilayer.
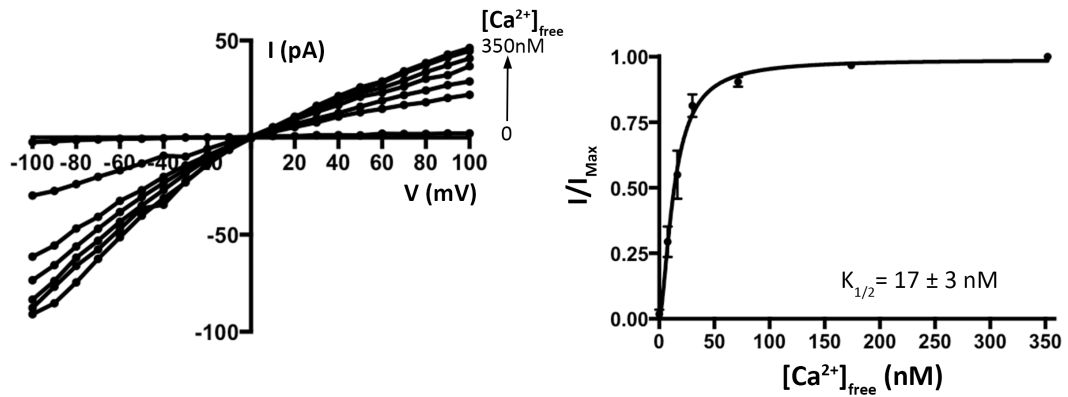
Figure. 2.4. (A) Reactivation of BEST1 currents by increasing the free Ca^{2+} concentration ($[Ca^{2+}]_{free}$). After observing currents in standard symmetrical solutions, 10 mM EGTA was added to the *cis* side to deactivate channels with their cytosolic side facing that dierection. Then, using perfusion, the $[Ca^{2+}]_{free}$ in the *trans* solution was varied from ~0 to 350 nM with a Ca-EGTA buffer system (*Methods*). *I-V* relationships are shown for data recorded using the same pulse protocol as Figure 2.1. (B) Ca^{2+} response curve. From three separate experiments as in *A*, average currents observed at -100 mV for different $[Ca^{2+}]_{free}$ were plotted as the fraction of the current recorded at -100 mV from the $[Ca^{2+}]_{free}$ = 350 nM condition (I_{Max}). The data were fit to a one-site binding model. (Liu et al., 2014).

the following form:

$$E_{\text{REV}} = \frac{RT}{zF} Ln \frac{P_X[X^-]_o}{P_{Cl}[Cl^-]_i}$$

where E_{REV} is the measured reversal potential, X is the permeant anion applied to the

trans solution in equimolar concentrations with chloride in the *cis* solution, and all other

terms have their usual meanings. As has been observed for human BEST1 channels

studied in whole cells, currents are inhibited by DIDS (Fig.2.5 C, D) with similar fractional

inhibition and IC_{50} values. Together, these results indicate that channels formed from

purified chicken BEST1 and inserted into synthetic lipid membranes have properties

comparable to mammalian BEST1 channels in cells.

2.4.2 The neck

Having established a system to study the ion selectivity and Ca^{2+} activation properties of

purified BEST1 channels, I wanted to address whether mutation of the neck region of the

pore would have an effect on ion selectivity. The side chains of three highly conserved

hydrophobic amino acids from each of the five subunits, I76, F80, and F84, form the

neck (Fig.2.6 A). A construct containing simultaneous substitutions of these residues

with alanine (I76A, F80A, and F84A, which I will refer to as BEST1$_{TripleA}$) was made and

the purified channel studied. Bilayers containing BEST1$_{TripleA}$, in the presence of ~300

nM free Ca^{2+}, yielded robust currents and *I-V* relationships with similar reversal

potentials to those of the wild-type channel (BEST1$_{WT}$) under both symmetric and

asymmetric KCl conditions (Fig.2.6B,C and Fig. 2.7). For example, asymmetric

conditions of 10 mM KCl on the *trans* side and 30 mM KCl on the *cis* side gave rise to a

reversal potential of 24.8 ± 1.3 mV (*n* = 7) for BEST1$_{TripleA}$ in comparison with the value

A

B

C

D
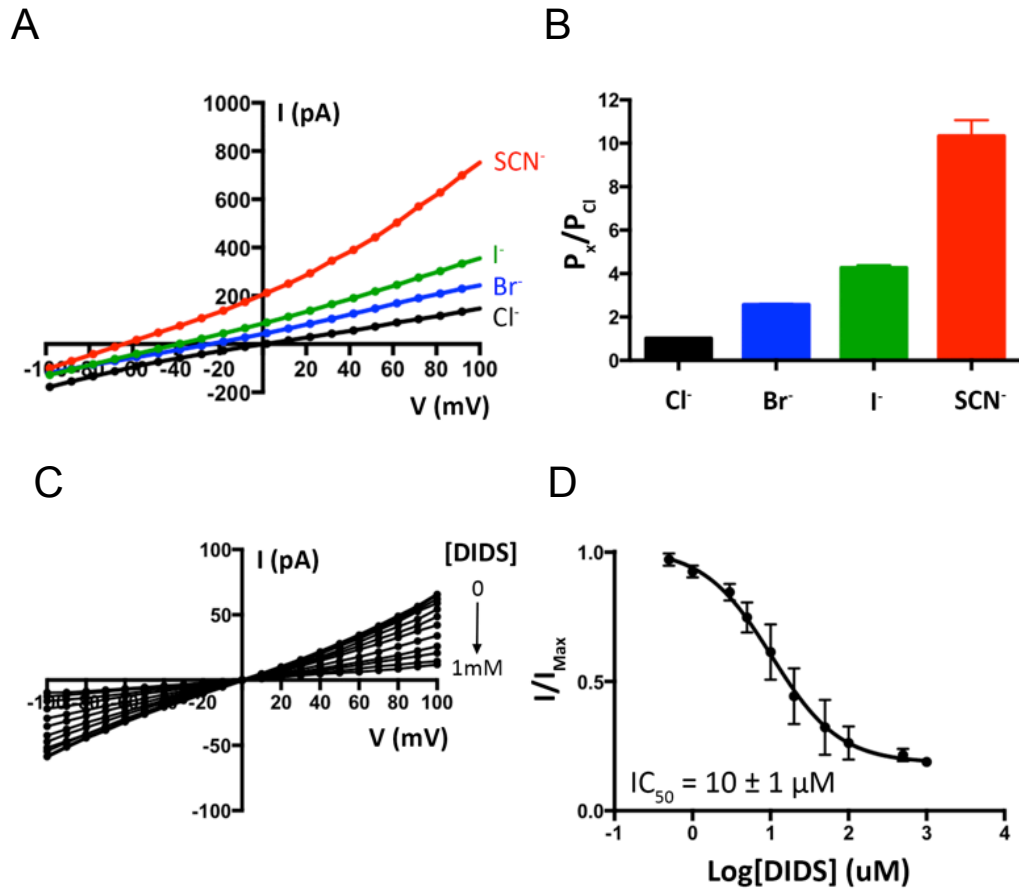
Figure 2.5. (A) Lyotropic series of anion permeability. After first recording using symmetric 30 mM KCl (black *I-V* trace), the solution on the *trans* side was replaced (by perfusion) with solutions containing 30 mM KBr, KI, or KSCN. *I-V* traces are shown for data collected using the standard voltage protocol. (B) Permeability ratios, determined using data from *A* by solving the Goldman-Hodgkin-Katz equation. Three separate experiments were used to compute the SE. (C and D) DIDS block. (C) *I-V* relationships show the decrease in current with increasing concentrations of DIDS. (D) Fit of the data from *C* and two analogous experiments to a standard dose-response curve. The data were plotted as the fraction of the current recorded at -100 mV in the absence of DIDS (I_{Max}).
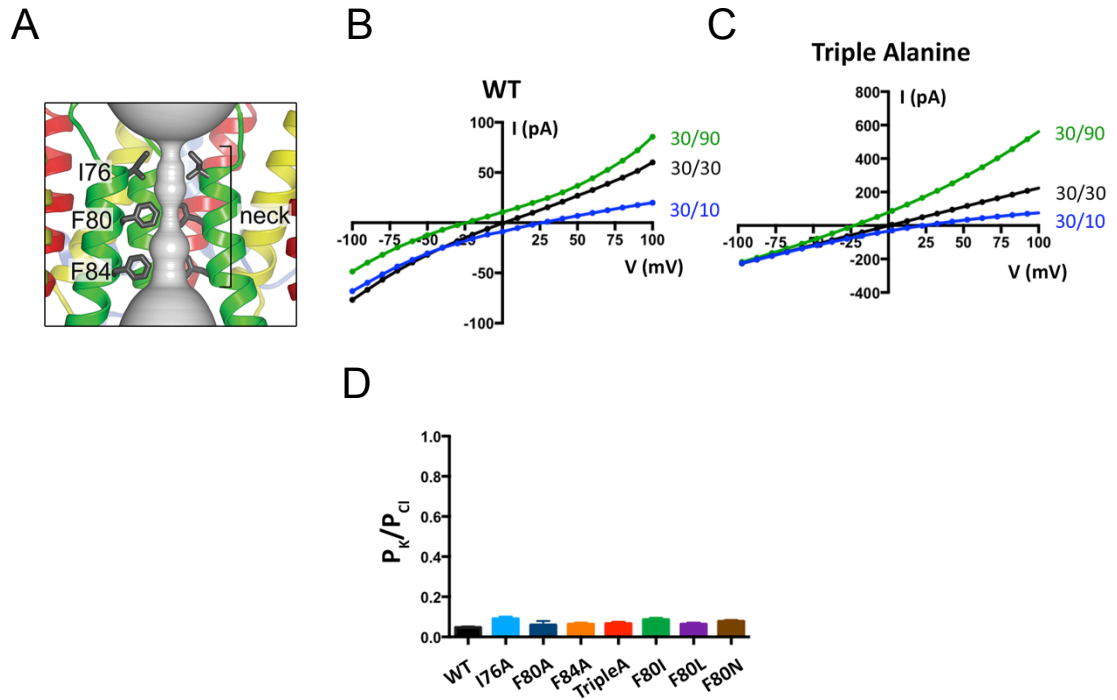
Figure 2.6. Mutation of the neck does not affect anion-vs.-cation selectivity in BEST1. (A) Close-up view of the neck region of the pore (gray surface) of BEST1 (illustrated in Fig.1.5) (B and C) Mutation of amino acids in the neck does not noticeably shift reversal potentials. *I-V* relationships are shown for BEST1$_{WT}$ (B) and BEST1$_{TripleA}$ (C) recorded from -100- to +100-mV voltage steps under symmetric (black) and asymmetric (blue, green) KCl conditions using standard solutions. Labeled values (e.g., "30/90") indicate the concentration of KCl (in millimolar) used for the *cis/trans* sides. (D) Permeability ratios (P_K/P_{Cl}) for BEST1$_{WT}$ and neck mutants. Using reversal potentials measured from both 30/10 and 30/90 mM KCl conditions, the Goldman-Hodgkin-Katz voltage equation was solved to compute an average P_K/P_{Cl} permeability ratio per experiment: WT, 0.05 ± 0.01; I76A 0.09 ± 0.01; F80A, 0.06 ± 0.03; F84A, 0.06 ± 0.01; TripleA, 0.07 ± 0.02; F80I, 0.09 ± 0.02; F80L, 0.06 ± 0.01; and F80N, 0.08 ± 0.01. Error bars denote the SEM from three separate experiments (using different bilayers).

of 25.1 ± 0.8 mV (n = 8) for BEST1$_{WT}$. Thus, the TripleA mutation did not noticeably alter

P_K/P_{Cl} of the channel. Not surprisingly, individual alanine substitutions of these amino

acids also had essentially no effect on P_K/P_{Cl} (Fig.2.6D and Fig.2.8A). To study the ion

selectivity of BEST1$_{TripleA}$ among anions, I measured the currents starting with symmetric

30 mM KCl and then replaced Cl$^-$ by Br$^-$, I$^-$, SCN$^-$ on the *cis* side using the same

procedure that I used for BEST1$_{WT}$ (Fig.2.8B, C). The resulting *I-V* curves are similar to

those obtained for BEST1$_{WT}$, and the reversal potentials and resulting permeability ratios

are statistically indistinguishable. Thus, both anion-over-cation selectivity and the

lytoropic sequence of permeability are essentially unaltered by the TripleA mutation in

the neck.

Next, I asked what effect more subtle mutations of F80, which is located in the middle of

the neck, might have on the channel. F80 has been postulated to be a determinant of ion

selectivity based on work stemming from the crystal structure of the prokaryotic KpBEST

channel, which is selective for cations over anions and has an isoleucine at the

corresponding position in the neck of its pore (Yang et al., 2014). I found that mutation of

F80 to isoleucine, or to leucine, or even to asparagine, does not significantly change

P_K/P_{Cl} of BEST1, as evidenced by the reversal potentials measured using

transmembrane KCl gradients (Fig.2.6D and Fig.2.8A). Among the neck mutants I

tested, there is a slight trend toward elevated P_K/P_{Cl} values (Fig. 2.6D), which is on the

order of the error in the measurements, but these effects, if any, are subtle. To compare

more directly with previous work that asserted that the neck determines the charge

selectivity of the channel, and that assessed P_{Na}/P_{Cl} (Yang et al., 2014), I studied the

channels using NaCl gradients and find that both BEST1$_{WT}$ and BEST1$_{F80I}$ are selective

for Cl$^-$
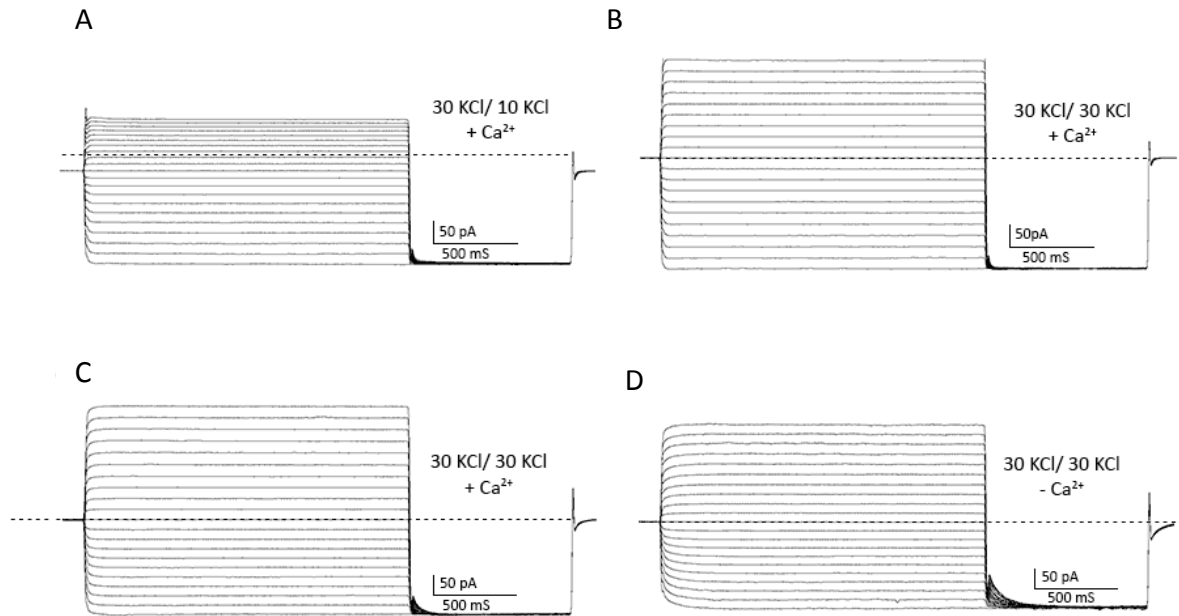
Figure 2.7. Current traces for BEST1$_{TripleA}$. (A and B) Current traces, using the same bilayer, from which *I-V* relationships presented in figure 2.6 C are derived. The dashed line represents the zero current level. (A) Asymmetric (30 mM *cis*, 10 mM *trans*) and (B) symmetric (30 mM *cis*, 30 mM *trans*) KCl conditions. (C and D) Current traces, from the same bilayer, in the presence of ~300 nM free Ca^{2+} (C) and after the addition of 10 mM EGTA to the *cis* and *trans* chambers (D). The protocols used are identical to those described in figure 2.2
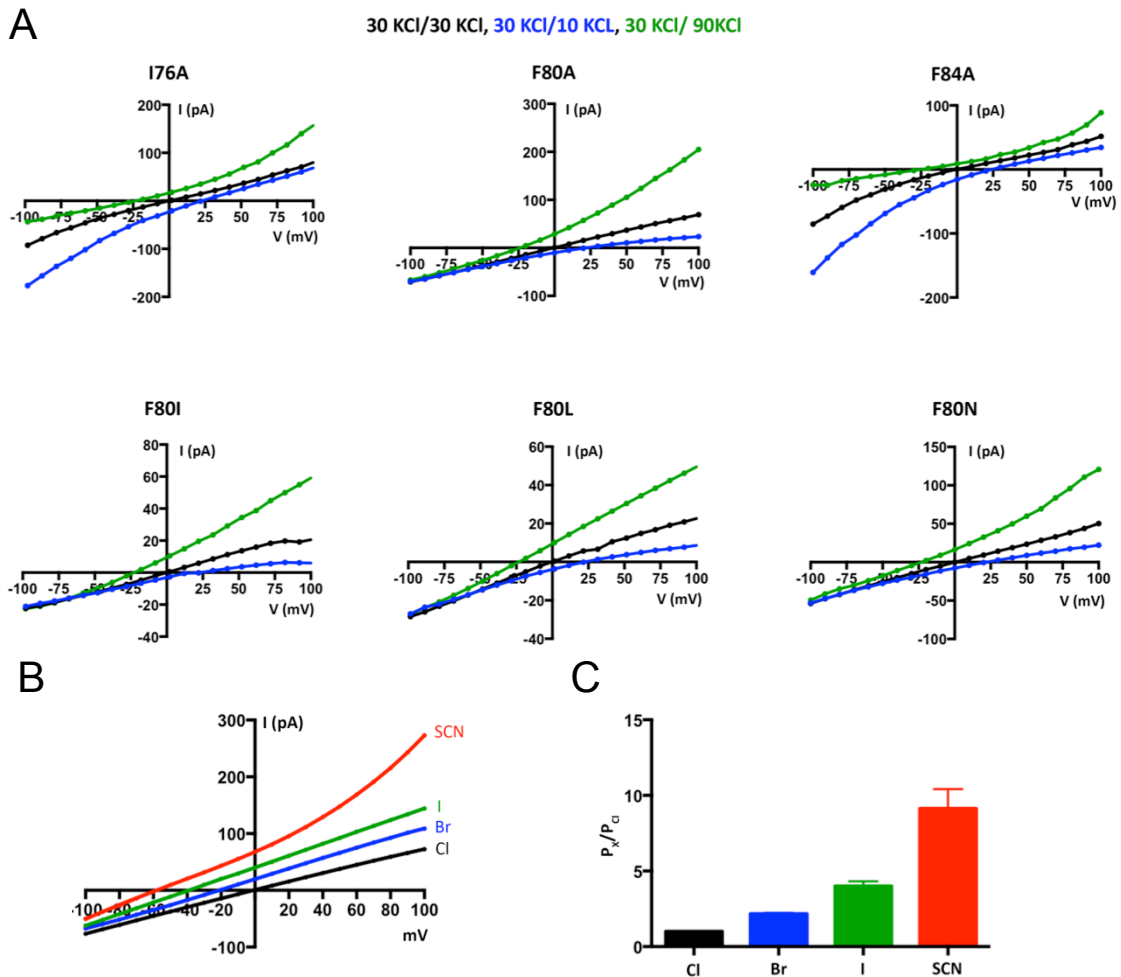
Figure 2.8. (A) Example *I-V* traces for BEST1 neck mutants used to compute the permeability ratios (P_K/P_{Cl}) presented in figure 2.6D. For each mutant, three separate experiments, using different bilayers, were used to compute P_K/P_{Cl}. (B and C) The lyotropic sequence of anion permeability is unaltered in the BEST1$_{TripleA}$ mutant. (A) Example *I-V* relationships recorded using voltage steps from -100 to +100 mV. Following the procedure outlined in figure 2.5A, after first recording using symmetric 30 mM KCl (black *I-V* trace), the solution on the *trans* side was replaced (by perfusion) with solutions containing 30 mM KBr, KI, or KSCN. *I-V* traces are shown for data collected using the standard voltage protocol. (C) Permeability ratios were determined by solving the Goldman-Hodgkin-Katz equation using three separate experiments to compute the SEM.

over Na$^+$ and exhibit nearly identical permeability ratios (Fig. 2.9, P_{Na}/P_{Cl} = 0.09 ± 0.01

and 0.12 ± 0.02 for BEST1$_{WT}$ and BEST1$_{F80I}$, respectively). Contrary to previous

implications, we conclude that the neck is not a major determinant of anion-vs.-cation

selectivity in BEST1.

In the course of the experiments, I noticed that macroscopic currents for BEST1$_{TripleA}$

were typically larger than for BEST1$_{WT}$ when roughly the same amount of

proteoliposomes were applied to the bilayer. Because it is difficult to determine the

actual amount of protein incorporated in the bilayer, I measured Cl$^-$ flux into liposomes

using an assay where the amount of protein being studied is known. Using

proteoliposomes containing nominally equivalent amounts of BEST1$_{WT}$ or BEST1$_{TripleA}$ I

observed substantially more Cl$^-$ flux for BEST1$_{TripleA}$ than for BEST1$_{WT}$ (Fig.2.10 A). This

indicates that individual BEST1$_{TripleA}$ channels support a higher overall Cl$^-$ transport rate

than BEST1$_{WT}$ channels. (The term "overall Cl$^-$ transport rate" is used to mean the time-

averaged rate at which ions flow through a single ion pore, which is proportional to the

product of the channel's open probability and the conductance of a single open channel.

Changes in the overall Cl$^-$ transport rate could be due to changes in the open probability

and/or the single-channel conductance, but these possibilities cannot be distinguished

by the present data.)

In contrast, the F80I and F80L mutant channels consistently yielded smaller

macroscopic currents than BEST1$_{WT}$ for a given amount of proteoliposomes applied to

the bilayer. Accordingly, for the electrical measurements of these latter mutants, I

applied proteoliposomes to the bilayer until we obtained sufficient currents to accurately
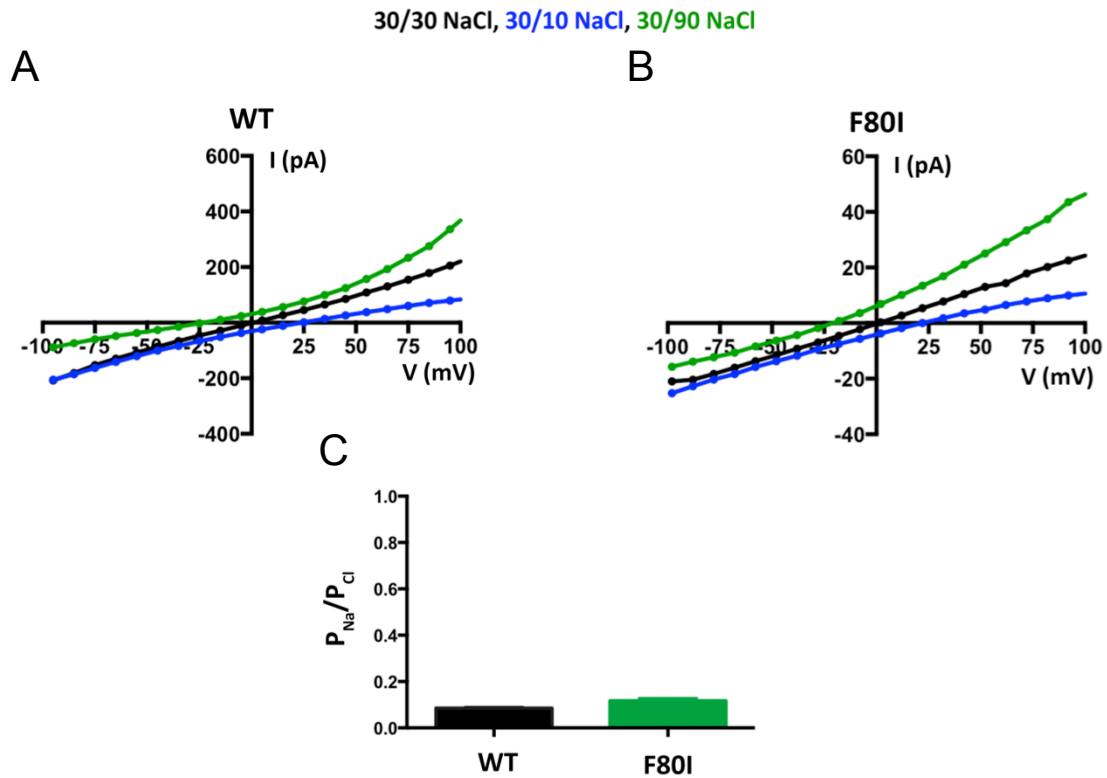
Figure 2.9. The F80I mutation does not make BEST a sodium-selective ion channel. (A and B) Experiments are performed as in figure 2.6A except bath solutions contained NaCl instad of KCl. Example *I-V* relationships are shown for WT (A) and F80I (B). (C) Using reversal potentials measured from both the 30/10 and 30/90 mM KCl conditions, the Goldman-Hodgkin-Katz voltage equation was solved to compute an average permeability ratio per experiment. Error bars are computed using the SEM from three separate experiments.
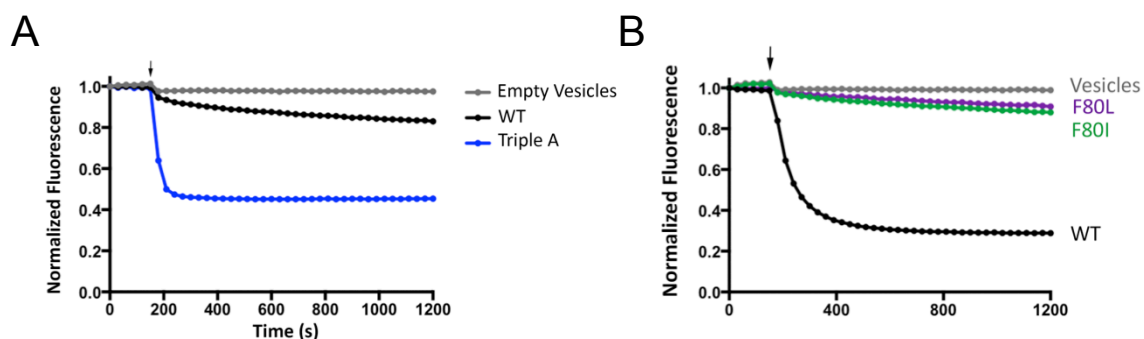
Figure 2.10. (A) BEST1$_{TripleA}$ has a higher unitary Cl$^-$ transport rate than BEST1$_{WT}$. To compare the activit of BEST1$_{WT}$ and BEST1$_{TripleA}$, channel protein (purified and incorporated into liposomes in parallel) was incorporated into liposomes using a 1:1000 protein:lipid ratio and the fluorescence-based Cl$^-$ flux assay. In this assay, a decrease in fluorescence is indicative of Cl$^-$ influx into liposomes. The arrow indicates when the assay was initiated by the addition of the proton ionophore CCCP (*Methods)*. (B) (B) Hydrophobic mutations at F80 reduce Cl$^-$ flux. Flux assay measurements for BEST1$_{WT}$, BEST1$_{F80I}$, and BEST1$_{F80L}$, and for empty vesicles were made on the same day to compare channel activity.

determine reversal potentails (>20 pA at 100 mV; Fig. 2.8A). Using the flux assay, I found that $BEST1_{F80I}$ and $BEST1_{F80L}$ showed substantially reduced Cl⁻ flux compared with $BEST1_{WT}$ for the same amount of protein, indicating that these mutant channels have lower overall Cl⁻ transport rates than $BEST1_{WT}$ (Fig.2.10 B). This suggests that, although F80 does not determine ion selectivity, this phenylalanine residue is important for Cl⁻ ion flow through the pore. These findings are consistent with F80L being described as a disease mutation that impairs BEST1 function (Chien and Hartzell, 2008; Milenkovic et al., 2011)

2.4.3 Ca^{2+}-dependent activation

I next assessed whether mutations in the neck affect the Ca^{2+} dependence of the channel. I found that unlike the currents observed for $BEST1_{WT}$, which depend on Ca^{2+}, chelation of Ca^{2+} in the bath solutions had almost no effect on the currents observed for $BEST1_{TripleA}$ (Fig.2.11 A, B and Fig.2.7 C, D). Analogous results were obtained using a flux assay. For $BEST1_{WT}$, I observed Cl⁻ flux with 2 μM Ca^{2+} present, but not when Ca^{2+} was chelated by EGTA (Fig.2.12 A). On the other hand, ion flux for $BEST1_{TripleA}$ was observed whether or not Ca^{2+} was present, indicating that the mutant channel is constitutively active and not dependent on Ca^{2+} (Fig.2.12 B). Studying single amino acid substitutions of F80, I found varying degrees of effects on the Ca^{2+} dependence of ionic currents (Fig.2.11 C-F). When Ca^{2+} is chelated, the F80A mutant retains almost 50% of the current in comparison with when Ca^{2+} is present. The hydrophobic substitution F80I yields channels with currents that are nearly as Ca^{2+} dependent as $BEST1_{WT}$. On the other hand, mutating F80 to asparagine, which is a similarly sized but hydrophilic amino acid, produces channels that retain ~70% of their current in the absence of Ca^{2+}. Evidently, I find that mutation of the neck has dramatic effects on the Ca^{2+} dependence of the channel.
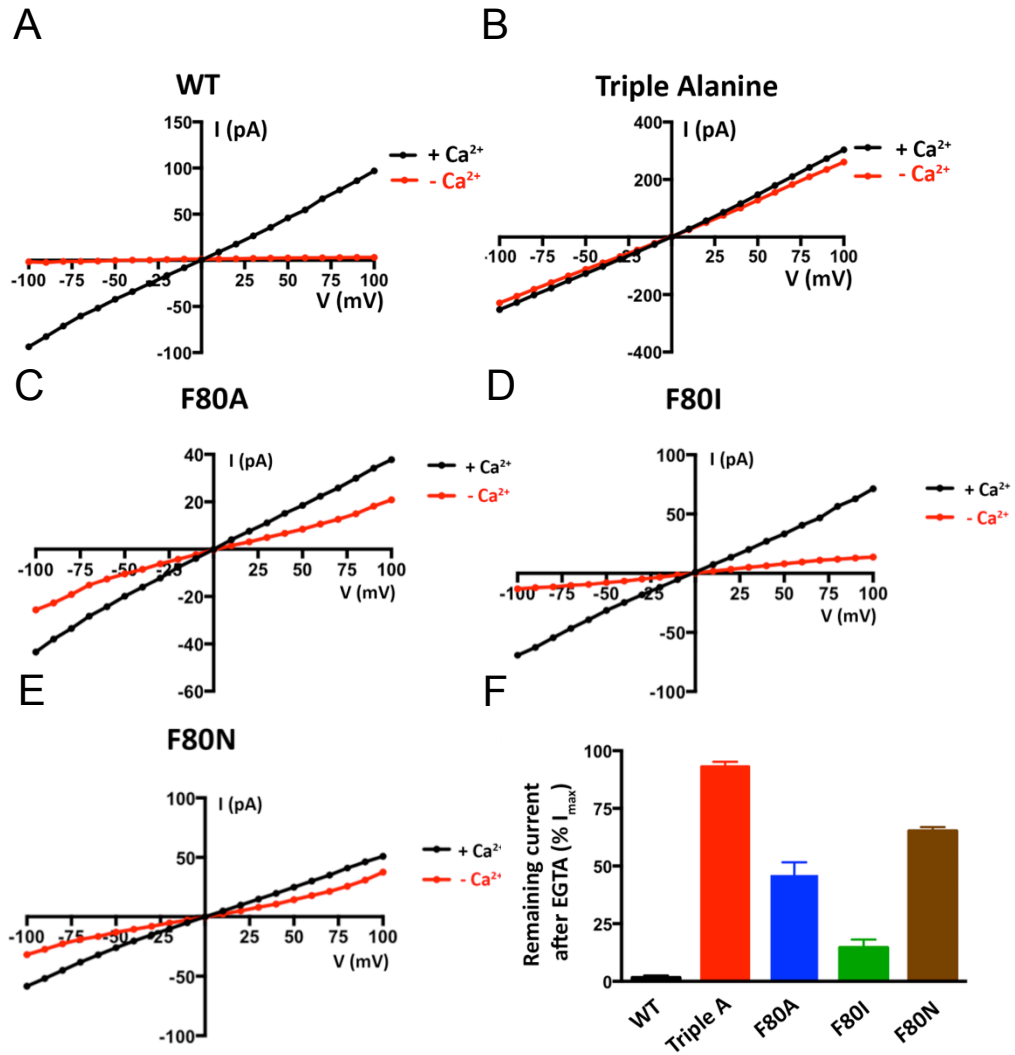
Figure 2.11. Size and hydrophobicity of the amino acids in the neck affect Ca^{2+}-dependent activation of BEST1. (A and B) Unlike BEST1$_{WT}$, BEST1$_{TripleA}$ currents are almost completely independent of [Ca^{2+}]. *I-V* relationships are shown for currents recorded by voltage steps to values between -100 and +100 mV under symmetric KCl (30/30) conditions before ("+ Ca^{2+}", [Ca^{2+}]$_{Free}$ ~300 nM) and after ("- Ca^{2+}") the addition of 10 mM EGTA to both *cis* and *trans* chambers. The current traces for BEST1$_{TripleA}$ are shown in figure 2.7. (C-E) *I-V* relationships are shown for BEST1$_{F80A}$, BEST1$_{F80I}$ and BEST1$_{F80N}$ for experiments performed as in *A* and *B*. (F) Mutations to the neck region have dramatic effects on Ca^{2+}-dependent activation. Macroscopic currents were recorded as in A and B for each mutant. The fraction of current remaining at +100 mV after the addition of EGTA is plotted. Erorr bars indicate the SEM from three separate experiments.
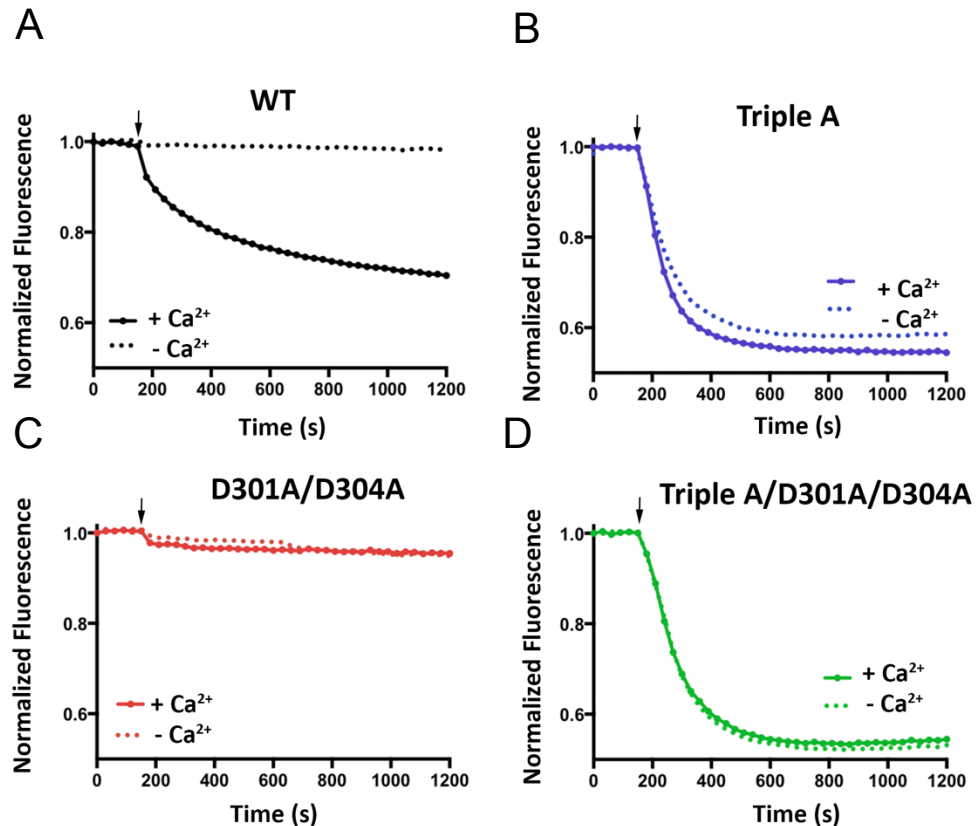
Figure 2.12. Cl⁻ flux analysis of BEST1$_{TripleA}$ and Ca^{2+} clasp mutants. (A-D) For each assay, proteoliposomes were diluted 100-fold into flux assay buffer containing either 1 mM EGTA (-Ca^{2+}) or 1 mM EGTA-CaSO$_4$ (+ Ca^{2+}, [Ca^{2+}]$_{Free}$ ~ 2 µM). The arrow indicates when the assay was initiated by the addition of the proton ionophore CCCP. (A) Cl⁻ flux of BEST1$_{WT}$ is Ca^{2+} dependent. (B) Cl⁻ flux through BEST1$_{TripleA}$ is observed regardless of the presence or absence of Ca^{2+}. (C) Mutation of aspartate amino acids that coordinate Ca^{2+} in the Ca^{2+} clasp to alanine (D301A/D304A) abolishes Cl⁻ flux and makes the channel unresponsive to 2 µM Ca^{2+}. (D) Combining the D301/D304A and the BEST1$_{TripleA}$ mutations produces a constitutively active channel that is not responsive to the Ca^{2+} concentration. The increased flux observed for BEST1$_{TripleA}$ relative to BEST1$_{WT}$ is partially due to the nature of the assay, where Ca^{2+} is only added to the outside of the vesicles. For BEST1$_{WT}$, only those channels with their Ca^{2+} sensors facing outside are reactivated, whereas Cl⁻ flux through BEST1$_{TripleA}$ channels in both orientation is detected because these channels conduct Cl⁻ in a Ca^{2+}-independent manner.

The X-ray structure of BEST1 identified a Ca^{2+} binding site, the Ca^{2+} clasp, in the channel's cytosolic region and it was speculated that this binding site could be responsible for the channel's regulation by intracellular $[Ca^{2+}]$ levels (Kane Dickson et al., 2014). The side chains of two conserved aspartate amino acids, D301 and D304, directly coordinate Ca^{2+} in the Ca^{2+} clasp (Fig.1.6). In previous whole-cell patch-clamp recordings, no currents that could be attributed to BEST1 were observed when these amino acids were mutated to alanine (Xiao et al., 2008). In accord with these results, no Cl^- flux was observed either in the presence or absence of Ca^{2+}, in experiments conducted by a postdoctoral researcher in the laboratory, Dr. Alexandria N. Miller, for a construct in which both D301 and D304 were mutated to alanine (Fig.2.12 C). It is unlikely that gross protein misfolding is responsible for the lack of activity because the purified protein migrates on a size exclusion column as a single Gaussian peak with approximately the same elution volume as $BEST1_{WT}$. It was hypothesized that incorporation of the TripleA mutation within the neck might restore activity to the D301/D304A mutant. Indeed, Cl^- flux assay measurements indicate that the combination of these mutations yields a channel that is active in the presence and absence of Ca^{2+} (Fig.2.12 D).

2.4.4 X-ray structure of $BEST1_{TripleA}$

To better understand how mutations to the neck cause the channel to be constitutively active irrespective of Ca^{2+}, I determined the X-ray structure of $BEST1_{TripleA}$ to 3.1 Å resolution (Fig.2.13 and Table 2.1). The overall structure is practically indistinguishable from that of $BEST1_{WT}$ (Fig. 2.14 C, D, rmsd of 0.2 Å). In both structures, Ca^{2+} ions are bound within the channel's five symmetry-related Ca^{2+} clasps. The entire cytosolic region of the channel, including the dimensions of the aperture, is unchanged. The only notable differences between the structures of $BEST1_{WT}$ and $BEST1_{TripleA}$ are within the neck

A BEST1$_{WT}$

B BEST1$_{TripleA}$

C

Out

In

Neck

Ca^{2+}

Aperture

I76
F80
F84

V205

I76A
F80A
F84A

V205

Neck

WT
Triple A
- - - Dehydrated Cl$^-$
- - - Hydrated Cl$^-$

Distance (Å)
Diameter (Å)
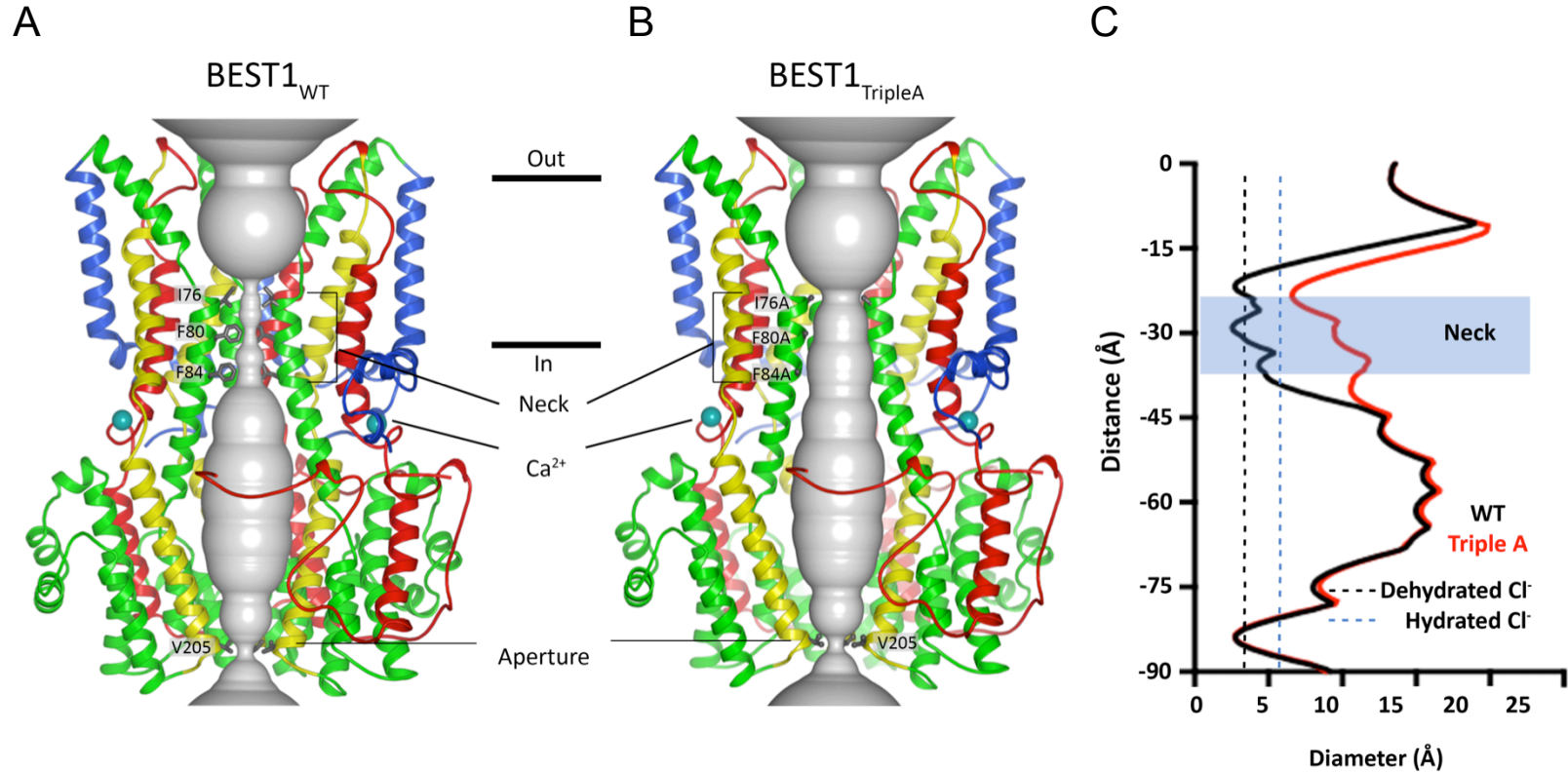
Figure 2.13. Comparison of the X-ray structure of BEST1$_{WT}$ (A) and BEST1$_{TripleA}$ (B). Ribbon representations are shown for three subunits (two in the foreground are removed for clarity). The ion pore (gray tube) is depicted as a representation of the minimal radial distance from the central axis to the nearest van der Waals protein contact. Secondary structural elements are colored according to the four segments of the channel (S1, blue; S2, green; S3, yellow; S4 and C-terminal tail, red), which contain corresponding transmembrane regions. Approximate boundaries of a lipid membrane are indicated by horizontal black lines. (C) Plots of the diameters of the pores from A and B along the ion conduction pathway. Vertical dashed lines indicate the diameters of hydrated and dehydrated Cl$^-$ ions.

Data Collection	
Space group	P2$_1$
Wavelength, Å	1.033
Cell dimensions, Å	
a	98.24
b	243.88
c	172.05
α = γ = 90°, β =, (°)	93.84
Resolution, Å	38-3.1 (3.15-3.10)
R_{merge}	0.25 (1.9)
R_{pim}	0.086 (0.646)
CC$_{1/2}$ in outer shell	0.604
I/σ/	9.7 (1.2)
Completeness, %	99.9 (99.9)
Redundancy	9.5 (9.7)
Refinement	
Resolution, Å	38-3.1
No. of reflections	145,877
No. of atoms	30,705
Ions	25
Water	10
R_{work}	0.218 (0.334)
R_{free}	0.242 (0.358)
Average B factors, Å^2	101.2
Protein	101.3
Ions	90.1
Water	72.82
Ramachandran, %	
Favored	95
Outliers	0.4
Rms deviations	
Bond lengths, Å	0.004
Bond angles, Å	0.95
Rotamer outliers, %	1.6
Clash score	7.6

Table 2.1. Data collection and refinement statistics for BEST1$_{TripleA}$. Data collection statistics are taken from HKL3000 (Minor et al., 2006), refinement staistics are from PHENIX (Adams et al., 2012), and CC$_{1/2}$ is defined in (Karplus and Diederichs, 2012). Numbers in parentheses indicate the highest resolution shells and their statistics. The 5% of reflections used for calculation of R_{free} were derived from the search model PDB ID code 4RDQ.

region. The alanine substitutions (I76A, F80A, and F84A) increase the average diameter of the neck, measured between van der Waals surfaces, from ~3.5 Å in $BEST1_{WT}$, which is approximately the diameter of a dehydrated Cl^- ion, to ~9 Å in $BEST1_{TripleA}$, which is amply wide to accommodate a hydrated Cl^- (Fig.2.13 C). There are also subtle shifts, on the order of ~0.3 Å, in the backbone positions of the helices lining the neck and the surrounding area (Fig.2.14). It is remarkable that the channel's selectivity for anions and its lyotropic permeability sequence, which is an indication that ion dehydration occurs during permeation, are unaffected by the widening of the neck in $BEST1_{TripleA}$. The structures of $BEST1_{TripleA}$ and $BEST1_{WT}$, together with the electrophysiological and flux assay analyses of the neck and Ca^{2+} clasp mutants support the conclusion that the Ca^{2+} clasp is the sensor that responds to intracellular Ca^{2+} levels and that conformational changes within the neck permit the permeation of Cl^- through BEST1 in a Ca^{2+}-dependent manner.

2.4.5 The aperture

The permeability sequence of BEST1 ($SCN^- > I^- > Br^- > Cl^-$) is lyotropic; that is, it corresponds to the inverse sequence of the energy of dehydration of the anions, with SCN^- being the most easily dehydrated and Cl^- being the least easily dehydrated. Lyotropic permeability sequences are an indication that ion permeation involves ion dehydration (Hille, 2001; Hartzell et al., 2005a; Qu and Hartzell, 2000). Because the structure of $BEST1_{TripleA}$ shows that it has a wide-enough neck region to accommodate hydrated anions and yet the $BEST1_{TripleA}$ channel exhibits a lyotropic permeability sequence, it was reasoned that permeating anions become dehydrated at other
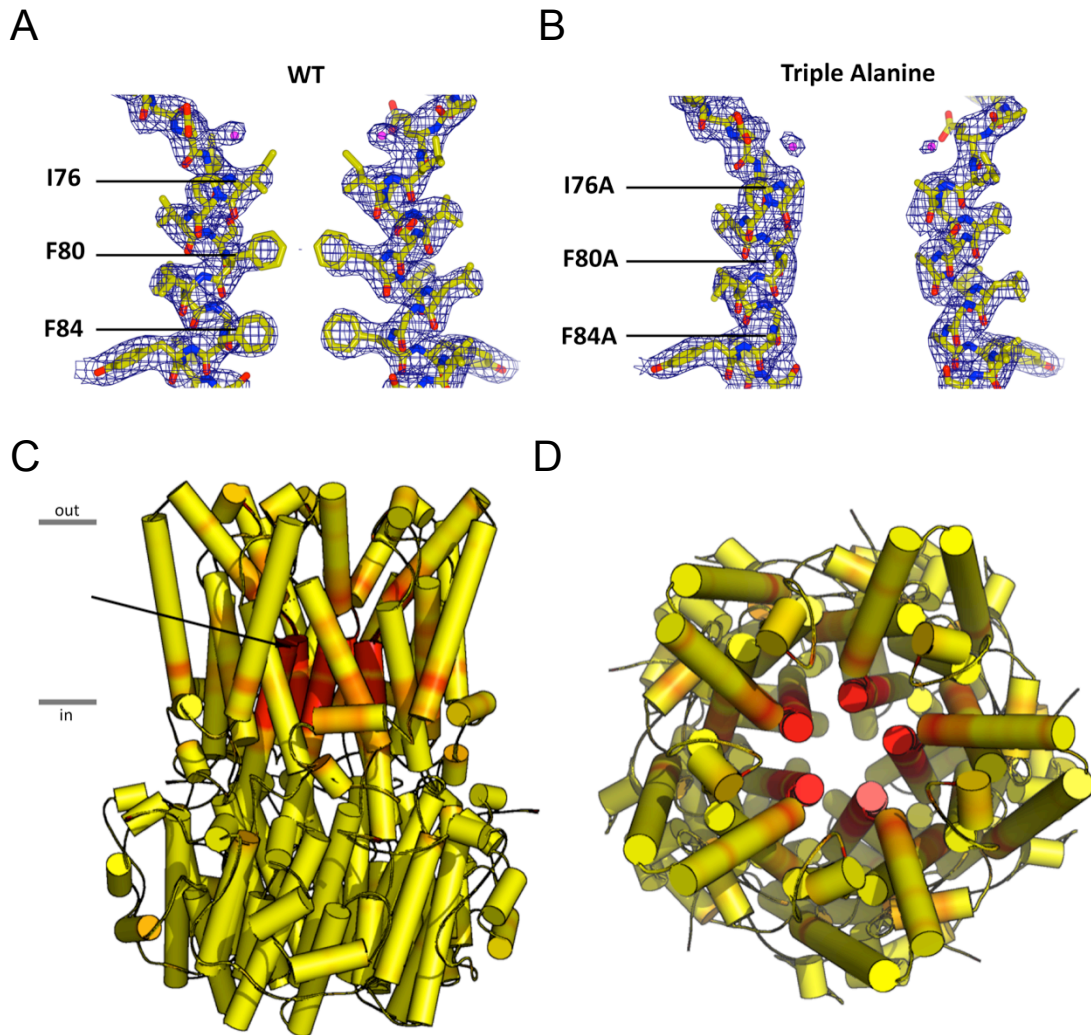
Figure 2.14. Differences at the neck in BEST1$_{WT}$ and BEST1$_{TripleA}$. $2F_o - F_c$ electron density is shown for the neck region for WT (A) and BEST1$_{TripleA}$ (B) with two subunits displayed for simplicity. The density is contoured at 1.3σ in the context of the final atomic model, which is shown as sticks and spheres (Cl$^-$ is depicted as a purple sphere). (C) side view and (D) top view of BEST1 channel with α-helices depicted as cylinders and colored on a yellow-to-red spectrum according to the displacement of Cα atoms between the refined atomic models of BEST1$_{WT}$ and BESt1$_{TripleA}$. Yellow color represents displacements less than 0.15 Å, and red color represents displacements greater than 0.4 Å. An arrow indicates the neck of the pore.

region(s) in the pore. I turned my attention to the other hydrophobic constriction of the channel, the ~3 Å-wide cytosolic aperture, which is formed from a ring of V205 side chains from the five subunits (Fig.2.13 A). To investigate the function of the aperture, I mutated V205 to alanine and studied the channel in the bilayer. Like BEST1$_{WT}$, I find that the V205A mutant is Ca^{2+} dependent and retains selectivity for anions over cations (P_K/P_{Cl} = 0.08 ± 0.01; n = 3; Fig.2.15 A). Strikingly, unlike BEST1$_{WT}$, the V205A mutant is essentially equally permeable to SCN$^-$, I$^-$, Br$^-$, and Cl$^-$ (Fig.2.15 B,C). Therefore, the V205A mutant does not exhibit a lyotropic sequence among permeant anions. Hence, this single hydrophobic amino acid is responsible for this aspect of the channel's ion selectivity. I also find that acetate, which is not detectably permeant through wild-type BEST1, is permeant through the V205A mutant (Fig.2.15 D). Like BEST1$_{WT}$, BEST1$_{V205A}$ remains essentially impermeable to larger anions such as gluconate and glutamate (Fig.2.15 E,F). Our data supports a conclusion that the aperture forms a molecular filter that discriminates on the basis of size, allowing small ions (e.g., SCN$^-$, I$^-$, Br$^-$, and Cl$^-$) to pass, while excluding larger molecules such as amino acids.

2.5 Discussion

I determined cation-vs.-anion permeability ratios and found that, among the mutants I made, including simultaneous substitution of all three amino acids lining the neck (I76, F80, and F84) by alanine (BEST1$_{TripleA}$), no mutant altered P_K/P_{Cl} in a substantial way. Previous studies have shown that replacing the hydrophobic amino acids lining the neck with acidic amino acids, or with cysteine residues that were subsequently modified with the negatively charged methanethiosulfonate (MTSES$^-$) reagent, can increase the
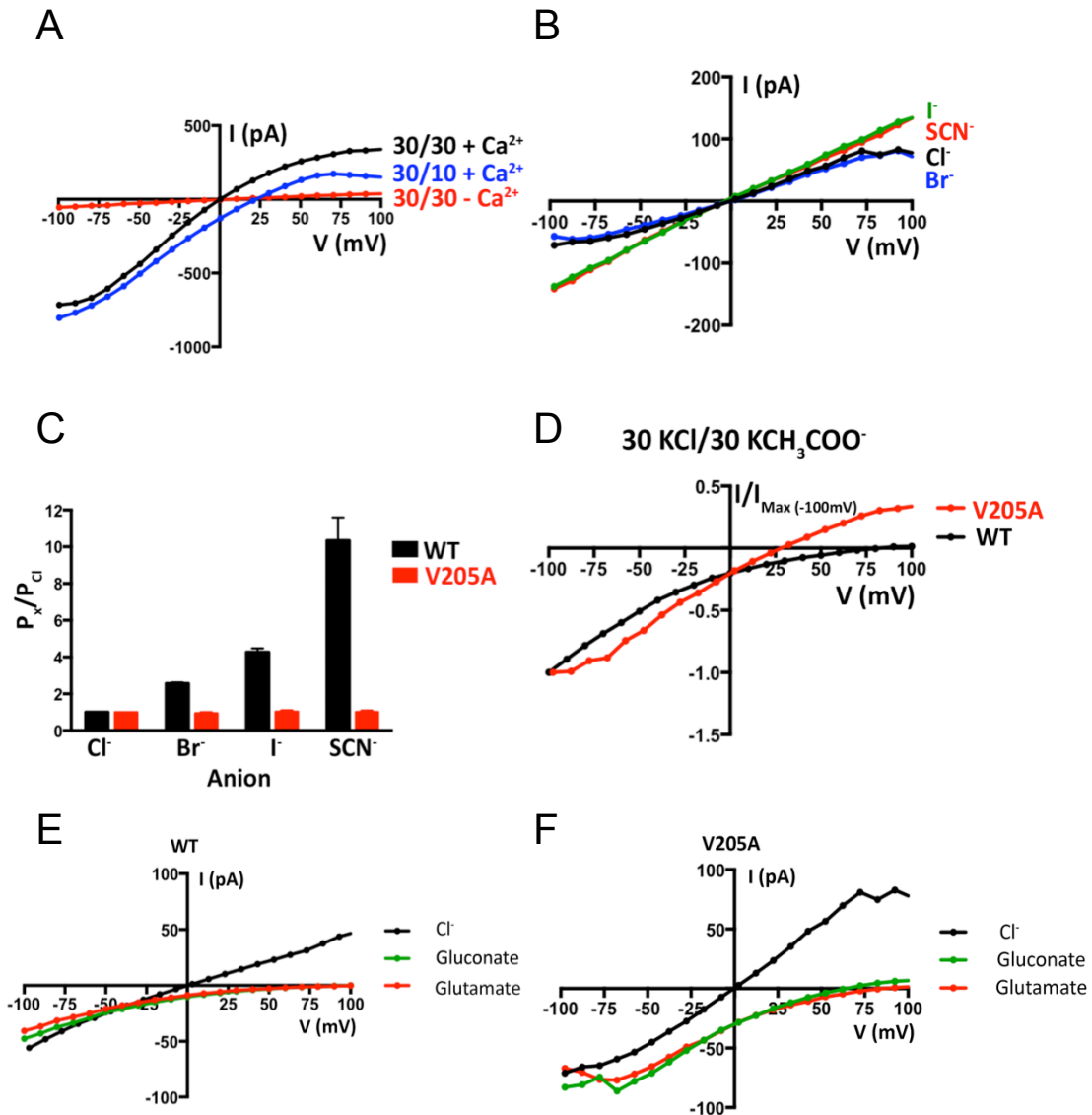
Figure 2.15. Function of the aperture. (A) Observed BEST1$_{V205A}$ currents are Cl$^-$ selective and Ca^{2+} dependent. Example *I-V* relationships are shown for voltages stepped from -100 to +100 mV for BEST1$_{V205A}$ for the indicated standard conditions [cis/trans KCl concentrations in millimolar, and 300 nM Ca^{2+} (+ Ca^{2+}) or 10 mM EGTA (- Ca^{2+})]. (B) The V205A mutation abolishes the lyotropic permeability sequence of BEST1. *I-V* traces are shown for procedures equivalent to figure 2.5A. (C) Comparison of P$_X$/P$_{Cl}$ for BEST1$_{WT}$ and BEST1$_{WT}$ and BEST1$_{V205A}$. Using data from experiments carried out as in B, permeability ratios were determined by solving the Goldman-Hodgkin-Katz equation. Three separate experiments were used to compute the SEM. (D) BEST1$_{V205A}$ shows increased permeability to acetate (CH$_3$COO$^-$) compared with BEST1$_{WT}$. Representative *I-V* relationships using solutions containing 30 mM KCl on the *cis* side and 30 mM KCH$_3$COO$^-$ on the *trans* side are shown for BEST1$_{WT}$ and the V205A mutant. For the comparison, the currents were normalized to the values recorded at -100 mV (I_{max} = -62 and -105 pA for BEST1$_{WT}$ and the V205A mutant, respectively, in this experiment).

permeability of cations relative to Cl⁻ (Chien and Hartzell, 2008; Yang et al., 2014). In

BEST2, mutation of F80 to cysteine also has modest effects on the relative

permeabilites among anions (Qu and Hartzell, 2004; Qu et al., 2006a). That the

permeation properties were perturbed by such modifications is an indication that this

region of the channel contributes to the ion pore, as was predicted before structural

knowledge (Chien and Hartzell, 2008; Qu and Hartzell, 2004; Qu et al., 2004; 2006a).

However, the effects of dramatic alterations of the chemical environment within the neck,

such as the introduction of charged amino acids, do not necessarily support a conclusion

that the neck underlies charge selectivity in the wild-type channel, as has been

postulated (Yang et al., 2014). The X-ray structure of BEST1$_{TripleA}$ shows that the neck is

made dramatically wider by the I76A, F80A, and F84A mutations and that the remainder

of the channel is essentially unperturbed. However, in the absence of phenylalanine

residues in the neck of BEST1$_{TripleA}$, the channel's selectivity for anions-over-cations is

maintained. In addition, despite the widened neck of BEST1$_{TripleA}$, which could

conceivably alter the hydration properties of anions passing through it, I found that the

lyotropic sequence of permeability among monovalent anions (SCN⁻ > I⁻ > Br⁻ > Cl⁻) was

also unaltered. In conclusion, the neck does not contribute to ion selectivity of BEST1 in

a substantial way for either the anion-vs.-cation selectivity or the relative permeabilites

among permeant anions.

Nevertheless, my data suggest that the particular amino acids lining the neck, which are

highly conserved, facilitate anion permeation through the channel. For example, I found

that mutating F80 to the similarly sized leucine or isoleucine amino acids dramatically

diminishes ion flux through the channel. These mutations could feasibly alter the single

channel conductance of the channel and/or the open probability, resulting in the smaller

unitary transport rates observed. In addition to the well-known negative electrostatic

potential associated with the face of their π system, the aromatic rings of phenylalanine

residues have positive electrostatic potential associated with their edges. If positioned

correctly, the ring edges can favorably interact with negatively charged species through

anion-quadrupole interactions, and it has been observed that such interactions

commonly occur in proteins (Jackson et al., 2007; Philip et al., 2011). As was proposed

on the basis of the initial structure of BEST1, it is possible that the aromatic side chains

of phenylalanines F80 and F84 within the neck interact with anions flowing through the

pore via encircling rings of anion-quadrupole interactions (Kane Dickson et al., 2014).

Such interactions have been observed in a bacterial fluoride channel and mutation of the

interacting phenylalanine residues to isoleucine also reduced ion flux through the

channel (Stockbridge et al., 2015). Alternatively, F80 could be important for stabilizing

the open conformation of the channel, perhaps by interacting with neighboring residues

in such a way that mutation to leucine or isoleucine disrupts this, reducing the open

probability of the channel.

My data indicate that the primary function of the neck is in Ca^{2+}-dependent activation. I

find that Cl^- flux through BEST1$_{TripleA}$, measured electrically and using a flux assay, is

almost completely independent of the presence or absence of Ca^{2+}. Additionally, single

amino acid substitutions in the neck yield channels with varying degrees of "leakiness" in

the absence of Ca^{2+}. Comparison of the structures of BEST1$_{WT}$ and BEST1$_{TripleA}$ reveals

that the differences are confined to the local environment of the neck. The TripleA

mutations (I76A, F80A, and F84A) have not caused changes elsewhere in the protein,

and, tellingly, they do not alter the diameter of the aperture, which is the other

constriction in the pore that could form a barrier to ion permeation. I conclude that, in the

wild-type channel, the neck functions as a gate that permits or prevents anion

permeation depending on the Ca^{2+} concentration. This conclusion is supported by the

observation that channels that are made constitutively closed by eliminating the Ca^{2+}

sensor can be made constitutively active by the introduction of the TripleA mutation of

the neck. When the 15 hydrophobic amino acids (I76, F80, and F84 from the five

subunits) lining the neck are truncated to alanine the neck constriction found in $BEST1_{WT}$

is eliminated and it is no longer able to prevent anion permeation in the absence of Ca^{2+}.

This implies that the neck undergoes a conformational change that depends on the Ca^{2+}

concentration to permit anion flux in the presence of Ca^{2+} and prevent ion flux in its

absence.

Although Ca^{2+} is bound in the Ca^{2+} clasp in the X-ray structure of BEST1, it is not yet

clear if the structure represents an open state, a nearly open state, or, possibly, an

inactivated state (Kane Dickson et al., 2014). A comparison of two nearly identical X-ray

structures that were determined with Ca^{2+} bound, but using slightly different

crystallization conditions gave a hint that motions near the Ca^{2+} clasps, which were small

in this instance (~0.3 Å displacements), are coupled to corresponding motions in the

neck (Kane Dickson et al., 2014). For Ca^{2+}-dependent gating, it is feasible to imagine

that the neck can dilate and constrict and that Ca^{2+} binding in the clasps directs these

movements, favoring channel opening when Ca^{2+} is present and favoring channel

closing when it is absent. Through mutagenesis of F80, I found that both the size and

hydrophobic nature of the neck contribute to its role as an ion barrier when Ca^{2+} is

absent. In this regard, the neck appears similar to the so-called "hydrophobic gates"

identified in other channels (Aryal et al., 2014; 2015; Wang et al., 2008). By this theory,

the bulk hydrophobic side chains at the neck region would prevent "wetting" of the

channel pore by forming a "vapor lock" (Aryal et al., 2015), blocking the passage of ions.

Relieving this restriction either by widening the region or making it more hydrophilic

would disable the gate. Analogous to experiments performed with the K2P1 (TWIK-1)

potassium channel (Aryal et al., 2014), I find that making a single hydrophobic to hydrophilic mutation (F80N) can considerably disrupt the neck's ability to act as a seal in the absence of Ca^{2+}, consistent with this notion of hydrophobic gating.

The other constriction in the pore, the cytosolic aperture, which is formed by V205, was also identified from the structure as a potential barrier in BEST1. Mutations to an analogous aperture in a prokaryotic homolog seemed to alter that channel's open probability (Yang et al., 2014). Although feasible that the aperture of BEST1 could act as a gate in some other way, my results show that current flow through BEST1$_{V205A}$ is still Ca^{2+} dependent and thus the aperture does not function as a Ca^{2+}-dependent gate in BEST1. The BEST1$_{V205A}$ channel also maintains selectivity for Cl^- over K^+ with approximately the same permeability ratio as wild-type BEST1. On the other hand, I find that ions that have dramatically different relative permeabilities in wild-type BEST1 and follow a lyotropic sequence ($SCN^- > I^- > Br^- > Cl^-$), have essentially equal permeabilities in the BEST1$_{V205A}$ aperture mutant. This indicates that BEST1 has a "division" of ion selectivity properties; one portion of the channel, the aperture, determines relative permeabilities among anions, whereas other region(s) give rise to anion-over-cation selectivity. Thus, unlike many ion channels, such as those belonging to the superfamily of tetrameric cation channels whose pore architecture is typified by a potassium channel (Doyle, 1998), BEST1 does not contain a single canonical selectivity filter that determines both the anion/cation selectivity and the selectivity among permeant ions.

If neither the neck constriction nor the aperture constriction gives BEST1 its anion-over-cation selectivity, what is responsible for this? A comparison between the X-ray structures of BEST1 and KpBEST, which is more permeable to cations than anions, may provide clues (Fig. 2.16). In BEST1, 3 Cl^-/Br^- binding sites per subunit (15 total sites per

channel) were observed within the ion pore (Kane Dickson et al., 2014). Two of the sites (sites 1 and 2) are situated in the "outer entryway" of the pore, and the other site (site 3) is located within the "inner cavity" (Fig.1.7). None of the sites is buried; all of them are exposed to wide sections of the pore such that the dissociation or association of anions could occur readily. Each site is formed by a break in an α-helix that exposes a backbone amino nitrogen that interacts with the anion (sometimes referred to as a helix-diplole interaction). Strikingly, analogous sites are absent in KpBest because this channel contains continuous helices through what correspond to the anion binding sites of BEST1 (Fig.2.16) (Yang et al., 2014). Akin to a proposal that was based on the structure of a glutamate-gated Cl^- channel (Hibbs and Gouaux, 2011), it is hypothesized that the anion binding sites in the pore of BEST1 contribute to ion selectivity by increasing the local concentration of anions that can bind in them (e.g., Cl^-, Br^-, etc.) relative to other ions.

2.6 Conclusion

In conclusion, in this chapter I have identified roles that the neck, aperture, and Ca^{2+} clasp play in ion selectivity and Ca^{2+}-dependent activation of BEST1 (Fig. 2.17). The Ca^{2+} clasp and the neck are the principal components of the Ca^{2+}-dependent gating apparatus with the clasp serving as the sensor and the neck as the activation gate of the channel. The neck is not the determinant of anion-vs.-cation selectivity nor of the channel's lyotropic permeability sequence among permeant anions. The cytosolic aperture does not function as a Ca^{2+}-dependent gate and mutation of the aperture also has essentially no effect on the anion-over-cation selectivity of the channel. However, I find that the aperture is responsible for establishing relative permeabilities among permeant anions. The aperture appears to act as a size-selective filter that allows small
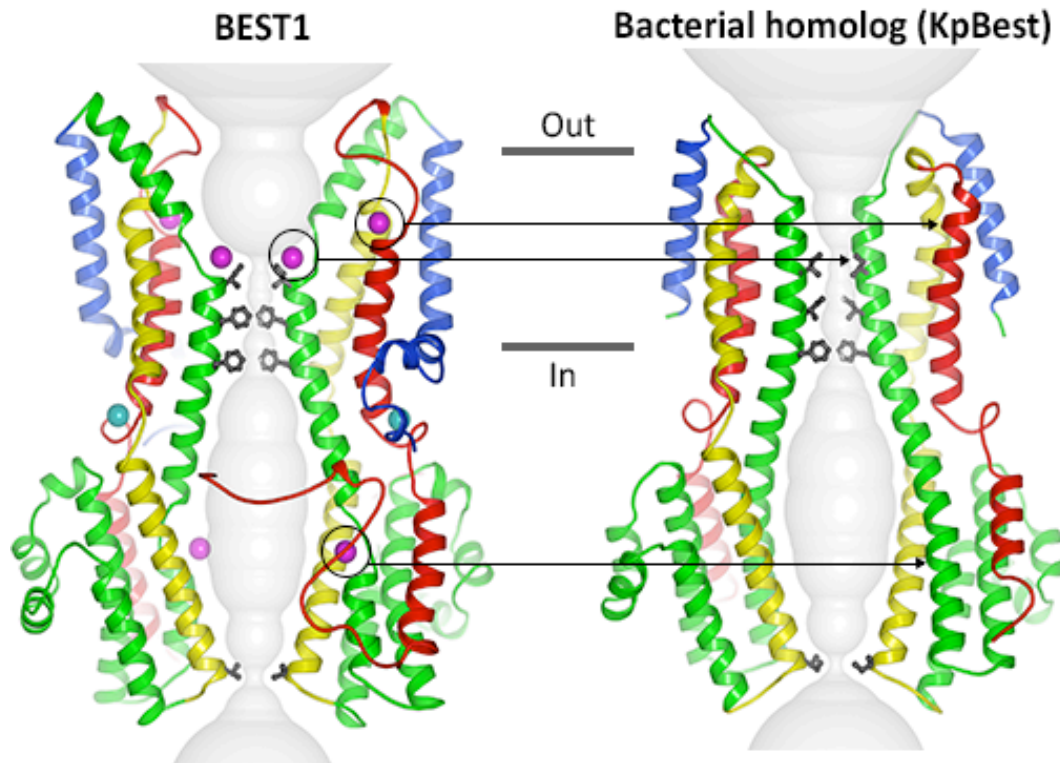
Figure 2.16. Cl⁻ binding sites observed in BEST1 are absent in prokaryotic KpBest. Structures are depicted similarly to figure 2.13A with two subunits shown. Cl⁻ binding sites (magenta spheres, the three sites for each subunit are knkown) in BEST1 (*Left*) are located at the N-terminal ends of α-helices. KpBEST (*Right*) has continuous α-helices in the corresponding locations (arrows) and does not contain these sites. Ca^{2+} ions in BEST1 are depicted as teal spheres.
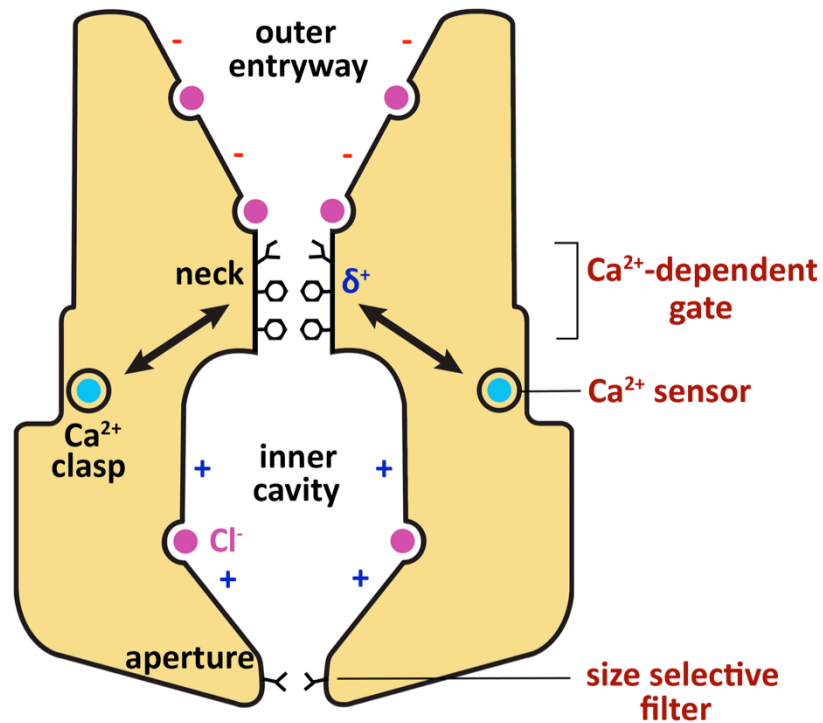
Figure 2.17. Regions of BEST1 involved in Ca^{2+}-dependent activation and ion selectivity. Structural features identified from the X-ray structure of BEST1 are labeled in black (Kane Dickson et al., 2014), and the mechanistic functions of these regions identified in this study are labeled in red (*Right*). Binding of intracellular Ca^{2+} (teal) to the Ca^{2+} clasp, which acts as a Ca^{2+} sensor, is coupled to conformational changes at the neck, which functions as a Ca^{2+}-dependent gate. The neck is lined by three conserved hydrophobic residues (I76, F80, F84, stick representations), and these residues do not contribute to ion selectivity. The cytosolic aperture, which is lined by the V205 residue, acts as a size-selective filter and endows BEST1 with its characteristic lyotropic permeability sequence. Selectivity for Cl^- and other monovalent anions over cations may be determined by anion binding sites observed in the pore of BEST1 (purple) (Kane Dickson et al., 2014). The minus (-) and plus (+) signs in the pore indicate that, aside from the anion binding sites, the walls of the outer entryway and inner cavity have predominately negative and positive electrostatic potentials, respsectively.

molecules such as dehydrated Cl$^-$ ions to pass, while excluding larger entities. It is

hypothesized that anion-binding sites within the pore are primarily responsible for

selectivity of anions over cations but further studies are needed to test this. Remarkably,

however, it is clear that distinct regions in BEST1, and by analogy in BEST2-4, govern

Ca^{2+}-dependent activation, size discrimination among permeant species, and anion-

over-cation selectivity.

Chapter 3

3. An allosteric mechanism of calcium-dependent inactivation in the BEST1 channel

3.1 Summary

Whole-cell recordings show that ionic currents through BEST1 run down over time but it is unclear whether this behavior is intrinsic to the channel or the result of cellular factors. Here, using planar lipid bilayer recordings of purified protein, I show that current rundown is an inherent property of BEST1 that can now be characterized as inactivation. Inactivation depends on the cytosolic concentration of Ca^{2+}, with higher concentrations stimulating inactivation. I identify a C-terminal peptide that is responsible for inactivation and locate its receptor site. Alterations of either the peptide or its receptor site prevent inactivation. Unlike inactivation peptides of certain other channels that bind within the ion pore, the receptor is on the cytosolic surface of the channel and separated from the pore. Biochemical, structural and electrophysiological analyses suggest that interaction of the peptide with its receptor promotes inactivation whereas dissociation disfavors inactivation. Alanine mutagenesis of the hydrophobic neck constriction within the pore, which is physically distant from the receptor site, also prevents inactivation and thus the neck appears to function as the inactivation gate. Unlike a ball-and-chain inactivation mechanism involving physical occlusion of the pore, inactivation in BEST1 occurs through an allosteric mechanism wherein binding of an inactivation peptide to a surface-exposed receptor controls a structurally distant gate. The work presented in this chapter has been published (Vaisey and Long, 2018).

3.2 Background

As well as activating the channel, Ca^{2+} has been shown to have an inhibitory effect on BEST1 currents. In whole cell recordings of human BEST1 the current initially increases after patch break-in and then runs down on a timescale of minutes (Xiao et al., 2008). The rate of rundown is faster at higher (µM) concentrations of Ca^{2+}. A slow, Ca^{2+}-dependent rundown has also been observed for currents of another Ca^{2+}-activated Cl^- channel (CaCC), TMEM16A (Dang et al., 2017; Ni et al., 2014). C-terminal truncations of BEST1 prevented or abolished current rundown (Xiao et al., 2008). Other studies on human BEST3, which gave no currents when expressed as the full-length gene in HEK 293 cells, identified an "autoinhibitory motif" within this C-terminal region and alanine substitutions within this motif ($_{356}$IPSFLGS$_{362}$) activated Cl^- currents (Qu et al., 2007; 2006b). In the crystal structure of chicken BEST1, we see that the corresponding sequence ($_{356}$RPSFLGS$_{362}$) is located within a C-terminal tail that adopts an extended conformation following the final α-helix (S4b) and wraps around the cytosolic domains of two other subunits (Fig.3.3 B) (Kane Dickson et al., 2014).

Questions remain about the molecular determinants of BEST1 Ca^{2+}-dependent rundown. First, is current rundown an intrinsic property of the channel or does it require other cellular factors? What role does the C-terminal motif play in the regulation of BEST1 and how does truncation or mutagenesis disrupt this? If binding or dissociation of the C-terminal motif controls rundown, where is the receptor site on the channel? Finally, which region(s) of the pore are responsible for current rundown? Here, using mutagenesis, electrophysiology and biochemical approaches, I identify the principal components of the channel responsible for inactivation: a C-terminal inactivation peptide, a cytosolic receptor, and an allosterically controlled inactivation gate.

3.3 Materials and methods

3.3.1 Electrophysiological recordings

BEST1 protein was expressed and purified as described in sections 2.3.1 and 2.3.2. The planar lipid bilayer setup and standard solutions used for recording are described in section 2.3.3. For inactivation experiments, after obtaining stable currents in symmetrical conditions containing 1 μM $CaCl_2$, $CaCl_2$ was added to both *cis* and *trans* chambers and solutions were stirred whilst recording.

3.3.2 Fab binding assay

To assess binding of Fab to BEST1 protein, 10 nM Fab was incubated (> 30 min at $4^{o}C$) with various concentrations of BEST1 ranging from 1 nM to 200 nM in buffer (20 mM Tris-HCl at pH 7.5, 75 mM NaCl, 75 mM KCl, 1 mM DDM) containing either 5 mM EGTA or 10 μM $CaCl_2$. 400 μl of each mixture was loaded onto an SEC column (Superose 6 increase 10/300 Gl, GE Healthcare), which was equilibrated in the same buffer, and the fraction of unbound Fab was quantified from the area under the elution peak corresponding to free Fab (at 27.5 ml using tryptophan fluorescence on a Shimadzu RF-20AXS fluorescence detector), which is well separated from the peaks for BEST1 and BEST-Fab complex (22.8 ml and 20.7 ml, respectively), in comparison to a Fab control.

3.3.3 Limited proteolysis analysis

15 μg purified BEST1 protein at ~0.6 mg ml^{-1} , in 150 mM NaCl, 20 mM Tris pH 7.5, 3 mM DM and ~ 10 μM Ca^{2+} was mixed with 1:556 wt:wt ratio of Asp-N (Sigma-Aldrich) and incubated for 1 hour at room temperature. The reaction was terminated by addition of 1 mM AEBSF. The samples were heated at 80 ^{o}C in SDS buffer containing 500 mM DTT for 5 mins before separation by SDS-PAGE using a 12% Bis-Tris gel (Invitrogen)

and then stained using coomassie. For experiments analyzing the Ca^{2+}-dependence of

proteolysis, varying concentrations of free Ca^{2+} were obtained by adding EGTA-Ca

buffers (for 10 nM – 750 mM $[Ca^{2+}]_{free}$) or 5 μM – 1 mM $CaCl_2$ during the reaction. For

Western blot analysis, approximately 50 ng of BEST1 protein was run on SDS-PAGE

and electrophoretically transferred onto PVDF membranes (Trans-Blot SD; Biorad).

Membranes were blocked with 5% milk powder (in TBST: 0.1% Tween 20, 20 mM Tris-

HCl, pH 7.5, 150 mM NaCl) overnight at 4^oC and then incubated with 690 ng ml^{-1}

primary antibody ($YL^1/_2$) for 1 hour at room temperature in TBST containing 2% powered

milk. After 3 washing steps in TBST milk, the membrane was incubated with 50 ng ml^{-1}

secondary antibody (Goat Anti-rat HRP, Zymed) for 1 hour at room temperature. Blots

were washed again and chemiluminescence was detected via ECL detection reagent

(Luminata Forte; Millipore) using a Chemidoc XRS imager (Biorad).

3.4 Results

3.4.1 Purified BEST1 exhibits Ca^{2+}-dependent inactivation

To make comparisons with the structure of chicken BEST1 (Kane Dickson et al., 2014), I

recorded currents using purified protein of the same construct (denoted $BEST1_{WT}$) in

planar lipid bilayers. At ~ 300 nM $[Ca^{2+}]_{free}$, and in symmetric 30 mM KCl conditions, ionic

currents through $BEST1_{WT}$ generated by 1 s pulses to ±100 mV from a holding voltage of

0 mV were relatively stable over time, decreasing by only ~11% after 10 minutes of

recording (Fig. 3.1B). However, when the $[Ca^{2+}]_{free}$ was increased to 100 μM, I observed

a time-dependent decrease in the ionic current using the same voltage protocol that

yielded a ~85% reduction in current after 10 minutes (Fig.3.1 A,B). Varying $[Ca^{2+}]_{free}$

concentrations between 300 nM and 100 μM resulted in graduated effects, which further

indicates the Ca^{2+}-dependence of the reduction (Fig.3.1 C).

To test whether current rundown is a reversible property of BEST1, or reflects

irreversible inhibition of the channel, I first caused currents to rundown using 100 μM

$[Ca^{2+}]_{free}$, and then restored $[Ca^{2+}]_{free}$ to 300 nM using perfusion. As shown in figure 3.1

D, most of the current was recovered by returning to 300 nM $[Ca^{2+}]_{free}$. Because rundown

is observed in a reconstituted system using purified BEST with minimal buffer

components (K+, Na^+, Cl^-, Ca^{2+}, EGTA, and HEPES; Section 2.3.3 and 3.3.1) and is

reversible, I refer to it as Ca^{2+}-dependent inactivation and conclude that inactivation is an

inherent property of the channel.

The dependence of inactivation on $[Ca^{2+}]_{free}$ that I observe in my experiments is less

dramatic compared to whole cell recordings of hBEST1 where the extent of current

rundown is ~90% after 10 minutes when using 11 μM $[Ca^{2+}]_{free}$ (Xiao et al., 2008). I

wondered whether a difference in salt concentration might be responsible for the

difference, since these previous whole cell studies used 146 mM CsCl and most of my

studies used 30 mM KCl. Indeed, the rate and extent of BEST1 inactivation is increased

at higher concentrations of KCl and this effect is more pronounced at higher $[Ca^{2+}]_{free}$

concentrations (Fig.3.2). Thus, inactivation is modulated by both $[Ca^{2+}]_{free}$ and [KCl]. In

this study, I focus on the effects of Ca^{2+} on BEST1 inactivation and, unless otherwise

noted, recordings were performed using 30 mM KCl.
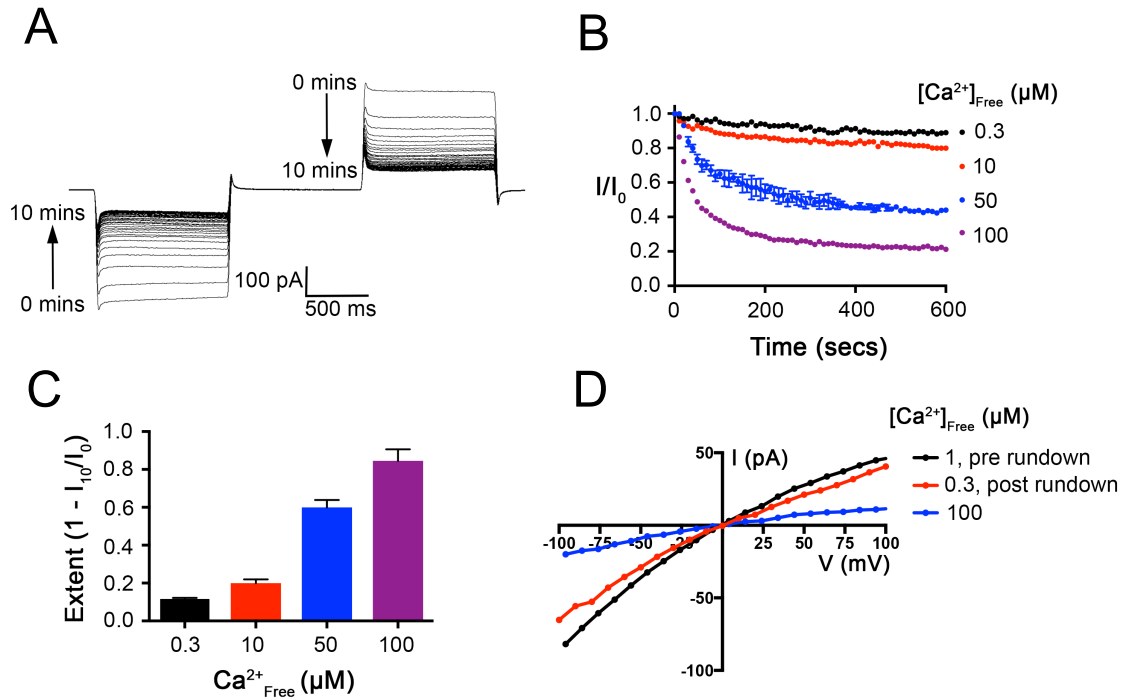
Figure 3.1. Ca^{2+}-dependent inactivation of purified BEST1$_{WT}$ in planar lipid bilayers. (A) Representative current traces. Under symmetric 30 mM KCl conditions containing 100 µM Ca^{2+}, currents were recorded using the following protocol: from a holding potential of 0 mV, the voltage was stepped to -100 mV for 1 s, returned to holding for 1 s and then stepped to +100 mV for 1 s before returning to the holding potential again. This protocol was repeated every 10 seconds for 10 minutes with continuous stirring of the solutions. The trace shown here is digitally low pass filtered to 20 Hz to remove noise caused by stirring. (B) Ionic currents decrease over time as a function of [Ca^{2+}]$_{free}$. I/I$_0$ is calculated as the current value at ± 100 mV at each time point (from 200 ms windows near the end of the 1 s pulses) as a fraction of the current value at the start of the experiment (I$_0$). Desired free Ca^{2+} concentrations were achieved using 0.21 mM/ 0.19 mM CaCl$_2$ for ~ 300 nM Ca^{2+} or adding CaCl$_2$ to ~ 1 µM CaCl$_2$ at the start of the experiment to achieve 10-100 µM free Ca^{2+}. Representative error bars are shown for the recording at 50 µM free Ca^{2+}. (C) Extent of inactivation at each Ca^{2+} concentration, calculated as 1-I$_{10}$/I$_0$, where I$_{10}$ is the current value observed at the end of the experiment (10 min), as performed in B, and I$_0$ is the current value at the start of the experiment (I$_0$). Three separate experiments were used to compute the SE. (D) Current rundown is reversible. After 10 mM EGTA was added to the cis chamber to deactivate channels with their cytosolic regions facing this side of the bilayer, currents were measured in symmetric 30 mM KCl conditions using the following protocol: from a holding potential of 0 mV, the voltage was stepped to test values between -100 and +100 mV, in 10-mV increments, for 2 s at each voltage. After a further 1 s step to -100 mV, the voltage was returned to 0 mV. I-V relationships were obtained by plotting the test voltages versus average currents (from 200 ms windows) near the end of the 2 s pulses. Recordings were made first using [Ca^{2+}]$_{free}$ ~ 1 µM (pre rundown, black). Currents were then recorded 10 min after the addition of 100 µM CaCl$_2$ to the trans chamber (blue). Finally, currents were recorded after perfusion-mediated replacement of the trans chamber with solution containing [Ca^{2+}]$_{free}$ ~ 300 nM (post rundown, red).
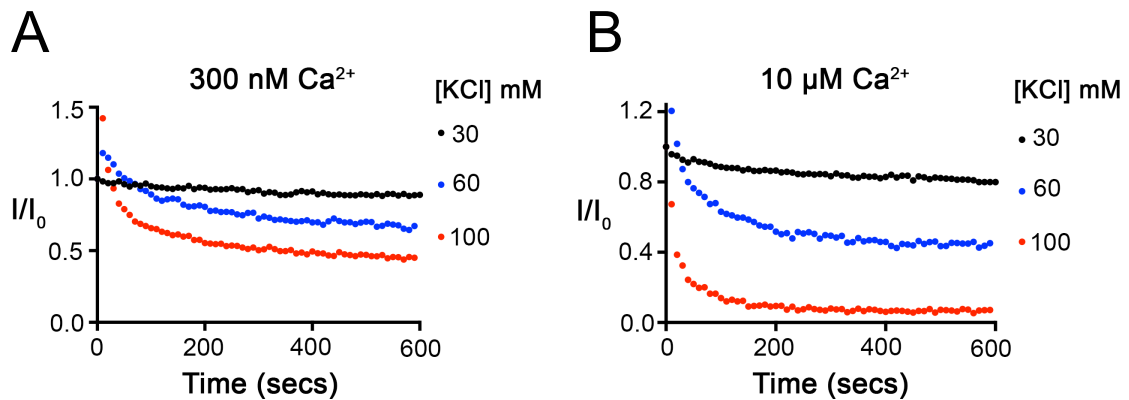
Figure 3.2. Inactivation is dependent on [KCl]. Current recordings were made as in figure 3.1 A and B at 3 different KCl concentrations, as indicated, in solutions containing either ~ 300 nM free Ca^{2+} (A) or 10 μM Ca^{2+} (B).

3.4.2 An inactivation peptide and its receptor site

Previous observations by the Hartzell laboratory characterized a C-terminal region of bestrophin as being autoinhibitory (Xiao et al., 2008). I explored the effects of removing the corresponding region of BEST1 ($_{356}$RPSFLGS$_{362}$) on Ca^{2+}-dependent inactivation. In the X-ray structure of BEST1$_{WT}$, each "C-terminal tail" (amino acids 326-327) of the five subunits adopts an extended conformation that wraps around the cytosolic portion of two adjacent subunits (the amino acids following residue 367 are disordered) (Fig.3.3 A,B). To begin to investigate the function of this peptide and the C-terminal tail I tested the properties of various C-terminal deletions. I found that a construct spanning amino acids 1-345 of BEST1 does not exhibit inactivation (Fig.3.3 C,D). Constructs spanning 1-360 and 1-380 inactivate somewhat, but to a lesser extent than BEST1$_{WT}$ (Fig.3.3 D). The data demonstrates a direct role for the C-terminal tail in inactivation, and we now refer to is as the "inactivation peptide".

To probe more specifically how the inactivation peptide contributes to Ca^{2+}-dependent inactivation, I studied channels with mutations in $_{356}$RPSFLGS$_{362}$ sequence. In the x-ray structure of BEST1 (Kane Dickson et al., 2014), the $_{356}$RPSFLGS$_{362}$ peptide makes a series of van der Waals and hydrogen bonding interactions with two different subunits (Fig3.4 A). Of note, S358 of the inactivation peptide packs closely with H178 and W309 (Fig.3.4 D). Phosphorylation of S358 in human BEST1 or the S358E mutation, which would mimic the phosphorylated state, has been shown to prevent current rundown in whole-cell recordings (Xiao et al., 2009). Accordingly, I found that the S358E mutant of chicken BEST1 does not inactivate, whereas the S358A mutant inactivates similarly to BEST1$_{WT}$ (Fig.3.4 B,C). Modeling of a glutamate or phosphoserine at position 358 in the X-ray structure produces atomic clashes (Fig.3.4 D) and this indicates that the conformation of the inactivation peptide observed in the structure could not be
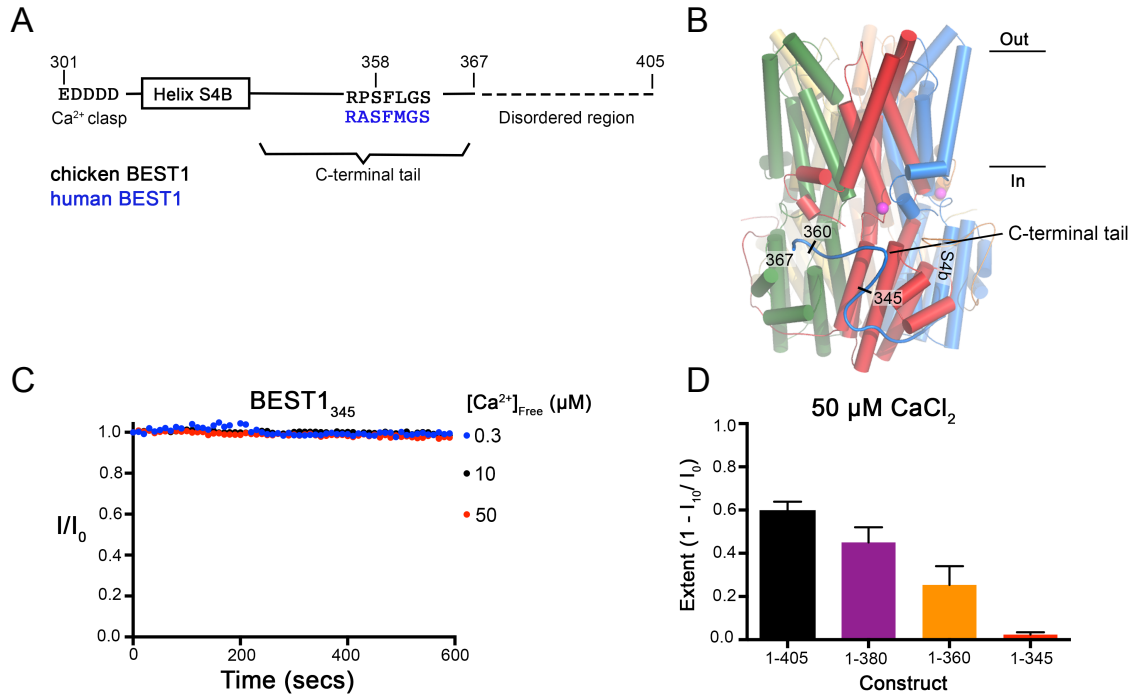
Figure 3.3. Truncations to the C-terminal tail disrupt Ca^{2+}-dependent inactivation of BEST1. (A) Schematic of the C-terminal region of BEST1, showing residues that contribute to the Ca^{2+}-clasp, helix S4b and the C-terminal tail. The inhibitory sequence, contained within this tail, is annotated for both chicken and human BEST1. (B) Structure of $BEST1_{WT}$ highlighting the position of a C-terminal tail from one of the five identical subunits. The perspective is from within the membrane, with subunits colored individually, α-helices depicted as cylinders, Ca^{2+} ions shown as magenta spheres, and approximate boundaries of the membrane indicated. Helix S4b, truncation points within the C-terminal tail, and the final ordered residue are annotated. (C) Bilayer electrophysiology shows that $BEST1_{345}$ does not undergo Ca^{2+}-dependent inactivation. Experimental conditions are identical to those for Fig.3.1 A,B. (D) The extent of inactivation in 50 μM Ca^{2+} is shown for different C-terminal truncations of BEST1. Experiments were carried out as in *C* and at least 3 independent experiments were performed for each construct to calculate SE.
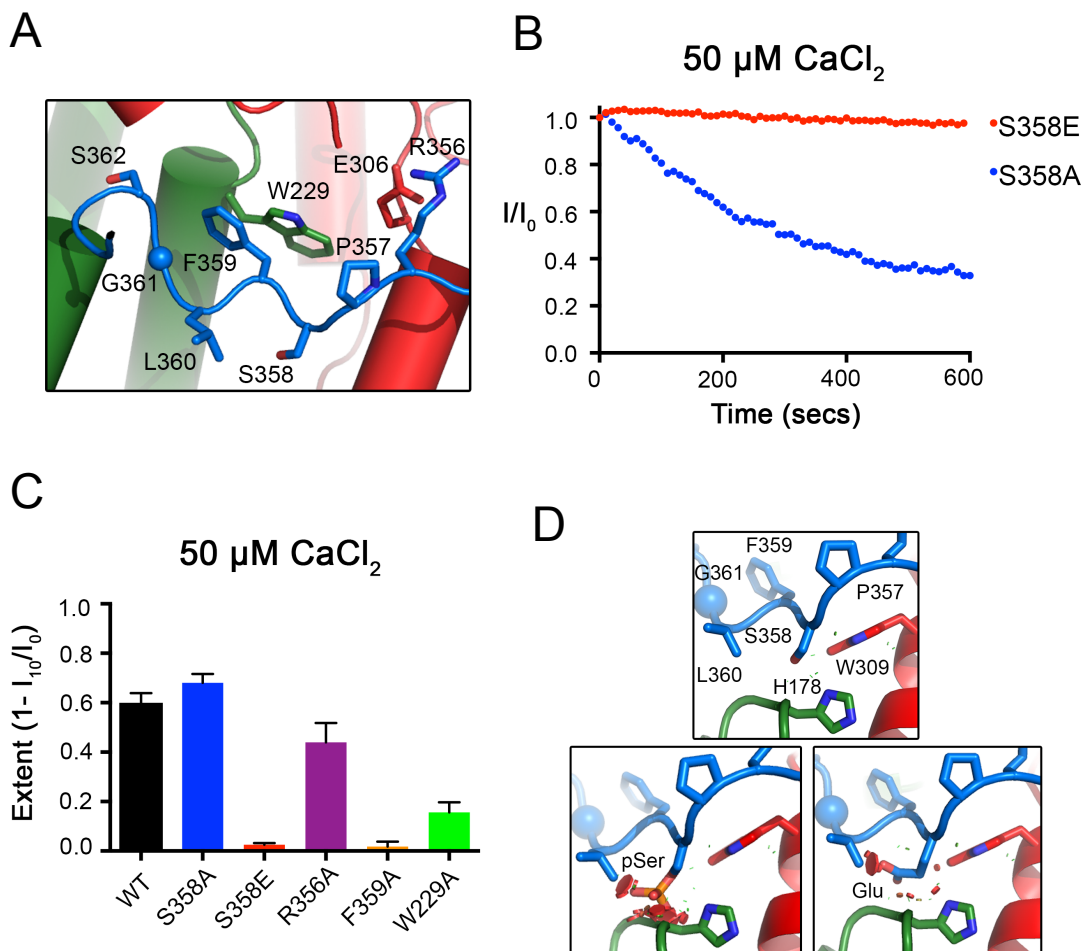
Figure 3.4. Mutations within the inactivation peptide or its receptor can prevent inactivation. (A) Close up view of the $_{356}$RPSFLGS$_{362}$ sequence of BEST1 as illustrated in Fig. 3.3 B. (B) Ca^{2+}-dependent inactivation of BEST1$_{S358A}$ and BEST1$_{S358E}$, using 50 μM Ca^{2+}, was recorded as described in Fig. 3.1A. (C) The extent of inactivation is shown for different mutants. Experiments were performed as in *B*, and at least three independent experiments were performed to calculate SD. (D) Modeling shows that mutation of S358 to glutamate or its phosphorylation would cause steric clashes. Top panel, stick representation of S358 of the inactivation peptide (blue colored carbon atoms) and surrounding contacts with the receptor (green and red colored carbon atoms). Lower panels, modeling of a phosphoserine (left) or S358E mutation (right) would cause clashes, which are depicted as red circles.

accommodated when S358 is phosphorylated or mutated to glutamate. The logical

hypothesis that follows is that disruption of the inactivation peptide from its "receptor"

binding site that was identified in the structure may prevent inactivation.

Additional mutagenesis supports this hypothesis. The interactions between the

inactivation peptide and its receptor, which involve residues that are conserved between

human and chicken BEST1, include a salt-bridge between R356 of the inactivation

peptide and E306 of one subunit, and a hydrophobic interaction between F359 of the

inactivation peptide and W229 of another subunit (Fig.3.4 A). I find that disruption of the

R356-E306 salt bridge by the R356A has a modest effect on inactivation. Disruption of

the F359-W229 hydrophobic interaction by introducing an F359A mutation in the

inactivation peptide essentially eliminates inactivation. Congruently, the W229A mutation

of the receptor site substantially reduces inactivation (Fig.3.4 C).

The mutations that disrupted Ca^{2+}-dependent inactivation did not alter other

characteristic properties of BEST1. Currents of $BEST1_{345}$ and $BEST1_{S358E}$ recorded in

asymmetric conditions of 10 mM KCl on the "trans" side and 30 mM KCl on the "cis" side

of the bilayer, gave reversal potentials very close to $BEST1_{WT}$ ($BEST1_{WT}$ = 25.1 ± 0.8

mV, $BEST1_{345}$ = 23.4 ± 0.3 mV, $BEST1_{S358E}$ = 24.0 ± 1.0 mV) (Fig.3.5 A-C),

demonstrating indistinguishable selectivity profiles for Cl^- versus K^+. Chelation of Ca^{2+}

using EGTA abolishes these currents, indicating that the channels are still Ca^{2+}-

dependent (Fig.3.5 A-C). Furthermore, titration of the $[Ca^{2+}]_{free}$, using perfusion-mediated

solution exchange, activated $BEST1_{S358E}$ and $BEST1_{345}$ in a dose-dependent manner

with similar $K_{1/2}$ values to $BEST1_{WT}$ (Fig.3.5 D-F) (Vaisey et al., 2016). For all of the

constructs tested, I find that mutations that disrupt inactivation have no detectable

effects on Cl^- selectivity or Ca^{2+}-dependent activation. I conclude that Ca^{2+}-dependent
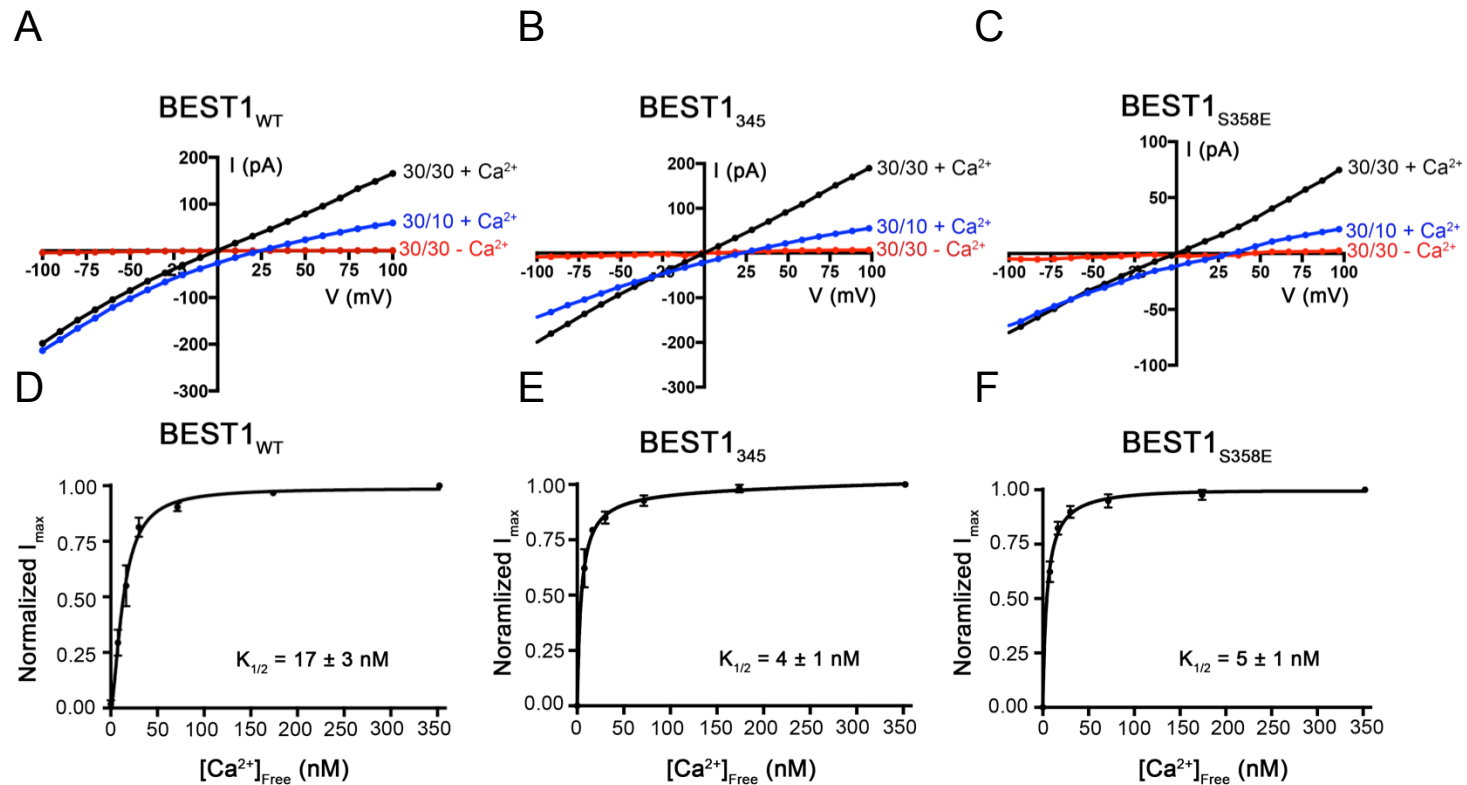
Figure 3.5. BEST1$_{345}$ and BEST1$_{S358E}$ are chloride selective, Ca^{2+}-dependent channels. (A-C) Example *I-V* relationships are shown for voltages stepped from -100 to +100 mV for BEST1$_{WT}$ (A), BEST1$_{345}$ (B) and BEST1$_{S358E}$ (C) for indicated conditions [*cis/trans* KCl concentrations in millimolar and 300 nM Ca^{2+} (+ Ca^{2+}) or 10 mM EGTA (-Ca^{2+})]. (D-F) Reactivation of BEST1 currents by increasing [Ca^{2+}]$_{free}$. After observing currents in symmetrical solutions, 10 mM EGTA was added to the *cis* side to deactivate channels with their cytosolic side facing that direction. Then, using perfusion, the [Ca^{2+}]$_{free}$ in the *trans* solution was varied from ~0 to 350 nM with a Ca-EGTA buffer system (section 2.3.3). Ca^{2+} response curves for BEST1$_{WT}$ (D), BEST1$_{345}$ (E) and BEST1$_{S358E}$ (F) are plotted as average currents observed at -100 mV for different [Ca^{2+}]$_{free}$ as a fraction of current recorded from the [Ca^{2+}]$_{free}$ = 350 nM condition (I$_{max}$). Three separate experiments were used to calculate SE and the data were fit to a one-site binding model.

activation, inactivation and ion selectivity are separate properties that can be uncoupled from one another by mutagenesis.

3.4.3 Antibodies that bind to the cytosolic region of the channel modulate inactivation

As part of previous efforts to determine the X-ray structure of BEST1, a cohort of monoclonal antibodies were developed for use as crystallization aids. The antibodies bind to structured regions of the channel and provide potential tools to further probe the function of the channel. The X-ray structure of BEST1 was determined in complex with a Fab fragment of one of these antibodies (denoted "10D10") (Kane Dickson et al., 2014). Five 10D10 Fabs bind to the pentameric channel (one per subunit) by interacting with a cytosolic region that contains a portion of the C-terminal tail of two adjacent subunits (amino acids 344-355 of one sununit and 363-365 of another,(Fig.3.6 A, B). The antibodies are bound at a distance from the pore and would not occlude it. Using bilayer electrophysiology, I find that addition of 10D10 Fab to BEST1$_{WT}$ using conditions that cause slow Ca^{2+}-dependent inactivation (10 µM $[Ca^{2+}]_{free}$), caused ionic currents to diminish rapidly (Fig.3.6 C). By contrast, addition of 10D10 during recordings of the non-inactivating mutant, BEST1$_{S358E}$, had no effect on currents (Fig.3.6 C). This difference in effect is due to a difference in binding. Whilst 10D10 binds to BEST1$_{WT}$ with high affinity ($K_d \leq 6$ nM), it has no apparent binding affinity for the BEST1$_{S358E}$ mutant (Fig.3.6 D). Interestingly, S358 is ~14 Å away from the antibody in the structure, ruling out a direct interaction with this residue (Fig3.6 B), but 10D10 does contact other regions of the C-terminal tail. The inability of 10D10 to bind to BEST1$_{S358E}$ supports the hypothesis that the S358E mutation causes a large portion of the C-terminal tail to dislodge. On the basis of the binding location of 10D10 and the biochemical and electrophysiological analyses presented herein, I hypothesize that the binding of 10D10 promotes

103
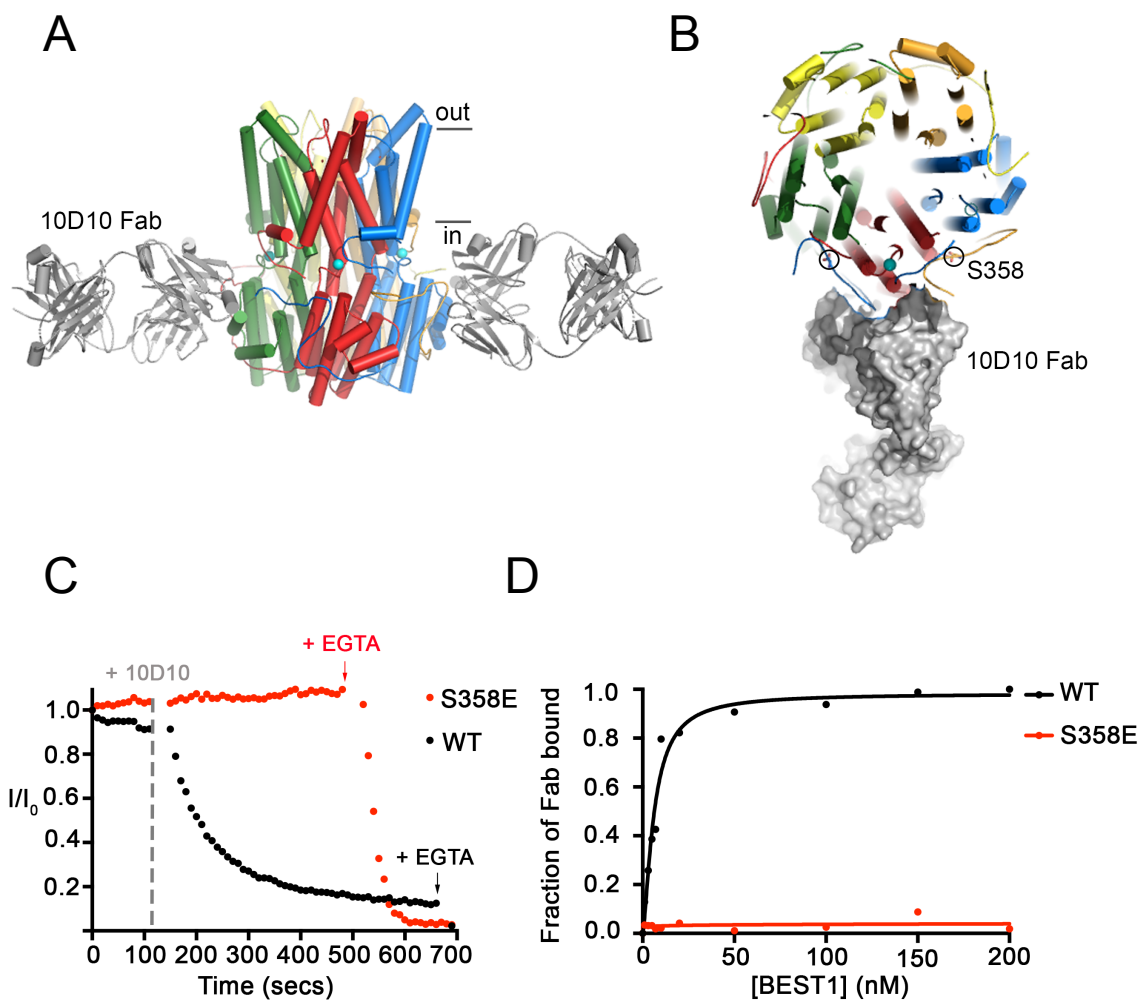
Figure 3.6. 10D10 Fab inhibits ionic currents of BEST1$_{WT}$, but not BrpEST1$_{S358E}$ (A) Structure of the BEST1-10D10 complex, viewed orthogonally and showing approximate boundaries of the membrane. For clarity, two 10D10 Fabs are drawn. (B) A slice of the representation from *A*, viewed from the top, depicting one 10D10 Fab in surface representation. Two S358 residues from different subunits are circled. (C) Ca^{2+}-dependent inactivation of BEST1$_{WT}$ and BEST1$_{S358E}$ currents in 10 μM Ca^{2+} was recorded as described in Figure 3.1 A and B. 200 nM 10D10 Fab was added to both *cis* and *trans* sides at the timepoint indicated (dashed line), followed by the addition of 10 mM EGTA near the end of the experiment (arrow). (D) The relative binding of 10D10 Fab to BEST1$_{WT}$ and BEST1$_{S358E}$ was assayed by determining the amount of free 10D10 as a function of the concentration of BEST1 (Section 3.3.2). The curves correspond to fits of: fraction of Fab bound = $[BEST1]^{h}/K_d^{h} + [BEST1]^{h})$ where K_d is the equilibrium dissociation constant, and *h* is the Hill coefficient. Derived parameters for BEST1$_{WT}$ are $K_d \leq 6$ nM and $h=1.5$, whilst BEST1$_{S358E}$ had no detectable binding to the 10D10 Fab.

inactivation of the channel by stabilizing the interaction of the inactivation peptide with its

receptor.

I tested whether other antibodies might have dfferent effects on BEST1 function and

identified one Fab (denoted "8G5") that prevents inactivation. Currents recorded from

$BEST1_{WT}$ were stable following the addition of 8G5 under conditions where $BEST1_{WT}$

inactivated substantially on its own (50 μM Ca^{2+}) (Fig.3.7 A, B). Further, I found that 8G5

is able to rescue inactivated $BEST1_{WT}$ channels. After inactivation of $BEST1_{WT}$ to ~17%

of its initial current level (using 100 μM Ca^{2+}), the addition of 8G5 rapidly restored the

current level to approximately 120% of its initial value, and the currents remained stable

over the time course of the experiment (5 min., Fig.3.7 C). On the other hand, the

addition of 8G5 to $BEST1_{S358E}$, which does not inactivate, had no effect on current levels

(Fig.3.7 C). For both $BEST1_{WT}$ and $BEST1_{S358E}$, the currents were reduced to zero when

EGTA was added, which indicates that 8G5 does not prevent deactivation (Fig.3.7 C).

Unlike 10D10, which has previously been shown to only bind Ca^{2+} bound BEST1 (Kane

Dickson et al., 2014), I find that the 8G5 Fab binds to $BEST1_{WT}$ and $BEST1_{S358E}$ with

high affinities in both Ca^{2+}-containing and Ca^{2+}-free conditions (Fig.3.7 D). Thus, the

variable effect of 8G5 on $BEST1_{WT}$ and $BEST1_{S358E}$ is due to differences in the abilities of

these channels to inactivate and not because of differences in 8G5 antibody binding.

3.4.4 Limited proteolysis supports a link between peptide binding and inactivation

Based on the aforementioned analyses, I hypothesized that the binding of the

inactivation peptide to its receptor causes the channel to inactivate and that mutations
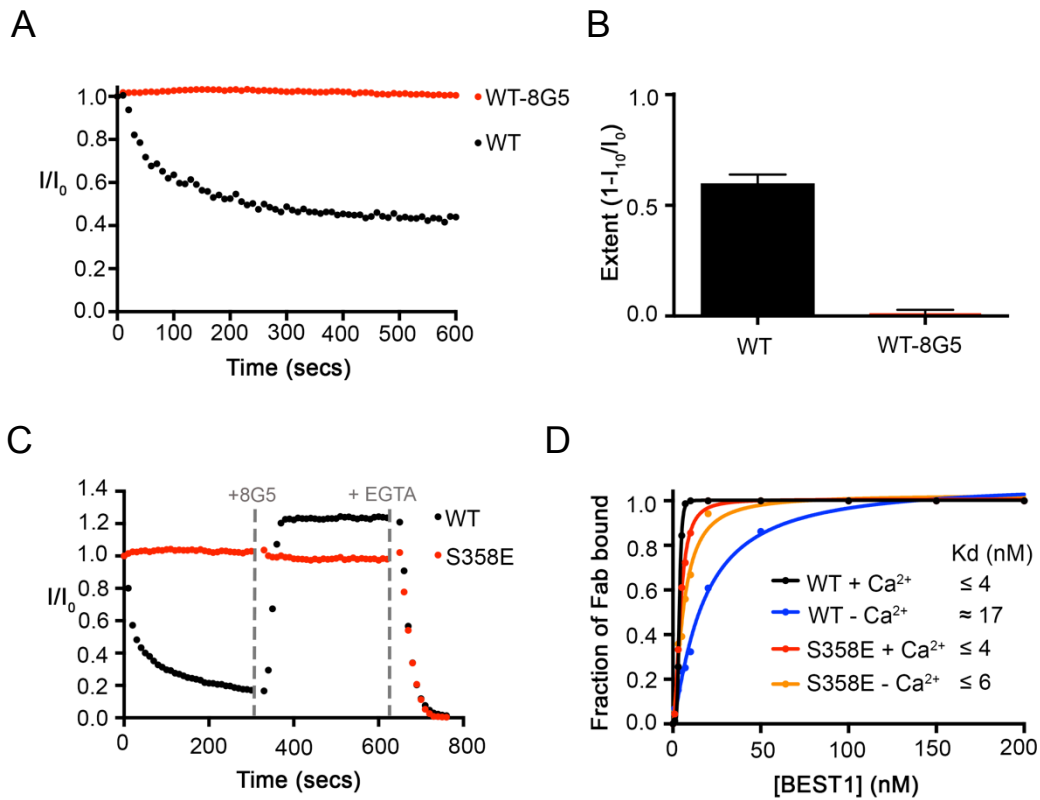
Figure 3.7. Binding of the 8G5 Fab prevents inactivation of BEST1$_{WT}$.
(A) Ca^{2+}-dependent inactivation of BEST1$_{WT}$ and BEST1$_{WT}$-8G5 complex. Recordings were done as described in Fig. 3.1A, using 50 μM Ca^{2+}. For the experiment with the 8G5 Fab, after currents for BEST1$_{WT}$ were obtained, 8G5 Fab was added (300 nM final concentration) to the *cis* and *trans* chambers, the chambers were stirred for 2 min, and $CaCl_2$ was added (at time = 0) at the start of the recording. (B) Extent of inactivation in 50 μM Ca^{2+} after 10 min is plotted for BEST1$_{WT}$ and BEST1$_{WT}$-8G5 complex. Experiments were carried out as in *A* and at least 3 separate experiments were performed to calculate SE. (C) Rescue of inactivated BEST1$_{WT}$ channels by 8G5. From time = 0, currents from BEST1$_{WT}$ and BEST1$_{S358E}$ were recorded using 100 μM Ca^{2+} conditions. At the 5 minute mark, 300 nM 8G5 Fab was added to both sides of the bilayer. At the 10 minute mark, 10 mM EGTA was added to both sides of the bilayer to chelate free Ca^{2+}. Solutions were stirred for the duration of the experiment. (D) The relative binding of 8G5 Fab to BEST1$_{WT}$ and BEST1$_{S358E}$ was determined as described for 10D10 in Figure 3.6 D. Derived parameters for BEST1$_{WT}$ are: $K_d \le 4$ nM, $h=5.4$ and $K_d \approx 17$ nM, $h=2.1$ in the presence of 10 μM Ca^{2+} or 5 mM EGTA, respectively. The parameters for BEST1$_{S358E}$ are: $K_d \le 4$ nM, $h=1.2$ and $K_d \le 6$ nM, $h=1.4$ in the presence of 10 μM Ca^{2+} or 5 mM EGTA, respectively.

106

that disrupt binding impair inactivation. An unlatched peptide, that is one that is not bound to its receptor site, would presumably be more susceptible to proteolytic cleavage than one that is bound, and so I tested this hypothesis by evaluating the protease susceptibility of constructs that inactivate and those that do not. Detergent-solubilized BEST1$_{WT}$ was resistant to proteolytic cleavage by the endoprotease Asp-N under conditions where I observe inactivation in the bilayer (~ 10 µM [Ca^{2+}]$_{free}$, Fig.3.8 A). On the other hand, I observed dramatic cleavage for BEST1$_{S358E}$, which does not undergo inactivation, using the same conditions (Fig.3.8 A). A western blot using an antibody that recognizes a C-terminal tag indicated that cleavage occurs within the C-terminal region of BEST1$_{S358E}$ (Fig.3.8 B), and this was confirmed by mass spectrometry. The data suggest a correlation between inactivation and binding of the inactivation peptide to its receptor. In further support of this hypothesis, I find that varying [Ca^{2+}]$_{free}$ within the range that causes inactivation dramatically affects the proteolytic susceptibility of the C-terminal tail (Fig.3.8 C). At > 200 nM [Ca^{2+}]$_{free}$, the C-terminal tail is resistant to cleavage by Asp-N, indicating that it was bound to its receptor, whereas it was readily cleaved at lower [Ca^{2+}]$_{free}$.

I wondered if the 8G5 antibody, which prevents inactivation of BEST1$_{WT}$, would have a similar effect on the C-terminus. Indeed, I found that addition of 8G5 to BEST1$_{WT}$ made the C-terminal region of BEST1$_{WT}$ susceptible to proteolytic cleavage by Asp-N (Fig.3.8 A, B). These results suggest that binding of the 8G5 Fab or mutagenesis of S358 to glutamate prevent BEST1 inactivation by disrupting the interaction of the inactivation peptide with its cytosolic receptor on the surface of the channel.
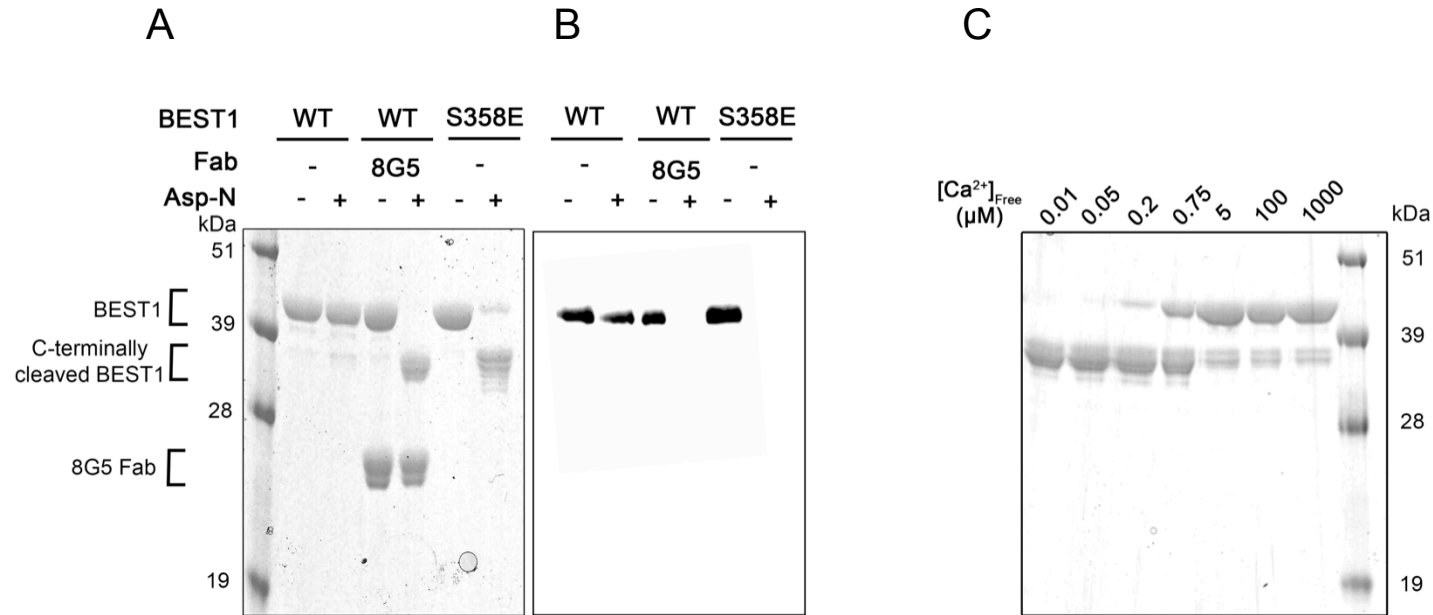
Figure 3.8. Conditions or mutations that prevent inactivation result in increased susceptibility of the C-terminal tail to proteolytic cleavage. (A) Protease susceptibility of $BEST1_{WT}$, BEST1WT-8G5 and $BEST1_{S358E}$. Purified proteins (in detergent and $[Ca^{2+}]_{free}$ ~ 10 μM) were incubated with and without Asp-N endoprotease for 1 hr at room temperature and analyzed by SDS-PAGE with coomassie staning. Bands corresponding to uncleaved, C-terminally cleaved BEST1, and 8G5 Fab are indicated. (B) Western blot of analogous SDS PAGE gel from *A* using a YL^1/$_2$ antibody that targets the C-terminal affinity tag used for purification of BSET1. (C) Protease susceptibility depends on $[Ca^{2+}]_{free}$. SDS PAGE analysis of $BEST1_{WT}$ treated with Asp-N for 1 hour at room temperature using different $[Ca^{2+}]_{free}$.

3.4.5 The neck is the inactivation gate

Because the receptor for the inactivation peptide is located on the surface of the channel and distant from the pore, the binding of the inactivation peptide must function to induce conformational changes in the pore that impede ion flow. I sought to identify the region within the pore that constitutes the "inactivation gate", that is, the region within the pore that undergoes the conformational changes that impede ion flow during inactivation. As described, there are two major constrictions in the pore of BEST1 that seemed to be likely candidates: the neck, consisting of three highly conserved hydrophobic residues, I76, F80 and F84 and the aperture, contributed by V205, which is less well-conserved (Fig.3.9 A) (Kane Dickson et al., 2014). I previously showed that the V205A mutation at the aperture has no effect on the Ca^{2+}-dependence of the channel (Fig.2.15 A) (Vaisey et al., 2016). Instead, the V205A mutation abolished the lyotropic permeability sequence among anions exhibited by BEST1$_{WT}$, which indicates that the aperture imparts certain ion selectivity properties to the channel (Fig.2.15 B, C) (Vaisey et al., 2016). Here I find that BEST1$_{V205A}$ currents recorded in 50 µM free Ca^{2+} showed inactivation equivalent to BEST1$_{WT}$, suggesting that the aperture is not responsible for channel inactivation (Fig.3.9 B, C).

I have shown that neck functions as the activation gate (Fig.2.11, 2.12) (Vaisey et al., 2016). Alanine mutagenesis in the neck (I76A, F80A, F84A; BEST1$_{TriipleA}$) produces a channel that is constitutively open and independent of $[Ca^{2+}]$. Here I find that current recordings of BEST1$_{TripleA}$ do not inactivate (Fig.3.9 B, C). As discussed in section 2.4.4, the X-ray structure of BEST1$_{TripleA}$ showed that the only conformational differences from
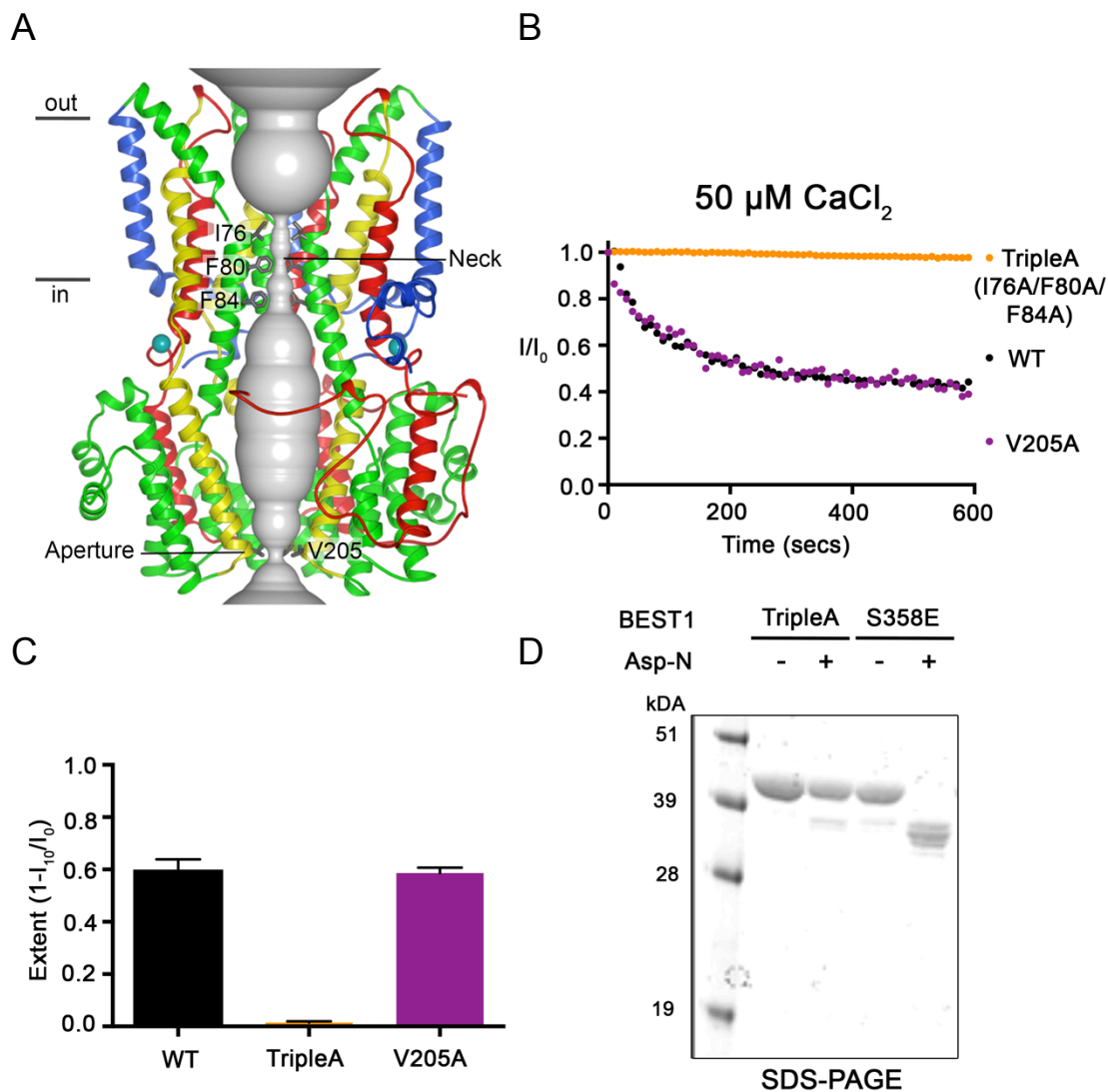
Figure 3.9. Mutations to the neck but not the aperture prevent Ca^{2+}-dependent inactivation. (A) Structure of $BEST1_{WT}$ with ribbon representations shown for three subunits (two in the foreground are removed for clarity). The ion pore (gray tube) is depicted as a representation of the minimal radial distance from the central axis to the nearest van der Waals protein contact. Secondary structural elements are colored according to the four segments of the channel (S1, blue; S2, green; S3, yellow; S4 and C-terminal tail, red) that contain corresponding transmembrane regions and the Ca^{2+} ions are depicted as teal spheres. Approximate boundaries of a lipid membrane are indicated. (B) Ca^{2+}-dependent inactivation of $BEST1_{WT}$, $BEST1_{TripleA}$ (I76A/F80A/F84A) and $BEST1_{V205A}$ in 50 µM Ca^{2+} conditions was recorded as described in Fig 3.1A and B. (C) Extent of inactivation in 50 µM Ca^{2+} is plotted for $BEST1_{WT}$, $BEST1_{TripleA}$ and $BEST1_{V205A}$. Experiments were carried out as in *B* and at least 3 separate experiments were performed to calculate SE. (D) SDS PAGE gel of $BEST1_{TripleA}$ and $BEST1_{S358E}$ (as a positive control for cleavage) with and without Asp-N endprotease treatment for 1hr at RT.

the BEST1$_{WT}$ structure are a widening at the neck due to the smaller alanine side chains (Fig.2.13, 2.14) (Vaisey et al., 2016). Of note for the present discussion, Ca^{2+} ions are bound within the Ca^{2+} clasps and the five inactivation peptides, one from each subunit, are bound in their receptor sites in the structure of BEST1$_{TripleA}$. Like BEST1$_{WT}$, and unlike BEST1$_{S358E}$, detergent-solubilized BEST1$_{TripleA}$ does not exhibit susceptibility to cleavage by Asp-N at ~ 10 μM [Ca^{2+}]$_{free}$, further confirming that the inactivation peptide is bound to the channel, even though BEST1$_{TripleA}$ does not inactivate. The TripleA mutant must nullify the effects on the neck that occur in the wild type channel as a result of the inactivation peptide binding to its receptor. I conclude that the neck functions as both the activation gate and the inactivation gate in bestrophin channels: the neck forms a seal that opens with Ca^{2+}-dependent activation and closes with Ca^{2+}-dependent inactivation.

3.4.6 Surface-exposed acidic residues are involved in the Ca^{2+}-dependence of inactivation

An important question is how high concentrations of Ca^{2+} cause BEST1 inactivation: where does Ca^{2+} bind and what conformational effect does this have on the channel? X-ray structures of BEST1 determined with Ca^{2+} concentrations of ~1 μM and 5 mM showed density attributed to Ca^{2+} only at the Ca^{2+}-clasp binding sites (Kane Dickson et al., 2014), consistent with these being the high-affinity sites required for BEST1 activation (Fig.2.12) (Vaisey et al., 2016). I observe increases in the rate and extent of inactivation up to concentrations of 1 mM Ca^{2+} (Fig.3.10 A), which suggests that rather than a discrete second Ca^{2+}-binding site, Ca^{2+} may be interacting with a more diffuse charged surface. In regions proximal to and including the C-terminal tail, there are
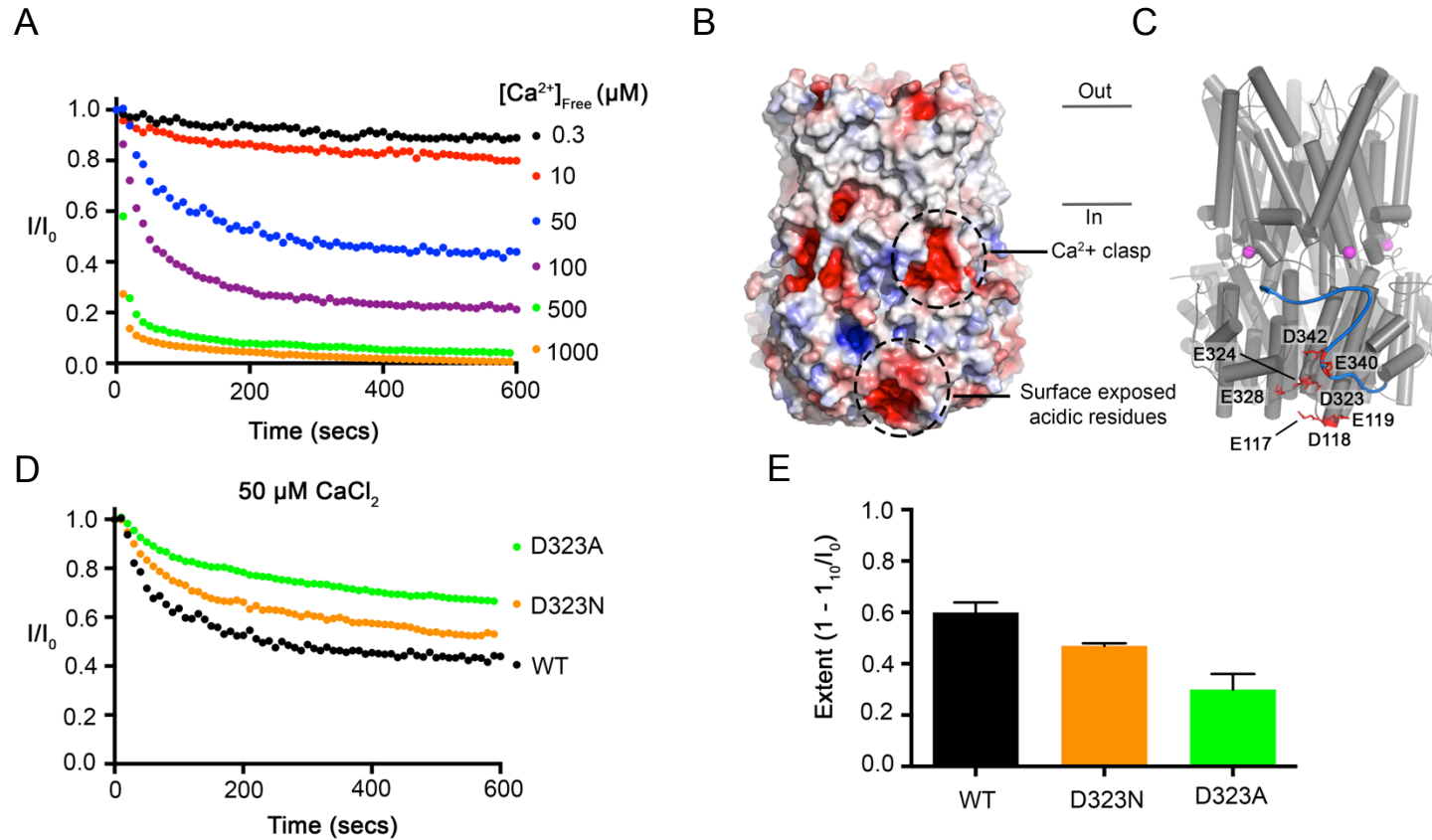
Figure 3.10. Surface-exposed acidic residues near the inactivation peptide may underlie the Ca^{2+}-dependence of inactivation. (A) Ca^{2+}-dependent inactivation of BEST1$_{WT}$ as shown in Figure 3.1B but here with additional recordings at 500 μM and 1 mM [Ca^{2+}]$_{free}$. (B) Surface representation of BEST1 colored by electrostatic potential; red, -5kT e^{-1}; white, neutral blue, + 5kT e^{-1}. (C) Structure of BEST1 with same perspective as in *B*. The C-terminal tail of one subunit is shown in blue and acidic residues corresponding to an electronegative surface-exposed region are depicted as red sticks. Ca^{2+} ions at the Ca^{2+} clasp are shown as magenta spheres. (D) Ca^{2+}-dependent inactivation of BEST1$_{WT}$, BEST1$_{D323A}$ and BEST1$_{D323N}$ in 50 μM Ca^{2+} conditions were carried out as described in Figure 3.1. (E) Extent of inactivation. Experiments were carried out as in *D* and at least 3 separate experiments were performed to calculate SE.

several surface-exposed acidic amino acids: E117, D118, E119, D323, E324, E328, E340 and D342 (Fig.3.10 B and C). In the X-ray structure these residues create a distinctly electronegative surface that might interact with Ca^{2+} (Fig.3.10 B), and consistent with a diffuse interaction, the residues do not appear geometrically arranged to create a high affinity Ca^{2+} binding site (Fig.3.10 C). A previous study showed that mutation of one of these in human BEST1 (D323N) produces channels that had less Ca^{2+}-dependent rundown in whole cell recordings (Xiao et al., 2008). Accordingly, I find that $BEST1_{D323N}$ inactivates to a lesser extent than $BEST1_{WT}$ (Fig.3.10 D and E). This effect is greater when D323 is mutated to the nonpolar residue alanine (Fig.3.10 D and E). These data are consistent with the hypothesis that the Ca^{2+}-dependence of inactivation is due to Ca^{2+} interaction with D323 and other nearby acidic residues. Although additional analysis is needed, the proximity of the electronegative patch to the receptor site for the inactivation peptide suggests a mechanism whereby Ca^{2+} interaction with the electronegative patch promotes and/or stabilizes the binding of the inactivation peptide to its receptor.

3.5 Discussion

In this chapter I have used bilayer recordings to show that the purified BEST1 channel inactivates. Using the X-ray structure as a framework (Kane Dickson et al., 2014), recordings of wild type and mutant channels have enabled identification of the regions of the channel involved in Ca^{2+}-dependent inactivation and provide insight into the molecular mechanisms of this regulatory behavior.

Electrophysiological recordings of purified channels with truncations or point mutations demonstrate the essential role of the C-terminal tail in BEST1 inactivation. Inactivation is disabled by truncating the C-terminal tail at amino acid 345, mutation of S358 within the

C-terminal tail to glutamate, mutation of the neighboring F359, or by mutation of W229 to alanine within its receptor site. Inactivation is also prevented by binding of a Fab (8G5). When the 8G5 antibody is bound to $BEST1_{WT}$ or when S358 is mutated to glutamate ($BEST1_{S358E}$), the C-terminal tail becomes dramatically susceptible to proteolysis. These findings suggest that disruptions to the tail that alter its interaction with the channel prevent inactivation. Thus, the C-terminal tail acts as a regulatory appendage to the BEST1 channel, reminiscent of the ball and chain, or N-type, inactivation mechanism of voltage-gated channels (Armstrong, 1977; Hille, 2001; Zhou et al., 2001). However, rather than acting as a pore blocker, as is well established for the inactivation peptide of voltage-gated channels (Choi et al., 1991; Zhou et al., 2001), I propose that the C-terminal tail of BEST1 acts as an inactivation peptide through an allosteric mechanism.

My data suggests that the neck within the pore of BEST1 acts as an inactivation gate. Mutagenesis of the hydrophobic residues that line the walls of the neck to alanine ($BEST1_{TripleA}$) prevents inactivation. The X-ray structure of $BEST1_{TripleA}$ shows that the only structural changes are a widening of the neck due to the alanine substitutions and in this structure, the C-terminal tail (inactivation peptide) is bound to its receptor site. (Fig.2.12 and 2.13) (Vaisey et al., 2016). Additionally, the C-terminal tail of $BEST1_{TripleA}$ appears protected from proteolysis, as it is in $BEST1_{WT}$. Thus, although the inactivation peptide is bound to its receptor, the $BEST1_{TripleA}$ mutant does not inactivate. A forced widening at the neck uncouples the channel from the effects of higher $[Ca^{2+}]$ and I conclude that the neck functions as the inactivation gate. On the basis of the dimensions of the neck in the X-ray structure of BEST1 (I76, F80 and F84), I hypothesize the neck acts to prevent ions from flowing through it because it is simply too narrow for hydrated ions to fit within it. This "hydrophobic seal" mechanism has been proposed previously for BEST1 on the basis of the dimensions of the neck within the structure (Aryal et al.,

114

2014; Rao et al., 2017). Previously I have shown the neck also functions as the activation gate by controlling the flow of Cl$^-$ through the pore in a Ca^{2+}-dependent manner (Section 2) (Vaisey et al., 2016). Thus, in the wild type channel, the neck functions as a variable constriction within the pore that is responsible for both Ca^{2+}-dependent activation and Ca^{2+}-dependent inactivation.

A hypothetical scheme is illustrated in Fig. 3.11. At low concentrations of Ca^{2+}, the Ca^{2+} clasps are empty and the neck is sealed shut; this corresponds to a "closed", nonconductive state of the ion pore. The binding of Ca^{2+} ions at the clasp causes local changes that induce changes within the neck, which presumably includes its widening, and these transition the channel into a conductive – "open" or "activated" – state. After opening, the channel begins to inactivate, and higher concentrations of Ca^{2+} increase the rate and extent of inactivation. Inactivation involves binding of the C-terminal tail – the inactivation peptide – to its cytosolic receptor located on the surface of the channel. Although further study is needed to be conclusive, my data suggest that the Ca^{2+}-dependence of inactivation is due to interaction of Ca^{2+} with an electronegative region adjacent to the receptor site, involving D323 and the surrounding acidic residues, and this stimulates and/ or stabilizes the binding of the inactivation peptide to its receptor. The binding of the inactivation peptide then induces conformational changes in the channel that lead to changes within the neck that seal it shut. The gating processes are reversible; lowering the Ca^{2+} concentration can restore inactivated channels to activated ones and also deactivated ones depending on the ultimate Ca^{2+} concentration.
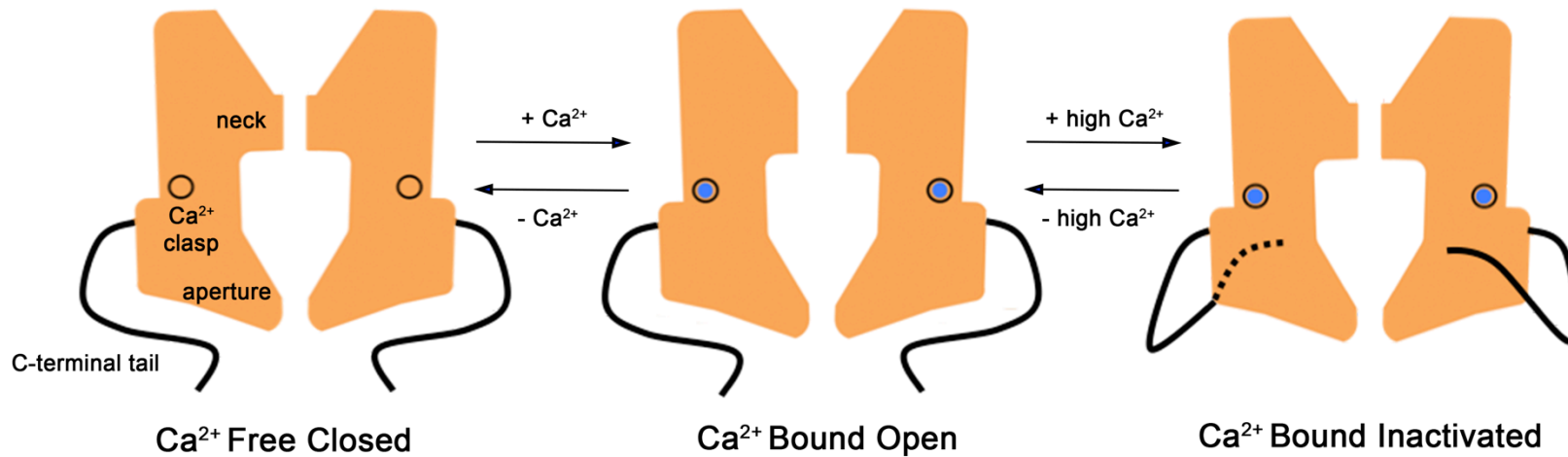
Figure 3.11. Hypothesized mechanisms for activation and inactivation in bestrophin channels. In the Ca^{2+} free state of the channel the neck of BEST1 is sealed shut and the channel is non-conductive. Binding of Ca^{2+} to the high affinity Ca^{2+} clasp is coupled to dilation at the neck of BEST1, which now permits ions to flow through it. In both the Ca^{2+}-free closed and Ca^{2+}-bound open states, the inactivation peptides (one from each subunit) are not engaged with their receptors. In the presence of higher (e.g. μM) concentrations of Ca^{2+}, the inactivation peptides bind to their receptor sites on the cytosolic surface of the channel (the dashed line indicates that this tail binds on the back surface). Inactivation peptide binding causes conformational changes in the channel that allosterically control the conformation of the neck of the pore, causing it to transition into a non-conductive conformation. The aperture does not have a role in activation or inactivation. Instead, the aperture bottleneck functions as a size-selective filter that permits the passage of small ions and requires them to become at least partially dehydrated as they move through it and thereby gives rise to the lyotropic sequence of permeability among permeant anions (Vaisey et al., 2016).

What could be the physiological relevance of BEST1 channel inactivation? Evidence is mounting that bestrophin channels are regulated by cell volume (Chien and Hartzell, 2007; 2008; Fischmeister and Hartzell, 2005; Milenkovic et al., 2015; Xiao et al., 2009) and it has been speculated that this could be linked to fluid transport homeostasis in the RPE (Hartzell et al., 2008; Xiao et al., 2010). Whole cell recordings of human BEST1 in HEK cells demonstrate a link between volume regulation and current rundown of BEST1 curents (Xiao et al., 2009), which we now know is due to inactivation. Phosphorylation of S358 in the inactivation peptide is involved in this process in cells. Dephosphorylation of S358 mediates, at least partially, hypertonic solution-mediated inhibition of human BEST1 and ceramide, which is an activator of PP2A phosphatase that is released during cell shrinkage, mimicked the effects of hypertonic stress (Xiao et al., 2009). Although the regulation of S358 phosphorylation *in vivo* is not fully understood, it has been shown that human BEST1 coimmunoprecipitates with PP2A in RPE cells (Marmorstein et al., 2002). Thus, the inactivation of BEST1 and its modulation by PKC and PP2a may be important regulatory mechanisms in the physiology of RPE cells. In addition to inactivation depending on the cytosolic concentration of Ca^{2+} and the phosphorylation state of S358, it is clear from my experiments that the concentration of KCl modulates inactivation, with higher (>30 mM) concentrations increasing its extent and kinetics. This behavior is investigated and discussed further in chapter 5.

Approximately 200 mutations in BEST1 have been associated with retinal degenerative disorders (Hartzell et al., 2008). Those mutations that have been characterized are predominantly associated with reduced Cl^- currents (Davidson et al., 2009; Marchant et al., 2006; Milenkovic et al., 2011; Sun et al., 2002) but most remain unstudied and some of these could affect BEST1 inactivation. A fairly recent study identified a mutation of BEST1 in a patient with ARB that produced currents that were actually larger than the

117

wild type channel when expressed in HEK293 cells (Johnson et al., 2015). This mutation causes a frameshift that produces a channel comprised of only the first 366 amino acids. Based on the findings presented here and by others, this mutant would have impaired inactivation, and this suggests that defects in inactivation of BEST1 may be pathological.

3.6 Conclusion

Current rundown is a commonly observed phenomenon among ion channels (Becq, 1996; Dang et al., 2017; Ni et al., 2014). In many cases, it is unclear whether rundown represents an intrinsic property of the channel or is due to depletion of cellular factors that are necessary for channel activity. Here, using a reconstituted system, I have shown that current rundown through BEST1 is due to inactivation and is an intrinsic property of the channel. The extent and kinetics of inactivation depend on the cytosolic concentration of Ca^{2+}, and inactivation can occur under physiological levels of Ca^{2+}. I have identified a C-terminal peptide that is necessary for inactivation and identified its receptor site on BEST1. The data indicates that binding of the inactivation peptide to its receptor causes the channel to inactivate through an allosteric mechanism by closing a structurally distant gate at the neck of the pore. Mutations to the inactivation peptide, mutations of its receptor site, and mutations within the neck can prevent inactivation. Further, my experiments point to the involvement of an acidic cytosolic region in the mechanism of Ca^{2+}-dependence of inactivation. This investigation provides a framework to further understand the molecular mechanism of inactivation, such as how the allosteric signal is relayed between the inactivation receptor site and the neck of the pore, and how mutations that cause disease may do so by altering the inactivation properties of the channel.

Chapter 4

4. Cryo-EM structures reveal mechanisms of BEST1 channel gating

4.1 Summary

Bestrophins are unrelated to any other family of ion channels. The X-ray structure of

chicken BEST1 was thus a major breakthrough, revealing for the first time the protein's

pentameric architecture and distinguishing features. As laid out in section 2,

electrophysiological recordings of purified BEST1 enabled identification of regions

important for Ca^{2+}-dependent activation and selectivity among anions. Still, what

conformation the X-ray structure represented and how the channel opens and closes

remained unclear. Here, I present high-resolution cryo-electron microscopy (cryo-EM)

structures of BEST1 in the presence and absence of Ca^{2+} that unambiguously reveal the

conformational changes underlying channel gating. Repositioning of tethered pore-lining

helices dramatically widen the pore at the neck to generate an open conformation. The

open pore contains a continuous 90 Å-long aqueous vestibule with a single constriction

at the cytosolic aperture and mutation of this region can drastically alter relative

permeability among anions. Ca^{2+} binding to the Ca^{2+} clasp instigates pore opening and a

Ca^{2+}-free structure reveals that, unlike voltage-gated Na^+ and K^+ channels, similar

molecular rearrangements are responsible for inactivation and deactivation. The

structures and accompanying electrophysiological studies define the principal gating

transitions of BEST1 and reveal a new molecular paradigm for gating in ligand-gated ion

channels. A manuscript on work presented here, in collaboration with a postdocotoral

researcher Dr. Alexandria N. Miller, has been submitted (Miller[*], Vaisey[*] and Long,

submitted).

4.2 Background

Electrophysiological recordings of purified BEST1, presented in section 2, demonstrate the clear Ca^{2+}-dependent activation of this channel. In the X-ray structure of BEST1, Ca^{2+} is bound at the Ca^{2+} clasp (Kane Dickson et al., 2014) and thus we might expect that the structure represents an activated, open conformation. The narrow pore dimensions observed at the neck challenge this idea, however. The neck is 15 Å in length and formed by a total of fifteen hydrophobic amino acids (three per subunit), generating a diameter and hydrophobicity at this region that would create a large energetic barrier to ion permeation, effectively sealing the channel shut (Aryal et al., 2015; Rao et al., 2017).

The notion that the X-ray structure represents a non-conductive conformation of BEST1 is supported by data discussed earlier in this thesis. First, I have shown that the neck region of BEST1 is the Ca^{2+}-dependent activation gate (Vaisey et al., 2016). Alanine mutagenesis of the neck residues generated a channel whose ionic currents were independent of Ca^{2+} (section 2.3), and an X-ray structure of this mutant confirmed that a widening only at the neck was sufficient for this behavior (section 2.4). Electrophysiological recordings analyzing relative anion permeation of wild type and mutant BEST1 channels support the hypothesis that the neck widens upon channel opening. In the X-ray structure of BEST1, the pore diameter at the neck region is narrow enough (~ 2-4 Å) that Cl^- and other monovalent anions would have to be dehydrated as they pass through. Dehydration of permeating ions is thought to give rise to the lyotropic permeability sequence of BEST1 ($SCN^- > I^- > Br^- > Cl^-$), whereby ions with lower energetic costs of dehydration are more permeable (Hille, 2001; Hartzell et al., 2005a; Qu and Hartzell, 2000). Thus we expect that if the structure represents a conductive conformation of the channel, mutation of the neck residues would affect the lyotropic

permeability sequence by altering the energetic costs of ion dehydration at this region. Instead, I found that mutation of the neck residues to alanine had no effect on relative anion permeabilities (section 2.4.2). This finding is consistent with channel opening involving a widening of the neck region, such that ions flowing through are not dehydrated.

In section 3 I laid out evidence supporting a mechanism whereby the C-terminal tail acts as an inactivation peptide and that binding to its receptor site on BEST1 enforces channel inactivation. In the X-ray structure of BEST1 the inactivation peptide is bound to its receptor site, suggesting that the structure may represent a closed, inactivated conformation. Further, the X-ray structure is of BEST1 bound to a Fab, 10D10, which I have shown causes current decrease when added to purified BEST1 in bilayers (section 3.4.3). Because 10D10 is unable to bind the non-inactivating mutant BEST1$_{S358E}$, I hypothesize that it binds to and stabilizes the inactivated channel conformation.

Based on the narrow dimensions of the neck, the bound C-terminal tail, and that the structure is in complex with the 10D10 Fab, the X-ray structure likely represents a Ca^{2+}-bound inactivated state. To overcome channel inactivation in the hopes of obtaining an open channel conformation, I have used mutants of BEST1 that are non-inactivating for structural studies. I have previously shown that mutations that prevent inactivation do not affect ion selectivity or Ca^{2+}-dependent activation properties of BEST1, suggesting that these separate behaviors can be uncoupled from one another (section 3.4.2). Initial efforts, not shown here, employed x-ray crystallography of non-inactivating BEST1 mutants but these were hampered by a lack of well-diffracting crystals.

More recently, single particle cryo-electron micrscopy (cryo-EM) has been used to obtain high-resolution structures of membrane proteins, including ion channels (Egelman, 2016; Liao et al., 2013). Technological developments to both the hardware and software used in cryo-EM has heralded what is popularly known as the "resolution revolution" (Kühlbrandt, 2014). Direct electron detectors, which are more sensitive than their predecessors and allow snapshots to be taken to correct for beam-induced motion, in combination with powerful maximum likelihood methods for data averaging (Scheres, 2012), have primarily driven this technology forward. A particular advantage of single particle cryo-EM analysis is the ability to use computational methods to separate particles into distinct classes, based on structural differences. For an ion channel like BEST1, which may adopt both closed and open conformations in activating conditions, this is a significant edge over X-ray crystallography.

Here single-particle cryo-EM analysis of BEST1 in Ca^{2+}-containing and Ca^{2+}-free conditions is performed to investigate the mechanism of BEST1 channel gating.

4.3 Materials and methods

4.3.1 EM sample preparation and data acquisition

BEST1 protein, expressed and purified as described (section 2.3.1) was purified in a final step by gel filtration (Superose 6 increase 10/300 GL; GE Healthcare) in buffer containing 20 mM Tris, pH 7.5, 50 mM NaCl, 1 mM DDM (Anatrace) and 0.1 mM cholesteryl hemisuccinate (CHS; Anatrace). Purified BEST1 was concentrated to 5 mg ml^{-1} using a 100 kDa concentrator (Amicon Ultra-4, Millipore) and divided in half, with 1 µM $CaCl_2$ added to one sample (Ca^{2+}-bound), and 5 mM EGTA, pH 7.5 added to the other (Ca^{2+}-free). These samples were immediately used for cryo-EM grid preparation.

5 µl of sample was pipetted on Quantifoil R1.2/R1.3 holy carbon grids (Au 400, Electron

Microscopy Sciences), glow discharged for 10 s using a PELCO easiGlow glow discharge

cleaning system (Ted Pella). A vitrobot Mark IV cryo-EM sample plunger (FEI), operated at

room temperature with a 1-2 s blotting time under a blot force of 0 and 100% humidity was

used to plunge-freeze the sample into liquid nitrogen-cooled liquid ethane. For Ca^{2+}-free

conditions, the blotting paper used for grid freezing was pre-treated with 2 mM EGTA

solution (4x), rinsed with ddH_2O (4x) and dried under vacuum. Grids were clipped and

loaded into a 300 keV Titan Krios microscope (FEI) equipped with a K2 Summit direct

electron detector (Gatan). Grids were screened first for quality control based on the

particle distribution and density, and images from the best grids were recorded with

SerialEM (Mastronarde, 2005) in super-resolution mode at a magnification of 22,500x,

with a super-resolution pixel size of 0.544 Å and a defocus range of -0.7 to -2.15 µm. The

dose rate was 9 electrons per physical pixel per second, and images were recorded for 10

seconds with 0.25 s subframes (40 total frames) corresponding to a total dose of 76

electrons per $Å^2$.

4.3.2 Image processing

Figures 4.1, 4.2, 4.9 and 4.12 show the cryo-EM workflow for Ca^{2+}-bound $BEST1_{405}$, Ca^{2+}-

bound $BEST1_{345}$, Ca^{2+}-free $BEST1_{345}$ and Ca^{2+}-free $BEST1_{345}$ W287F datasets,

respectively. Movie stacks were gain-corrected, two-fold Fourier cropped to a calibrated

pixel size of 1.088 Å, motion corrected and dose weighted using MotionCor2 (Zheng et al.,

2017). Contrast Transfer Function (CTF) estimates for motion-corrected micrographs were

performed in CTFFIND4 using all frames (Rohou and Grigorieff, 2015).

Ca^{2+}-bound $BEST1_{405}$ and $BEST1_{345}$ datasets

All subsequent image processing was carried out with RELION2.1 (Fernandez-Leiro and

Scheres, 2017), using a particle box size of 384 pixels and a mask diameter of 140-160 Å. A total of 1740 and 1644 micrographs were collected for Ca^{2+}-bound $BEST1_{405}$ and $BEST1_{345}$, respectively, and all were inspected manually; poor quality micrographs and those having CTF estimation fits lower than 5 Å were discarded. Approximately 1000 particles were selected manually for reference-free 2D classification to generate templates used for automatic particle picking. Auto-picking yielded ~312,000 and ~309,000 particles for $BEST1_{405}$ and $BEST1_{345}$, respectively, and one round of 2D classification, asking for 100 classes, was used to remove outlier particles, resulting in ~290,000 particles for each dataset. An initial 3D model from a previously collected, lower resolution cryo-EM dataset of Ca^{2+}-free BEST1 was generated using EMAN2 (Tang et al., 2007). 3D refinement was performed using the selected particles from 2D classification for each dataset and the initial model, low-pass filtered to 60 Å resolution to prevent model bias. This yielded a reconstruction at 3.1 Å ($BEST1_{405}$) and 2.9 Å ($BEST1_{345}$) overall resolution with an applied C5 symmtery and the maps were inspected using UCSF Chimera (Pettersen et al., 2004). All resolution estimates are based on the gold-standard Fourier shell correlation (FSC) calculations.

In order to identify distinct conformational states of Ca^{2+}-bound $BEST1_{345}$, I performed 3D classification using the particle angular assignments and final reconstruction from 3D refinement (initial model, 5 Å low pass filter), sorting the particles into 9 classes. One 3D class reconstruction with a widened "neck" ($BEST1_{345}$ open) was isolated, containing ~ 30,000 particles. To select for more open channel particles in the dataset, the $BEST1_{345}$ open class was subjected to 3D refinement and the final reconstruction was used as an initial model (5 Å low pass filter) for 3D classification with the entire dataset, sorting particles into 4 classes. One class yielded the open conformation (~40,000 particles) and the three other classes were in the same, closed conformation. One class for the closed

conformation was chosen (~44,000 particles) because it contained better resolved electron density at the neck. Each of these classes was individually subjected to 3D refinement, yielding reconstructions to 3.0 Å overall resolution. Particles from these two classes were "polished" using aligned movie frames generated from MotionCor2 (Zheng et al., 2017). 3D refinement using the polished particles and a global angular sampling threshold of 1.75^o yielded reconstructions of 3.0 Å and 2.9 Å overall resolution for the Ca^{2+}-bound $BEST1_{345}$ closed and open class, respectively.

For the Ca^{2+}-bound $BEST1_{405}$ dataset, a similar 3D classification procedure was performed to search for the open conformation using the final reconstruction of $BEST1_{405}$ from 3D refinement or the Ca^{2+}-bound $BEST1_{345}$ open class as an initial model. No open classes were identified from this dataset.

Ca^{2+}-free $BEST1_{345}$ and $BEST1_{345}$ W287F datasets

Initial image processing was carried out with RELION2.1, using a particle box size of 384 pixels and a mask diameter of 140. A total of ~1000 or ~1600 micrographs were collected for Ca^{2+}-free $BEST1_{345}$ and $BEST1_{345}$ W287F, respectively, and manually pruned as described for the Ca^{2+}-bound dataset. Auto-picking templates were generated as described and the selected particles (~150,000 for the Ca^{2+}-free $BEST1_{345}$ and ~185,000 particles for the $BEST1_{345}$ W287F datasets) were subjected to one round of 2D classification with 100 classes. 3D refinement was performed using the selected particles from 2D classification (~130,000 for the Ca^{2+}-free $BEST1_{345}$ and ~150,000 paricles for the $BEST1_{345}$ W287F datasets) and the EMAN2-generated initial model described. This yielded reconstructions of 3.4 Å and 3.2 Å overall resolution for each dataset with an applied C5 symmetry. Particle polishing was performed on each refined dataset and these data were imported into the cisTEM cryo-EM software package for further refinement and

classification(Grant et al., 2018).

3D refinement was performed in cisTEM applying C5 symmetry and a BEST1$_{345}$ channel mask, with the micelle region outside of the mask low-pass filtered at 15 Å, yielding reconstructions to 3.0 Å overall resolution for each datatset. To isolate distinct conformational states of Ca^{2+}-free BEST1$_{345}$ and BEST1$_{345}$ W287F, the 3D refined particles were subjected to 3D classification, and spatial frequencies up to 6 Å were used to determine particle alignment parameters. The particles were sorted into 6 classes for the Ca^{2+}-free BEST1$_{345}$ and 8 classes for the BEST1$_{345}$ W287F datasets. After inspection of the 3D reconstructions, two 3D classes appeared in each dataset that had a ~ 5° degree of rotation in their cytosolic regions relative to one another when aligned along their membrane-spanning regions. Each of these 3D classes was refined in cisTEM with final overall resolutions of 3.6 Å (Ca^{2+}-free BEST1$_{345}$ conformation A, ~11,000 particles), 3.4 Å (Ca^{2+}-free BEST1$_{345}$ conformation B, ~21,000 particles), 3.4 Å (Ca^{2+}-free BEST1$_{345}$ W287F conformation A, ~21,000 particles) and 3.5 Å (Ca^{2+}-free BEST1$_{345}$ W287F conformation B, ~17,000 particles).

Estimation of the local resolution of the final maps were done using RELION2.1 (Fernandez-Leiro and Scheres, 2017). The maps shown in figures are combined maps, which were sharpened (using a *B*-factor of -50 Å^{2}) and low-pass filtered at the final overall resolution of each map.

4.3.3 Model building and refinement

The atomic models of BEST1$_{345}$ were manually built into one of the half-maps (sharpened using the *B*-fcator of -50 Å^{2} and low-pass filtered at the final overall resolution of each map) using the BEST1 X-ray structure as a template. The manually built structures were refined in real space using the COOT software (Emsley et al., 2010). Further refinement of

the atomic model was carried out in PHENIX (Adams et al., 2012) using real-space

refinement against the same half-map. The final model had good stereochemistry and

good Fourier shell correlation with the other half-map as well as the combined map

(extended data/ table). Structural figures were prepared with Pymol (pymol.org), Chimera

(Pettersen et al., 2004), and HOLE (Smart et al., 1996).

4.3.4 Electrophysiological recordings

BEST1 protein was expressed and purified as described in sections 2.3.1 and 2.3.2. The

planar lipid bilayer setup and standard solutions used for recording are described in

section 2.3.3.

4.4 Results

4.4.1 Cryo-EM structure determination of Ca^{2+}-bound $BEST1_{405}$

To see if an open conformation of BEST1 could be identified by single particle cryo-EM

analysis, we first collected data on $BEST1_{405}$, the same construct used to obtain the x-ray

structure (Kane Dickson et al., 2014). As figure 4.1 A shows, BEST1 channels appear as

clearly distinguishable particles on the micrographs, frozen in multiple orientations. In

particular, the five-fold symmetry of BEST1 can easily be observed in the top-down views

of the channel, which appear as stars with central holes (the pore). Using a low-pass

filtered 3D model generated by EMAN (Tang et al., 2007), 3D refinement was able to

generate a high-resolution map, to ~ 3.1 Å. An atomic model, using the x-ray structure as

a template, was refined to good stereochemistry and correlation with the cryo-EM density

(Fig.4.3). Overall, the structure appears essentially indistinguishable from the x-ray

structure (Fig.4.1 B and C). From a cutaway view, we can see that the conformations of

the major constrictions, the neck and the aperture, are the same between the x-ray and

cryo-EM structures (Fig.4.1 C) and the overall RMSD between the structures is 0.2 Å.
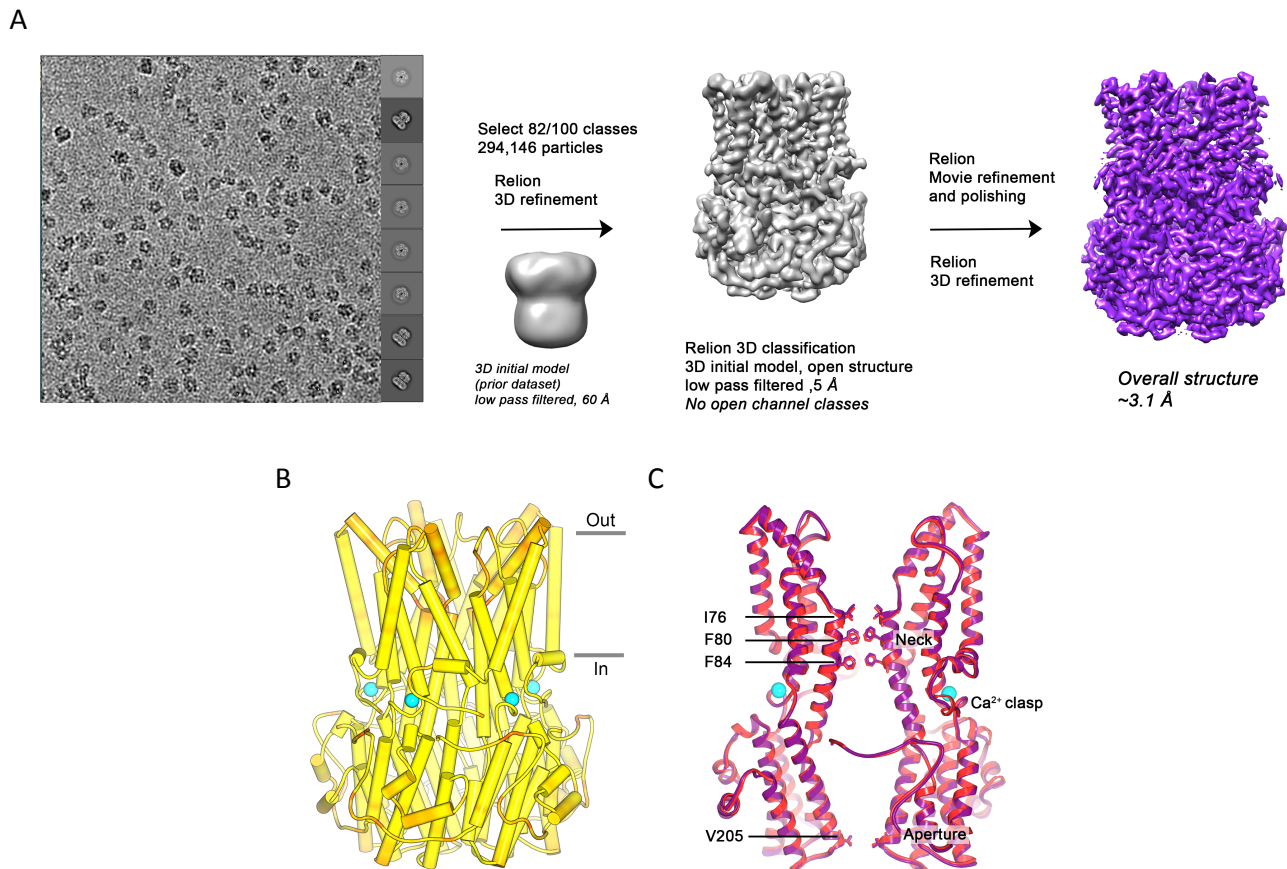
Figure 4.1. Cryo-EM workflow for BEST1$_{405}$ Ca^{2+}-bound dataset and comparison of Ca^{2+}-bound EM and X-ray structures. (A) A detailed description of the workflow can be found in the Methods section. (B) The X-ray and EM structures of BEST1$_{405}$ are essentially indistinguishable. BEST1$_{405}$ model with α-helices depicted as cylinders, is colored on a yellow-to-red spectrum according to the displacement of Cα atoms between BEST1$_{405}$ cryo-EM and x-ray structures. Yellow color represents displacements less than 0.5 Å and red color represents displacements greater than 2 Å. Ca^{2+} ions are depicted as cyan spheres and the approximate boundaries of the bilayer are indicated. (C) Overlay of BEST$_{405}$ cryo-EM (purple) and x-ray (red) structures. Two channel subunits in ribbon are shown as a cutaway from the side. Ca^{2+} ions are highlighted as cyan spheres and side chains of labeled residues are shown. Data collection and analysis of BEST1$_{405}$ was performed by Dr. Alexandria N. Miller.

From single particle analysis we obtained only one structural conformation. Based on its similarity to the x-ray structure, including a closed neck and the bound C-terminal tail, the BEST1$_{405}$ cryo-EM structure likely represents a Ca^{2+}-bound, inactivated conformation.

4.4.2 Cryo-EM structures of Ca^{2+}-bound BEST1$_{345}$

To overcome channel inactivation in my structural studies I used a BEST1 C-terminal deletion construct, which truncates the channel to residue 345 (BEST1$_{345}$), removing the inactivation peptide. I have shown that whilst BEST1$_{345}$ does not inactivate, truncation of the C-terminus does not affect Cl$^-$ versus K$^+$ selectivity or Ca^{2+}-dependent activation of the channel (section 3.4.2). Single particle analysis of Ca^{2+}-bound BEST1$_{345}$ (Fig.4.2) uncovered two distinct channel conformations (Fig.4.5, 4.6), both to high resolution that allowed unambiguous building of amino acid sidechains (Fig.4.4). The first, determined to 3.0 Å resolution (Fig.4.3, Table 4.1), appears almost indistinguishable from the structure of BEST1$_{405}$ (Fig.4.5 A), with the exception of the missing C-terminal tail, and is thus identified as a Ca^{2+}-bound closed conformation. The second structure, determined to 2.9 Å resolution (Fig. 4.3, Table 4.1), is similar overall to that of the closed structure, but contains a dramatically widened pore within the neck region (Fig.4.5). Based on discussions presented herein I conclude that this is the Ca^{2+}-bound open conformation.

The neck observed in the Ca^{2+}-bound closed BEST1 structure is a narrow pore constriction (< 3.5 Å) positioned near the inner leaflet of the membrane that I have previously shown forms the Ca^{2+}-dependent activation gate (Section 2). The neck is 15 Å in length and formed by three highly conserved hydrophobic residues, I76, F80 and F84, located along the pore lining helix S2b, that protrude from each subunit into the pore (Fig.4.5 A, 4.6). The diameter and hydrophobicity at this region would create a
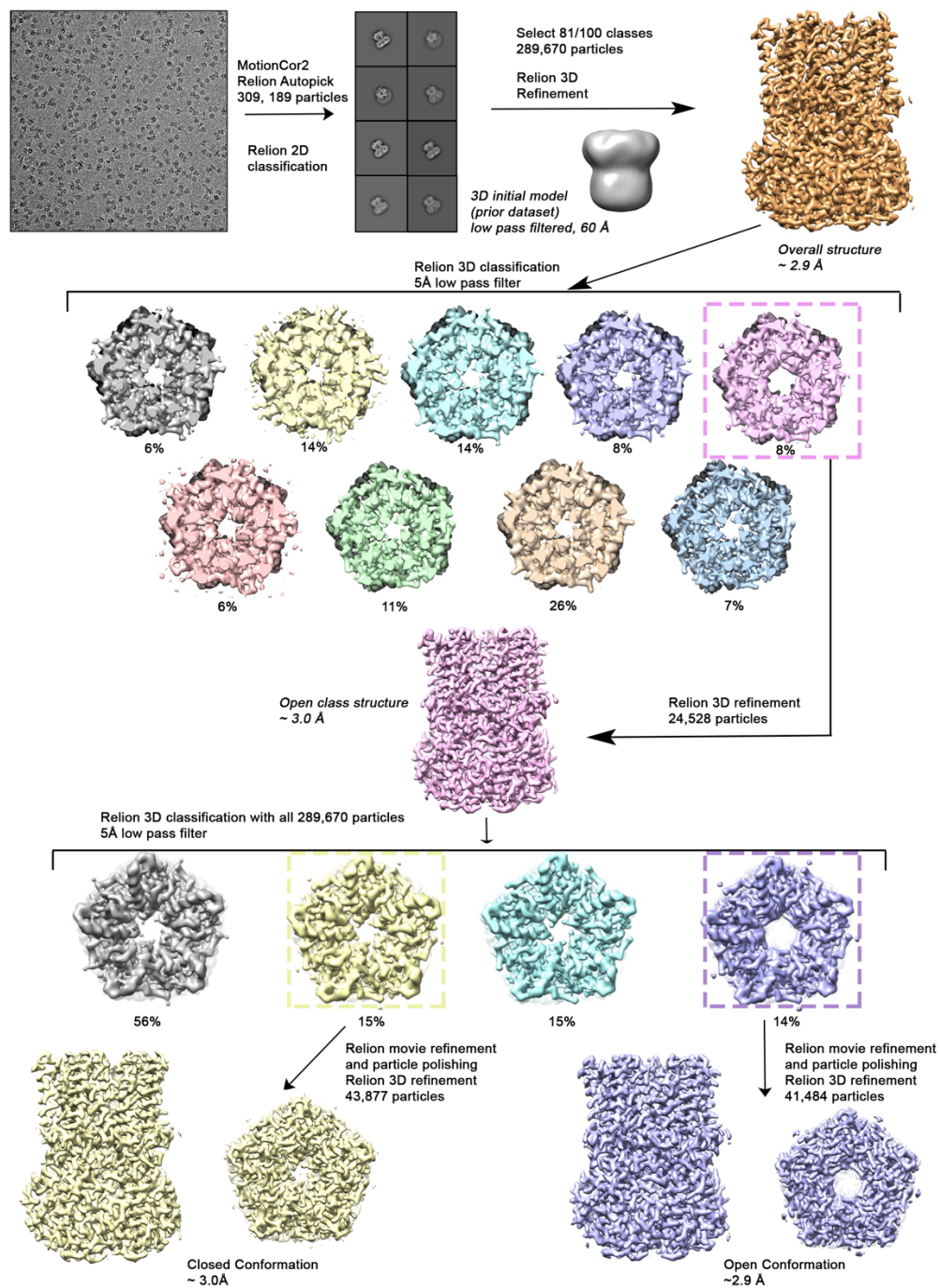
Figure 4.2. Cryo-EM workflow for BEST1$_{345}$ Ca^{2+}-bound dataset. A detailed description of the workflow can be found in the methods section.
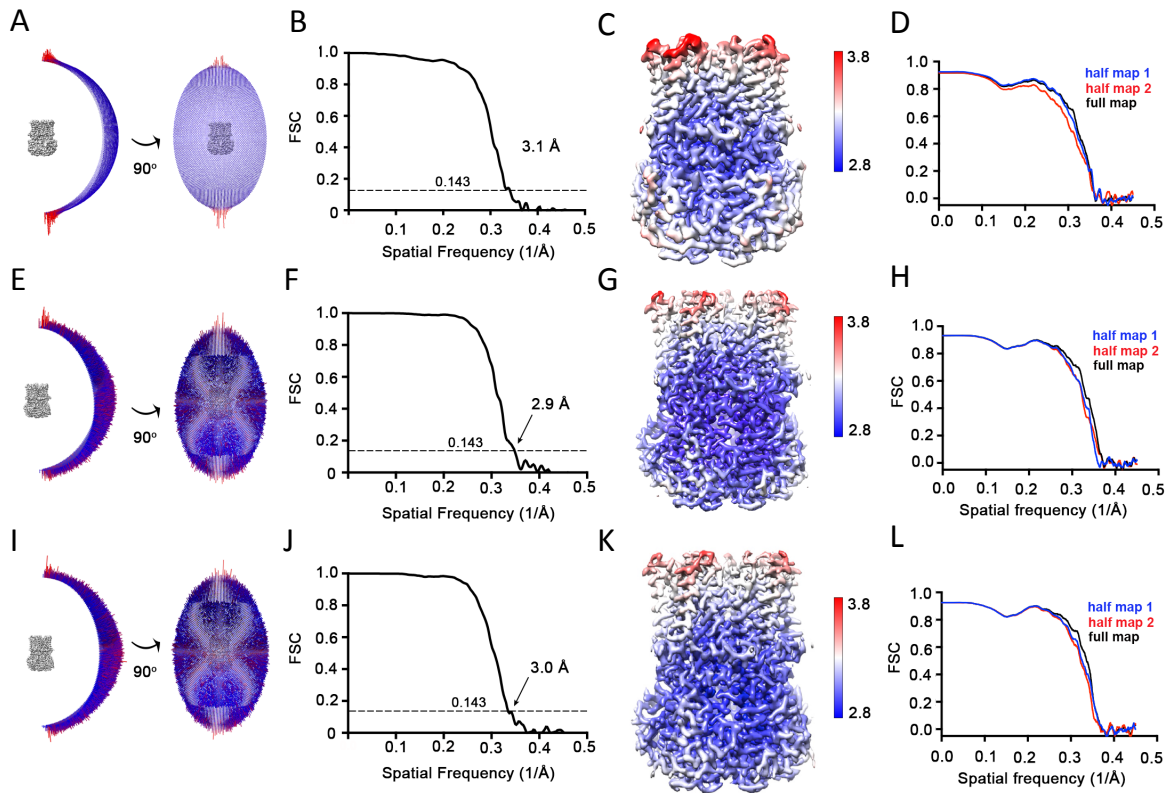
Figure 4.3. Cryo-EM structural determination of Ca^{2+}-bound $BEST1_{405}$ and open and closed Ca^{2+}-bound $BEST1_{345}$. (A-D), Structural determination of $BEST1_{405}$. (A) Angular orientation distribution of particles used in final reconstruction. The particle distribution is indicated by color shading, with blue to red representing low and high numbers of particles. (B) Gold-standard Fourier shell correlation (FSC) curve of the final 3D reconstruction. The resolution is 3.1 Å at the FSC cutoff of 0.143 (dotted line). (C) Local resolution of the map estimated using Relion and colored as indicated. (D) Model validation. Comparison of the FSC curves between the model and half map 1 (work), model and half map 2 (free) and model and full map. (E-H), Structural determination of the Ca^{2+}-bound open BEST1 structure (E) Angular orientation distribution of particles used in final reconstruction, similar to *A*. (F) Gold-standard Fourier shell correlation (FSC) curve of the final 3D reconstruction. The resolution is 2.9 Å at the FSC cutoff of 0.143 (dotted line). (G) Local resolution of the map similar to *C*. (H) Model validation, similar to *D*. (I-L) Structural determination of the Ca^{2+}-bound closed BEST1 structure. (I) Angular orientation distribution of particles used in final reconstruction, similar to *A*. (J) Gold-standard Fourier shell correlation (FSC) curve of the final 3D reconstruction. The resolution is 3.0 Å at the FSC cutoff of 0.143. (K) Local resolution of the map similar to *C*. (L) Model validation, similar to (D).

A

Data collection of cryo-EM BEST1 datasets

Microscope	FEI Titan Krios
Camera	Gatan K2 Summit
Magnification	22,500x
Voltage (kV)	300
Electron exposure ($e^-/Å^2$)	76
Defocus range (μM)	-0.7 ~ -2.5
Pixel size (Å)	1.088

B

	BEST1$_{405}$ (EMD-XXXX)	BEST1$_{345}$ open (EMD-XXXX)	BEST1$_{345}$ closed (EMD-XXXX)
Data processing			
Software	RELION 2.1	RELION 2.1	
Symmetry imposed	C5	C5	
Initial particle images (no.)	311,890	309,189	
Final particle images (no.)	294,146	41,484	43,877
Overall map resolution (Å) FSC threshold 0.143	3.1	2.9	3.0
Map sharpening B-factor ($Å^2$)	-50	-50	-50

C

	BEST1$_{405}$ (PDB XXXX)	BEST1$_{345}$ open (PDB XXXX)	BEST1$_{345}$ closed (PDB XXXX)
Refinement			
Software	Phenix 1.13 real-space-refine	Phenix 1.13 real-space-refine	Phenix 1.13 real-space-refine
Initial model used (PDB code)	4RDQ	4RDQ	4RDQ
Model resolution (Å) FSC threshold 0.5	3.1	3.0	3.0
Model composition			
Non-hydrogen atoms	14975	13995	14040
Protein residues	1815	1690	1695
Ligands	5	5	5
B factors ($Å^2$)			
Protein	87.64	74.46	68.09
Ligands	80.29	56.8	59.67
R.m.s. deviations			
Bond length (Å)	0.008	0.0068	0.0079
Bond angle (°)	0.776	1.10	1.17
Validation			
MolProbity score	1.24	1.24	1.14
Clashscore	2.46	3.56	3.44
Poor rotamers	0	0	0
Ramachandran plot			
Favored (%)	96.68	97.56	98.16
Allowed (%)	3.32	2.44	1.84
Disallowed (%)	0.0	0.0	0.0

Table 4.1. Data collection and model statistics for the Ca^{2+}-bound BEST1$_{405}$ and Ca^{2+}-bound open and closed BEST1$_{345}$ structures.

A

S2b-S2c
Resi. 75-113

B

S2d-S2f
Resi. 118-159

C

S3a-S3b
Resi. 204-253

D

S3-S4 linker-S4a
Resi. 254-293

E

S4b-C terminal tail
Resi. 306-339
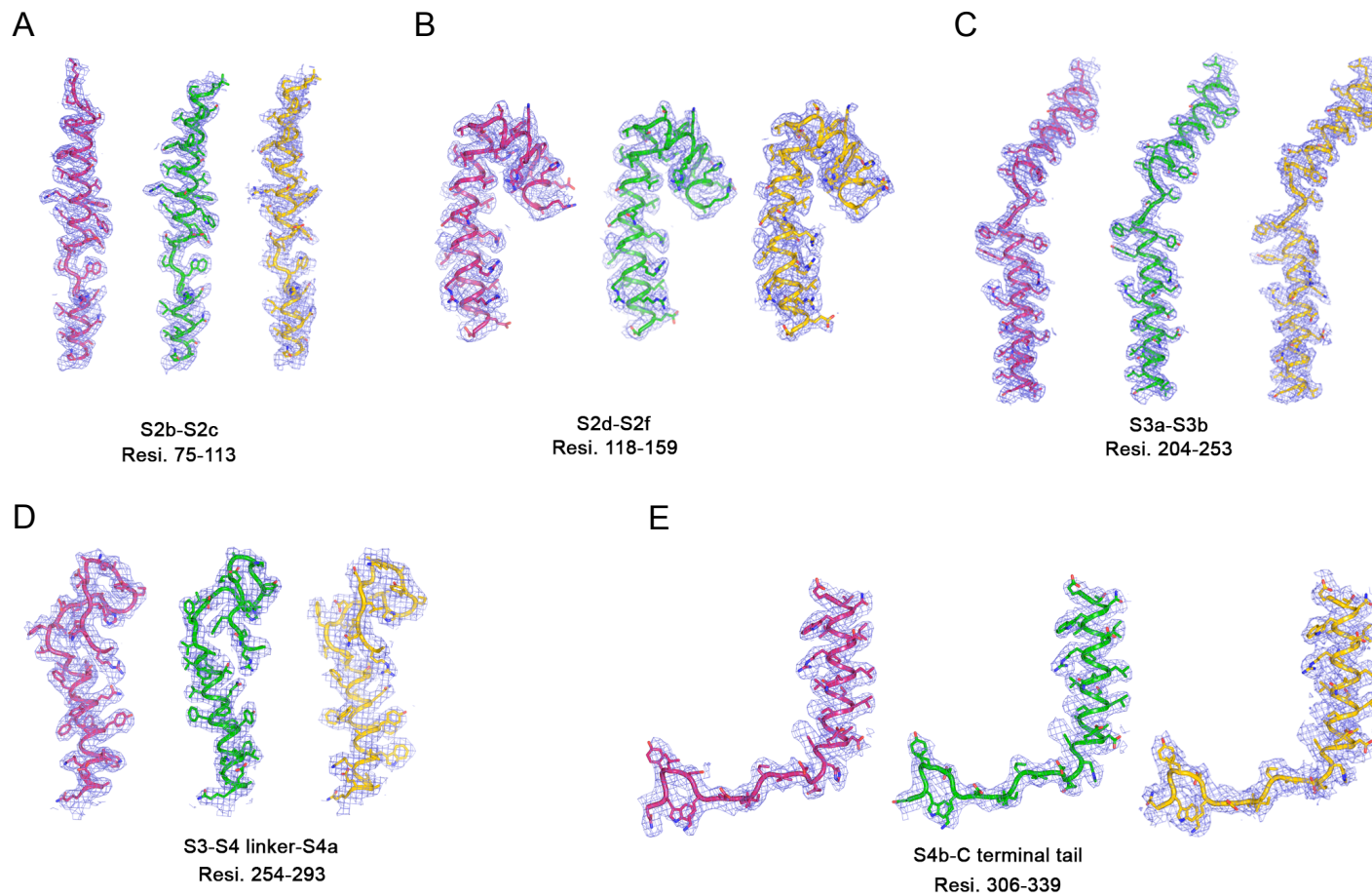
Figure 4.4. (A-E) Representative map density (blue mesh 5σ) highlighting different regions of channel in the Ca^{2+}-bound open BEST1$_{345}$ (pink), Ca^{2+}-bound closed BEST1 (green) and Ca^{2+}-free BEST1$_{345}$ (yellow).
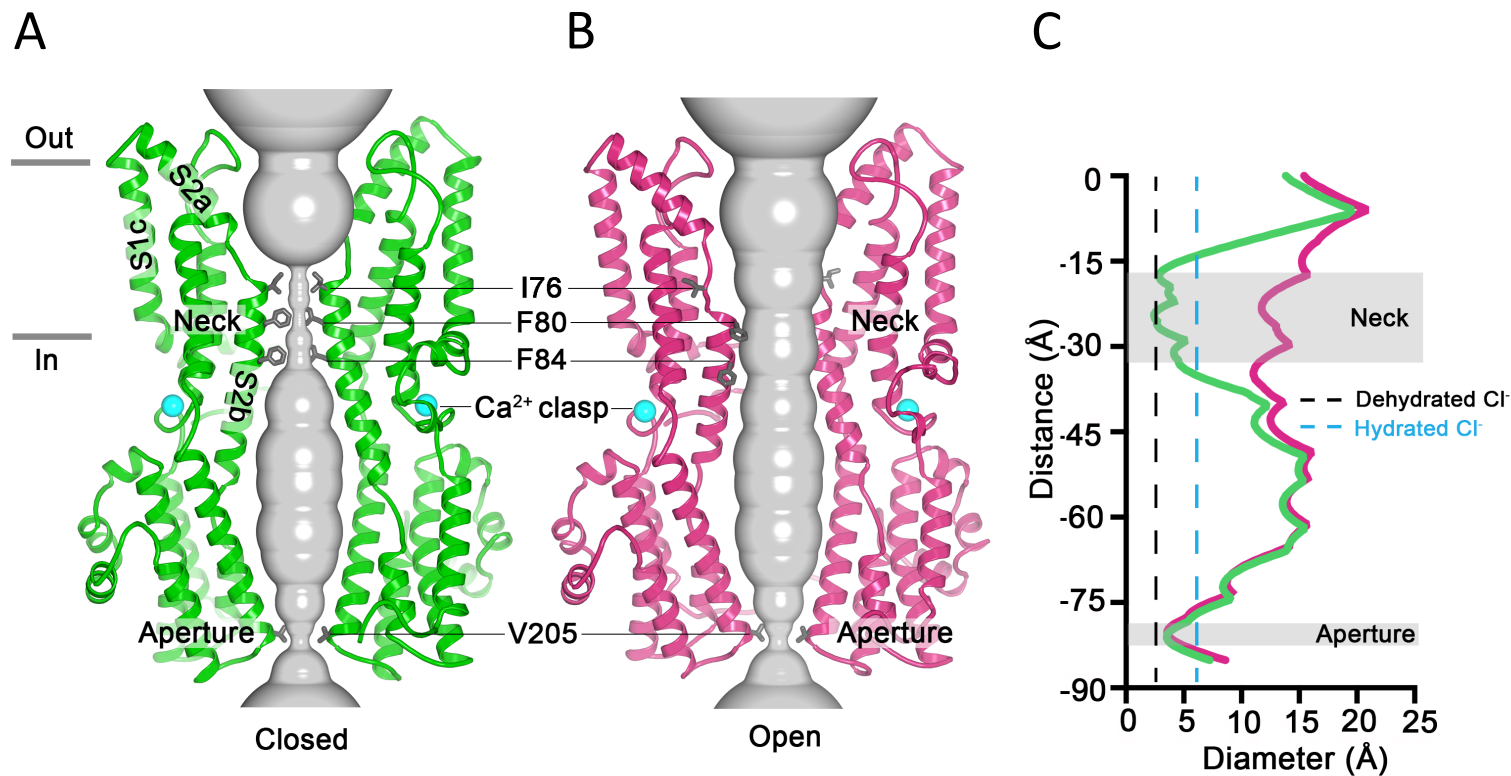
Figure 4.5. The open and closed pores of Ca^{2+}-bound BEST1. (A-B) Cutaway views of the Ca^{2+}-bound closed (green; nonconductive) and Ca^{2+}-bound open (pink) conformations of BEST1$_{345}$. The minimal radial distance from the center of the pore to the nearest van der Waals protein contact is shown as a grey surface. Two subunits are depicted as ribbons; three are omitted for clarity. Amino acids in the neck and aperture regions are drawn as gray sticks; Ca^{2+} ions are cyan spheres. Approximate boundaries of the lipid membrane are indicated. (C) Pore dimensions in the open and closed conformations. Dashed lines indicate the diameters of a dehydrated (black) and hydrated (cyan) Cl^- ion.
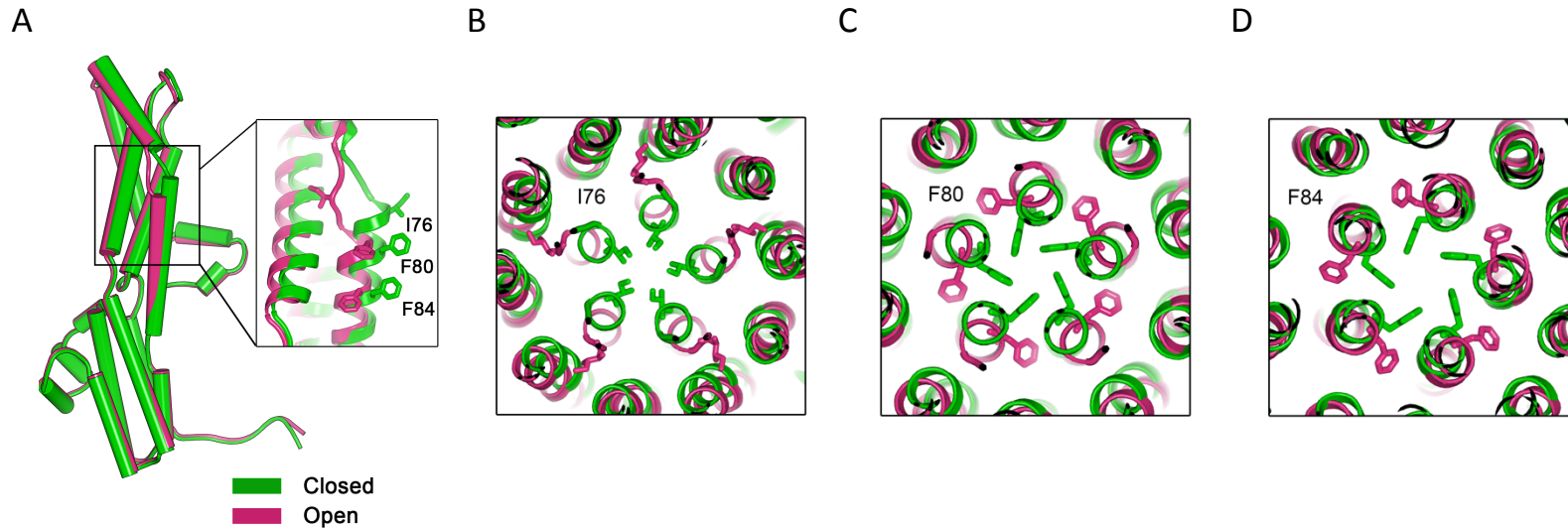
Figure 4.6. Conformational changes between the open and closed structures of Ca^{2+}-bound BEST1. (A) Superposition of individual subunits from the closed and open conformations with α-helices depicted as cylinders. The boxed area shows a close-up of the neck region, with residues depicted as sticks. (B-D) Comparison of neck-lining residues I76, F80 and F84 between the Ca^{2+}-bound open (pink) and Ca^{2+}-bound closed (green) structures. Side chains of labeled residues are depicted in each panel, viewed as a cutaway from the extracellular space

large energetic barrier to ion permeation (Aryal et al., 2015; Kane Dickson et al., 2014; Rao et al., 2017). Opening of BEST1 involves an appreciable widening at the neck region, ~ 10 Å in diameter, that is reminiscent of the dilating iris of a camera lens (Fig.4.6). No appreciable conformational difference is present in the cytosolic region of the channel, and in particular, the aperture constriction of the pore retains its dimensions.

The large expansion observed at the neck in the BEST1 open structure provides an unambiguous mechanism of channel opening and is consistent with electrophysiological studies described previously in this work. Mutagenesis of the hydrophobic neck residues to alanine generated a channel that was active independently of Ca^{2+} (section 2), supporting the observation that the neck is the activation gate of BEST1. Further, in the open conformation the neck residues face away from the pore and would not interact with permeating ions (Fig.4.5 B, 4.6), in line with the finding that the relative permeability of Cl^- versus K^+ remains unaltered by mutations in this region (section 2). Mutagenesis of the neck also had no affect on the lyotropic permeability sequence of BEST1 (section 2), which likely reflects the observation that in the open, conductive channel conformation, the ~ 13 Å diameter at the neck is large enough to allow fully hydrated ions to pass through (Fig.4.5 C).

Comparison of the open and closed conformations of the neck highlights an unusual structural element of the pore that distinguishes the mechanism of gating in BEST1 from most other channels. The neck helix (S2b) is flanked on both of its ends by disruptions of α-helical secondary structure. These disruptions provide impressive flexibility on the one hand and tethering on the other that allow the helix to "float" between closed and open conformations (Fig. 4.7). In the closed conformation, hydrophobic packing at the center
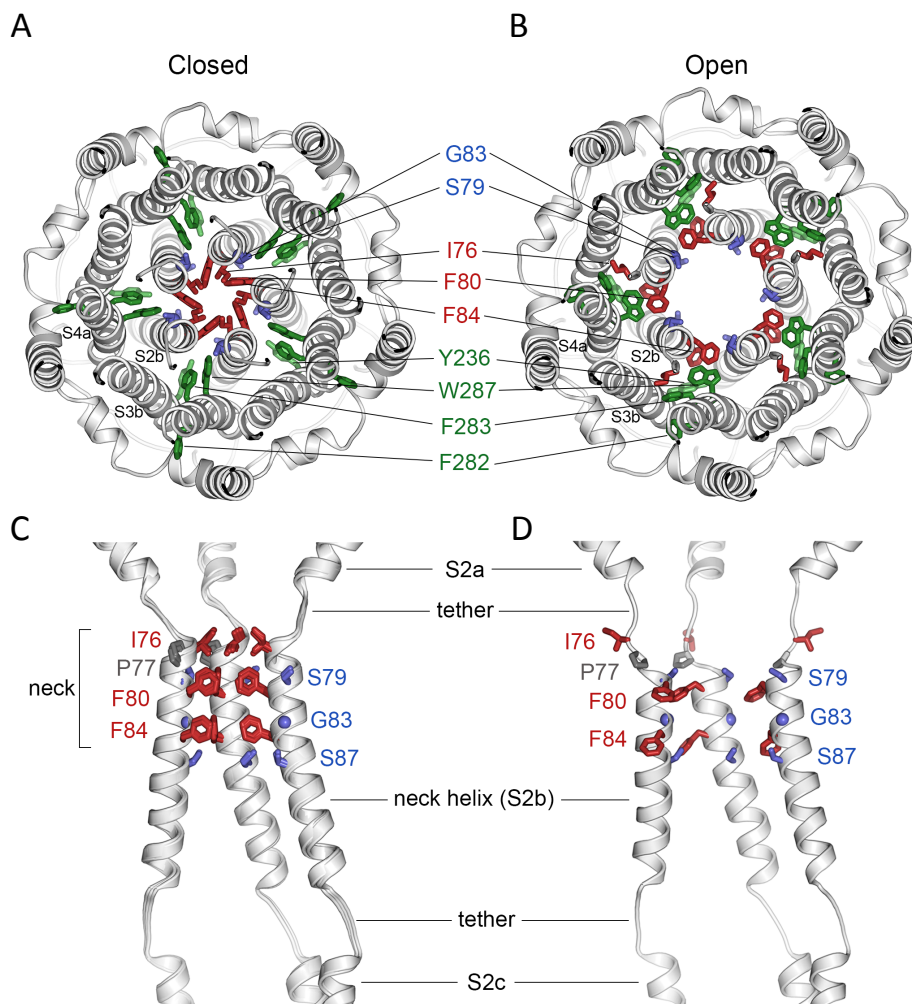
Figure 4.7. Opening transitions. (A-B) Cutaway views of the neck region for the closed (A) and open (B) conformations, viewed from the extracellular side and shown as ribbons. Residues that form the hydrophobic seal in the closed conformation (I76, F80, F84) are colored red in both conformations. Surrounding aromatic residues that move to accommodate opening are colored green. Residues that become exposed to the pore in the open conformation (S79, sticks, and G83, sphere) are blue. A supplementary video shows the transition. (C-D) Side view of the conformational changes in the neck; closed (C) and open (D). In (C), a superposition of the structures of $BEST1_{405}$ in the Ca^{2+}-bound inactivated conformation, $BEST1_{345}$ in the Ca^{2+}-bound closed conformation, and $BEST1_{345}$ in the Ca^{2+}-free closed conformation shows that the neck adopts an indistinguishable (closed) conformation in each. The S2a,b, and c helices from three subunits are shown. Residues are depicted and colored as in A-B; P77 is gray; S87 is shown for reference.

of the neck among the I76, F80 and F84 residues themselves stabilizes this conformation. In the open conformation, the tendency of these amino acids to seclude their hydrophobicity from an aqueous environment is satisfied by their interactions with other hydrophobic amino acids (Y236 and W287) on the S3b and S4a helices located behind the neck helix (Fig.4.7 B). The conformational change moves F80 and F84 away from the center of the pore and involves a slight rotation along the helical axis of S2b (~ 10° clockwise viewed from the extracellular side), outward displacement of S2b (~ 2.5 Å at F80), a slight expansion of the entire transmembrane region (~1 Å increase in radius), and a coordinated set of side chain rotamer changes (Fig.4.7 A and B). Both F80 and F84 move from the most commonly observed rotamer for phenylalanine (observed 44% of the time in the pdb) in the closed conformation to the second most commonly-observed rotamer conformation (observed 33% of the time) in the open conformation. By these conformational changes, F80 and F84 rotate away from the axis of the pore by 80° and 105°, respectively (Fig.4.7). In a domino effect, side chain rotamer changes of Y236, F282, F283, and W287 allow for the movements of F80 and F84 (Fig.4.7. A and B). The conformational change in I76 is also dramatic (Fig.4.7 C and D). When the channel opens, the first α-helical turn of the neck helix unravels such that I76 packs with F247, F276, L279 and F283 in the open conformation and has shifted by approximately 10 Å (Fig.4.8 A). The unraveling is facilitated by P77, which is perfectly conserved among BEST channels and is part of the neck helix in its closed conformation, but marks its N-terminal end in the open conformation (Fig.4.7 C and D). The repositioning within the neck also exposes S79 and G83 on the neck helix, which are secluded behind the F80 and F84 in the closed conformation, to the pore in the open conformation (Fig 4.7 A and B). Thus, through a concertina of coordinated conformational changes in and around the helix, amino aicds that formed the hydrophobic barrier that prevented ion permeation have dispersed and reveal a wide aqueous vestibule.
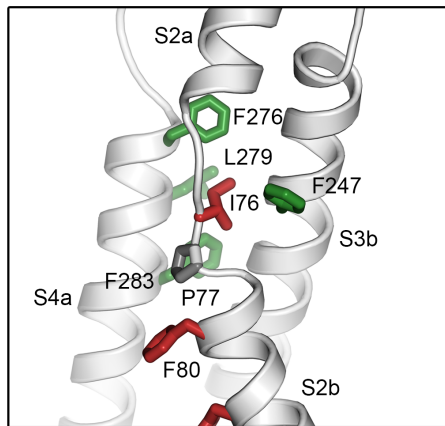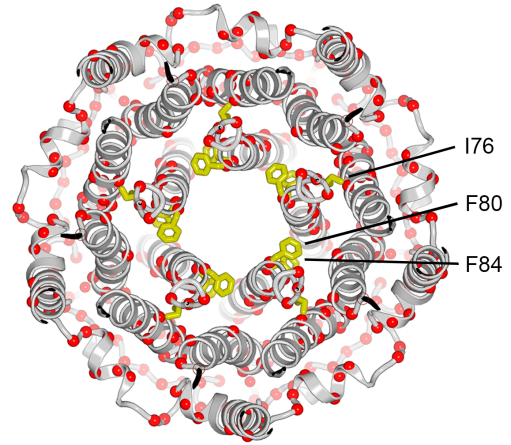
Figure 4.8. A close-up view showing the hydrophobic packing of I76 in the open conformation. Neck residues are highlighted in red, neighboring hydrophobic residues that interact with I76 are shown in green, and P77 is depicted in gray. (B) Location of missense mutations associated with retinal diseases at amino acid positions in and around the neck of BEST1 (red spheres indicate the Cα positions of the mutations).
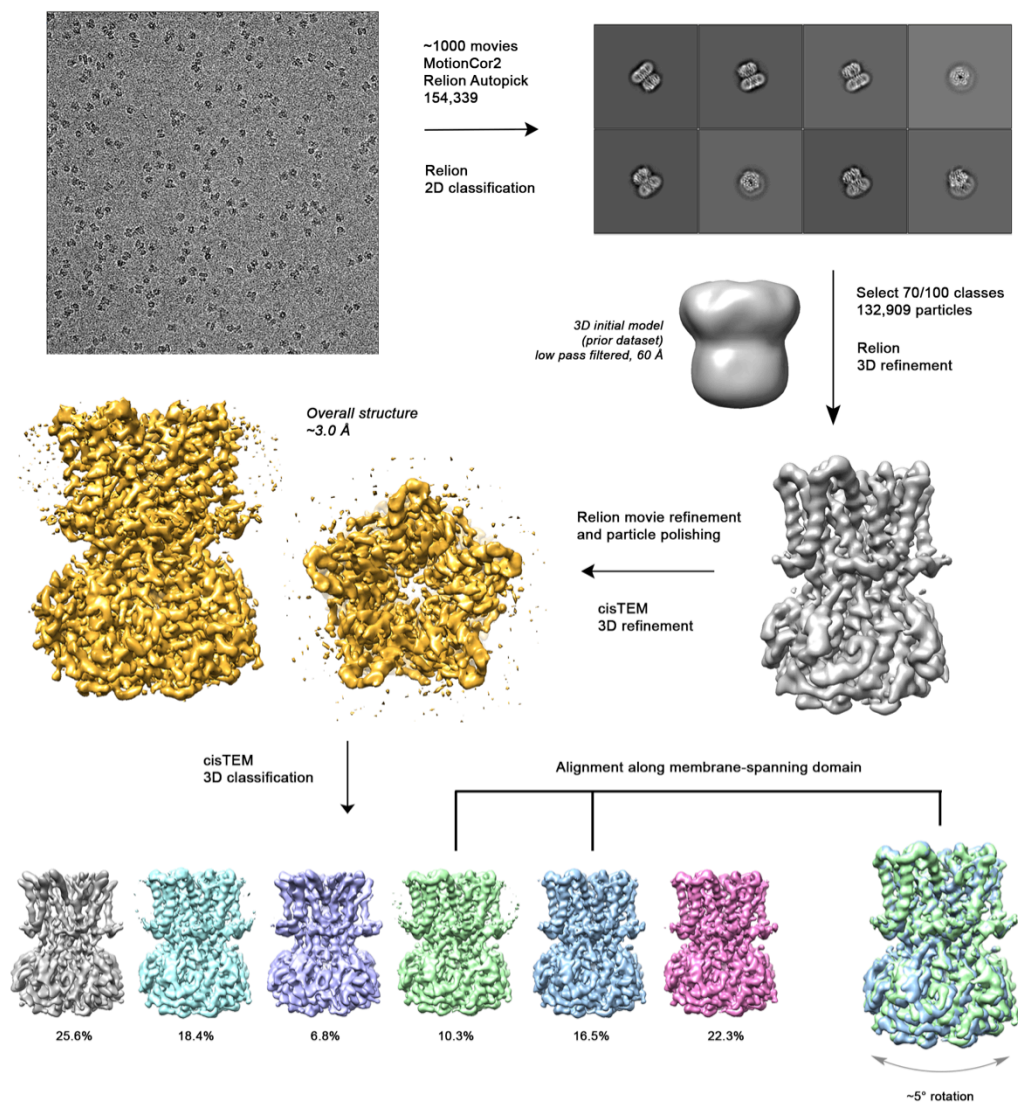
Figure 4.9. Cryo-EM workflow for BEST1 Ca^{2+}-free dataset. A detailed description of the workflow can be found in the Methods section.
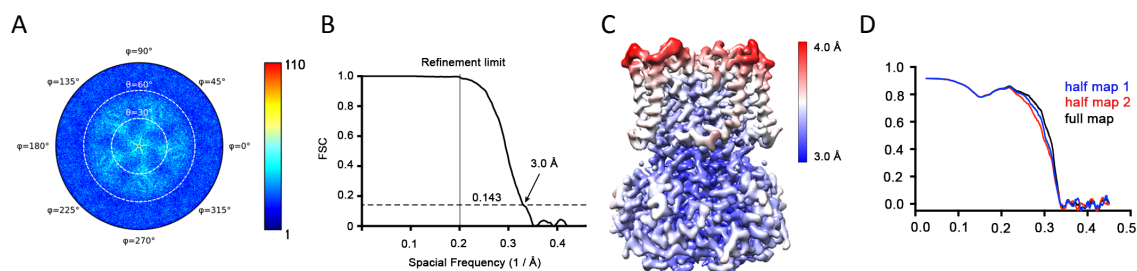
E

	BEST1$_{345}$ Ca^{2+} Free (EMD-XXXX) (PDB-XXXX)	Overall, Ca^{2+}-free BEST1$_{345}$ (EMD-XXXX) XXXX)	Overall, Ca^{2+}-free BEST1$_{345}$ W287F (EMD-XXXX) (PDB XXXX)
Data processing			
Software	RELION 2.1, cisTEM 1.0	ON 2.1, cisTEM 1.0	RELION 2.1, cisTEM 1.0
Symmetry imposed	C5		C5
Initial particle images (no.)	154,339	39	185,568
Final particle images (no.)	132,909	09	153,592
Overall map resolution (Å)			3.0
FSC threshold 0.143	3.0		
Map sharpening B-factor (Å^2)	-50		-50
Refinement			
Software	Phenix 1.13 real-space-refine	κ 1.13 real-space-refine	Phenix 1.13 real-space-refine
Initial model used (PDB code)	4RDQ		4RDQ
Model resolution (Å)			3.6
FSC threshold 0.5	3.2		
Model composition			8076
Non-hydrogen atoms	13395		972
Protein residues	1620		0
Ligands	0		
B factors (Å)			0.007
Protein	102.72		0.77
Ligand			
R.m.s. deviations from ideality			1.47
Bond length (Å)	0.008		4.40
Bond angle (°)	0.824		0.27
Validation			
MolProbity score	1.27		
Clashscore	2.94		96.27
Poor rotamers	0		3.73
Ramachandran plot statistics (%)			0
Preferred	96.89		
Allowed	3.11		
Outliers	0		

Figure 4.10. Cryo-EM structural determination of Ca^{2+}-free BEST1$_{345}$. (A-D) Structural determination of the overall Ca^{2+}-free BEST1$_{345}$ structure. (A) Angular orientation distribution of particles used in final reconstruction, obtained from cisTEM. The particle distribution is indicated by color shading with blue to red representing low to high numbers of particles. (B) Gold-standard Fourier shell correlation (FSC) curve of the final 3D reconstruction. (C) Local resolution of the map estimated using Relion and colored as indicated. (D) Model validation. Comparison of the FSC curves between the model and half map 1 (work), half map 2 (free) and full map are plotted. (E) Table of data collection and model statistics for Ca^{2+}-free BEST1$_{345}$.

4.4.3 Cryo-EM structure of Ca^{2+}-free BEST1$_{345}$

To address how Ca^{2+} binding contributes to BEST1 channel gating, the structure of BEST1$_{345}$ in the absence of Ca^{2+} was determined to 3.0 Å resolution (Fig.4.9, 4.10). From single particle analysis, only a closed conformation could be obtained for Ca^{2+}-free BEST1$_{345}$. The structure appears practically indistinguishable from the inactivated and Ca^{2+}-bound closed BEST1 structures, with most of the differences confined to the area including and surrounding the Ca^{2+} clasp (Fig.4.11). In structures with Ca^{2+}-bound, the five Ca^{2+} clasps, one from each subunit, resemble a belt that wraps around the midsection of BEST1. Without Ca^{2+}, the majority of the Ca^{2+} clasp becomes disordered (Fig.4.11 B). 3D classification of the Ca^{2+}-free dataset yielded only closed conformations of the neck but did indicate a degree of flexibility in the channel between the transmembrane and cytosolic regions that was manifested as a ~5° rotation along the symmetry axis (Fig.4.11 C). This conformational flexibility was not observed in the Ca^{2+}-bound datasets, which suggests that Ca^{2+} binding rigidifies the channel and that this may be necessary for stabilization of the open conformation.

4.4.4 A Ca^{2+}-independent mutant of BEST1

The ratio of particles in the closed and open Ca^{2+}-bound BEST1 dataset (86% to 14% , respectively) indicates that the closed state of BEST1 is energetically favored over the open state. Since the overall movements between these two conformations are minimal, we hypothesized that the free energy difference is also small, and that the transition to the open conformation could be easily biased by mutagenesis. Located behind the neck is a highly conserved tryptophan (W287) that, in the closed structure, buttresses the space between two pore-lining helices, appearing crucial for the structural integrity of this conformation (Fig.4.14 A). The conservative W287F mutation had a dramatic effect on BEST1 channel gating. Whilst BEST1$_{W287F}$ retained equivalent Cl$^-$ versus K$^+$
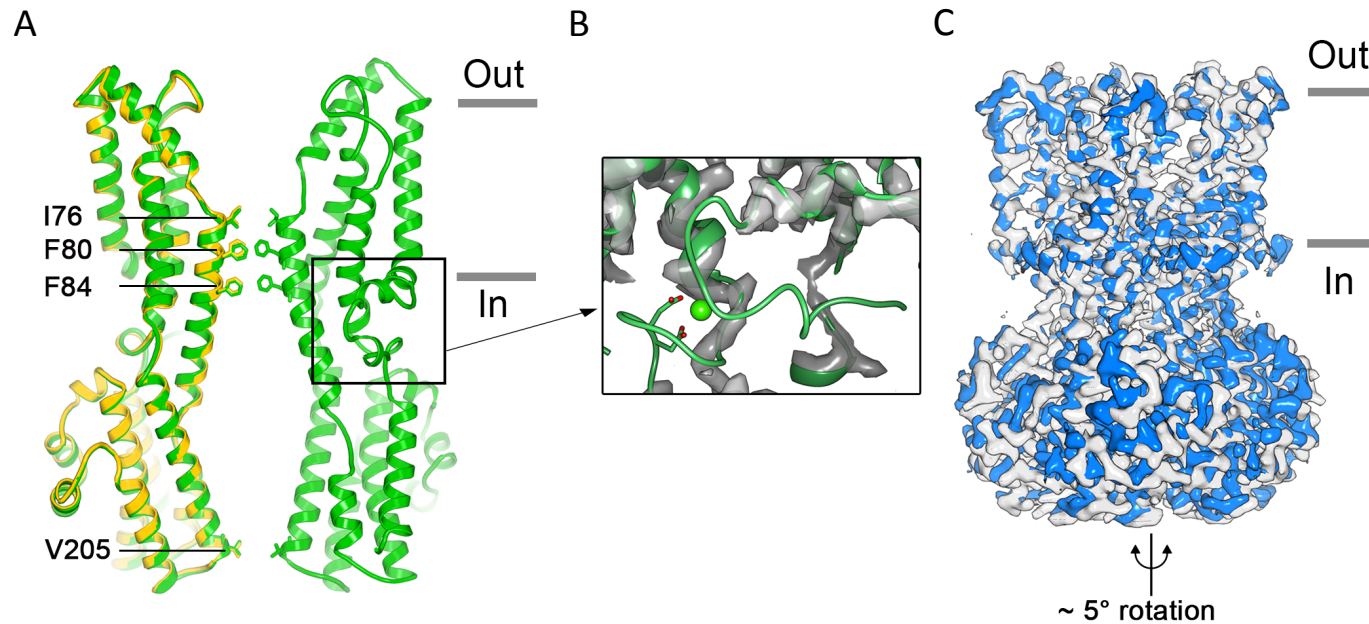
Figure 4.11. Structure of Ca^{2+}-free BEST1$_{345}$. (A) Overlay comparison of the Ca^{2+}-free conformation of BEST1$_{345}$ (yellow) with the Ca^{2+}-bound closed conformation of BEST1$_{345}$ (green). One (Ca^{2+}-free) or two (Ca^{2+}-bound) channel subunits in ribbon are shown as a cutaway from the side with the approximate boundaries of the bilayer indicated. The side chains of labeled residues are shown. The boxed area highlights the location of the Ca^{2+}-clasp. (B) Density for the Ca^{2+}-clasp is missing in the absence of Ca^{2+}. The structure of the Ca^{2+}-clasp region that is observed in the Ca^{2+}-bound closed structure (green) is shown in comparison with the cryo-EM density in this region in the Ca^{2+}-free map, showing that the density for the Ca^{2+} ion and surrounding protein residues are missing in the absence of Ca^{2+}. Ca^{2+} is depicted as a green sphere and two aspartate residues that coordinate Ca^{2+} as part of the Ca^{2+} clasp are shown as sticks. (C) Cryo-EM maps of two conformations (blue, gray) of Ca^{2+}-free BEST1$_{345}$ that were identified using 3D classification are depicted. The cryo-EM maps are aligned according to their membrane-spanning regions, with the relative rotation between the cytosolic regions indicated
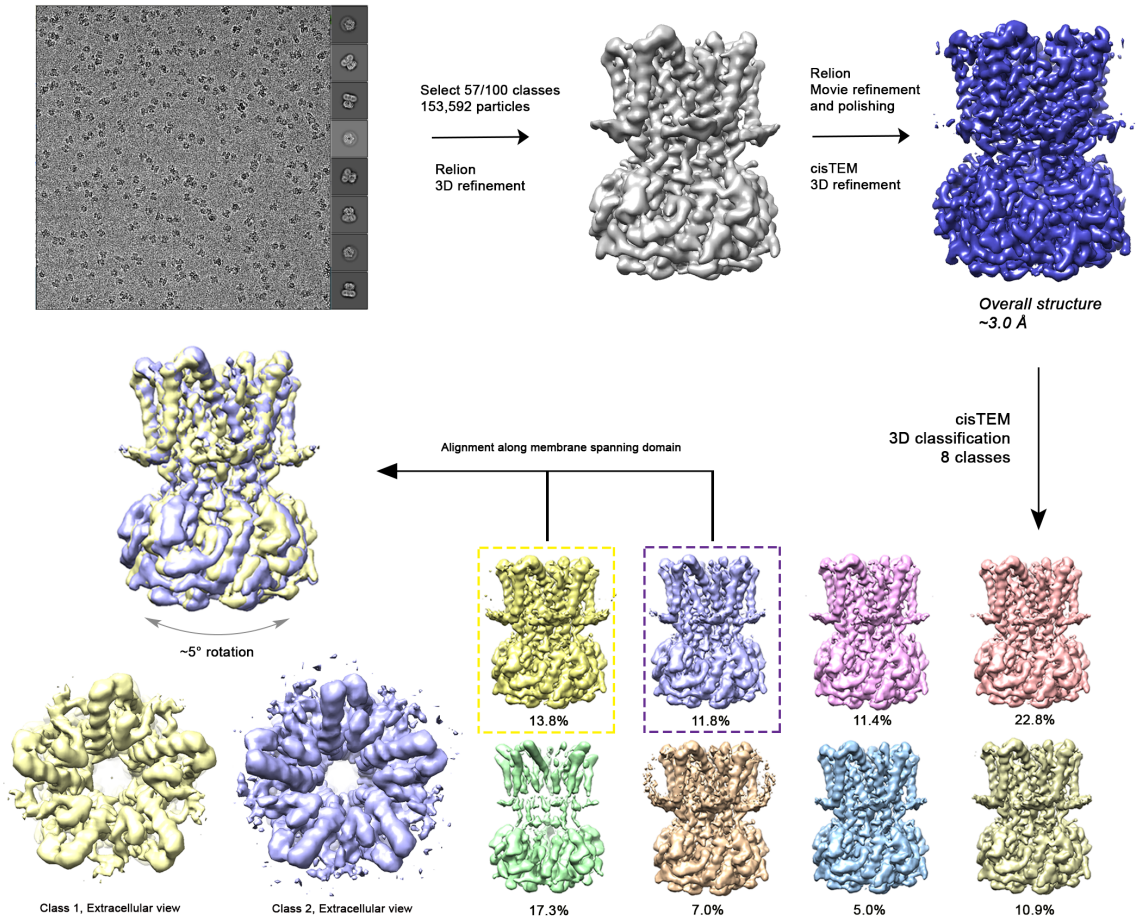
Figure 4.12. Cryo-EM workflow for Ca^{2+}-free BEST1$_{W287F}$. A detailed description of the Ca^{2+}-free BEST1$_{W287F}$ workflow can be found in the methods section. Dr Alexandria N. Miller collected, processed and analyzed this data.
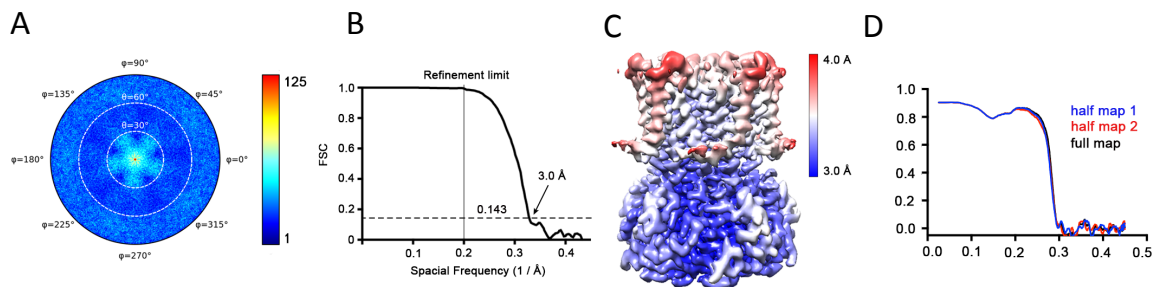
E

	Overall, Ca²⁺-free BEST1₃₄₅ W287F (EMD-XXXX) (PDB XXXX)
Data processing	
Software	RELION 2.1, cisTEM 1.0
Symmetry imposed	C5
Initial particle images (no.)	185,568
Final particle images (no.)	153,592
Overall map resolution (Å) *FSC threshold 0.143*	3.0
Map sharpening B-factor (Å²)	-50
Refinement	
Software	Phenix 1.13 real-space-refine
Initial model used (PDB code)	4RDQ
Model resolution (Å)	
FSC threshold 0.5	3.6
Model composition	
Non-hydrogen atoms	8076
Protein residues	972
Ligands	0
B factors (Å)	
Protein	
R.m.s. deviations from ideality	
Bond length (Å)	0.007
Bond angle (°)	0.77
Validation	
MolProbity score	1.47
Clashscore	4.40
Poor rotamers	0.27
Ramachandran plot statistics (%)	
Preferred	96.27
Allowed	3.73
Outliers	0

Figure 4.13. Cryo-EM structural determination of Ca^{2+}-free BEST1$_{345}$ W287F. (A) Angular orientation distribution of particles used in final reconstruction, obtained from cisTEM. The particle distribution is indicated by color shading, with blue to red representing low and high numbers of particles. (B) Gold-standard Fourier shell correlation (FSC) curve of the final 3D reconstruction. (C) Local resolution of the map estimated using Relion and colored as indicated. (D) Model validation. Comparison of the FSC curves between the model and half map 1 (work), half map 2 (free) and full map. (E) Table of data collection and model statistics for the Ca^{2+}-free BEST1$_{345}$ and Ca^{2+}-free BEST1$_{345}$ W287F.

selectivity compared to wild-type channel (Fig.4.14 B), robust Cl⁻ currents in the absence of Ca^{2+} were observed (Fig.4.14 B, C; ~80% current measured with Ca^{2+}), suggesting that $BEST1_{W287F}$ is able to adopt a conductive conformation independently of Ca^{2+}.

To confirm this, $BEST1_{W287F}$ was analyzed by single particle cryo-EM in the absence of Ca^{2+} and a structure was determined to ~ 3.0 Å (Fig.4.12, 4.13). In spite of missing density for Ca^{2+} and a disordered Ca^{2+}-clasp region, the neck also adopts an open conformation (Fig. 4.12, 4.14, 4.15). Thus, in accord with the electrophysiological recordings, the W287F mutation decouples Ca^{2+} binding from the conformational changes in the activation gate. Modeling of the W287F mutation on a closed conformation of the channel introduces a cavity behind the neck (Fig.4.15 D), which may energetically disfavor the closed conformation.

4.4.5 The open pore and the aperture

In the open conformation of BEST1, the channel pore is a remarkable ~ 90 Å continuous aqueous hole with a single constriction at the cytosolic end of the channel: the aperture (Fig.4.5 B, 4.16 A). In chicken BEST1, the aperture consists of five valine residues (V205) with their side chains directed into the pore. Mutation at this position in human BEST1 is associated with Retinitis pigmentosa disease (Davidson et al., 2009), suggesting that the aperture has an important role in channel function. The structures reveal that the aperture has the same conformation in the open and closed states (Fig. 4.5); accordingly the V205A mutation of chicken BEST1, which would be expected to widen the aperture markedly, has no effect on Ca^{2+}-dependent activation (Fig. 2.15 A and 3.9 B). Thus the aperture is not the activation of inactivation gate. Based on the narrow dimensions at the aperture, Cl⁻ and larger monovalent anions would have to be
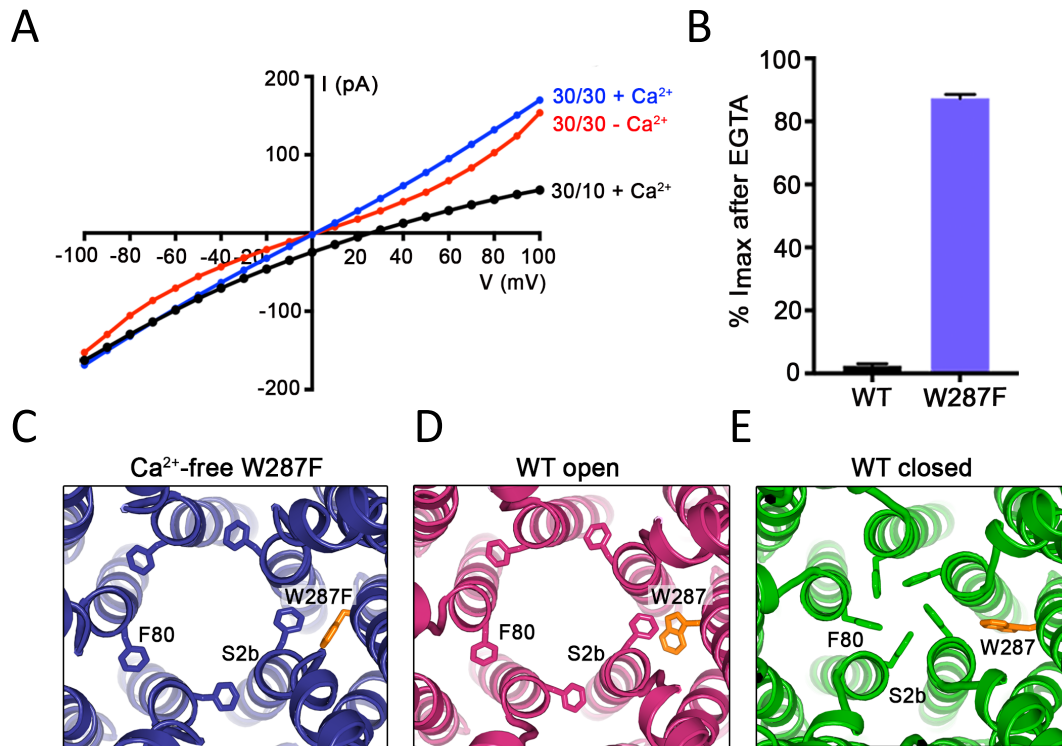
Figure 4.14. The W287F mutant decouples the Ca^{2+} ligand from the activation gate. (A-B) Dramatically reduced Ca^{2+}-dependence but normal Cl^- versus K^+ selectivity of the W287F mutant. *I-V* relationships (A) are shown for voltages stepped from -100 to +100 mV for the indicated conditions [cis/trans KCl concentration in mM, and ~ 300 nM $[Ca^{2+}]_{free}$ ($+Ca^{2+}$) or 10 mM EGTA ($-Ca^{2+}$)]. The reversal potential (E_{rev}) measured using asymmetric KCl (30/10 mM) indicates normal Cl^- versus K^+ selectivity: E_{rev} = 24.8 ± 0.8 mV for $BEST1_{345}$ W287F in comparison to 23.4 ± 0.3 mV for $BEST1_{345.}$ (B) Bar graph showing the percentage of current remaining after addition of 10 mM EGTA for $BEST1_{345}$ (WT) and the W287F mutant. I_{max} indicates the current measured at +100 mV in the presence of 300 nM $[Ca^{2+}]_{free}$. Error bars denote the SEM calculated from four (WT) or six (W287F) separate experiments. (C-E) The W287F mutant locks the neck open, even in the absence of Ca^{2+}. c, Structure of the W287F mutant in the absence of Ca^{2+}, showing the open conformation of the neck region (ribbons, cutaway view from an extracellular orientation). The W287F mutation (orange sticks) is shown for one subunit. F80 residues are drawn as sticks.
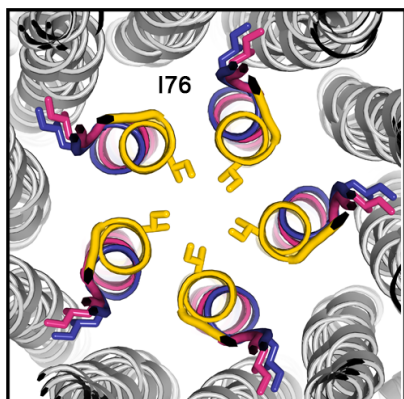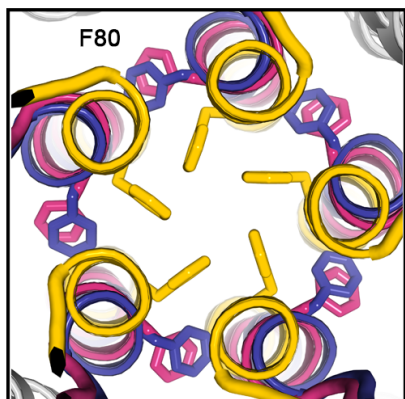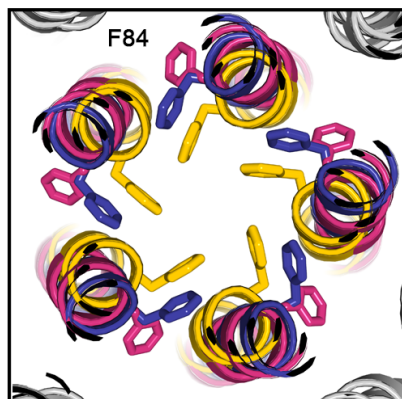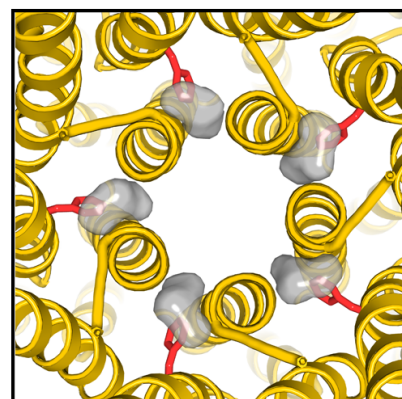
Figure 4.15. (A-C), Comparison of neck-lining residues I76, F80 and F84 between the Ca^{2+}-free W287F (dark blue), Ca^{2+}-bound open WT (pink) and Ca^{2+}-free WT (yellow) structures. Side chains of labeled residues are depicted in each panel, viewed as a cutaway from the extracellular space. Helices are represented as ribbons and those not lining the pore are colored in gray. (D), A cavity is introduced behind the neck with a hypothetical substitution of W287F in a closed BEST1 channel. Cavity (gray) was calculated as a surface representation in pymol using the Ca^{2+}-free BEST1 model (yellow). Modeled F287 is shown in sticks (red).

dehydrated as they pass through and this would give rise to the characteristic lyotropic

permeability sequence of BEST1. Consistently, I showed previously that alanine

mutagenesis of V205 abolished this permeability sequence (Fig.2.15). Surprisingly, this

residue is not fully conserved among BEST1 channel paralogs and homologs (Fig.4.16

B), hinting that amino acid identity at this position might be responsible for differences in

ion permeabilities among BEST channels. To begin to address this point, I generated

several mutations to the aperture residue of $BEST1_{345}$: V205I, V205S and V205G,

mimicking human BEST1, human BEST2 and pig BEST2, respectively, and observed

dramatic effects on the relative permeabilities of anions (Fig.4.16 C, 4.17). Mutation to

smaller or hydrophilic residues, such as glycine or serine, abolishes the lyotropic

sequence whereas mutation to the larger hydrophobic amino acid, isoleucine, increases

relative differences, with ~2 fold increases in P_{SCN}/P_{Cl} compared to wild type BEST1.

The permeability to large anions such as acetate, propionate and butyrate increases

when V205 is substituted by alanine or glycine (Fig.4.16 D, 4.18), and thus, the aperture

functions as a size-selective filter that would tend to prevent permeation of large cellular

constituents such as proteins or nucleic acids. Data suggest that the inhibitory

neurotransmitter GABA permeates through BEST1 to underlie a tonic form of synaptic

inhibition in glia (Lee et al., 2010). While this seemed incongruous with the narrowness

of the neck observed in the initial structure, the widened neck of the open conformation

and the presence of a single constriction that controls permeability make the possibility

of slow conductance of GABA or other large solutes of similar size more plausible.

Although the aperture adopts an indistinguishable conformation in all of the structures,

"breathing" (e.g. thermal motions) of the protein could allow larger ions to move through

the aperture than might otherwise fit. It is also conceivable that the binding of cellular

ligands could influence channel behavior by changing the dimensions of the aperture.
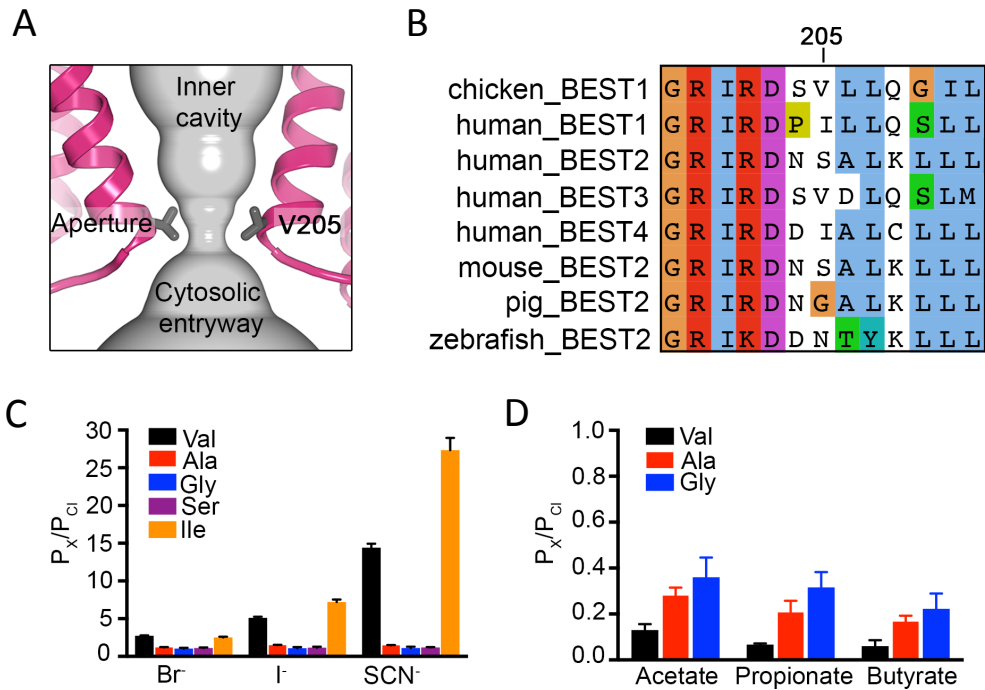
Figure 4.16. The aperture. (A) Close up of the aperture. (B) Sequence alignment around the aperture. (C-D) Mutation of V205 affects ion permeability. c, Comparison of the permeabilities of Br$^-$, I$^-$, and SCN$^-$ relative to Cl$^-$ (P_X/P_{Cl}) for wild type (Val) and the indicated mutants of V205. P_X/P_{Cl} values were calculated from reversal potentials recorded in 30 mM KCl (cis) and 30 mM KX (trans) where X is Br, I, or SCN. IV traces are shown in Extended Data Figure 10. d, Permeabilities of larger anions. Comparison of the permeabilities of acetate, propionate and butyrate relative to Cl$^-$ for wild type (Val) and the indicated mutants of V205 (calculated as in c). For c-d, error bars denote the SEM from three experiments.
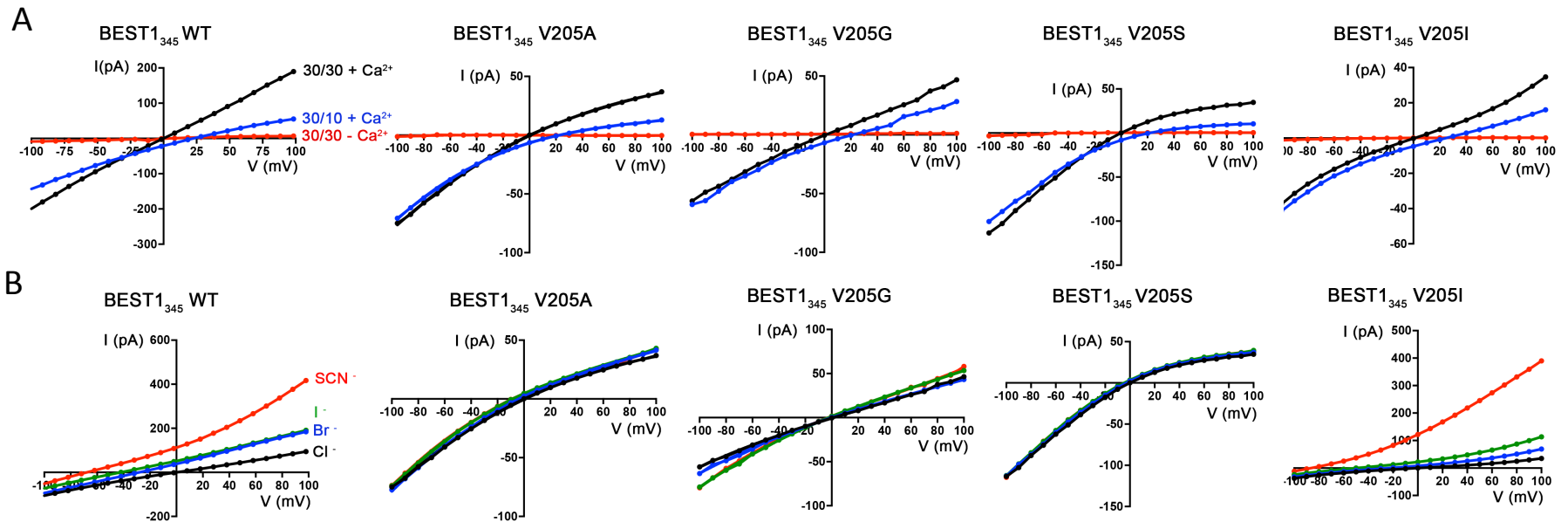
Figure 4.17. Current-voltage (I-V) relationships of BEST1 aperture mutants. (AL) All aperture mutants exhibit comparable Cl$^-$ versus K$^+$ selectivity to wild-type BEST1 and are Ca^{2+}-dependent. I-V relationships are shown for voltages stepped from -100 to +100 mV for the indicated standard conditions [cis/trans KCL concentration in mM, and ~ 300 nM Ca^{2+} (+Ca^{2+}) or 10 mM EGTA (-Ca^{2+})]. (B) Lytropoic sequence of anion permeability of wild-type and aperture mutants. After first recording using symmetric 30 mM KCl (black *I-V* trace), the solution on the *trans* side was replaced (by perfusion) with solutions containing 30 mM KBr (blue), KI (green), or KSCN (red). *I-V* traces are shown for data collected using the standard voltage protocol described in figure 2.2.
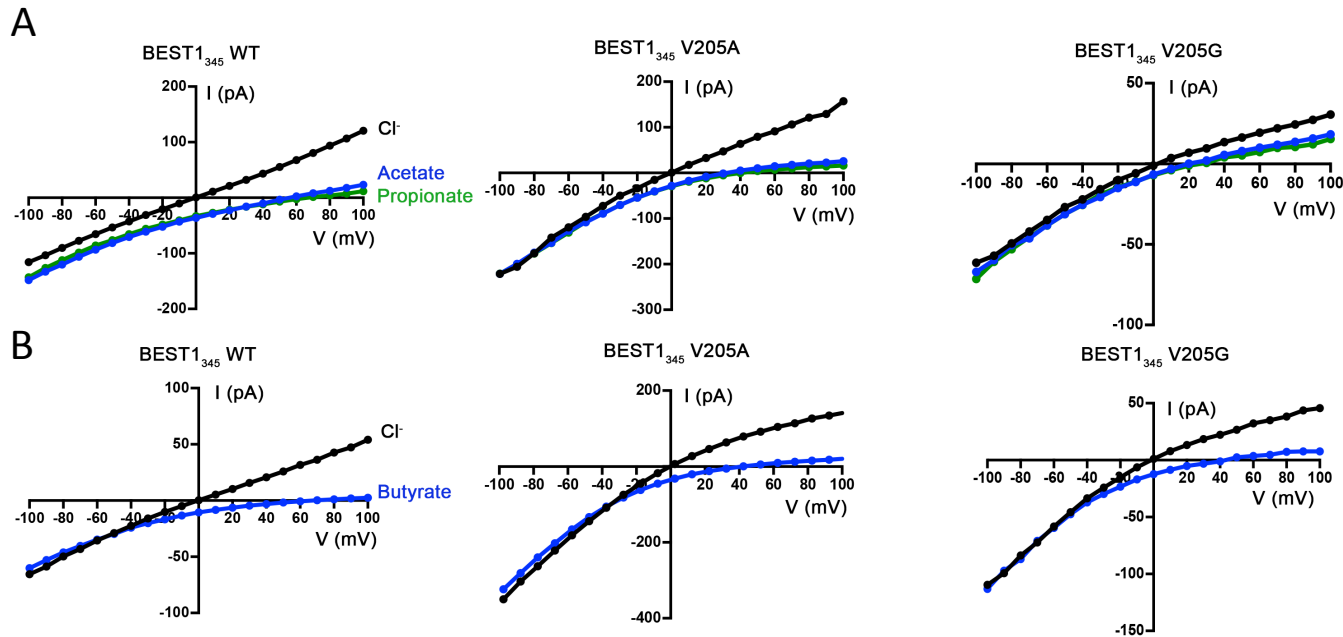
Figure 4.18. (A) Representative *I-V* relationships that were used to determine permeabilities of acetate and propionate relative to Cl⁻. Experiments were performed as in Fig. 4.16 B except that the solution on the *trans* side was replaced with a solution containing 30 mM KCH_3COO (blue) or KC_2H_5COO (green). (B) Representative *I-V* relationships that were used to determine permeabilities of butyrate relative to Cl⁻ for the indicated constructs. Experiments were performed analogously to those described in Fig. 4.16 B but used sodium salts: after recording in symmetric 30 mM NaCl (black *I-V* trace) the solution on the *trans* side was replaced with solution containing 30 mM NaC_3H_7COO (blue).

The structure of the open pore hints at a rich diversity of potential physiological functions for BEST channels that are largely unexplored.

4.5 Discussion

In this chapter I have presented high-resolution cryo-EM structures of Ca^{2+}-bound and Ca^{2+}-free BEST1 that reveal the conformational changes underlying channel gating. Using a non-inactivating mutant, I have been able to obtain the open channel structure, allowing visualization for the first time of the conductive state of BEST1. Together with electrophysiological studies of mutants discussed earlier in this thesis, a detailed description of how BEST1 opens and closes, and what parts of the channel endow it with its characteristic properties, is now possible. A schematic illustrating the mechanisms of channel activation and inactivation is shown in figure 4.19.

One challenging point is the difference between an inactivated state of BEST1 versus one that is Ca^{2+}-bound and closed (but in equilibrium between closed and open states). Electrophysiology data described in sections 2 and 3 demonstrate that the neck is both the activation and inactivation gate. So whilst we would expect the neck to be closed in both these channel states, whether it closes to the same extent is unclear. Data presented in section 3 clearly demonstrates the importance of the C-terminal tail (inactivation peptide) for channel inactivation. The truncated $BEST1_{345}$ is unable to inactivate and so we would expect that the closed conformation obtained by cryo-EM does not represent an inactivated channel state. Whilst BEST1 inactivation appears to be driven by a specific mechanism involving the inactivation peptide binding to its receptor site, ultimately this may serve to stabilize the native closed conformation of the
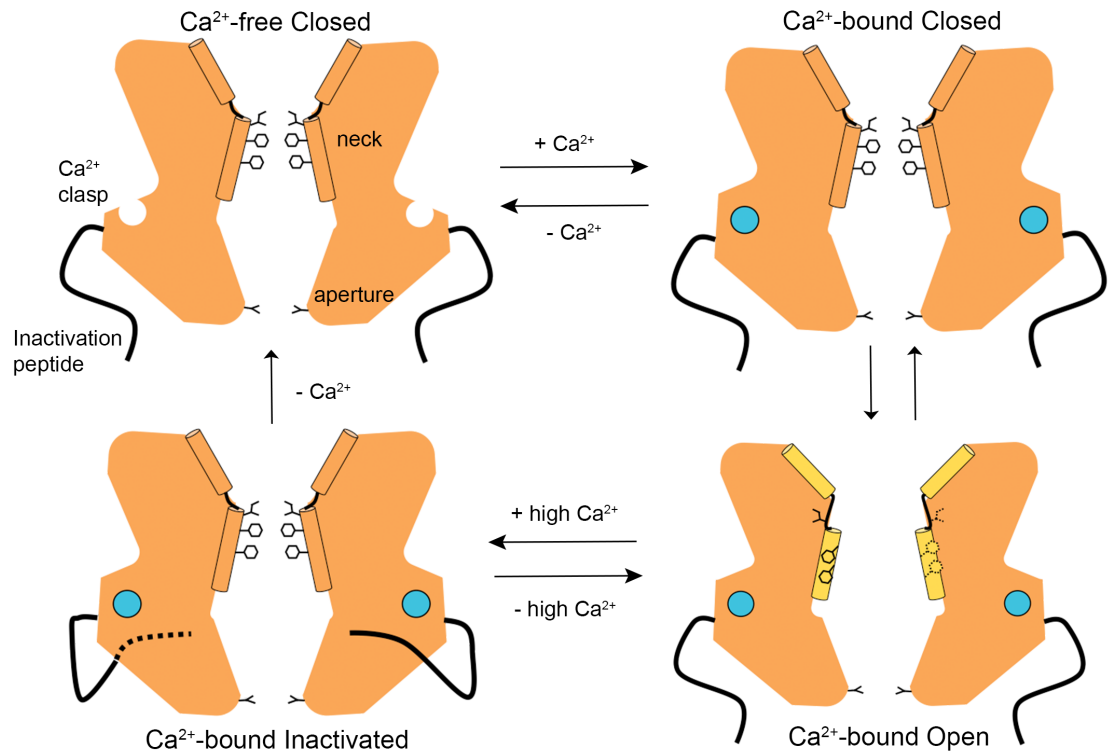
Figure 4.19. A schematic depicting Ca^{2+}-dependent gating of BEST1, with two channel subunits shown for simplicity. In the absence of Ca^{2+}, BEST1 is closed at the neck region. The Ca^{2+} clasp is disordered which results in increased flexibility of the cytosolic region relative to the transmembrane region of the channel, preventing channel opening. Ca^{2+} binding to the clasp induces local order in this region, clamping the transmembrane and cytosolic regions together. This enables channel opening, which involves extension of a tethered pore-lining helix and rotation of the hydrophobic neck residues out of the pore, reducing the energy barrier to ion permeation. In the presence of higher concentrations of Ca^{2+}, the inactivation peptide binds to its receptor site on the cytosolic surface of the channel, inducing a conformational change that causes channel closure at the neck. The aperture remains fixed between different channel conformations and acts as a bottleneck that enforces dehydration of permeating ions, giving rise to the lyotropic permeability sequence. In a biological context it may act as a size-selective filter to prevent the diffusion of larger anions, such as glutamate, into the channel pore.

channel, explaining why structures proposed to represent inactivated and closed states appear essentially identical.

The subtle overall structural changes between open and closed states suggest that the free energy difference between these conformations is minimal. This appears to be borne out in the limited single channel recordings that have been made of bestrophin. In both single-channel recordings of Drosophila BEST1 (Chien et al., 2006) and the prokaryotic homolog of bestrophin (Yang et al., 2014), current recordings appear "flickery" – that is the open dwell time of bestrophin is short (~1 ms), and the channel rapidly transitions between conductive and non-conductive states. The finding that a single conservative mutation of W287 to phenylalanine generates a channel that is essentially Ca^{2+}-independent, both in electrophysiological recordings and by cryo-EM analysis, supports the notion that the free energy difference between the closed and open states is small.

In the open conformation of BEST1, the channel pore is a continuous ~90 Å aqueous hole that for much of its length is wider than 10 Å, with the major constriction being at the aperture. It is somewhat surprising then that the single channel conductance of the channel is low, with estimations from recordings on Drosophila BEST1 being ~2 pS (Chien et al., 2006). As discussed, ions passing through the aperture would have to be dehydrated, which comes at an energetic cost, and so this constriction likely throttles the flow of ions that would otherwise be limited by the rate of diffusion. Supportively, mutation of the aperture residue I205 to alanine significantly increased macroscopic currents of human BEST1 recorded in HEK-293 cells (Yang et al., 2014).

My electrophysiological studies have clearly demonstrated the importance of the aperture residue in determining the relative permeabilities of anions. It is thus interesting that the identity of the amino acid at this position varies significantly among bestrophin homologs and paralogs. It is feasible that the amino acid identity at the aperture may encode distinct anion permeability properties suited to the distinct functions of different bestrophin channels. For example, the variability at this position between human BEST1 (isoleucine) and human BEST2 (valine) may be responsible for the ~ 2-fold increased relative permeabilitiy of HCO_3^- versus Cl^- for BEST2 compared to BEST1 (Qu and Hartzell, 2008). And this may pertain to BEST2's proposed unique role in mediating HCO_3^- transport in goblet cells (Yu et al., 2010).

Over 200 mutations in BEST1 have been associated with retinal degenerative disorders, but it is still unclear why most are disease-causing. A more detailed understanding of BEST1 channel gating and function from structural and functional data presented here enables better rationalization of how some mutations affect BEST1 activity. For example, a myriad of missense mutations associated with retinal diseases cluster behind the neck and could potentially disrupt channel gating. The neck residue mutation, F80L, is also disease-causing and is associated with reduced anion conductance in HEK cells (Chien and Hartzell, 2008; Milenkovic et al., 2011). In section 2 I showed that purified F80L displayed severely impaired activity in a Cl^- flux assay compared to wild type channel. In the open, conductive conformation, F80 faces away from the pore, and so it is unlikely that mutation to leucine reduces channel conductance. Instead, based on the apparent importance of the packing of hydrophobic residues in this region (e.g., the dramatic effect W287F has on channel activity), I hypothesize that the F80L mutation destabilizes the open conformation, reducing the open probability of the channel. Single channel recordings of this mutant would need to be performed to confirm this.

4.6. Conclusion

Together with insights from electrophysiological recordings of purified BEST1, the structural studies presented here provide an unprecedented account of BEST1 channel gating and function. We now have a better framework in which to understand how disease-causing mutation disrupt channel function and how better to design therapeutics targeted to BEST1 for treatment of retinal degenerative disorders. Further, this characterization of BEST1 is a lens through which we can begin to understand the other members of the bestrophin channel family, and how differences in sequence and structure might give rise to distinct channel properties and biological roles.

5. Chloride-dependent inhibition of BEST1

5.1 Summary

BEST1 is regulated by cell volume: increases in cell volume activate BEST1 currents whereas conditions that cause cell shrinkage lead to current decrease. The mechanism of BEST1 volume-dependent regulation is not fully understood but one possibility is that the channel responds to variations in ionic strength caused by cell volume changes. Here, using recordings of the purified channel in bilayers, I show that BEST1 currents respond specifically to the concentration of Cl^-. Higher concentrations of Cl^- leads to decreases in channel currents and this effect occurs only at the cytosolic face of the channel, in line with a mechanism whereby BEST1 responds to cell volume changes by sensing the intracellular $[Cl^-]$. This Cl^--dependent inhibition is increased at higher concentrations of Ca^{2+} and mutants that do not inactivate are either less responsive or immune to the effects of $[Cl^-]$, suggesting a link between $[Cl^-]$ sensing and Ca^{2+}-dependent inactivation of BEST1. Proximal to the inactivation peptide of BEST1 is an electrostatically positive pocket which initial data suggests may serve as a Cl^- sensing site that is tied to channel inactivation.

5.2 Background

Volume-regulated ion channels are thought to play a vital role in the regulation of cell volume (Hoffmann et al., 2009). When cells are placed into hypotonic solutions, water flows down its concentration gradient into the cell, causing swelling. The opening of volume-activated ion channels and the consequent efflux of ions alter the osomotic

gradient across the cellular membrane, causing the efflux of water and volume decrease of the cell.

Initial recordings of hBEST1 or mBEST2 heterologously expressed in cells demonstrated that Cl⁻ currents through these channels were strongly inhibited by hyperosmotic solutions and stimulated by hyposmotic solutions (Fischmeister and Hartzell, 2005). Further, Cl⁻ currents of native dBest1 in Drosophila S2 cells have been shown to be sensitive to osmolarity and RNAi-mediated knockdown of dBEST1 abolishes this sensitivity (Chien and Hartzell, 2007). More recent studies in an iPSC-based model of RPE cells demonstrate that cells derived from patients with mutations in BEST1 exhibit severely diminished Cl⁻ currents in response to cell volume-changes (Milenkovic et al., 2015). Interestingly, spermatocytes from mice, where BEST1 is highly expressed, also show reduced volume-sensitivity when taken from BEST1 knockout mice (Milenkovic et al., 2015). This suggests that while physiological roles of bestrophin channels may differ in organisms (e.g RPE in humans and sperm in mice), volume-regulation is at least one major biological purpose of these channels.

Whilst experiments clearly demonstrate hypotonicity-induced cell swelling-dependent activation of bestrophin currents, the underlying mechanism(s) responsible for this behavior is unclear. Water influx into cells has multiple consequences including changes to the local ion concentration and macromolecular crowding (Zhou et al., 2008), changes in bilayer tension (Anishkin et al., 2014; Brohawn et al., 2014b), and activation of second messenger pathways, including kinases and phosphatases (Hoffmann et al., 2009; Pedersen et al., 2015). Currently, the best evidence for a potential mechanism of volume-dependent regulation of bestrophin comes from studies of hBEST1 in HEK cells. It was shown that inhibition of hBEST1 by hypertonic solution occurs through

dephosphorylation of the S358 residue, by PP2A (Xiao et al., 2009). Ceramide, which is a PP2A activator, mimicked the effects of hypertonic solution, and an inhibitor of sphingomyelinase was shown to block the effects of hypertonic stress (Xiao et al., 2009). Together, this data suggests that hypertonic stress activates sphingomyelinase to release ceramide, which dephosphorylates S358 to cause channel inhibition. How this regulation occurs in an *in vivo* context, in the RPE for example, and whether it is the sole means of volume-dependent regulation of BEST1 remains unclear.

Direct sensing of membrane stretch in response to cell-swelling is another mechanism for volume-dependent regulation and is exemplified by the prokaryotic mechanosensitive channels of large (MscL) and small (MscS) conductance: the first mechanosensitive channels molecularly and structurally characterized (Haswell et al., 2011; Kung, 2005; Kung et al., 2010; Walton et al., 2015). In microbes, these channels function as safety release valves to protect cells from osmotic shock, for example as a result of rain, by responding to elevated membrane tension and opening large nonselective and high-conductance pores that release solutes. Patch clamp electrophysiology and X-ray crystallographic structure determination have led to physical models for mechanosensation of these channels whereby force activation, transmitted directly through the membrane, is a result of shape changes between the open and closed conformations that make the open state more favorable in the presence of tension (Chang et al., 1998; Lai et al., 2013; Moe and Blount, 2005; Sukharev et al., 1994; Wang et al., 2008; 2014). Experiments to assess membrane stretch-activation of bestrophin channels, such as cell poking assays or patched membrane stretching (Besch et al., 2002; Del Mármol et al., 2018; Hao and Delmas, 2011) do not appear to have been conducted. The possible mechanosensation of BEST1, based on structural observations, is discussed in section 5.5.

A less explored mechanism of volume-dependent regulation involves changes to ionic strength. As water flows into a cell during swelling, the local concentration of ions is decreased, which in turn could modulate channel activity. Activation of swell-induced Cl^- currents by decreases to intracellular ionic strength was first demonstrated in Chinese hamster ovary cells and bovine endothelial cells (Cannon et al., 1998; Nilius et al., 1998; Sabirov et al., 2000). More recently, studies of the volume-regulated leucine-rich repeat-containing protein 8A (LRRC8A) in a reconstituted system, without cellular components, have demonstrated clear channel activation by reduction of ionic strength (Syeda et al., 2016). How these channels sense ionic strength remains unknown.

Here, using recordings of purified channel in bilayers, I ask how BEST1 currents are regulated by [Cl^-] and discuss my findings in the context of volume-dependent regulation of the channel.

5.3 Materials and methods

5.3.1 Electrophysiological recordings

BEST1 protein was expressed and purified as described in sections 2.3.1 and 2.3.2. The planar lipid bilayer setup and standard solutions used for recording are described in section 2.3.3. Details of individual electrophysiology experiments are described in figure legends.

5.4 Results

5.4.1 Cytosolic Cl⁻-dependent inhibition of BEST1 currents

For the first recordings I made of purified BEST1 in bilayers, I used starting conditions of

300 mM KCl *cis* and 30 mM KCl *trans.* This was based on similar types of experiments

from other groups, where higher salt concentrations are used to maximize current signal

(Accardi et al., 2004; Lee et al., 2013). Whilst I was able to observe currents in these

starting asymmetric solutions, upon making the solutions symmetric (300 mM KCl *cis*

and *trans*) the currents would decrease almost to zero. This result suggested that the

higher salt concentration was in fact inhibiting BEST1 currents and that initial currents

could be obtained because some of the channels, due to their orientation in the bilayer,

were not inhibited by the lower, 30 mM KCl solution. To test this hypothesis, I added 10

mM EGTA, chelating free Ca^{2+}, first to the *cis* side, containing 300 mM KCl, and then to

the *trans* side, containing 30 mM KCl, to deactivate channels. As figure 5.1 A shows,

addition of EGTA to the *cis* side had a negligible effect on current level, whilst adding

EGTA to the *trans* side essentially brought the current to zero. This observation indicates

that channels with their cytosolic region facing the *cis* side are already inhibited by the

300 mM KCl, and so chelating Ca^{2+} has no effect. Therefore, the majority of the current

being recorded is from those channels with their cytosolic region facing the *trans* side of

the bilayer, where there is only 30 mM KCl. Only after addition of EGTA to the *trans* side,

to deactivate these channels, does the current decrease to near zero.

To address whether this observation was due to differences in overall ionic strength or

the concentration of a particular ion, I carried out the same experiment with different salt

162
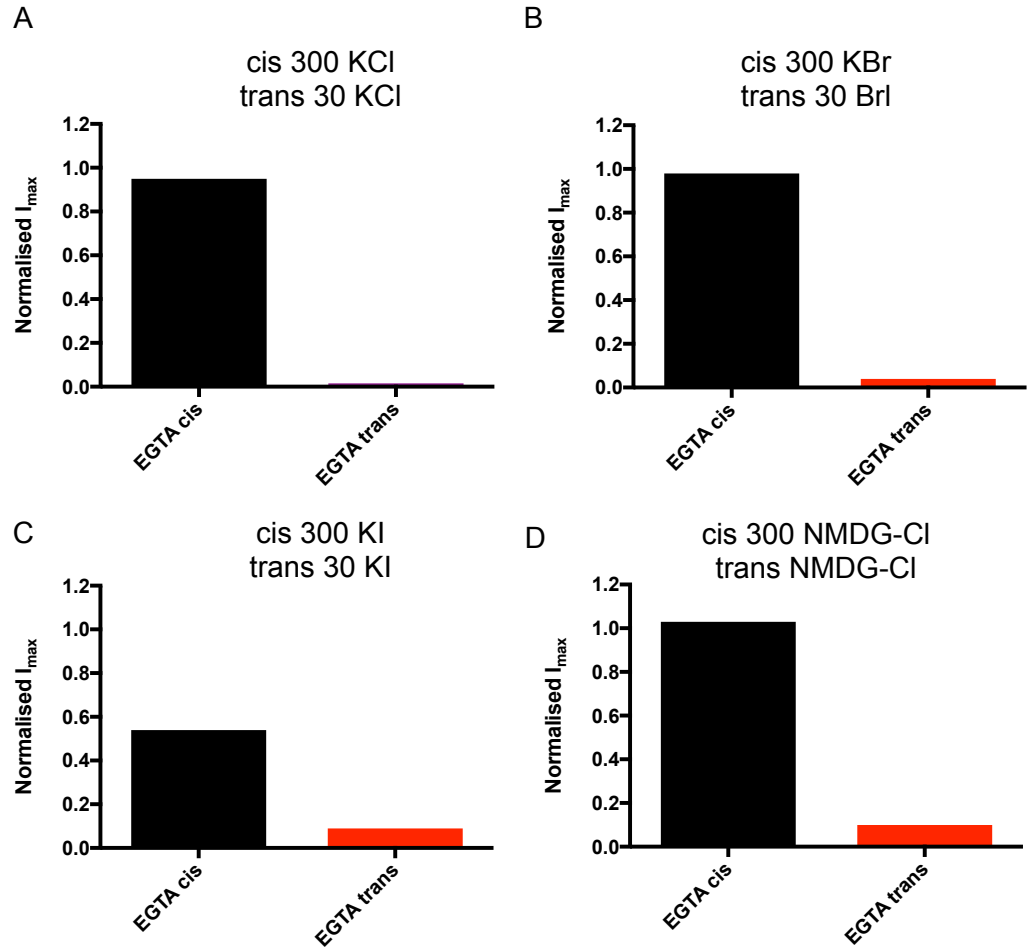
Figure 5.1. High concentrations of Cl$^-$ inhibit BEST1 currents. (A-D) With ~300 nM Ca^{2+} on both sides of the membrane, currents were measured using asymmetric salt conditions (300 mM *cis* and 30 mM *trans*), where the salt is indicated, using the same voltage pulse protocol described in figure 2.2. 10 mM EGTA was then added to either the *cis* or *trans* side and after recording currents with the same protocol, normalized I$_{max}$ was calculated as the current value at -100 mV after the addition of EGTA as a fraction of the current value before.

A

KCl

B

KBr

C

KI
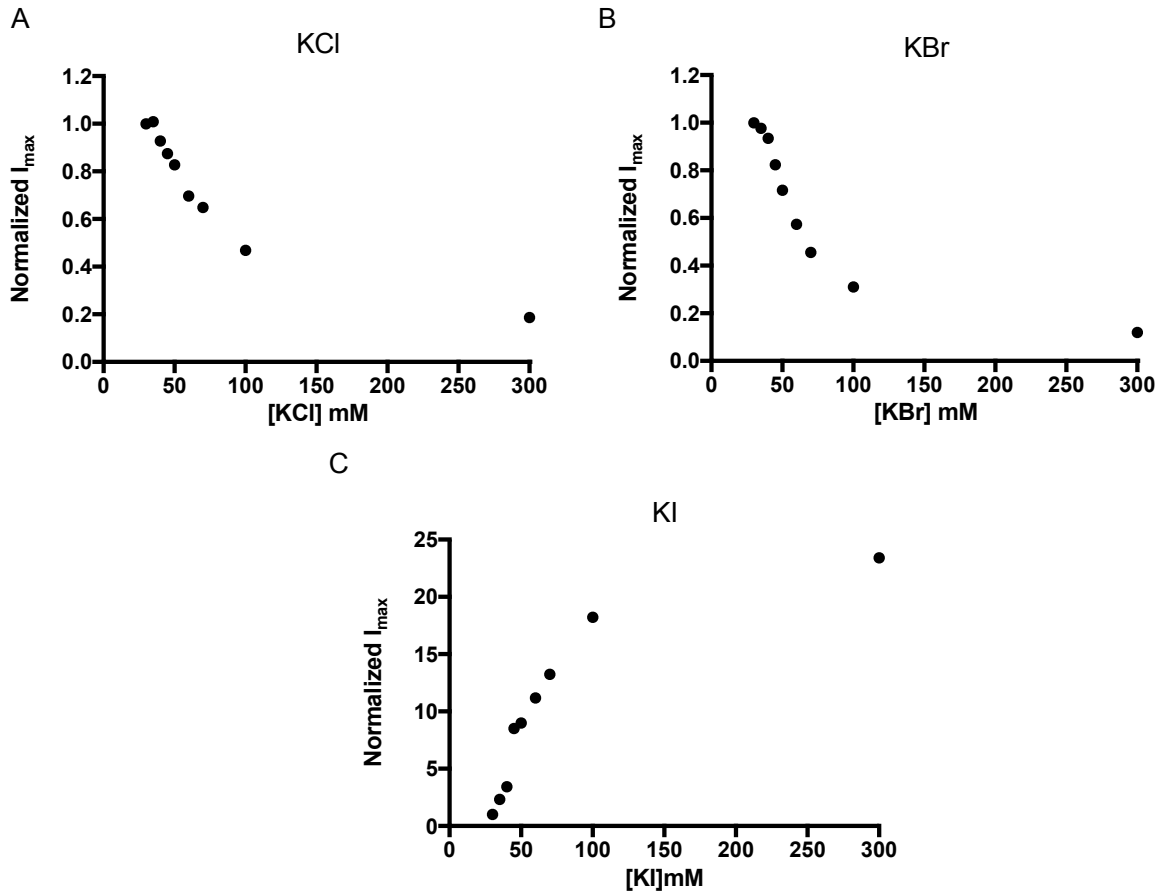
Figure 5.2. Concentration dependence of anion-mediated inhibitory effects on BEST1 currents. (A-C) With ~300 nM Ca^{2+} on both sides of the membrane, currents were measured in symmetric salt conditions, where the salt is indicated, using the same voltage pulse protocol described in figure 2.2. Normalized I_{max} was calculated as the current value at -100 mV for each recording at the indicated [salt] as a fraction of the current value in 30 mM salt conditions.

conditions (Fig.5.1). In the analogous experiment with KBr, I observe the same result, whereby adding EGTA only to the *trans* side, with lower [KBr], significantly reduces the current (Fig.5.1 B). By contrast, when recording in solutions containing KI, chelation of Ca^{2+} to the *cis* side reduces the current level by ~ 50%, with the remaining current being reduced after addition of EGTA to the *trans* side (Fig.5.1 C). This data indicates that like KCl, 300 mM KBr has an inhibitory effect on BEST1 channels oriented with their cytosolic regions facing this solution, whereas KI does not. Therefore, it appears that the identity of the anion is important for whether or not this inhibition is observed, since K^+ is present in all solutions. The similar effects observed for Br^- and the biologically relevant Cl^- may be due to their more comparable hydrated and dehydrated ionic radii compared to I^- (Tansel, 2012). Confirming that this effect appears to be predominantly determined by the anion present, I find that replacing K^+ with the much larger N-methyl-D-glucamine (NMDG) gives the same results as when recording solutions containing KCl (Fig.5.1 D).

To more specifically probe the concentration-dependence of this effect, I titrated the levels of salt on both sides of the bilayer and recorded currents in a stepwise manner (Fig.5.2). At concentrations of KCl greater than 35 mM the current decreases (Fig.5.2 A). Although the exact fluctuations of local [Cl^-] that BEST1 would experience during cell volume changes are unknown, it is worth noting that this concentration range is within that estimated for cells (Hille, 2001), particularly the RPE, where the overall intracellular concentration of Cl^- is thought to reach at least 60 mM (Wimmers et al., 2007). A similar titration curve is observed for KBr, whereas current levels increase dramatically as the concentration of KI is increased, consistent with data in figure 5.1.
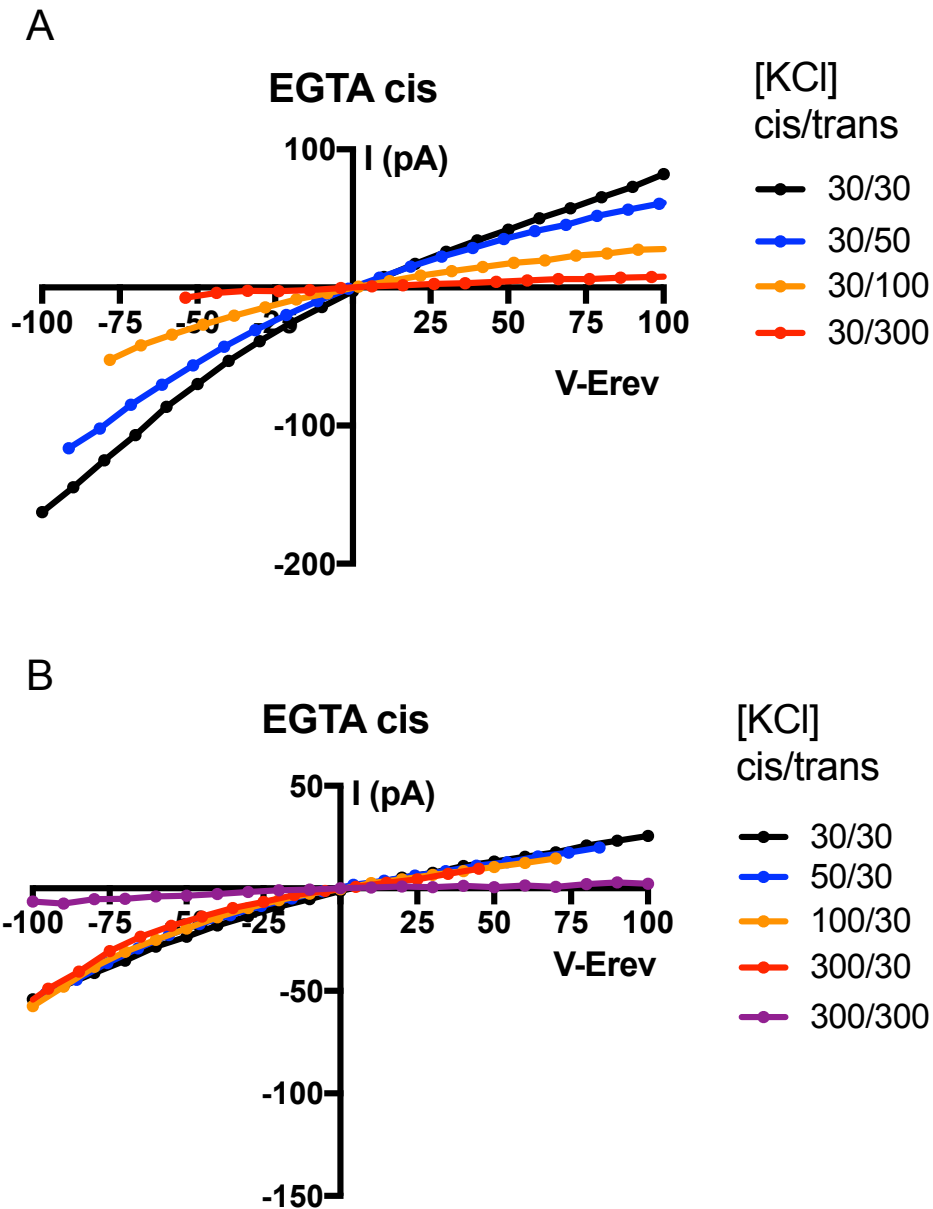
Figure 5.3 The cytosolic region of BEST1 responds to higher [Cl⁻]. With 10 mM EGTA on the *cis* side to deactivate channels with their cytosolic side facing this way (~0 $[Ca^{2+}]_{free}$), and ~ 300 nM Ca^{2+} on the *trans* side, currents were measured first in symmetric KCl conditions, using the same voltage pulse protocol described in figure 2.2. The [KCl] was then titrated either on the *cis* side or the *trans* side and currents recorded. To control for shifts in reversal potential (E_{rev}) caused by recording in asymmetric solutions, the voltage applied minus E_{rev} (V-E_{rev}) is plotted on the x axis.

To confirm that the cytosolic region of BEST1 is responsible for sensing increases in [Cl⁻]

I recorded currents through only those channels oriented with their cytosolic region

facing the *trans* side of the bilayer. To do this, I added EGTA to the *cis* side, to

deactivate BEST1 channels with their cytosolic region facing this way. I then added KCl

in a stepwise manner either to the same (*cis*) or opposite (*trans*) side. We can see in

figure 5.3 that increasing the [Cl⁻] on the *trans* side leads to stepwise decreases in

currents, indicating that as the [Cl⁻] on the cytosolic side of the channel increases, the

channel is inhibited (Fig.5.3 A). By contrast, increasing [Cl⁻] on the cis side, where those

channels I am recording from have their extracellular regions oriented, does not cause

current decrease (Fig.5.3 B). Making solutions contain symmetric 300 mM KCl at the

end of the experiment brings the currents to almost zero. Inhibition of BEST1 specifically

by changes to intracellular [Cl⁻] levels is consistent with a mechanism of volume

regulation whereby decreases in cell volume as water flows outwardly cause an increase

in the local intracellular salt concentration.

5.4.2. A link between [Cl⁻] and Ca^{2+}-dependent inactivation

There are multiple ways that increases in cytosolic [Cl⁻] could lead to decreases in

BEST1 currents. For example, Cl⁻ ions might act as permeant blockers in a directional

manner, where only ions entering from the cytosolic side of the channel become trapped

within the ion pore and cause blockade. Cl⁻ ions could also bind to a specific site on

BEST1, biasing the conformational state of the channel to one that is less conductive or

has a reduced open probability. Since inactivation of BEST1 appears to be a mechanism

of channel regulation coordinated by multiple signals, such as rises in cytosolic [Ca^{2+}]
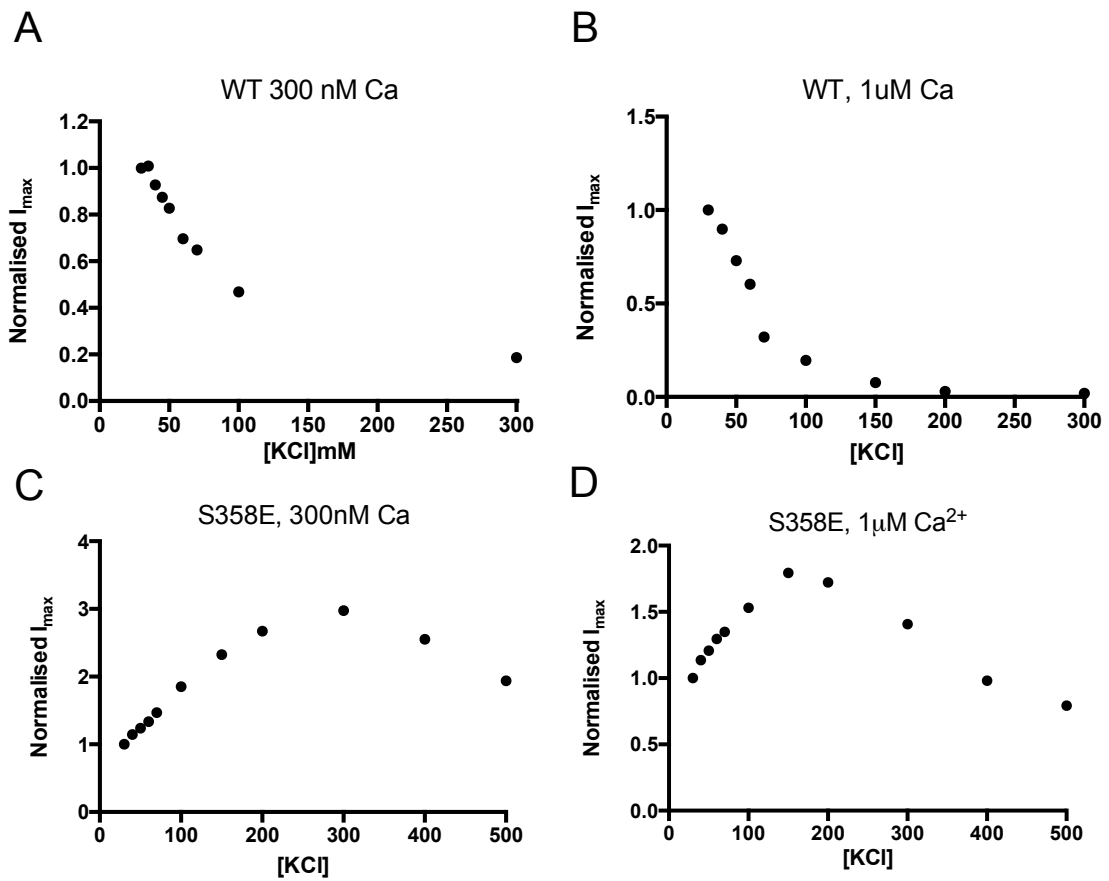
Figure 5.4. Effect of $[Ca^{2+}]_{free}$ on Cl^- dependent current decrease. (A-D) With either ~300 nM Ca^{2+} (A and C) or 1µM Ca^{2+} (B and D) on both sides of the membrane, currents were measured in symmetric salt conditions, with stepwise increases in [KCl], as indicated, using the same voltage pulse protocol described in figure 2.2, for either $BEST1_{WT}$ (A and B) or $BEST1_{S358E}$ (C and D). Normalized I_{max} was calculated as the current value at -100 mV for each recording at the indicated [KCl] as a fraction of the current value in 30 mM KCl conditions.

and phosphorylation (section 3) (Xiao et al., 2008; 2009), I wanted to explore whether the effects of [Cl⁻] might be linked to this behavior.

I have shown previously that the rate and extent of Ca^{2+}-dependent inactivation of BEST1 are increased at higher [KCl] (Fig.3.2), which we can now attribute to increased [Cl⁻]. Another way to study this relationship is to look at steady state current levels at different $[Ca^{2+}]_{free}$ as the [Cl⁻] is titrated. For BEST1$_{WT}$, the inhibitory effect of increasing [Cl⁻] is greater at 1 µM $[Ca^{2+}]_{free}$ compared to ~ 300 nM $[Ca^{2+}]_{free}$ (Fig.5.4 A,B). Whilst recordings were made in a timeframe where I would not expect significant inactivation at 1 µM $[Ca^{2+}]_{free}$, this data does not necessarily rule out that [Cl⁻] and $[Ca^{2+}]$ affect separate behaviors of BEST1. To further explore a possible relationship between [Cl⁻] and $[Ca^{2+}]$, I performed analogous experiments with BEST1$_{S358E}$, which I have shown does not experience Ca^{2+}-dependent inactivation in the conditions that I have tested (Fig.3.4). In conditions containing ~ 300 nM $[Ca^{2+}]_{free}$, BEST1$_{S358E}$ currents increase monotonically as the [Cl⁻] is raised to 300 mM (Fig.5.4 C), consistent with a channel not inhibited by its permeant ion (Hille, 2001). At concentrations of Cl⁻ above 300 mM, however, the current begins to gradually decrease. Thus, compared to BEST1$_{WT}$, the non-inactivating mutant BEST1$_{S358E}$ is much more resistant to the effects of increasing [Cl⁻], indicating a relationship between [Cl⁻] and Ca^{2+}-dependent inactivation of BEST1. In further support of this, at 1 µM $[Ca^{2+}]_{free}$ the relationship between the current level and [Cl⁻] for BEST1$_{S358E}$ is shifted to the left, with currents decreasing at ~ 150 mM Cl⁻ (Fig.5.4 D). It therefore appears that the rate and extent of BEST1 inactivation are tuned by both the $[Ca^{2+}]_{free}$ and the [Cl⁻].
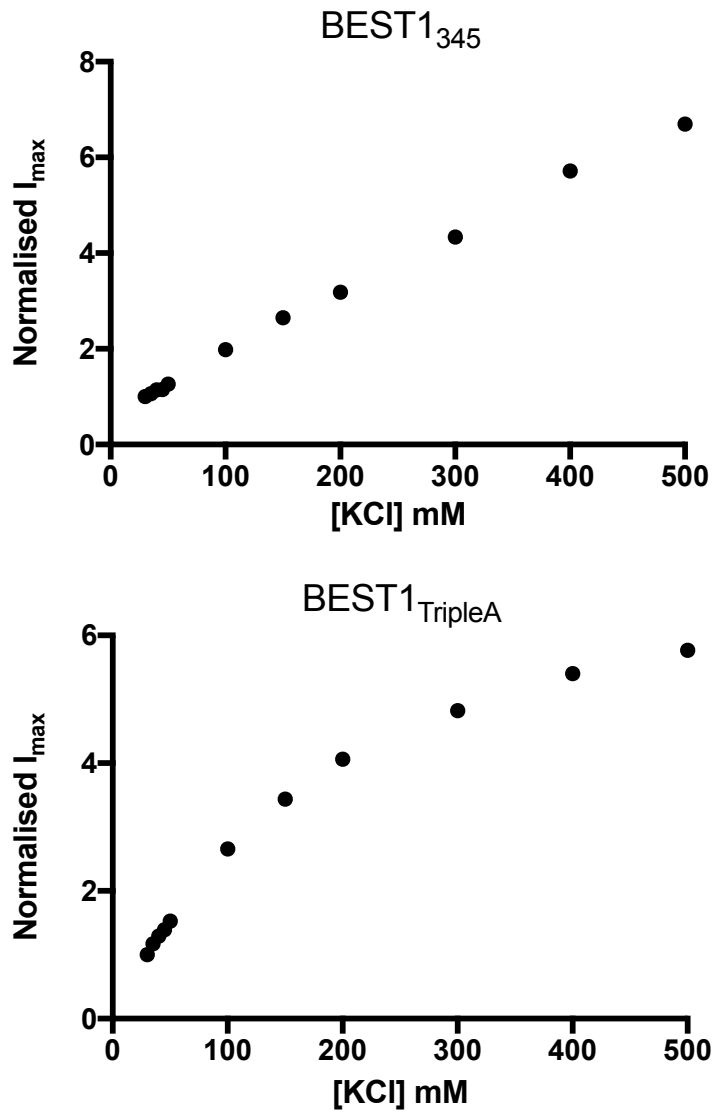
Figure 5.5. Effect of [Cl⁻] currents recorded from $BEST1_{345}$ and $BEST1_{TripleA}$. With 1 µM Ca^{2+} on both sides of the membrane, currents were measured in symmetric salt conditions, with stepwise increases in [KCl], as indicated, using the same voltage pulse protocol described in figure 2.2, for either $BEST1_{345}$ (above) or $BEST1_{TripleA}$ (below). Normalized I_{max} was calculated as the current value at -100 mV for each recording at the indicated [KCl] as a fraction of the current value in 30 mM KCl conditions.

I have shown that BEST1$_{S358E}$ is likely resistant to Ca^{2+}-dependent inactivation because this mutation disrupts the interaction of the inactivation peptide with its receptor site (Fig.3.4, 3.8). Increasing both [Cl$^-$] and [Ca^{2+}]$_{free}$ may help to stabilize the interaction of the inactivation peptide and the receptor site, even in the context of the S358E mutant, explaining why currents through this mutant decrease at higher concentrations of [Cl$^-$]. In support of this hypothesis, when I remove the inactivation peptide altogether (BEST1$_{345}$) or disable the inactivation gate (BEST1$_{TripleA}$), increasing [Cl$^-$] up to 500 mM, even at 1 µM [Ca^{2+}]$_{free}$, does not lead to current decrease (Fig.5.5).

How might [Cl$^-$] affect inactivation of BEST1? On the surface of the BEST1 channel, proximal to the inactivation peptide, is an exposed electrostatically positive pocket (Fig.5.6 A). This positively charged surface-exposed region is predominantly formed by the sidechain of R141, and the nearby K180 likely also contributes (Fig.5.6 B). Mutation of R141 to alanine does not affect the Cl$^-$ versus K$^+$ selectivity of the channel (E$_{rev}$ = 24 mV in conditions containing 30 mM KCl on the *cis* side and 10 mM KCl on the *trans* side), and the channel requires Ca^{2+} for activation (Fig.5.6 C). However, in conditions containing 1 µM [Ca^{2+}]$_{free}$, BEST1$_{R141A}$ currents are much more resistant to the effects of [Cl$^-$] compared to BEST1$_{WT}$, with currents not decreasing until ~ 150 mM Cl$^-$ is present (Fig.5.6 D). This is the first indication that R141 may form part of a binding site that interacts with Cl$^-$, which in turn affects inactivation of BEST1. In further support of a link between [Cl$^-$] and Ca^{2+}-dependent inactivation of BEST1, in conditions containing 30 mM KCl and 50 µM [Ca^{2+}]$_{free}$, the rate and extent of inactivation for BEST1$_{R141A}$ is significantly diminished compared to BEST1$_{WT}$ (Fig.5.6 E).
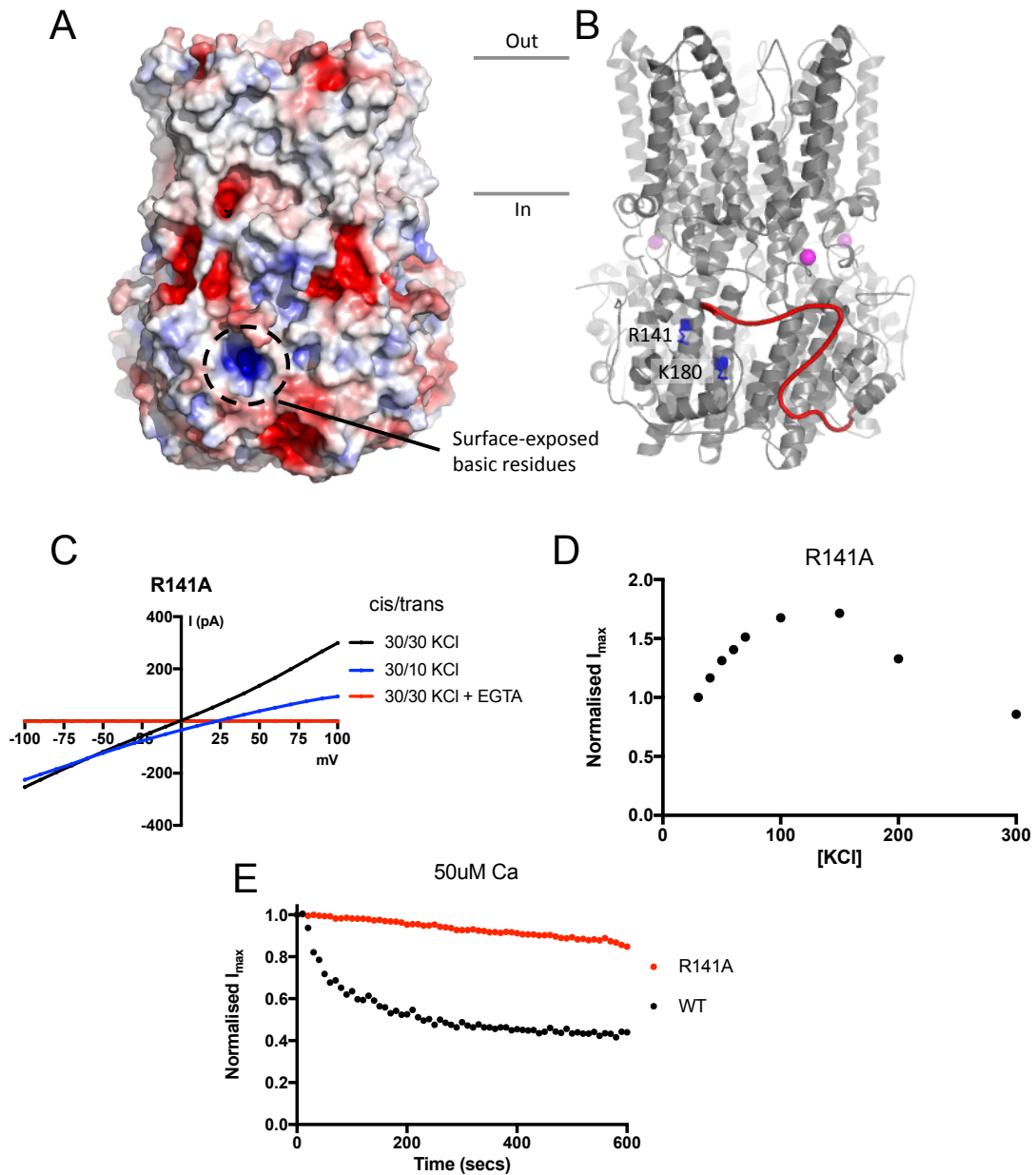
Figure 5.6 Surface-exposed basic residues proximal to the inactivation peptide may form a [Cl⁻] sensing site. (A) Surface representation of BEST1 colored by electrostatic potential; red, $-5kT\,e^{-1}$; white, neutral, blue, $+5kT\,e^{-1}$. (B) Structure of BEST1 with same perspective as in *A*. The inactivation peptide of one subunit is shown in red and basic residues corresponding to the electropositive surface-exposed region are annotated. (C) Example *I-V* relationships are shown for voltages stepped from -100 to +100 mV for BEST1$_{R141A}$ with conditions annotated. (D) In conditions containing 1µM Ca²⁺, currents were measured in symmetric salt conditions, with stepwise increases in [KCl], as indicated, using the same voltage pulse protocol described in figure 2.2. (E) Ca²⁺-dependent inactivation of BEST1$_{WT}$ and BEST1$_{R141A}$ in 50 µM Ca²⁺ conditions. Experiments were carried out as in figure 3.1. Experiments (C-E) were performed by a graduate student, Ellen Horste.

5.5 Discussion

In this chapter I have investigated the effects of [Cl⁻] on BEST1 channel activity.

Studying purified BEST1 protein in bilayers I have shown that concentrations of [Cl⁻]

greater than ~ 30 mM have an inhibitory effect on channel currents. This concentration

of [Cl⁻] is physiologically relevant (Hiller, 2001; Wimmers et al., 2007) and, as discussed

in chapter 3, this behavior could explain why recordings of BEST1 expressed in HEK

cells, in which 146 mM Cl⁻ is used, show faster current rundown (Xiao et al., 2008)

compared to my experiments of BEST1 in bilayers, with 30 mM Cl⁻.

Experiments in which [Cl⁻] is added to only one side of the channel clearly demonstrate

that it is the cytosolic region of BEST1 that senses and responds to increases in [Cl⁻].

Importantly, this is consistent with a proposed mechanism of volume-regulation whereby

BEST1 would be regulated by changes in intracellular [Cl⁻] that arise as the cell volume

increases or decreases, depending on the osmotic gradient across the cell membrane.

This mechanism of volume-regulation is similar to that established for the LRRC8 family

of channels. Studies of the volume-regulated LRRC8 channel in cells and reconstituted

systems show that increases in the intracellular ionic strength cause a decrease in

currents (Deneka et al., 2018; Syeda et al., 2016). How these channels sense ionic

strength, and indeed whether they sense ionic strength generally or the concentration of

a specific ion, remains unclear. For BEST1, my experiments demonstrate clearly that it

is specifically [Cl⁻] that causes current decrease. Nevertheless, how [Cl⁻] inhibits the

BEST1 channel, such as by pore blockade or inducing conformational changes that

decrease the channel open probability, is unknown.

Initial investigations presented here indicate a link to the C-terminal tail, or inactivation peptide, of BEST1. Along with previous studies and data presented here, evidence is mounting that the C-terminal tail of bestrophins is an important regulatory nexus, and that its ability to mediate inactivation is controlled by $[Ca^{2+}]$, phosphorylation and now likely $[Cl^-]$ (Qu et al., 2007; Xiao et al., 2008; 2009). Currents through the $BEST1_{S358E}$ mutant, which is resistant to Ca^{2+}-dependent inactivation, are much less sensitive to $[Cl^-]$ than $BEST1_{WT}$. Mutations that remove the inactivation peptide altogether ($BEST1_{345}$) or disable the inactivation gate ($BEST1_{TripleA}$) abolish the effect of $[Cl^-]$, supporting the hypothesis that increases in cytosolic $[Cl^-]$ may stimulate inactivation of the channel. One possible mechanism for the effects of $[Cl^-]$ involve a surface-exposed electropositively charged pocket, proximal to the inactivation peptide in the cytosolic region of BEST1. Mutation of a conserved arginine, R141, to alanine, significantly diminishes the effect of $[Cl^-]$, with much higher concentrations needed to cause current decrease, relative to the wild type channel. Further, in identical conditions, $BEST1_{R141A}$ inactivates to a lesser extent than $BEST1_{WT,}$ supporting the hypothesis that Cl^- sensing is linked to channel inactivation. Future studies including mutation of the nearby K180 residue and assessment of Cl^- binding to these mutants will be needed to properly characterize the role of this electrostatically positive pocket in Cl^- sensing and inactivation of BEST1.

In addition to this proposed mechanism of volume regulation, whereby BEST1 senses the intracellular $[Cl^-]$, experimental evidence indicates that phosphorylation of the channel is also a means by which the channel responds to changes in cell volume (Xiao et al., 2009). Currents of hBEST1 expressed in HEK, HeLa and ARPE-19 cells are inhibited when these cells are placed in hypertonic solutions, which cause cell shrinkage (Fischmeister and Hartzell, 2005). Additional studies have shown that pretreating these cells with phorbol 12-myristate 13-aceatate (PMA), an activator of PKC, or okadaic acid

(OA), an inhibitor of PP2A, reduces the inhibition caused by hypertonic solutions (Xiao et al., 2009). Further, in the context of the S358E mutant, which approximates a phosphorylated hBEST1, hypertonic inhibition of hBEST1 currents is abolished (Xiao et al., 2009). What is the link between cell volume decrease and phosphorylation of hBEST1? Ceramide is an important lipid secondary messenger involved in many cellular responses to diverse external stimuli, including cell volume changes (Kolesnick and Krönke, 1998; Ruvolo, 2001) and has been shown to activate PP2A (Dobrowsky et al., 1993). Indeed, addition of ceramide to HEK cells expressing hBEST1 inhibited currents similarly to hypertonic solution exchange, and this effect could be prevented by addition of OA or in the context of the S358E mutant (Xiao et al., 2009). Thus, changes to cell volume regulate BEST1 activity through signaling mechanisms, such as the release of ceramide during cell shrinkage, that alter the phosphorylation state of the channel. Together with data presented here, the inactivation peptide, and its binding to its receptor site, which is disrupted by phosphorylation, appears to be an important regulatory mechanism of the channel that may be responsible for volume-sensitivity of BEST1.

An additional mechanism by which channels may respond to cell volume changes is through sensitivity to membrane stretch that occurs as a result of cells expanding (Hoffmann et al., 2009). Experiments to assess whether bestrophin channels can be activated in this way, including cell poking assays or patched membrane stretching (Besch et al., 2002; Del Mármol et al., 2018; Hao and Delmas, 2011) do not appear in the literature, but my structural findings, presented in section 4, hint at the possible mechanosensation of BEST1. The archetypal models for understanding mechanosensation are the prokaryotic membrane-stretch regulated ion channels MscL and MscS (Haswell et al., 2011). A combination of electrophysiological and structural

studies has given a description of channel mechanosensation that depends on a conformational equilibrium of structural states that is sensitive to membrane tension. Thus, mechanosensitive channels can be described by a tension-dependent equilibrium between two states, closed (C) and open (O), that differ in conductance (Haswell et al., 2011; Sukharev et al., 1997), as described below:

$$C \overset{K}{\leftrightarrow} O$$
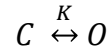
where K is the equilibrium constant between closed and open states in the absence of tension. An important structural parameter related to this is the cross-sectional area difference between the membrane-spanning regions of the conformational states of the channel, where $\Delta A = A_{open} - A_{closed}$. If ΔA is nonzero, then the contribution of membrane tension σ to the free energy of channel opening ΔG can be considered as:

$$\Delta G = \Delta G^{o} - \sigma \Delta A,$$

where $\Delta G^{o} = -RT \ln K$ is the standard free energy for channel opening (Haswell et al., 2011). As the equation above describes, the larger the value of ΔA, the greater the shift in equilibrium in response to tension and the more mechanosensitive the channel. The key determinant of whether a channel is mechanosensitive is the ability to transition between closed and open states at physiologically relevant tensions (where $\sigma \Delta A$ is roughly the energy difference between conformations in the absence of tension). The rupture point of membrane patches sets the upper limit on the tension required to gate mechanosensitive channels, and this is typically 20-30 mN m^{-1} (Haswell et al., 2011). Studies of MscL, the best characterized mechanosensitive channel, yield values of $\sigma_{1/2}$ = 10.4 mN m^{-1} and ΔA = 20.4 nm^{2} (Chiang et al., 2004).

BEST1$_{Closed}$ BEST1$_{open}$

4.83 nM   5.0 nM
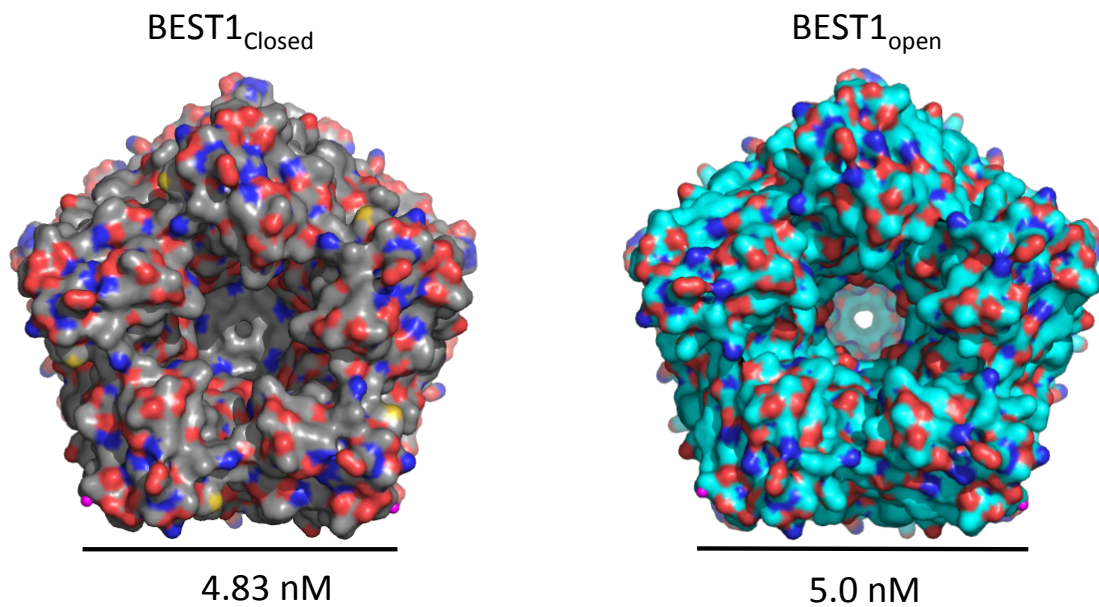
Figure 5.7. Surface representations of BEST1$_{closed}$ and BEST1$_{open}$, looking down from the extracellular side of the channel. Although crude, the cross-sections of the membrane-spanning region of these conformations may be approximated as regular pentagons, giving values for the corresponding areas of BEST1$_{closed}$ and BEST1$_{open}$ as ~ 40 and 43 nm^2, respectively.

As discussed in chapter 4, opening of the BEST1 channel involves a lateral expansion of the transmembrane helices in plane with the membrane. Looking at surface representations of the closed and open conformations from the extracellular side of the channel, I can crudely estimate the cross-sectional areas of the membrane-spanning regions analogously to measurements made for MscL (Haswell et al., 2011) (Figure 5.7). Depending on the section of the membrane-spanning region, estimated ΔA vaues are 1.2-3 nM^2 between the closed and open structures of BEST1 (Figure 5.7).

This change in cross-sectional area is much smaller than values for MscL (Chiang et al., 2004; Haswell et al., 2011). It is, however, comparable to values calculated for the mechanosensitive two-pore domain potassium (K2P) channels, of which there are multiple crystal structures (Brohawn et al., 2013; 2012; Dong et al., 2015). The area expansion for the open and closed states of these channels is approximated to be ~ 2.7 4.7 nm^2, similar to BEST1. Interestingly, however, these K2P channels are more mechanosensitive than MscL, responding to a much broader membrane tension range of ~ 0.5-12 mN/m (Brohawn et al., 2014b) compared to MscL, which is activated at membrane tensions of ~10-12 mN/m (Moe and Blount, 2005; Nomura et al., 2012). Whilst the larger ΔA for MscL would favor opening in the presence of lower membrane tensions, additional energetic penalties associated with the dramatic conformational changes of opening, including lipid bilayer deformation, increase the overall free energy difference between the closed and open structures (Brohawn, 2015). By contrast, the conformational changes between the open and closed states of mechanosensitive K2P channels are relatively modest, and the energy difference between them expected to be small (Brohawn, 2015; Brohawn et al., 2014a). In this way, BEST1 appears more comparable to mechanosensitive K2P channels, whereby an increase in cross-sectional area of the membrane-spanning region is coupled with modest overall conformational

changes that would not appear to cause significant bilayer deformation or membrane thinning.

Future work to assess possible mechanosensation of BEST1 should start with experiments that measure currents through the channel as a direct response to membrane tension, such as the patched membrane technique of channels in cells or reconstituted into vesicles (Del Mármol et al., 2018). Whether or not these channels are activated by increases in membrane tension, and how this mode of regulation might work in concert with other mechanisms of volume regulation, including ceramide-mediated dephosphorylation and intracellular [Cl⁻] sensing, is an exciting direction for research on this unusual channel.

5.6. Conclusion

Multiple bestrophin paralogs and homologs, studied in different cell types, have been shown to be regulated by cell volume (Chien and Hartzell, 2007; 2008; Fischmeister and Hartzell, 2005; Xiao et al., 2009). However, the mechanism of volume-regulation of bestrophins is unclear. Here, I provide the first evidence for one possible mechanism: inhibition of BEST1 by increases in intracellular [Cl⁻]. Further studies are needed to resolve the mechanism of Cl⁻ -dependent inhibition of BEST1, but initial studies presented here suggest a link to inactivation of the channel. A surface-exposed, electropositively charged pocket, proximal to the inactivation peptide of BEST1, might serve as a Cl⁻ sensor. Binding of Cl⁻ to this site may stabilize the binding of the inactivation peptide, analogous to the effects proposed for higher [Ca^{2+}]. The regulation of BEST1 by its permeant anion, Cl⁻, would be an efficient mechanism to control the opening and closing of the channel. Depending on the net influx or efflux of Cl⁻ in response to osomotic changes that occur as the cell volume increases and decreases,

changes in [Cl⁻] could help dictate whether the channel is open or not. Such a mode of regulation would be well suited for BEST1's proposed role in the RPE, the most phagocytically active cells in the human body (Mazzoni et al., 2014), where constant changes in cell volume, and subsequent changes to the direction of ion flow, are thought to be important for fluid transport homeostasis, which in turn plays an integral role in RPE phagocytosis (Marmorstein et al., 2009; 2018).

SUMMARY AND FUTURE DIRECTIONS

Using a combination of electrophysiological recordings, biochemical methods and structural analyses of purified chicken BEST1 I have investigated the fundamental mechanisms of bestrophin channel function. Electrical recordings of BEST1 in bilayers have enabled a detailed description of how different regions of the channel are responsible for its selectivity among anions and Ca^{2+}-dependent activation. I have been able to define a previously uncharacterized inactivation behavior of BEST1, and describe an allosteric mechanism that drives it. Together with visualization of distinct closed and open conformational states obtained by single particle cryo-EM, we now have a much more sophisticated understanding of how the bestrophin channel works and can begin to address why some mutations are disease-causing.

The work discussed here lays the groundwork to investigate additional regulatory mechanisms of bestrophin, such as cell volume-dependent regulation. This behavior is likely very important in bestrophins function in the RPE, but currently we have little understanding about the molecular mechanisms involved. Preliminary studies suggest that increases in cytosolic Cl^- concentration, which reduces ionic currents of BEST1, might be one means by which cell volume decreases inhibit channel function. Conclusions drawn from experiments presented here on chicken BEST1 will also serve as a framework with which we can begin to address the function of human bestrophin channels: all four paralogs. Future experiments can seek to understand how molecular differences between bestrophin paralogs lead to different biophysical properties, such as different ion permeabilites of BEST2 compared to BEST1, or how BEST3 appears fully inactivated in whole-cell recordings. Insights gained from these analyses will help our understanding of the distinct physiological roles these channels appear to have.

REFERENCES

Accardi, A., Kolmakova-Partensky, L., Williams, C., and Miller, C. (2004). Ionic currents mediated by a prokaryotic homologue of CLC Cl- channels. The Journal of General Physiology *123*, 109–119.

Adams, P.D., Afonine, P.V., Bunkóczi, G., Chen, V.B., Davis, I.W., Echols, N., Headd, J.J., Hung, L.W., Kapral, G.J., Grosse-Kunstleve, R.W., et al. (2012). PHENIX: a comprehensive Python-based system for macromolecular structure solution. (Chester, England: International Union of Crystallography), pp. 539–547.

Allikmets, R., Seddon, J.M., Bernstein, P.S., Hutchinson, A., Atkinson, A., Sharma, S., Gerrard, B., Li, W., Metzker, M.L., Wadelius, C., et al. (1999). Evaluation of the Best disease gene in patients with age-related macular degeneration and other maculopathies. Hum. Genet. *104*, 449–453.

Anishkin, A., Loukin, S.H., Teng, J., and Kung, C. (2014). Feeling the hidden mechanical forces in lipid bilayer is an original sense. Proc. Natl. Acad. Sci. U.S.a. *111*, 7898–7905.

Arden, G.B. (1962). Alterations in the standing potential of the eye associated with retinal disease. Trans Ophthalmol Soc U K *82*, 63–72.

Arden, G.B., Barrada, A., and Kelsey, J.H. (1962). New clinical test of retinal function based upon the standing potential of the eye. Br J Ophthalmol *46*, 449–467.

Armstrong, C.M. (1977). Inactivation of the sodium channel. II. Gating current experiments. The Journal of General Physiology *70*, 567–590.

Aryal, P., Abd-Wahab, F., Bucci, G., Sansom, M.S.P., and Tucker, S.J. (2014). A hydrophobic barrier deep within the inner pore of the TWIK-1 K2P potassium channel. Nature Communications *5*, 559.

Aryal, P., Sansom, M.S.P., and Tucker, S.J. (2015). Hydrophobic Gating in Ion Channels. Journal of Molecular Biology *427*, 121–130.

Bakall, B., Radu, R.A., Stanton, J.B., Burke, J.M., McKay, B.S., Wadelius, C., Mullins, R.F., Stone, E.M., Travis, G.H., and Marmorstein, A.D. (2007). Enhanced accumulation of A2E in individuals homozygous or heterozygous for mutations in BEST1 (VMD2). Exp. Eye Res. *85*, 34–43.

Bakall, B., Marmorstein, L.Y., Hoppe, G., Peachey, N.S., Wadelius, C., and Marmorstein, A.D. (2003). Expression and localization of bestrophin during normal mouse development. Invest. Ophthalmol. Vis. Sci. *44*, 3622–3628.

Bakall, B., McLaughlin, P., Stanton, J.B., Zhang, Y., Hartzell, H.C., Marmorstein, L.Y., and Marmorstein, A.D. (2008). Bestrophin-2 Is Involved in the Generation of Intraocular Pressure. Investigative Opthalmology & Visual Science *49*, 1563–1570.

Becq, F. (1996). Ionic channel rundown in excised membrane patches. Biochimica Et Biophysica Acta (BBA) - Reviews on Biomembranes *1286*, 53–63.

Bers, D.M., Patton, C.W., and Nuccitelli, R. (1994). A Practical Guide to the Preparation of Ca2 + Buffers. Methods in Cell Biology *40*, 3–29.

Besch, S.R., Suchyna, T., and Sachs, F. (2002). High-speed pressure clamp. Pflügers Archiv - European Journal of Physiology *445*, 161–166.

Best, F. (1905) Ueber eine hereditare Maculaaffektion: beiträge zur Vererbungslehre. Z Augenheilkd. *13*, 199-212

Boon, C.J.F., Klevering, B.J., Leroy, B.P., Hoyng, C.B., Keunen, J.E.E., and Hollander, den, A.I. (2009). The spectrum of ocular phenotypes caused by mutations in the BEST1 gene. Progress in Retinal and Eye Research *28*, 187–205.

Brohawn, S.G. (2015). How ion channels sense mechanical force: insights from mechanosensitive K2P channels TRAAK, TREK1, and TREK2. Ann. N. Y. Acad. Sci. *1352*, 20–32.

Brohawn, S.G., Campbell, E.B., and MacKinnon, R. (2013). Domain-swapped chain connectivity and gated membrane access in a Fab-mediated crystal of the human TRAAK K+ channel. Proc. Natl. Acad. Sci. U.S.a. *110*, 2129–2134.

Brohawn, S.G., Campbell, E.B., and MacKinnon, R. (2014a). Physical mechanism for gating and mechanosensitivity of the human TRAAK K+ channel. Nature *516*, 126–130.

Brohawn, S.G., Del Mármol, J., and MacKinnon, R. (2012). Crystal structure of the human K2P TRAAK, a lipid- and mechano-sensitive K+ ion channel. Science *335*, 436–441.

Brohawn, S.G., Su, Z., and MacKinnon, R. (2014b). Mechanosensitivity is mediated directly by the lipid membrane in TRAAK and TREK1 K+ channels. Proc. Natl. Acad. Sci. U.S.a. *111*, 3614–3619.

Brunger, A.T. (2007). Version 1.2 of the Crystallography and NMR system. Nature Protocols *2*, 2728–2733.

Burgess, R., Millar, I.D., Leroy, B.P., Urquhart, J.E., Fearon, I.M., De Baere, E., Brown, P.D., Robson, A.G., Wright, G.A., Kestelyn, P., et al. (2008). Biallelic mutation of BEST1 causes a distinct retinopathy in humans. Am. J. Hum. Genet. *82*, 19–31.

Cannon, C.L., Basavappa, S., and Strange, K. (1998). Intracellular ionic strength regulates the volume sensitivity of a swelling-activated anion channel. Am. J. Physiol. *275*, C416–C422.

Chang, G., Spencer, R.H., Lee, A.T., Barclay, M.T., and Rees, D.C. (1998). Structure of the MscL homolog from Mycobacterium tuberculosis: a gated mechanosensitive ion channel. Science *282*, 2220–2226.

Chiang, C.-S., Anishkin, A., and Sukharev, S. (2004). Gating of the large mechanosensitive channel in situ: estimation of the spatial scale of the transition from channel population responses. Biophysical Journal *86*, 2846–2861.

Chien, L.-T., and Hartzell, H.C. (2007). Drosophila Bestrophin-1 Chloride Current Is Dually Regulated by Calcium and Cell Volume. The Journal of General Physiology *130*, 513–524.

Chien, L.-T., and Hartzell, H.C. (2008). Rescue of volume-regulated anion current by bestrophin mutants with altered charge selectivity. The Journal of General Physiology *132*, 537–546.

Chien, L.-T., Zhang, Z.-R., and Hartzell, H.C. (2006). Single Cl- channels activated by Ca2+ in Drosophila S2 cells are mediated by bestrophins. The Journal of General Physiology *128*, 247–259.

Choi, K.L., Aldrich, R.W., and Yellen, G. (1991). Tetraethylammonium blockade distinguishes two inactivation mechanisms in voltage-activated K+ channels. Proceedings of the National Academy of Sciences *88*, 5092–5095.

Cooper, P.R., Nowak, N.J., Higgins, M.J., Simpson, S.A., Marquardt, A., Stoehr, H., Weber, B.H., Gerhard, D.S., de Jong, P.J., and Shows, T.B. (1997). A sequence-ready high-resolution physical map of the best macular dystrophy gene region in 11q12-q13. Genomics *41*, 185–192.

Cross, H.E., and Bard, L. (1984). Electro-Oculography in Best's Macular Dystrophy. American Journal of Ophthalmology *77*, 46–50.

Cross, S.D., Johnson, A.A., Gilles, B.J., Bachman, L.A., Inoue, T., Agata, K., Marmorstein, L.Y., and Marmorstein, A.D. (2015). Control of Maintenance and Regeneration of Planarian Eyes by ovo. Investigative Opthalmology & Visual Science *56*, 7604–7610.

Cui, C.-Y., Childress, V., Piao, Y., Michel, M., Johnson, A.A., Kunisada, M., Ko, M.S.H., Kaestner, K.H., Marmorstein, A.D., and Schlessinger, D. (2012). Forkhead transcription factor FoxA1 regulates sweat secretion through Bestrophin 2 anion channel and Na-K-Cl cotransporter 1. Proc. Natl. Acad. Sci. U.S.a. *109*, 1199–1203.

Dalvin, L.A., Johnson, A.A., Pulido, J.S., Dhaliwal, R., and Marmorstein, A.D. (2015). Nonantibestrophin Anti-RPE Antibodies in Paraneoplastic Exudative Polymorphous Vitelliform Maculopathy. Transl Vis Sci Technol *4*, 2.

Dang, S., Feng, S., Tien, J., Peters, C.J., Bulkley, D., Lolicato, M., Zhao, J., Zuberbühler, K., Ye, W., Qi, L., et al. (2017). Cryo-EM structures of the TMEM16A calcium-activated chloride channel. Nature *552*, 426–429.

Davidson, A.E., Millar, I.D., Urquhart, J.E., Burgess-Mullan, R., Shweikh, Y., Parry, N., O'Sullivan, J., Maher, G.J., McKibbin, M., Downes, S.M., et al. (2009). Missense Mutations in a Retinal Pigment Epithelium Protein, Bestrophin-1, Cause Retinitis Pigmentosa. The American Journal of Human Genetics *85*, 581–592.

Del Mármol, J., Rietmeijer, R.A., and Brohawn, S.G. (2018). Studying Mechanosensitivity of Two-Pore Domain K+ Channels in Cellular and Reconstituted Proteoliposome Membranes. Methods Mol. Biol. *1684*, 129–150.

Deneka, D., Sawicka, M., Lam, A.K.M., Paulino, C., and Dutzler, R. (2018). Structure of a volume-regulated anion channel of the LRRC8 family. Nature *558*, 254–259.

Deutman, A.F. (1969). Electro-oculography in Families With Vitelliform Dystrophy of the Fovea. Archives of Ophthalmology *81*, 305–316.

Dobrowsky, R.T., Kamibayashi, C., Mumby, M.C., and Hannun, Y.A. (1993). Ceramide activates heterotrimeric protein phosphatase 2A. Journal of Biological Chemistry *268*, 15523–15530.

Dong, Y.Y., Pike, A.C.W., Mackenzie, A., McClenaghan, C., Aryal, P., Dong, L., Quigley, A., Grieben, M., Goubin, S., Mukhopadhyay, S., et al. (2015). K2P channel gating mechanisms revealed by structures of TREK-2 and a complex with Prozac. Science *347*, 1256–1259.

Doyle, D.A. (1998). The Structure of the Potassium Channel: Molecular Basis of K+ Conduction and Selectivity. Science *280*, 69–77.

Egelman, E.H. (2016). The Current Revolution in Cryo-EM. Biophysical Journal *110*, 1008–1012.

Eldred, G.E., and Lasky, M.R. (1993). Retinal age pigments generated by self-assembling lysosomotropic detergents. Nature *361*, 724–726.

Ellis-Davies, G.C., and Kaplan, J.H. (1994). Nitrophenyl-EGTA, a photolabile chelator that selectively binds Ca2+ with high affinity and releases it rapidly upon photolysis. Proceedings of the National Academy of Sciences *91*, 187–191.

Emsley, P., Lohkamp, B., Scott, W.G., and Cowtan, K. (2010). Features and development of Coot. Acta Cryst (2010). D66, 486-501 [Doi:10.1107/S0907444910007493] 1–16.

Fernandez-Leiro, R., and Scheres, S.H.W. (2017). A pipeline approach to single-particle processing in RELION. Acta Crystallogr D Struct Biol *73*, 496–502.

Fischmeister, R., and Hartzell, H.C. (2005). Volume sensitivity of the bestrophin family of chloride channels. The Journal of Physiology *562*, 477–491.

Forsman, K., Graff, C., Nordström, S., Johansson, K., Westermark, E., Lundgren, E., Gustavson, K.H., Wadelius, C., and Holmgren, G. (1992). The gene for Best's macular dystrophy is located at 11q13 in a Swedish family. Clin. Genet. *42*, 156–159.

Gallemore, R.P., Hughes, B.A., and Miller, S.S. (1997). Retinal pigment epithelial transport mechanisms and their contributions to the electroretinogram. Progress in Retinal and Eye Research *16*, 509–566.

Gouras, P., Braun, K., Ivert, L., Neuringer, M., and Mattison, J.A. (2009). Bestrophin detected in the basal membrane of the retinal epithelium and drusen of monkeys with drusenoid maculopathy. Graefes Arch. Clin. Exp. Ophthalmol. *247*, 1051–1056.

Grant, T., Rohou, A., and Grigorieff, N. (2018). cisTEM, user-friendly software for single-

particle image processing. Elife *7*, e14874.

Hagen, A.R., Barabote, R.D., and Saier, M.H., Jr (2009). The bestrophin family of anion channels: identification of prokaryotic homologues. Molecular Membrane Biology *22*, 291–302.

Hao, J., and Delmas, P. (2011). Recording of mechanosensitive currents using piezoelectrically driven mechanostimulator. Nature Protocols *6*, 979–990.

Hartzell, C., Putzier, I., and Arreola, J. (2005a). Calcium-activated chloride channels. Annual Review of Physiology *67*, 719–758.

Hartzell, C., Qu, Z., Putzier, I., Artinian, L., Chien, L.-T., and Cui, Y. (2005b). Looking chloride channels straight in the eye: bestrophins, lipofuscinosis, and retinal degeneration. Physiology (Bethesda) *20*, 292–302.

Hartzell, H.C., Qu, Z., Yu, K., Xiao, Q., and Chien, L.-T. (2008). Molecular Physiology of Bestrophins: Multifunctional Membrane Proteins Linked to Best Disease and Other Retinopathies. Physiological Reviews *88*, 639–672.

Haswell, E.S., Phillips, R., and Rees, D.C. (2011). Mechanosensitive Channels: What Can They Do and How Do They Do It? Structure *19*, 1356–1369.

Hibbs, R.E., and Gouaux, E. (2011). Principles of activation and permeation in an anion-selective Cys-loop receptor. Nature *474*, 54–60.

Hille, B. (2001). Ionic channels of excitable membranes (Sinauer Associates, Sunderland, MA).

Hoffmann, E.K., and Ussing, H.H. (1992). Membrane Mechanisms in Volume Regulation in Vertebrate Cells and Epithelia. In Membrane Transport in Biology, (Berlin, Heidelberg: Springer Berlin Heidelberg), pp. 317–399.

Hoffmann, E.K., Lambert, I.H., and Pedersen, S.F. (2009). Physiology of cell volume regulation in vertebrates. Physiological Reviews *89*, 193–277.

Ito, G., Okamoto, R., Murano, T., Shimizu, H., Fujii, S., Nakata, T., Mizutani, T., Yui, S., Akiyama-Morio, J., Nemoto, Y., et al. (2013). Lineage-specific expression of bestrophin-2 and bestrophin-4 in human intestinal epithelial cells. PLoS ONE *8*, e79693.

Jackson, M.R., Beahm, R., Duvvuru, S., Narasimhan, C., Wu, J., Wang, H.-N., Philip, V.M., Hinde, R.J., and Howell, E.E. (2007). A Preference for Edgewise Interactions between Aromatic Rings and Carboxylate Anions: The Biological Relevance of Anion−Quadrupole Interactions. The Journal of Physical Chemistry B *111*, 8242–8249.

Johnson, A.A., Bachman, L.A., Gilles, B.J., Cross, S.D., Stelzig, K.E., Resch, Z.T., Marmorstein, L.Y., Pulido, J.S., and Marmorstein, A.D. (2015). Autosomal Recessive Bestrophinopathy Is Not Associated With the Loss of Bestrophin-1 Anion Channel Function in a Patient With a Novel BEST1Mutation. Investigative Opthalmology & Visual Science *56*, 4619–4630.

Johnson, A.A., Guziewicz, K.E., Lee, C.J., Kalathur, R.C., Pulido, J.S., Marmorstein, L.Y., and Marmorstein, A.D. (2017). Bestrophin 1 and retinal disease. Progress in Retinal and Eye Research *58*, 45–69.

Kane Dickson, V., Pedi, L., and Long, S.B. (2014). Structure and insights into the function of a Ca2+-activated Cl− channel. Nature *516*, 213–218.

Karplus, P.A., and Diederichs, K. (2012). Linking Crystallographic Model and Data Quality. Science *336*, 1030–1033.

Kaufman, S.J., Goldberg, M.F., Orth, D.H., Fishman, G.A., Tessler, H., and Mizuno, K. (1982). Autosomal dominant vitreoretinochoroidopathy. Archives of Ophthalmology *100*, 272–278.

Kilmartin, J.V., Wright, B., and Milstein, C. (1982). Rat monoclonal antitubulin antibodies derived by using a new nonsecreting rat cell line. J. Cell Biol. *93*, 576–582.

Kolesnick, R.N., and Krönke, M. (1998). Regulation of ceramide production and apoptosis. Annual Review of Physiology *60*, 643–665.

Krämer, F., Stöhr, H., and Weber, B.H.F. (2004). Cloning and characterization of the murine Vmd2 RFP-TM gene family. Cytogenet. Genome Res. *105*, 107–114.

Krämer, F., White, K., Pauleikhoff, D., Gehrig, A., Passmore, L., Rivera, A., Rudolph, G., Kellner, U., Andrassi, M., Lorenz, B., et al. (2000). Mutations in the VMD2 gene are associated with juvenile-onset vitelliform macular dystrophy (Best disease) and adult vitelliform macular dystrophy but not age-related macular degeneration. Eur. J. Hum. Genet. *8*, 286–292.

Kundaiker, S., Hussain, A.A., and Marshall, J. (1996). Component characteristics of the vectorial transport system for taurine in isolated bovine retinal pigment epithelium. The Journal of Physiology *492 (Pt 2)*, 505–516.

Kung, C. (2005). A possible unifying principle for mechanosensation. Nature *436*, 647–654.

Kung, C., Martinac, B., and Sukharev, S. (2010). Mechanosensitive channels in microbes. Annu. Rev. Microbiol. *64*, 313–329.

Kühlbrandt, W. (2014). Biochemistry. The resolution revolution. Science *343*, 1443–1444.

Lai, J.Y., Poon, Y.S., Kaiser, J.T., and Rees, D.C. (2013). Open and shut: crystal structures of the dodecylmaltoside solubilized mechanosensitive channel of small conductance from Escherichia coli and Helicobacter pylori at 4.4 Å and 4.1 Å resolutions. Protein Sci. *22*, 502–509.

Lang, F., Busch, G.L., Ritter, M., Völkl, H., Waldegger, S., Gulbins, E., and Häussinger, D. (1998). Functional significance of cell volume regulatory mechanisms. Physiological Reviews *78*, 247–306.

Lapan, S.W., and Reddien, P.W. (2012). Transcriptome analysis of the planarian eye identifies ovo as a specific regulator of eye regeneration. Cell Rep *2*, 294–307.

Lee, S., B.-E. Yoon, K. Berglund, S.-J. Oh, H. Park, H.-S. Shin, G.J. Augustine, and C.J. Lee. 2010. Channel-mediated tonic GABA release from glia. *Science*. 330:790–796. doi:10.1126/science.1184334.

Lee, S., Zheng, H., Shi, L., and Jiang, Q.-X. (2013). Reconstitution of a Kv Channel into Lipid Membranes for Structural and Functional Studies. Journal of Visualized Experiments.

Lee, W.-K., Chakraborty, P.K., Roussa, E., Wolff, N.A., and Thévenod, F. (2012). ERK1/2-dependent bestrophin-3 expression prevents ER-stress-induced cell death in renal epithelial cells by reducing CHOP. Biochim. Biophys. Acta *1823*, 1864–1876.

Li, Y., Zhang, Y., Xu, Y., Kittredge, A., Ward, N., Chen, S., Tsang, S.H., and Yang, T. (2017). Patient-specific mutations impair BESTROPHIN1's essential role in mediating Ca2+-dependent Cl- currents in human RPE. Elife *6*, 213.

Liao, M., Cao, E., Julius, D., and Cheng, Y. (2013). Structure of the TRPV1 ion channel determined by electron cryo-microscopy. Nature *504*, 107–112.

Liu, Y., Zhang, H., Huang, D., Qi, J., Xu, J., Gao, H., Du, X., Gamper, N., and Zhang, H. (2014). Characterization of the effects of Cl− channel modulators on TMEM16A and bestrophin-1 Ca2+ activated Cl− channels. Pflügers Archiv - European Journal of Physiology *467*, 1417–1430.

Lotery, A.J., Munier, F.L., Fishman, G.A., Weleber, R.G., Jacobson, S.G., Affatigato, L.M., Nichols, B.E., Schorderet, D.F., Sheffield, V.C., and Stone, E.M. (2000). Allelic variation in the VMD2 gene in best disease and age-related macular degeneration. Invest. Ophthalmol. Vis. Sci. *41*, 1291–1296.

Marchant, D., Yu, K., Bigot, K., Roche, O., Germain, A., Bonneau, D., Drouin-Garraud, V., Schorderet, D.F., Munier, F., Schmidt, D., et al. (2006). New VMD2 gene mutations identified in patients affected by Best vitelliform macular dystrophy. Journal of Medical Genetics *44*, e70–e70.

Marmorstein, A.D., Marmorstein, L.Y., Rayborn, M., Wang, X., Hollyfield, J.G., and Petrukhin, K. (2000). Bestrophin, the product of the Best vitelliform macular dystrophy gene (VMD2), localizes to the basolateral plasma membrane of the retinal pigment epithelium. Proceedings of the National Academy of Sciences *97*, 12758–12763.

Marmorstein, A.D., Cross, H.E., and Peachey, N.S. (2009). Functional roles of bestrophins in ocular epithelia. Progress in Retinal and Eye Research *28*, 206–226.

Marmorstein, A.D., Johnson, A.A., Bachman, L.A., Andrews-Pfannkoch, C., Knudsen, T., Gilles, B.J., Hill, M., Gandhi, J.K., Marmorstein, L.Y., and Pulido, J.S. (2018). Mutant Best1 Expression and Impaired Phagocytosis in an iPSC Model of Autosomal Recessive Bestrophinopathy. Sci Rep *8*, 4487.

Marmorstein, A.D., Kinnick, T.R., Stanton, J.B., Johnson, A.A., Lynch, R.M., and

Marmorstein, L.Y. (2015). Bestrophin-1 influences transepithelial electrical properties and Ca2+ signaling in human retinal pigment epithelium. Mol. Vis. *21*, 347–359.

Marmorstein, L.Y., McLaughlin, P.J., Stanton, J.B., Yan, L., Crabb, J.W., and Marmorstein, A.D. (2002). Bestrophin interacts physically and functionally with protein phosphatase 2A. Journal of Biological Chemistry *277*, 30591–30597.

Marmorstein, L.Y., Wu, J., McLaughlin, P., Yocom, J., Karl, M.O., Neussert, R., Wimmers, S., Stanton, J.B., Gregg, R.G., Strauss, O., et al. (2006). The light peak of the electroretinogram is dependent on voltage-gated calcium channels and antagonized by bestrophin (best-1). The Journal of General Physiology *127*, 577–589.

Marquardt, A., Stöhr, H., Passmore, L.A., Krämer, F., Rivera, A., and Weber, B.H. (1998). Mutations in a novel gene, VMD2, encoding a protein of unknown properties cause juvenile-onset vitelliform macular dystrophy (Best's disease). Hum. Mol. Genet. *7*, 1517–1525.

Mastronarde, D.N. (2005). Automated electron microscope tomography using robust prediction of specimen movements. Journal of Structural Biology *152*, 36–51.

Mazzoni, F., Safa, H., and Finnemann, S.C. (2014). Understanding photoreceptor outer segment phagocytosis: use and utility of RPE cells in culture. Exp. Eye Res. *126*, 51–60.

McCarty, N.A., and O'Neil, R.G. (1992). Calcium signaling in cell volume regulation. Physiological Reviews *72*, 1037–1061.

Milenkovic, A., Brandl, C., Milenkovic, V.M., Jendryke, T., Sirianant, L., Wanitchakool, P., Zimmermann, S., Reiff, C.M., Horling, F., Schrewe, H., et al. (2015). Bestrophin 1 is indispensable for volume regulation in human retinal pigment epithelium cells. Proceedings of the National Academy of Sciences *112*, E2630–E2639.

Milenkovic, V.M., Röhrl, E., Weber, B.H.F., and Strauss, O. (2011). Disease-associated missense mutations in bestrophin-1 affect cellular trafficking and anion conductance. J. Cell. Sci. *124*, 2988–2996.

Miller, C. (2013) Ion channel reconstitution (Springer Science & Business Media, New York)

Minor, W., Cymborowski, M., Otwinowski, Z., and Chruszcz, M. (2006). HKL-3000: the integration of data reduction and structure solution – from diffraction images to an initial model in minutes. Acta Crystallographica Section D Biological Crystallography *62*, 859–866.

Moe, P., and Blount, P. (2005). Assessment of potential stimuli for mechano-dependent gating of MscL: effects of pressure, tension, and lipid headgroups. Biochemistry *44*, 12239–12244.

Mohler, C.W., and Fine, S.L. (1981). Long-term evaluation of patients with Best's vitelliform dystrophy. Ophthalmology *88*, 688–692.

Ni, Y.-L., Kuan, A.-S., and Chen, T.-Y. (2014). Activation and Inhibition of TMEM16A

Calcium-Activated Chloride Channels. PLoS ONE *9*, e86734.

Nilius, B., Prenen, J., Voets, T., Eggermont, J., and Droogmans, G. (1998). Activation of volume-regulated chloride currents by reduction of intracellular ionic strength in bovine endothelial cells. The Journal of Physiology *506 (Pt 2)*, 353–361.

Nomura, T., Cranfield, C.G., Deplazes, E., Owen, D.M., Macmillan, A., Battle, A.R., Constantine, M., Sokabe, M., and Martinac, B. (2012). Differential effects of lipids and lyso-lipids on the mechanosensitivity of the mechanosensitive channels MscL and MscS. Proceedings of the National Academy of Sciences *109*, 8770–8775.

Nordström, S., and Barkman, Y. (1977). Hereditary maculardegeneration (HMD) in 246 cases traced to one gene-source in central Sweden. Hereditas *84*, 163–176.

Pedersen, S.F., Klausen, T.K., and Nilius, B. (2015). The identification of a volume-regulated anion channel: an amazing Odyssey. Acta Physiol (Oxf) *213*, 868–881.

Petrukhin, K., Koisti, M.J., Bakall, B., Li, W., Xie, G., Marknell, T., Sandgren, O., Forsman, K., Holmgren, G., Andreasson, S., et al. (1998). Identification of the gene responsible for Best macular dystrophy. Nat. Genet. *19*, 241–247.

Pettersen, E.F., Goddard, T.D., Huang, C.C., Couch, G.S., Greenblatt, D.M., Meng, E.C., and Ferrin, T.E. (2004). UCSF Chimera--a visualization system for exploratory research and analysis. J Comput Chem *25*, 1605–1612.

Philip, V., Harris, J., Adams, R., Nguyen, D., Spiers, J., Baudry, J., Howell, E.E., and Hinde, R.J. (2011). A Survey of Aspartate−Phenylalanine and Glutamate−Phenylalanine Interactions in the Protein Data Bank: Searching for Anion−π Pairs. Biochemistry *50*, 2939–2950.

Pianta, M.J., Aleman, T.S., Cideciyan, A.V., Sunness, J.S., Li, Y., Campochiaro, B.A., Campochiaro, P.A., Zack, D.J., Stone, E.M., and Jacobson, S.G. (2003). In vivo micropathology of Best macular dystrophy with optical coherence tomography. Exp. Eye Res. *76*, 203–211.

Qu, Z.Q., Yu, K., Cui, Y.-Y., Ying, C., and Hartzell, C. (2007). Activation of bestrophin Cl-channels is regulated by C-terminal domains. Journal of Biological Chemistry *282*, 17460–17467.

Qu, Z., and Hartzell, C. (2004). Determinants of anion permeation in the second transmembrane domain of the mouse bestrophin-2 chloride channel. The Journal of General Physiology *124*, 371–382.

Qu, Z., and Hartzell, H.C. (2000). Anion Permeation in Ca 2+-Activated Cl −Channels. The Journal of General Physiology *116*, 825–844.

Qu, Z., and Hartzell, H.C. (2008). Bestrophin Cl- channels are highly permeable to HCO3-. Am. J. Physiol., Cell Physiol. *294*, C1371–C1377.

Qu, Z., Chien, L.-T., Cui, Y., and Hartzell, H.C. (2006a). The anion-selective pore of the bestrophins, a family of chloride channels associated with retinal degeneration. J.

Neurosci. *26*, 5411–5419.

Qu, Z., Cui, Y., and Hartzell, C. (2006b). A short motif in the C-terminus of mouse bestrophin 4 inhibits its activation as a Cl channel. FEBS Letters *580*, 2141–2146.

Qu, Z., Fischmeister, R., and Hartzell, C. (2004). Mouse Bestrophin-2 Is a Bona fide Cl −Channel. The Journal of General Physiology *123*, 327–340.

Qu, Z., Wei, R.W., Mann, W., and Hartzell, H.C. (2003). Two bestrophins cloned from Xenopus laevis oocytes express Ca(2+)-activated Cl(-) currents. Journal of Biological Chemistry *278*, 49563–49572.

Rao, S., Klesse, G., Stansfeld, P.J., Tucker, S.J., and Sansom, M.S.P. (2017). A BEST example of channel structure annotation by molecular simulation. Channels *11*, 347–353.

Rohou, A., and Grigorieff, N. (2015). CTFFIND4: Fast and accurate defocus estimation from electron micrographs. Journal of Structural Biology *192*, 216–221.

Ruvolo, P.P. (2001). Ceramide regulates cellular homeostasis via diverse stress signaling pathways. Leukemia *15*, 1153–1160.

Sabirov, R.Z., Prenen, J., Tomita, T., Droogmans, G., and Nilius, B. (2000). Reduction of ionic strength activates single volume-regulated anion channels (VRAC) in endothelial cells. Pflügers Archiv - European Journal of Physiology *439*, 315–320.

Salceda, R., López-Colomé, A.M., and Pasantes-Morales, H. (1977). Light-stimulated release of [35S]taurine from frog retinal rod outer segments. Brain Res. *135*, 186–191.

Scheres, S.H.W. (2012). RELION: implementation of a Bayesian approach to cryo-EM structure determination. Journal of Structural Biology *180*, 519–530.

Schmidt, S.Y. (1978). Taurine fluxes in isolated cat and rat retinas: effects of illumination. Exp. Eye Res. *26*, 529–535.

Seddon, J.M., Afshari, M.A., Sharma, S., Bernstein, P.S., Chong, S., Hutchinson, A., Petrukhin, K., and Allikmets, R. (2001). Assessment of mutations in the Best macular dystrophy (VMD2) gene in patients with adult-onset foveomacular vitelliform dystrophy, age-related maculopathy, and bull's-eye maculopathy. Ophthalmology *108*, 2060–2067.

Smart, O.S., Neduvelil, J.G., Wang, X., Wallace, B.A., and Sansom, M.S.P. (1996). HOLE: A program for the analysis of the pore dimensions of ion channel structural models. Journal of Molecular Graphics *14*, 354–360.

Song, W., Yang, Z., and He, B. (2014). Bestrophin 3 Ameliorates TNFα-Induced Inflammation by Inhibiting NF-κB Activation in Endothelial Cells. PLoS ONE *9*, e111093.

Sparrow, J.R., and Boulton, M. (2005). RPE lipofuscin and its role in retinal pathobiology. Exp. Eye Res. *80*, 595–606.

Stanton, J.B., Goldberg, A.F.X., Hoppe, G., Marmorstein, L.Y., and Marmorstein, A.D.

(2006). Hydrodynamic properties of porcine bestrophin-1 in Triton X-100. Biochim. Biophys. Acta *1758*, 241–247.

Stockbridge, R.B., Kolmakova-Partensky, L., Shane, T., Koide, A., Koide, S., Miller, C., and Newstead, S. (2015). Crystal structures of a double-barrelled fluoride ion channel. Nature *525*, 548–551.

Stone, E.M., Nichols, B.E., Streb, L.M., Kimura, A.E., and Sheffield, V.C. (1992). Genetic linkage of vitelliform macular degeneration (Best's disease) to chromosome 11q13. Nat. Genet. *1*, 246–250.

Stöhr, H., Marquardt, A., Rivera, A., Cooper, P.R., Nowak, N.J., Shows, T.B., Gerhard, D.S., and Weber, B.H. (1998). A gene map of the Best's vitelliform macular dystrophy region in chromosome 11q12-q13.1. Genome Res. *8*, 48–56.

Stöhr, H., Marquardt, A., Nanda, I., Schmid, M., and Weber, B.H.F. (2002). Three novel human VMD2-like genes are members of the evolutionary highly conserved RFP-TM family. Eur. J. Hum. Genet. *10*, 281–284.

Sukharev, S.I., Blount, P., Martinac, B., and Kung, C. (1997). Mechanosensitive channels of Escherichia coli: the MscL gene, protein, and activities. Annual Review of Physiology *59*, 633–657.

Sukharev, S.I., Blount, P., Martinac, B., Blattner, F.R., and Kung, C. (1994). A large-conductance mechanosensitive channel in E. coli encoded by mscL alone. Nature *368*, 265–268.

Sun, H., Tsunenari, T., Yau, K.-W., and Nathans, J. (2002). The vitelliform macular dystrophy protein defines a new family of chloride channels. Proceedings of the National Academy of Sciences *99*, 4008–4013.

Syeda, R., Qiu, Z., Dubin, A.E., Murthy, S.E., Florendo, M.N., Mason, D.E., Mathur, J., Cahalan, S.M., Peters, E.C., Montal, M., et al. (2016). LRRC8 Proteins Form Volume-Regulated Anion Channels that Sense Ionic Strength. Cell *164*, 499–511.

Tang, G., Peng, L., Baldwin, P.R., Mann, D.S., Jiang, W., Rees, I., and Ludtke, S.J. (2007). EMAN2: an extensible image processing suite for electron microscopy. Journal of Structural Biology *157*, 38–46.

Tansel, B. (2012). Significance of thermodynamic and physical characteristics on permeation of ions during membrane separation: Hydrated radius, hydration free energy and viscous effects. Separation and Purification Technology *86*, 119–126.

Tsunenari, T., Nathans, J., and Yau, K.-W. (2006). Ca 2+-activated Cl −Current from Human Bestrophin-4 in Excised Membrane Patches. The Journal of General Physiology *127*, 749–754.

Tsunenari, T., Sun, H., Williams, J., Cahill, H., Smallwood, P., Yau, K.-W., and Nathans, J. (2003). Structure-function analysis of the bestrophin family of anion channels. Journal of Biological Chemistry *278*, 41114–41125.

Vaisey, G., Miller, A.N., and Long, S.B. (2016). Distinct regions that control ion selectivity and calcium-dependent activation in the bestrophin ion channel. Proc. Natl. Acad. Sci. U.S.a. *113*, E7399–E7408.

Vaisey, G., and S.B. Long. 2018. An allosteric mechanism of inactivation in the calcium-dependent chloride channel BEST1. *The Journal of General Physiology*. jgp.201812190–14. doi:10.1085/jgp.201812190.

Walton, T.A., Idigo, C.A., Herrera, N., and Rees, D.C. (2015). MscL: channeling membrane tension. Pflügers Archiv - European Journal of Physiology *467*, 15–25.

Wang, W., Black, S.S., Edwards, M.D., Miller, S., Morrison, E.L., Bartlett, W., Dong, C., Naismith, J.H., and Booth, I.R. (2008). The Structure of an Open Form of an E. coli Mechanosensitive Channel at 3.45 A Resolution. Science *321*, 1179–1183.

Wang, Y., Liu, Y., Deberg, H.A., Nomura, T., Hoffman, M.T., Rohde, P.R., Schulten, K., Martinac, B., and Selvin, P.R. (2014). Single molecule FRET reveals pore size and opening mechanism of a mechano-sensitive ion channel. Elife *3*, e01834.

Weber, B.H., Walker, D., Müller, B., and Mar, L. (1994). Best's vitelliform dystrophy (VMD2) maps between D11S903 and PYGM: no evidence for locus heterogeneity. Genomics *20*, 267–274.

Weingeist, T.A., Kobrin, J.L., and Watzke, R.C. (1982). Histopathology of Best's Macular Dystrophy. Archives of Ophthalmology *100*, 1108–1114.

Wimmers, S., Karl, M., and Strauss, O. (2007). Ion channels in the RPE. Progress in Retinal and Eye Research *26*, 263–301.

Xiao, Q., Hartzell, H.C., and Yu, K. (2010). Bestrophins and retinopathies. Pflügers Archiv - European Journal of Physiology *460*, 559–569.

Xiao, Q., Prussia, A., Yu, K., Cui, Y.-Y., and Hartzell, H.C. (2008). Regulation of bestrophin Cl channels by calcium: role of the C terminus. The Journal of General Physiology *132*, 681–692.

Xiao, Q., Yu, K., Cui, Y.-Y., and Hartzell, H.C. (2009). Dysregulation of human bestrophin-1 by ceramide-induced dephosphorylation. The Journal of Physiology *587*, 4379–4391.

Yang, T., Liu, Q., Kloss, B., Bruni, R., Kalathur, R.C., Guo, Y., Kloppmann, E., Rost, B., Colecraft, H.M., and Hendrickson, W.A. (2014). Structure and selectivity in bestrophin ion channels. Science *346*, 355–359.

Yannuzi, L.A. (1987). Stereoscopic Atlas of Macular Diseases. Diagnosis and Treatment. American Journal of Ophthalmology *104*, 446.

Yardley, J., Leroy, B.P., Hart-Holden, N., Lafaut, B.A., Loeys, B., Messiaen, L.M., Perveen, R., Reddy, M.A., Bhattacharya, S.S., Traboulsi, E., et al. (2004). Mutations of

VMD2 splicing regulators cause nanophthalmos and autosomal dominant vitreoretinochoroidopathy (ADVIRC). Invest. Ophthalmol. Vis. Sci. *45*, 3683–3689.

Yu, K., Cui, Y., and Hartzell, H.C. (2006). The bestrophin mutation A243V, linked to adult-onset vitelliform macular dystrophy, impairs its chloride channel function. Invest. Ophthalmol. Vis. Sci. *47*, 4956–4961.

Yu, K., Lujan, R., Marmorstein, A., Gabriel, S., and Hartzell, H.C. (2010). Bestrophin-2 mediates bicarbonate transport by goblet cells in mouse colon. J. Clin. Invest. *120*, 1722–1735.

Yu, K., Qu, Z., Cui, Y., and Hartzell, H.C. (2007). Chloride channel activity of bestrophin mutants associated with mild or late-onset macular degeneration. Invest. Ophthalmol. Vis. Sci. *48*, 4694–4705.

Zhang, Y., Davidson, B.R., Stamer, W.D., Barton, J.K., Marmorstein, L.Y., and Marmorstein, A.D. (2009). Enhanced inflow and outflow rates despite lower IOP in bestrophin-2-deficient mice. Investigative Opthalmology & Visual Science *50*, 765–770.

Zheng, S.Q., Palovcak, E., Armache, J.-P., Verba, K.A., Cheng, Y., and Agard, D.A. (2017). MotionCor2: anisotropic correction of beam-induced motion for improved cryo-electron microscopy. Nat. Methods *14*, 331–332.

Zhou, M., Morais-Cabral, JH., Mann, S., and Mackinnon, R (2001). Potassium channel receptor site for the inactivation gate and quaternary amine inhibitors. Nature *411*, 657-661

Zhou, H.-X., Rivas, G., and Minton, A.P. (2008). Macromolecular crowding and confinement: biochemical, biophysical, and potential physiological consequences. Annu Rev Biophys *37*, 375–397.

Zhuk, S.A., and Edwards, A.O. (2006). Peripherin/RDS and VMD2 mutations in macular dystrophies with adult-onset vitelliform lesion. Mol. Vis. *12*, 811–815.